Structure-composition-property Relations in B-site Deficient Hexagonal Perovskite Systems

By

Ruth Margaret Adams

A thesis submitted to the University of Huddersfield in partial fulfilment of the requirements for the degree of Doctor of Philosophy.

September 2010

The Department of Chemical and Biological Sciences

University of Huddersfield

Queensgate

Huddersfield

HD1 3DH

I would like to dedicate this work to my father.

Acknowledgements

Firstly, I would like to thank my supervisor Dr. Lisa J. Gillie for her continued support, advice and guidance (not to mention her impeccable grammar skills!). She has not only re-assured me throughout my constant worrying but has also been completely willing to listen to me moan about everything and anything and for that I am extremely grateful. Thanks also go to colleagues at the Department of Engineering and materials at the University of Sheffield. In particular Prof. Derek C. Sinclair for his constant advice, Mr Andrew Mould and Tutu Sebastian for help performing all electrical measurements, especially Andrew, without all his help I would have been lost, and Dr. Nik Reeves-Mclaren for assistance in collection of high resolution XRD patterns.

Acknowledgements go to my fellow contemporaries in the PhD office. To the people who have supported me, given me a shoulder to cry on (probably whilst drunk!) and helped with all issues, work and home related, thanks, and to the people who have annoyed me, no end, thanks for spurring me on to achieve my best.

Recognition goes to all my close friends and family, Ian, Mark, Becky and, especially my mum, for being constantly proud despite not being completely sure of what I do! To my niece and nephews who are a joy to be around and manage to cheer me up every time I see them. Finally to Ryan who has bore the brunt of all my highs and lows and been supportive none the less.

Abstract

This thesis describes the structural and preliminary electrical characterisation of various "shifted" hexagonal B-site deficient perovskites, of generic formula, $A_4B_3O_{12}$. These ceramics are reported to possess promising microwave dielectric properties, which are a requirement for use in the ever evolving mobile telecommunications industry.

The 12R crystal structures of the $Ba_{3-x}Sr_xLaNb_3O_{12}$ series (x = 1 – 3) were refined at variable temperatures using NPD data in space group R-3 and some interesting behaviour was exhibited. All compositions were found to be antiphase tilted, the extent of which being dependent on the A-cation size. Upon heating, the tilt angle for all members of the series was found to decrease, although no tilt transitions from R-3 to R-3m were witnessed for all phases up to 900 °C, and a change in the magnitude of permittivity at 1 MHz was observed for all members except, $BaSr_2LaNb_3O_{12}$. Additionally evidence from preliminary low temperature data suggest relaxor ferroelectric type behaviour. $Ba_2SrLaNb_3O_{12}$ was found to possess the most promising dielectric properties although room exists for further improvement of the quality factor (Q value).

To facilitate further tuning of the dielectric properties, specifically Q, the $Ba_{3-x}Sr_xLaNb_{3-y}Ta_yO_{12}$ series (x = 0 - 3, y = 1 - 2) was investigated, with the introduction of Ta^{5+} on the B-site. Some interesting ordering of A- and B-sites was found to occur, and furthermore, Nb^{5+} was found to display a preference to inhabit the distorted environment of B(1), adjacent to the "shifted" region, compared to the undistorted B(2) site, in the perovskite block. Unusual microwave dielectric properties were displayed with all compositions exhibiting small and positive temperature coefficient of resonant frequency (TCF) values and significantly small Q values, the reverse of what is expected, thus implying that the B-site has some influence on TCF values in this case. The interesting dielectric properties may be explained by several factors, including, the increased strength associated with the covalency of the Ta-O bond compared to that of Nb-O and the presence of some significant impurity phases, particularly in the intermediate compositions that are richer in Ta^{5+}. The LCR data

collected revealed similar results as found for the $Ba_{3-x}Sr_xLaNb_3O_{12}$ series (x = 1 – 3), highlighting the limiting nature of the temperature range which did not, in fact reflect the true response of the compositions' behaviour. All of the compositions are antiphase tilted at room temperature therefore the collection of variable temperature diffraction data is warranted.

A range of novel Ta-based intergrowth compounds were synthesised and preliminarily characterised. No detailed structural or electrical data were collected for these compounds, however, the ability to form Ta-based intergrowths, in the first instance, has been established. It is postulated that by the formation of these intergrowth phases, the dielectric properties will be effectively tuned in comparison to those of the parent oxides that they are composed of, due to the regularisation of the octahedral layers that occurs upon the formation of such intergrowth structures. This often leads to improved TCF values, and by the introduction of Ta^{5+}, can also give improved Q values. Ta^{5+} was substituted for Nb^{5+} in the untilted 5^x6^y (x = 1 – 3, y = 1) layered compounds, however, it was found that to facilitate this, the replacement of Ba^{2+} for Sr^{2+} was also required on the A-site. This double substitution was a requirement to obtain compositions closer to single phase Ta-rich phases compared to Nb-rich compositions.

Contents

Chapter 1

1. Introduction

The perovskite structure with general formula ABX_3 is extremely flexible and lends itself to a variety of substitutions from nearly all elements in the periodic table. It is the ideal multifunctional structure, with many members of the perovskite family exhibiting various interesting physical properties including, electrical, magnetic, dielectric, optical, and catalytic behaviour which are directly related to the respective crystal structures. There are many compounds that are structurally derived from perovskites, such as Ruddlesden-Popper phases, Brownmillerite materials, and structures deficient in anions and / or cations that also exist.

1.1 Perovskite Structure

1.1.1 Cubic Perovskites

The ideal cubic perovskite structure is typified by the oxide compound $SrTiO_3$ with space group $Pm\bar{3}m$. The Sr^{2+} ions are located at the corners of the cubic unit cell, with the Ti^{4+} ions located at the body-centre, and the O^{2-} ions located at the edge centres. The Ti^{4+} ions are surrounded by an octahedron of O^{2-}, and these octahedra are linked together by their corners to form continuous sheets which are stacked one on top of another giving a corner-sharing array. The Sr^{2+} ions reside in the interstices. In this structure, A-site cations are arranged in cubo-octahedral coordination surrounded by twelve oxide anions (X) and the B-site cations are surrounded by six oxide anions (X) in octahedral coordination, ***figure 1.1***.

(a)   (b)
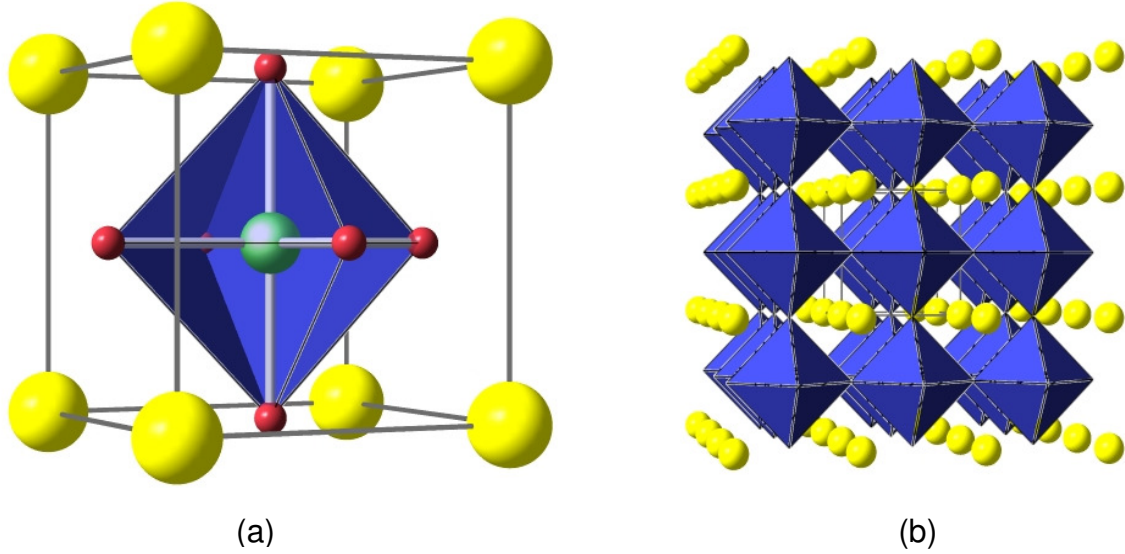
Figure 1.1: Depiction of $SrTiO_3$, Ti^{4+} ions, green, O^{2-} ions, red, and Sr^{2+} ions, yellow; (a) Octahedral coordination of B-cation; (b) corner sharing array of BO_6 octahedra.

In addition to the cubic perovskite structure described previously, a variety of non-cubic structures also exist. These structures are often distorted and of lower symmetry with a structural distortion occurring due to size incompatibility between all three ions. Repulsion within the structure results in distortion to accommodate these size differences. The degree of distortion within the structure can be predicted by the Goldschmidt tolerance factor, *t*, **equation 1.1**:[1]

$$t = \left(\frac{r(A) + r(X)}{\sqrt{2(r(B)+r(X))}} \right) \qquad \textbf{Equation 1.1}$$

where, $r(A)$ is the radius of the A-cation, $r(B)$ is the radius of the B-cation, and $r(X)$ is the radius of the X-anion.

The ideal cubic perovskite structure $SrTiO_3$ has a tolerance factor of 1, where $r_{(A)}$ = 1.44 Å, $r_{(B)}$ = 0.605 Å and $r_{(X)}$ = 1.40 Å. In fact cubic perovskites occur within the tolerance range $0.89 < t < 1$. If the A-site ion is smaller than the ideal value then $t<1$ and hence the octahedra can rotate or tilt, the magnitude of which increases when the tolerance factor decreases.[2] In most cases, tilting can reduce the coordination

number of the A-cation. If t >1, the A-site ion is large or the B-site ion is much smaller and hexagonal variants of the perovskite structure form. Various electrostatic considerations need to be taken into account within perovskite structures, these are defined by Pauling's rules,[3] given below:

1. Coordination Polyhedra – A coordination polyhedron of anions is formed around every cation. The cation-anion distances are determined by the sum of the ionic radii, and the coordination number of the cation by the radius rule, **table 1.1**.[1] Generally it is found that large cations tend to be surrounded by a cubic arrangement of anions, medium sized cations by an octahedral arrangement of anions and small cations are surrounded by a tetrahedron of anions. The smallest of cations are surrounded by a triangle of anions.[4]

Coordination	Minimum Radius Ratio R_{cation}/R_{anion}
Linear, 2	N/A
Trigonal, 3	0.155
Tetrahedral, 4	0.225
Octahedral, 6	0.414
Cubic, 8	0.732
Dodecahedral, 12	1.000

*Radius (R)

Table 1.1: Minimum Radius Ratios.

2. *The electrostatic valence rule* – In a stable ionic structure the valence (ionic charge) of each anion is exactly or nearly equal to the sum of the electrostatic bond strengths to it from adjacent cations. The electrostatic bond strength is defined as the ratio of the charge on a cation to its coordination number.[1]

This is related to the experimentally observed bond lengths using **equation 1.2** and **equation 1.3,** known as the bond valence sum.

$$V = \sum v_j \hspace{4cm} \textbf{\textit{Equation 1.2}}$$

The bond valence of an ion (V) is calculated from the individual bond valences (v_j) surrounding the ion.

$$v_j = exp\left(\frac{R_0 - R_j}{b}\right) \hspace{3cm} \textbf{\textit{Equation 1.3}}$$

The individual bond valences are calculated from observed bond lengths where R_j is the observed bond length, R_0 is the tabulated bond length, and b is a constant (~0.37 Å). Tabulated bond lengths are obtained from published values, and when more than one type of ion share a crystallographic site the refined fractional occupancies are also taken into account. Bond valence sums are then compared to theoretical values using formal cation vacancies. If the bond valence sum is found to be larger than the formal cation vacancy the ion is said to be over bonded, if the bond valence sum is found to be smaller than the formal cation vacancy then the ion is said to be under bonded.[4, 5]

3. Linking of polyhedra – The presence of shared edges, and especially shared faces, of coordination polyhedra decreases the stability of the structure since the positive ions are therefore brought closer together. This effect is large for positive ions of high charge and small coordination number, and this repulsion effect leads to distortion in the structure.[6]

4. Linking of polyhedra having different central cations – In a crystal containing different cations, those with large charge and small coordination number tend not to share polyhedral elements with each other, *i.e.* they keep as far apart as possible.[1]

Dependent on the degree of distortion within the structure, different crystal systems are adopted to provide the best possible packing of ions. There are seven in total:

cubic, tetragonal, orthorhombic, hexagonal, trigonal, monoclinic and triclinic, and each crystal system is governed by the presence or absence of symmetry and the lattice type.[7]

1.1.2 Octahedral Tilting

As mentioned previously due to size incompatibilities between ions, as predicted by the Goldschmidt tolerance factor, distortion of the structure can occur where the octahedra tilt to accommodate the A-cations. This leads to a lowering of symmetry structures from cubic. This tilting has a significant effect on the properties displayed by perovskite structures, which will be discussed later in ***Chapter 1.2***. Although some cation displacements and octahedral distortions are also witnessed in tilted structures, it is the tilting of octahedra that has a greater influence on properties. Tilting in perovskite structures was classified by Glazer in 1972 and he defined 23 tilt systems that are still in use today. [8]

Glazer describes octahedral tilting by specifying the rotation of the octahedra about each of the three Cartesian axes, this is specified by two parameters: (i) a letter detailing the degree of rotation about that axis, relative to the magnitude of the rotations about the other Cartesian axes; (ii) a superscript indicating whether the rotations in adjacent layers are in the same or opposite directions. A positive superscript indicates that the rotations about the tilt axis for two neighbouring octahedra are in the same direction and a negative superscript indicates the opposite, whereas a zero superscript indicates no tilting about that axis.[9] This positive and negative notation is often described as in-phase tilt and anti-phase tilt respectively. An untilted cubic perovskite would be described as $a^0a^0a^0$, an in-phase tilted structure as $a^+b^+c^+$, and an anti-phase tilted structure as $a^-b^-c^-$.

Another factor also defined by Glazer is the cooperative effect of tilting, which is when an octahedron in the perovskite structure is tilted in some particular way so that it causes tilting of the neighbouring octahedra. Hence considering structures with Glazer notation $a^0a^0c^+$ and $a^0a^0c^-$, it can be seen that there is only tilting along the z-axis, ***figure 1.2***, but tilting of the octahedra from the top layer causes tilting of all other octahedra in that layer, whether it be in-phase or anti-phase.

(a)   (b)
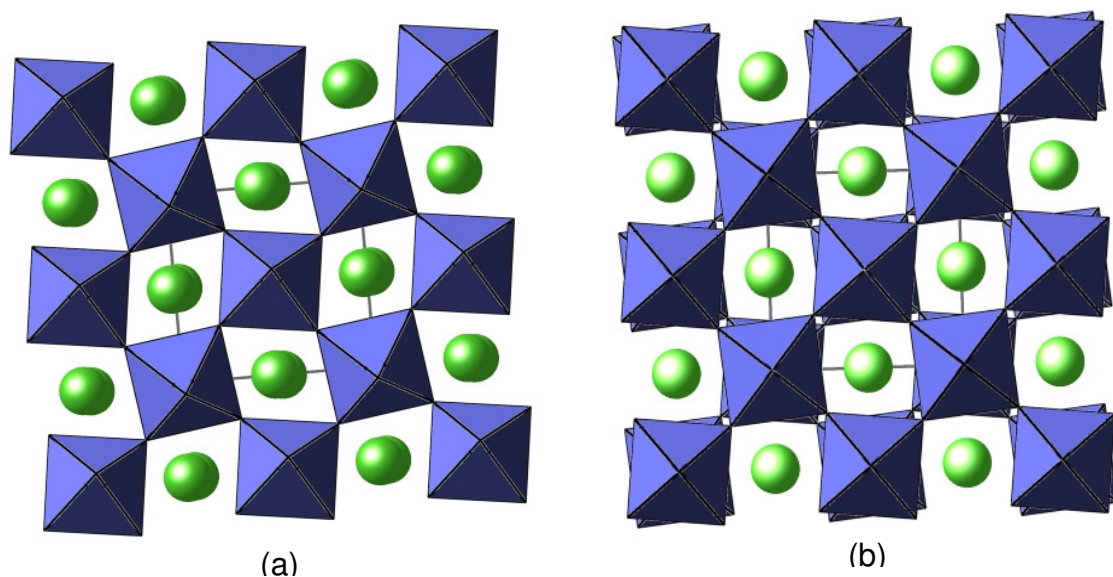
Figure 1.2: Perspective views along the *z*-axis of (a) tilt system $a^0a^0c^+$ (orthorhombic unit cell), and (b) tilt system $a^0a^0c^-$ (tetragonal unit cell).

Tilting of the BX_6 octahedra induces distortion of the AX_{12} polyhedra which may, in turn, result in a decrease of the A-site coordination number. In an ideal, untilted perovskite, the A-site cation is coordinated to twelve equidistant anions, situated at the corners of an ideal cubo-octahedron. If there is tilting about any axis, the A-X bond lengths change and become unequal. If the amount of rotation is small, the 12-fold coordination persists and the polyhedron becomes a distorted cubo-octahedron. Increasing tilt, however, results in six short, three medium and three long bonds, resulting in lower A-site coordination. With the exception of the $a^+a^+c^-$ tilt system, BX_6 octahedra do not undergo any distortion during tilting; however, octahedra can possess an inherent distortion, **figure 1.3**.

Distorted NbO_6 octahedra, bond lengths: (3 x ~1.854 Å), and (3 x ~2.179 Å).

Undistorted NbO_6 octahedra, bond lengths: (6 x ~1.987 Å).
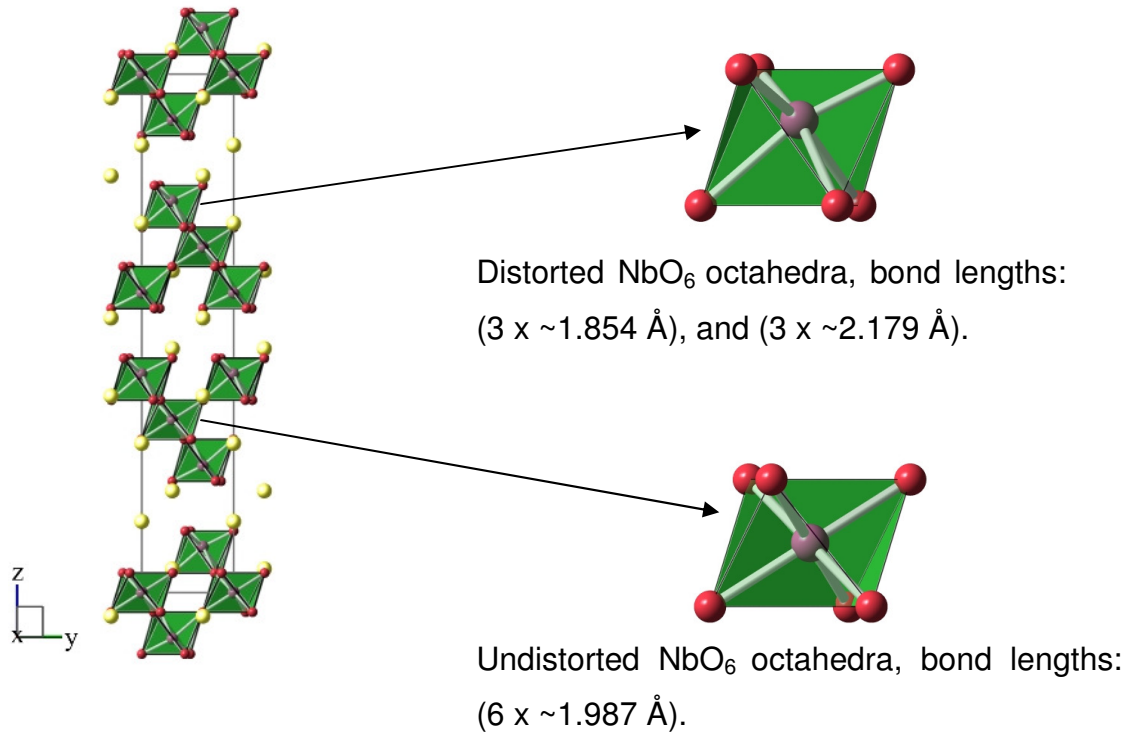
Figure 1.3:Depiction of $Ba_2SrLaNb_3O_{12}$, (Ba^{2+}/Sr^{2+} yellow spheres, O^{2-} red spheres, Nb^{5+} purple spheres, NbO_6 green octahedra) demonstrating distorted and undistorted octahedra.

Octahedral distortions may result in an increase or decrease of bond lengths and / or distortion of bond angles from the ideal value of 90°. Polyhedral bond length distortion Δd can be defined by **equation 1.4**:

$$\Delta d \ (\times \ 10^{-4}) = \sum \left(\frac{d-\bar{d}}{\bar{d}}\right)^2 \qquad \textbf{\textit{Equation 1.4}}$$

where d is the individual B-O bond length and $\bar{d}$ is the average B-O bond length.[10]

1.1.3 Hexagonal Perovskites

Perovskite types exist where the BX_6 octahedra are connected by sharing faces along the hexagonal z-axis, to form hexagonal perovskites. The relationship between cubic and hexagonal unit cells of the ABX_3 perovskite structure can be seen in **figure 1.4**. As stated earlier in Pauling's third rule, structures containing face-sharing octahedra are less stable than those with corner-sharing octahedra, but hexagonal perovskites can overcome this restriction by forming metal-metal bonds between the

B ions of the BX_6 octahedra, which are strong enough to overcome the metal-metal repulsion.

Hexagonal perovskites usually form when the Goldschmidt tolerance factor is greater than unity hence the structure is distorted to such an extent due to ion size mismatch, that face-sharing octahedra are formed. The ideal hexagonal perovskite structure adopts space group *P6₃/mmc*; $BaNiO_3$ typifies the ideal hexagonal perovskite structure, with a tolerance factor of 1.015. Akin to cubic perovskites, hexagonal perovskites can undergo distortion and / or cation ordering leading to a variety of structures with lower symmetry.
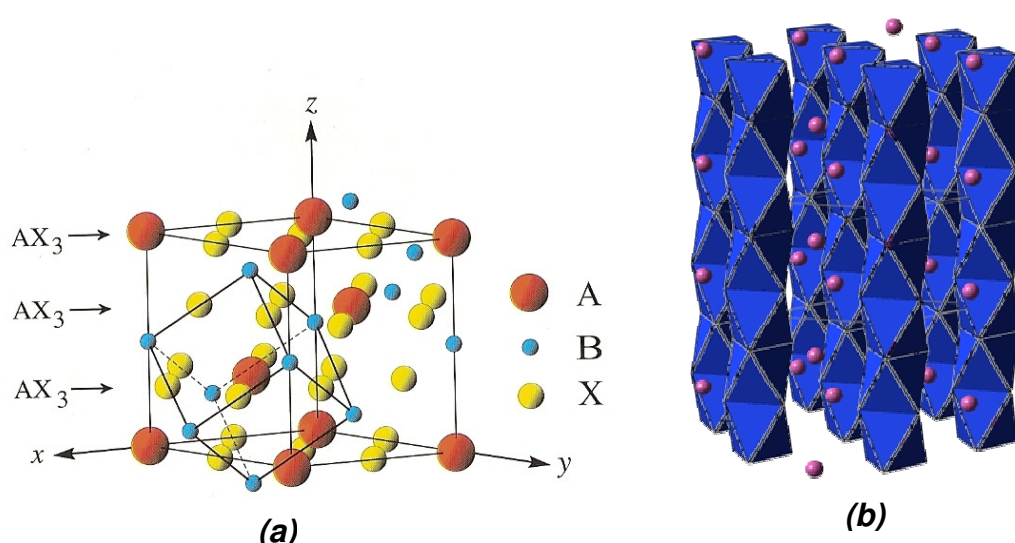
Figure 1.4: **(a)** The relationship between cubic and hexagonal unit cells of the ABX_3 perovskite structure[11] **(b)** Ideal hexagonal perovskite structure, 2H $BaNiO_3$ (NiO_6 octahedra, blue, and Ba^{2+} ions, pink.)

1.1.4 Hybrid Hexagonal Perovskites

Intermediate hexagonal polytypes exist containing different proportions of corner-sharing and face-sharing octahedra. The stacking sequences of the mixed hexagonal and cubic AX_3 layers can be described using Jagodzinski notation,[12] where a layer in the sequence is denoted *h* or *c* whether its neighbouring layers are alike or different. Typically, hybrid hexagonal perovskites are designated by a number indicating the number of AX_3 layers stacked along the *c*-axis in a unit cell and an upper case letter indicating the symmetry *i.e.* H indicating hexagonal setting and 'R' indicating rhombohedral setting.

The more common species of these polytypes are the 4H, 6H and 9R structures, typified by $SrMnO_3$,[13] $BaTiO_3$[14] and $BaRuO_3$[15] respectively, *figure 1.5*. Many of the higher order polytypes are less common and can often be non-stoichiometric.

1.1.5 B-Cation Deficient Perovskites $A_xB_{x-1}O_{3x}$

There are many non-stoichiometric hexagonal perovskites, and in particular a wide variety of B-cation deficient perovskites with the general formula $A_xB_{x-1}O_{3x}$. These non-stoichiometric structures often form to overcome cation repulsion effects which can lead to a less stable structure. Other ways of overcoming these effects are by the formation of metal-metal bonds, for example $BaRuO_3$,[15] or the ordered substitution of small valence cations, for example, $Ba_4Nb_3LiO_{12}$.[16]

Non-stoichiometric B-cation deficient perovskites can be subdivided into two classes, based on the distribution of the B-site cations, these classes are known as "shifted" and "twinned", *figure 1.6*. Shifted hexagonal perovskites have ordered vacancies between the *hh* layers resulting in a completely vacant layer in the middle of the face-sharing octahedral sequences, and can be described as (n - 1) layers of corner sharing octahedra with a vacant site in the centre of face sharing trimers, with the (*hhc...c*)-type sequence. They are referred to as shifted structures due to the resulting periodic shift by a vector of ⅓<01-10>$_H$ of neighbouring corner sharing octahedral blocks. Twinned hexagonal perovskites possess a mirror plane and have partial occupation of face sharing dimers, as opposed to a fully vacant octahedral site, and have the (*hc..c*)-type sequence.[17]
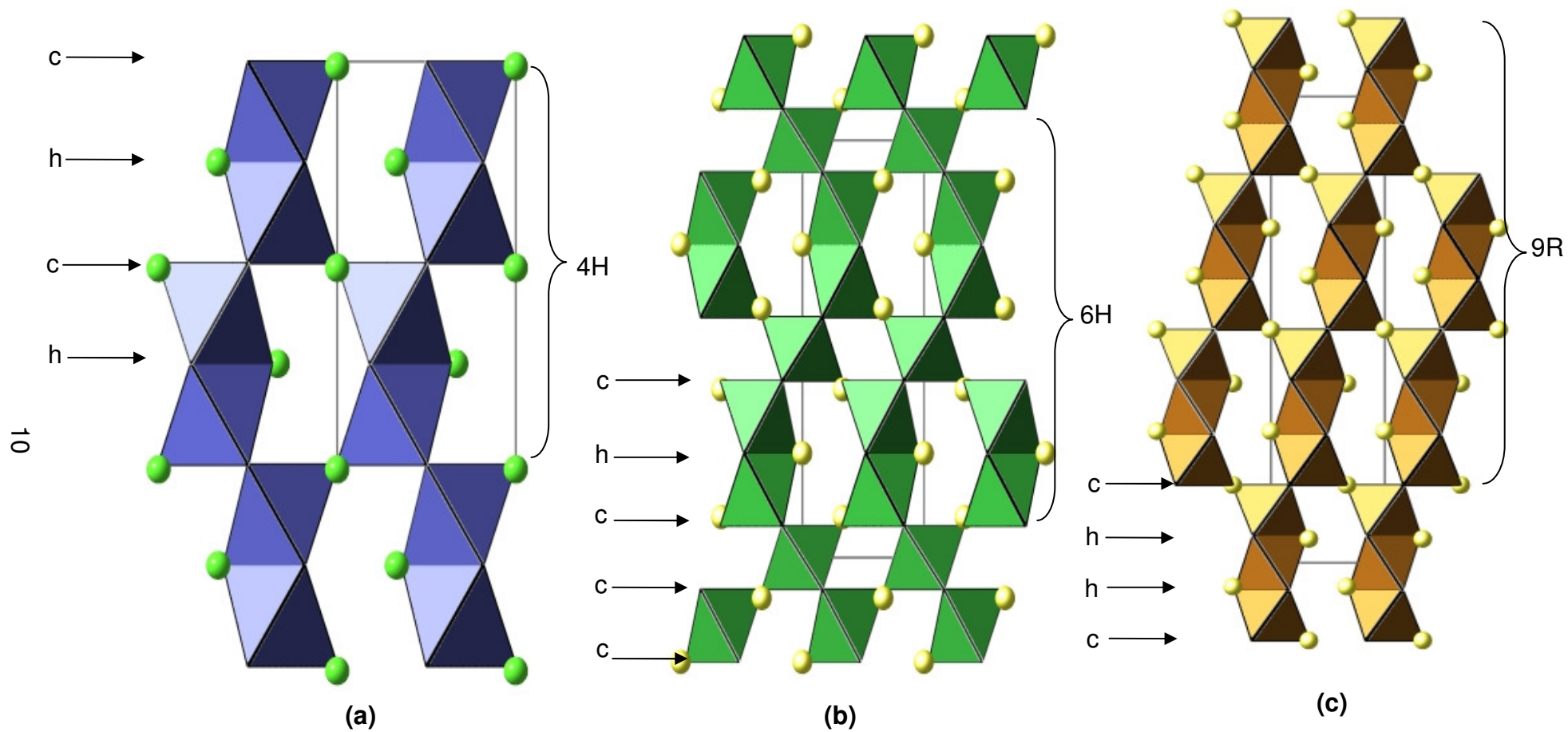
Figure 1.5: Hybrid hexagonal structures *(a)* SrMnO₃, 4H polytype *(b)* BaTiO₃, 6H polytype *(c)* BaRuO₃, 9R polytype.
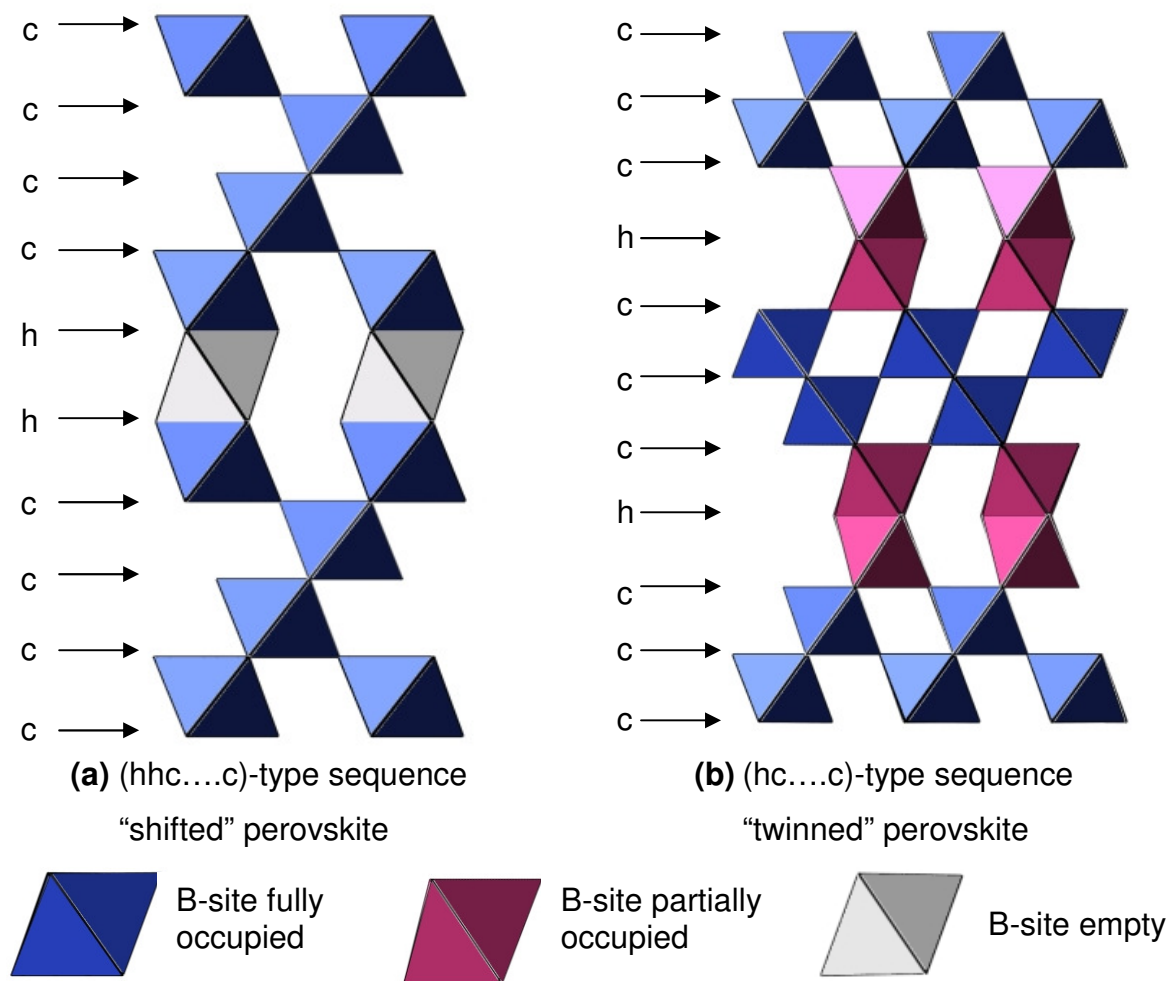
Figure 1.6: Example of **(a)** "shifted", and **(b)** "twinned" perovskites, reproduced from Trolliard *et al.*[17]

The stability of the "shifted" type structure is due to the relaxation of the body-centred cubic (*bcc*) AB-cationic sublattice across the shifted region, resulting in the occurrence of long range ordering of the vacant octahedral layers, every n octahedral layers along the *z*-axis. The stability of the "twinned" type structure is due to the drastic decrease of the periodicity of vacancies along the *z*-axis, but needs an expanded three dimensional BO_6 octahedral sublattice. To achieve this a high tolerance factor, a larger value of n and specific B-site ordering in the face-sharing octahedral blocks in the twinned region is required. However the majority of B-cation deficient perovskites are shifted and the twinned structure is rarely encountered.[18]

Many examples of B-site deficient perovskites of various compositions are discussed later in **section 1.2.4**.

1.1.6 Intergrowth Structures

Intergrowth structures are a rarer type of B-site deficient hexagonal perovskite, which are derived from simple parent structures, but possessing specific structural characteristics. They consist of the amalgamation of different compositions of perovskite blocks, for example Boullay *et al.*[19] demonstrated that the intergrowth structure $Ba_{11}TiNb_8O_{33}$ can be formed by combining stacking sequences of $Ba_5Nb_4O_{15}$ (n = 5) and $Ba_6TiNb_4O_{18}$ (n = 6). The resulting composition can be formulated as: 1 x $Ba_5Nb_4O_{15}$ + 1 x $Ba_6TiNb_4O_{18}$, and thus in a compact form 5^16^1, **figure 1.7**. It is also possible to expand the intergrowth series by altering the number of different perovskite blocks, for example the intergrowth structure 5^26^1 can be formed by 2 x $Ba_5Nb_4O_{15}$ + 1 x $Ba_6TiNb_4O_{18}$, resulting in the composition $Ba_{16}TiNb_{12}O_{48}$.

Examples of Intergrowth structures can be found in **section 1.2.4.5**.

$A_nB_{n-1}O_{3n}$; n=5 　　　　 Intergrowth 5^16^1 　　　　 $A_nB_{n-1}O_{3n}$; n=6
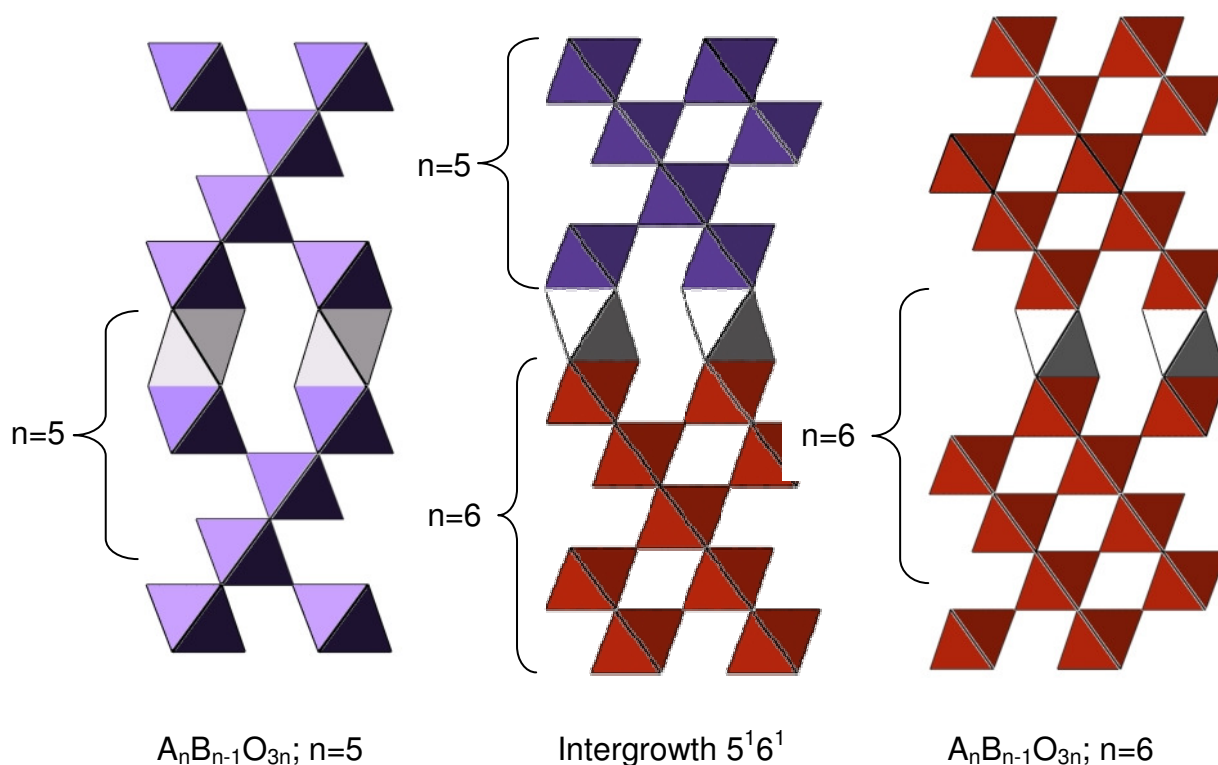
Figure 1.7: Example of intergrowth structure 5^16^1 reproduced from Boullay *et al.*[19] (centre), parent n=5 (left) and n=6 (right) oxides also illustrated.

1.2 Dielectric Behaviour

Perovskites possess a variety of useful electrical properties, including superconductivity, piezoelectricity and ferroelectricity.[20] Of specific interest here are perovskite structures for their dielectric properties which can be applied in the rapidly growing mobile telecommunications industry, where they are used as functional ceramics for application as resonators and filters in mobile phones, and global positioning systems. The advancement of such telecommunication devices has led to the requirement of miniaturisation of device components and highlighted the need for improved efficiency and performance of the component ceramics. Perovskites and related structure types also exhibit other useful properties such as colossal magnetorestistance and high Tc superconductivity, however these will not be discussed further here.

A dielectric material is one that is electrically insulating and exhibits an electric dipole structure, *i.e.* it can be polarised on application of an applied electric field. As a result of dipole interactions with electric fields, dielectric materials are often utilised as capacitors. Electronic polarisation is found in all dielectric materials and results from the displacement of the centre of the negatively charged electron cloud relative to the positive nucleus of an atom by the electric field. The polarisability of a dielectric material can be expressed by the dielectric constant ε_r, also known as the relative permittivity. Dielectric materials are often placed between oppositely charged plates in capacitors to increase their capacitance therefore the relative permittivity is an important factor when considering which dielectric material to use, as a high permittivity allows a greater charge to be stored at a given voltage.[21]

Within the microwave telecommunications industry the application of a dielectric material is as a resonator or filter. These ensure that signals are confined to closely defined allotted frequency bands and prevent the intrusion of unwanted signals. They are narrow band, frequency stable filters and oscillators which provide selectivity and stability. In its simplest form a dielectric resonator (DR) is a cylinder of ceramic which requires a high relative permittivity ($30 < \varepsilon_r < 100$), to ensure that the electromagnetic energy is adequately confined to the resonator, a temperature coefficient of resonant frequency TCF, close to zero to ensure stability against

frequency drift with temperature, and a maximised quality factor, Q usually greater than 1000 GHz to optimise frequency selectivity.[22] These factors will be elaborated upon throughout the following chapter.

1.2.1 Dielectric Properties

1.2.1.1 Relative Permittivity (ε_r)

Capacitance is a property closely related to permittivity, capacitance is a measure of the ability of a material to hold charge if a voltage is applied across it, *figure 1.8*.

$+Q$

Dielectric Laver $\updownarrow d$

$- Q$
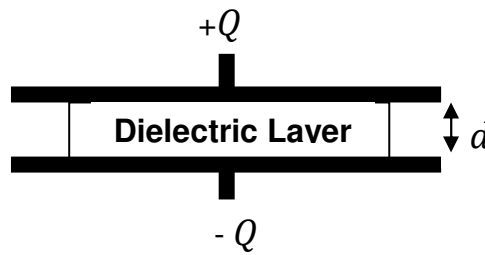
Figure 1.8: A model of a capacitor

If a voltage (V) is applied across a capacitor of capacitance (C), then the charge (Q) that it can hold is directly proportional to the applied voltage (V), with the capacitance (C) as the proportionality constant, ***equations 1.5*** and ***1.6***.

$$Q = CV \hspace{4cm} \textbf{\textit{Equation 1.5}}$$

$$C = Q/V \hspace{4cm} \textbf{\textit{Equation 1.6}}$$

The capacitance of a capacitor depends on the permittivity, ε of the dielectric layer, as well as the area (A) of the capacitor and the separation distance (d) between the two conductive plates. Permittivity and capacitance are mathematically related by ***equation 1.7***.

$$C = \varepsilon(A/d) \hspace{3.5cm} \textbf{\textit{Equation 1.7}}$$

When the dielectric used is a vacuum, then,

$$C_0 = \varepsilon_0(A/d) \hspace{3.5cm} \textbf{\textit{Equation 1.8}}$$

Where ε_0 is the permittivity of vacuum (8.85 x 10^{-12} F/m).

The dielectric constant ($\boldsymbol{\varepsilon_r}$) of a material is the ratio of its permittivity, ε to the permittivity of vacuum, ε_0, **equation 1.9**.

$$\varepsilon_r = \varepsilon/\varepsilon_0 \qquad\qquad \textbf{\textit{Equation 1.9}}$$

The ε_r is therefore also known as the relative permittivity of the material.

Given its definition, the dielectric constant of vacuum is 1. Any material is able to polarise more than vacuum, so the ε_r of a material is always > 1.

The relative permittivity is related to the resonant frequency, f_o by **equation 1.10**:

$$f_o \approx \frac{c}{\lambda_d\ \varepsilon_r^{1/2}} \approx \frac{c}{D\ \varepsilon_r^{1/2}} \qquad\qquad \textbf{\textit{Equation 1.10}}$$

where c is the speed of light in a vacuum and λ_d is the wavelength of the standing wave along the diameter, D, of a resonator. Subsequently if permittivity is increased, the size of the resonator may be decreased whilst still maintaining a selected frequency.[23]

The dielectric constants (or relative permittivity, $\boldsymbol{\varepsilon_r}$), of ceramics can be calculated theoretically using the Clausius-Mossotti (CM) Equation,[24] **equation 1.11**:

$$\varepsilon_r = \frac{3V_m + 8\pi\alpha_D^T}{3V_m - 4\pi\alpha_D^T} \qquad\qquad \textbf{\textit{Equation 1.11}}$$

where V_m is the molar volume and α_D^T is the sum of the polarisabilities of individual ions. It has been reported that values calculated by this equation agree well with measured values for cubic, hexagonal and mixed perovskites having useful dielectric properties.[25-31] The term α^T_m/V_m, derived from the CM equation is essentially a weighted average of the polarisabilities of all the ions per unit molar volume and has also been used to explain variations in permittivity amongst different perovskites. Shannon[32] showed that the dielectric constant calculated usually agrees with the experimental value for well behaved ceramics, however an inconsistency does arise when calculating the dielectric constant of lanthanum-containing oxides. Therefore

the ionic polarisability of La^{3+} is taken as 4.82 $\mathring{A}^3$, as suggested by Veneis *et al.*[33] instead of 6.09 $\mathring{A}^3$ reported by Shannon[34] in order to avoid this inconsistency.

1.2.1.2 Quality Factor (Q)

The quality factor, or rather as it is sometimes known, it's inverse dielectric loss (1 / tanδ) is a measure of the selectivity of a resonator at a particular frequency. A higher Q reduces the risk of cross talk within a selected frequency range. Q can be defined by **equation 1.12**, where f_0 is the resonant frequency divided by the bandwidth, Δf, measured at 3 dB below the maximum height at resonance, **figure 1.9**. The Q decreases with increasing frequency and $Q \times f_0$, should be constant for any given material; however, experimentally, samples measured at higher frequencies always give higher $Q \times f_0$, values than those measured at lower frequencies

.
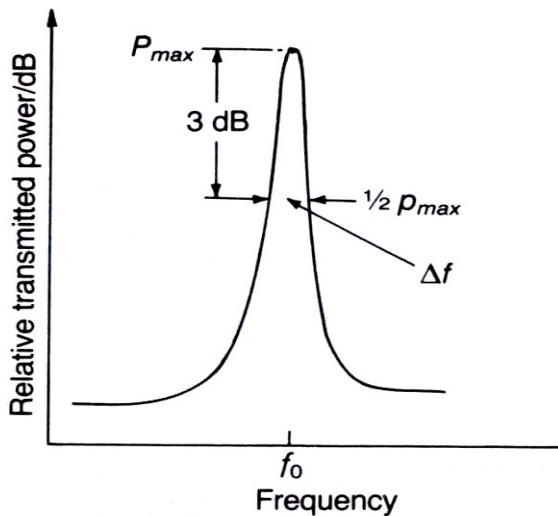
$$Q = \frac{f_0}{\Delta f}$$

Equation 1.12

Figure 1.9: Schematic resonance peak. [22]

Dielectric losses, which are inversely proportional to Q, are often impurity sensitive and there are many factors which contribute to these losses including:

(a) Intrinsic losses: where losses occur in an ideal crystal because of anharmonic lattice forces that mediate the interaction between the crystals' phonons. This leads to damping of the optical phonons and therefore of the microwave radiation.

16

(b) Losses occurring in real but homogeneous crystals caused by deviations from the perfect lattice periodicity or periodicity defects such as point defects, dopant atoms, vacancies or defect pairs that lead to quasi-bonded states. These defects lead to scattering of the phonons and thus to dampening of the phonons.

(c) Extrinsic losses: where losses occur in real inhomogeneous ceramics caused by extended dislocations, grain boundaries, inclusions and second phases. These losses are caused by either dipole relaxations of impurities concentrated at interfaces or relaxations of space charge polarisations present at interfaces.[35]

1.2.1.3 Temperature Coefficient of Resonant Frequency (TCF)

The temperature coefficient of resonant frequency (TCF ppm / °C) ensures stability against frequency drift with temperature and can be defined by **equation 1.13**, where τ_ε is the temperature coefficient of permittivity and α_L is the linear expansion coefficient. This is the temperature coefficient of one of the resonator's dimensions, usually length.[35]

$$TCF = -\left({}^{1}\!/_{2}\,\tau_\varepsilon \;+\; \alpha_L \right) \qquad\qquad \textbf{\textit{Equation 1.13}}$$

The aim is to achieve a temperature-independent resonant frequency *i.e.* $TCF = 0$ and this requires balanced control over τ_ε and α_L, where τ_ε is related to TCF by **equation 1.14**:

$$\tau_\varepsilon \approx -2\alpha_L \qquad\qquad \textbf{\textit{Equation 1.14}}$$

1.2.2 Structure-Dielectric Property Relationships

1.2.2.1 Complex cubic close-packed perovskites.

1.2.2.1.1 Ionic Polarisability

Dielectric behaviour is highly influenced by careful selection of cations in perovskite structures. Dielectric properties are closely correlated to transition metal ions present on the B-site and their filled 3d electron shells. The B-site transition metal choice is highly correlated with ε_r, and it is often found that a high ε_r is based on collective polar displacements of the metal ions with respect to the oxygen sublattice, this is a highly non-linear and anisotropic phenomenon, described by the CM equation.[36] There is a strong correlation between TCF and ε_r; in the 1960s Harrop[37] found that compounds with low ε_r exhibit a low TCF and *vice versa*, and demonstrated by using the CM equation that in microwave dielectrics, the ionic polarisability dominates ε_r, and thus TCF.

1.2.2.1.2 Octahedral Tilt Transition

It has long been established that Sr-based complex perovskites have positive TCFs and Ba-based complex perovskites have negative TCFs, the reasoning for this was thought to be due to phase transitions, and was explained by Colla *et al.*[38] The onset of octahedral tilt transitions in Ba- and Sr-based complex perovskites were studied, and it became evident that the dependence of TCF was not limited to ε_r, as these types of perovskites typically possess $25 < \varepsilon_r < 40$. It was therefore proposed by Reaney *et al.*[39] that the tolerance factor controls the temperature of the onset of octahedral tilt transitions, and thus TCF. Lower tolerance factors favour distorted structures that have undergone phase transitions on cooling, involving rotations of the BO_6 octahedra. Previous data from various series of Ba- and Sr-based complex perovskites were united, ***figure 1.10***, and τ_ε was plotted against the tolerance factor. This clearly demonstrates that cation choice dictates tolerance factor, which in turn affects octahedral tilt transition temperature and thus τ_ε.

Tolerance factor not only influences the onset temperature of an octahedral tilt transition but also the amplitude of rotation of the octahedra within any given perovskite crystal structure at room temperature, as described in **section 1.1.1**.

1.2.2.1.3 Bond Valence Sum

Another factor to be considered, that was reinvestigated recently by Lufaso et al.[40], is the bond valence sum of the B-site cation. It was found that for Ba-based ordered 1:2 compounds that neither ε_r nor tolerance factor correlated well with TCF for niobates and tantalates, although a correlation was found between TCF and the bond valence sum of the B-site M^{2+} ion, plotted in **figure 1.11**. A strong linear correlation was observed for the six structures considered, however this is by no means a universal approach although it does highlight that within narrow groups of similar composition, the degree of under-bonding for the B-site M^{2+} ion plays a role in the magnitude and sign of TCF.
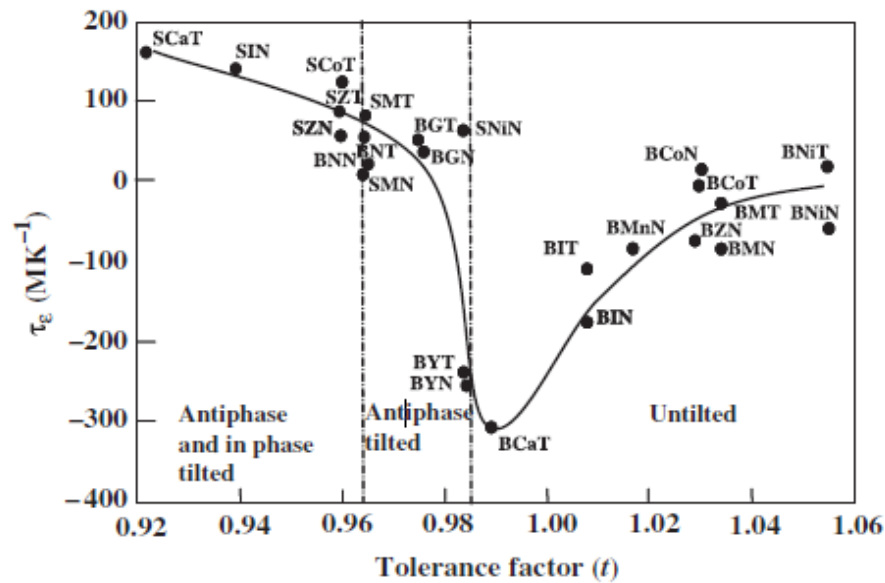
Figure 1.10: Tolerance factor, t *vs.* τ_ε at room temperature for A(B'B")O$_3$ (A = Sr, Ba; B' = In, Ca, Mn, Co, Ni, Zn, Mg, Nd, Gd; B" = Ta and Nb) 1:1 and 1:2 complex perovskites, reproduced from Reaney et al. [39]

19
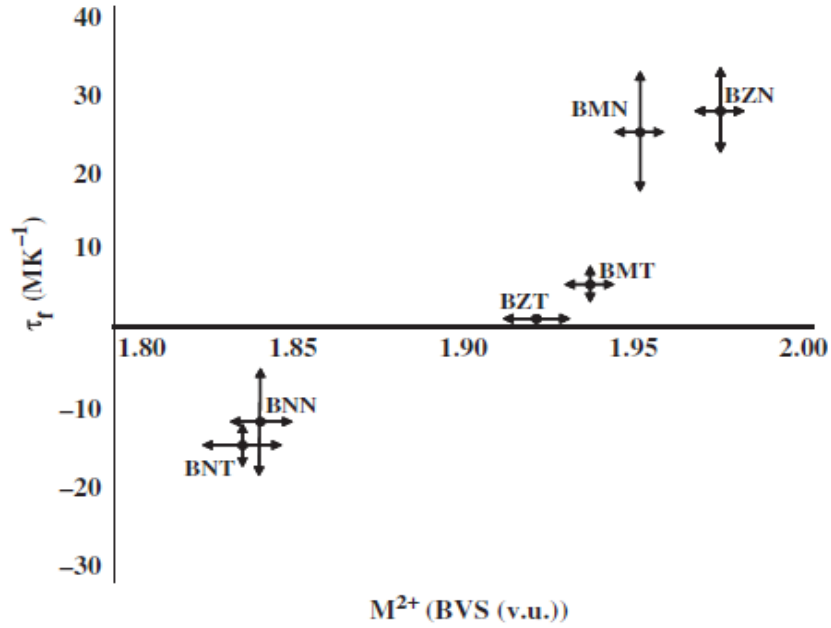
Figure 1.11: Average TCF vs. M^{2+} bond valence sum. BNT, $Ba(Ni_{1/3}Ta_{2/3})O_3$; BNN, $Ba(Ni_{1/3}Nb_{2/3})O_3$; BZT, $Ba(Zn_{1/3}Ta_{2/3})O_3$; BMT, $Ba(Mg_{1/3}Ta_{2/3})O_3$; BMN, $Ba(Mg_{1/3}Nb_{2/3})O_3$; BZN, $Ba(Zn_{1/3}Nb_{2/3})O_3$, from Lufaso.[40] (Error bars represent standard deviation).

1.2.2.1.4 Processing, Composition and Structure Dependence

Q is perhaps the most important dielectric property to be optimised for the purpose of commercial use, as previously mentioned in **section 1.2.1.2**. Intrinsic losses are controlled by anharmonic interaction of the a.c. electric field with the phonon system of the crystal, leading to dampening of the optical phonons.[35] These losses can be estimated using infra-red spectroscopy, as described by Ferreira *et al.*[41] Conversely it is the extrinsic losses that dominate Q in reality and several mechanisms are known to assist in the minimisation of extrinsic losses, including order / disorder behaviour, processing and careful selection of solid solution compositions.

Therefore it has been established that to maximise Q without any detrimental effect on other dielectric properties, ceramic processing has to be optimised to avoid coring issues, inhomogeneity, second phases, impurities and pressing defects. Compositions where short-range ordering dominates are to be avoided, and complex perovskites where long-range ordering dominates are preferential. For solid-solutions large differences in ionic radii are to be avoided.

1.2.2.2 Hexagonal B-Site Deficient Perovskites

Although a lot of research has investigated the relationship between structural factors and dielectric properties in complex cubic close-packed perovskites only a modest selection of literature is available on the structure-property relationships for the less common hexagonal B-cation deficient perovskite structures and their respective dielectric properties. The majority of the general trends hold true for hexagonal perovskites, that is, ionic polarisability and in particular a transition metal on the B-site influence dielectric properties greatly, more specifically the relative permittivity and cation choice have a significant effect. Processing, composition and structure dependence all influence the Q as in complex perovskites, and cation ordering in particular is an important issue. Octahedral tilt transitions do greatly influence dielectric properties however no direct empirical correlation has been established between TCF and tolerance factor in hexagonal perovskites[42]. Nevertheless, the general trend witnessed by Reaney *et al.*[39] has been demonstrated where TCF decreases as tilting increases[43] to a certain extent. It is, however, important to note that these studies were carried out on only a small selection of compounds, and the correlation is only valid for a selection of these.

To date the solitary structure-property relationship established for B-site deficient hexagonal perovskites is by Zue *et al.*[44] A structure related parameter, v, has been proposed to characterise the octahedral thickness variance, hence a correlation between the value of TCF and v has been established, ***equation 1.15***. v is the octahedral thickness variance parameter (%), and t_V and t_F are the vacant and filled octahedral thicknesses (the thickness or height of the blocks (Å)), respectively.

$$v = \frac{n \sum (t_V - t_F)}{c(n-1)}$$ ***Equation 1.15***

This approach illustrates that the octahedral thickness variance plays an important role in the magnitude and sign of TCF. As the octahedral thickness variance corresponds to the changes in bond strength or the restoring force on the ionic polarisation, the trend is generally identical to that found in some complex perovskite

materials with respect to the bond valence sum of the B-site M^{2+} ions.[40] The study investigated n=4, 5 and 6 layered B-site deficient hexagonal perovskites, however studies were mainly concentrated on n=5 samples as little structural data are available for the other layered compounds. There is a definite correlation between octahedral thickness variance and TCF, **figure 1.12**, however there are several issues with the study of the cited data. The inclusion of complex compositions possibly masking the effect of octahedral thickness variance by the greater effect of the change of A-site and B-site occupancy may make the data less reliable, and in addition, the compounds became denser with increasing number of octahedral layers per unit-cell, which also influences TCF. Other processing issues that affect dielectric properties, specifically Q, have an effect and the reliability of the cited data must also be considered.[44]

Legend:
- BN: $Ba_5Nb_4O_{15}$
- BT: $Ba_5Ta_4O_{15}$
- BNT: $Ba_5Nb_2Ta_2O_{15}$
- B4L: $Ba_4LaTiNb_3O_{15}$
- BLT: $BaLa_4Ti_4O_{15}$
- CLT: $CaLa_4Ti_4O_{15}$
- LZT: $La_5Zn_{0.5}Ti_{3.5}O_{15}$
- LMT: $La_5Mg_{0.5}Ti_{3.5}O_{15}$
- LGT: $La_5GaTi_3O_{15}$
- LAT: $La_5AlTi_3O_{15}$
- B2LT: $Ba_2La_4Ti_5O_{15}$
- B6NT: $Ba_6Nb_4TiO_{18}$
- B3L3: $Ba_3La_3Ti_4NbO_{18}$
- B4L2: $Ba_4La_2Ti_3Nb_2O_{18}$
- L4T3: $La_4Ti_3O_{12}$
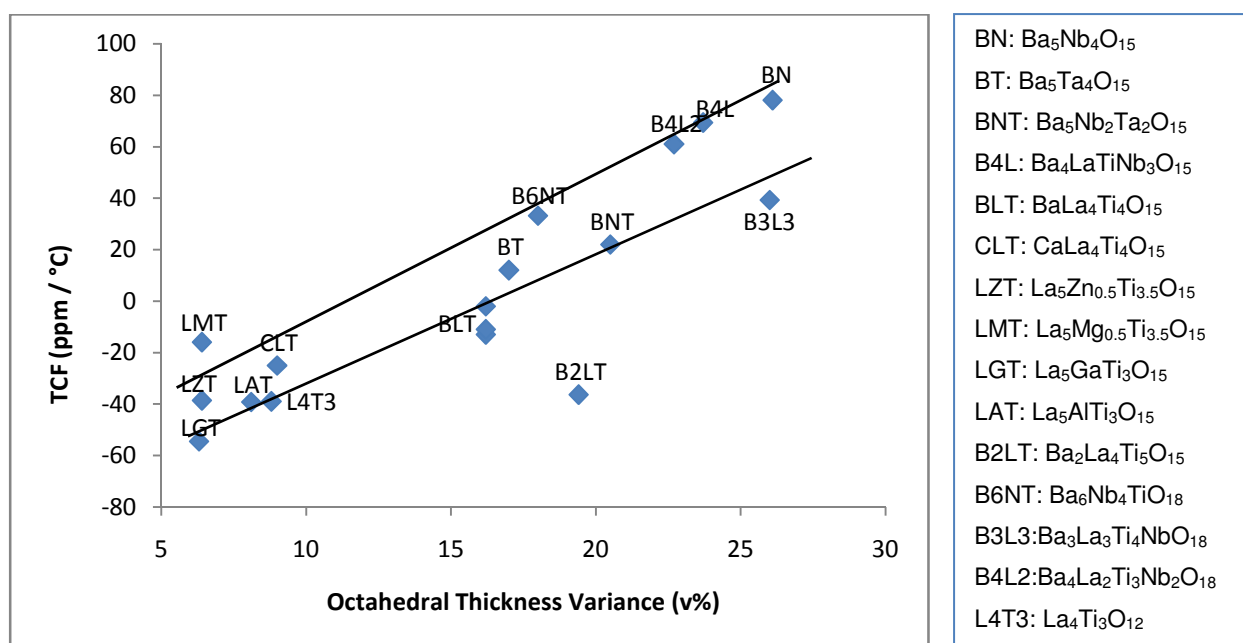
Figure 1.12: Octahedral thickness variance *vs.* temperature coefficient of resonant frequency for B-site deficient perovskites, reproduced from Yue *et al.*[45]

Zhao *et al.*[46] examined the dielectric properties of intergrowth compounds, which are formed from B-cation deficient perovskites, discussed previously in **section 1.1.6**, with an aim to improve the TCF by formation of these structures. It was found that intergrowth compounds allow the degree of atomic displacements to be reduced and therefore the TCF is improved by the formation of intergrowths. Hence the

change in TCF was evaluated by the degree of atomic displacements and a parameter d (**equation 1.16**) was established on the basis of octahedral layer thickness to evaluate the degree of atomic displacements. TCF was reported to increase with increasing d value.

$$d = \frac{1/n_f \sum(t_V - t_F)}{t_A}$$

Equation 1.16

where n_f is the filled octahedral layer numbers, and d is the degree of atomic displacements (%). t_V, t_F, and t_A are the vacant, filled, and average thickness of octahedral layers, respectively.

After taking all current theories into consideration a parameter known as the variance, Δ was introduced to this study to assess the degree of distortion within "shifted" structures. "Shifted" type structures derive their stability from the reconstruction of the *bcc* cation sublattice across the "shifted" region. Therefore the variance of eight A-B distances from three *bcc* unit cells across the "shifted" region is taken, and Δ is obtained by taking the average for the three *bcc* unit cells. This parameter allows the degree of distortion across the "shifted" region to be compared between structures irrespective of the number of layers. Variance and Δ are calculated using **equations 1.17** and **1.18**. **Figure 1.13** depicts the A- and B-cations involved in the three *bcc* unit cells and the construction of the three *bcc* unit cells. The black bonds highlight the eight A-B bonds selected for each unit cell.
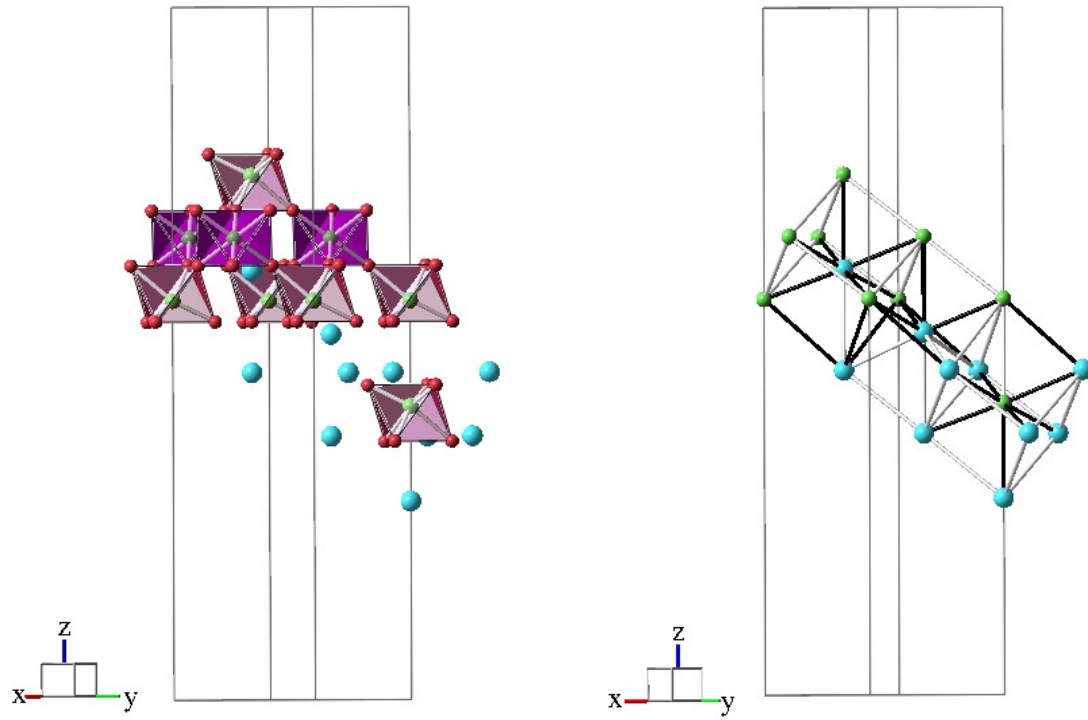
Figure 1.13: Example of a structural view of the *bcc* lattice, employed in the calculation of the variance parameter, Δ. Black bonds highlight the A-B distances selected for calculation of the variance:

$$Variance = \frac{(x-\bar{x})^2}{(n-1)}$$

Equation 1.17

where x is the A-B distance, $\bar{x}$ is the mean of eight A-B distances within a *bcc* unit cell and n is the number of A-B distances.

$$\Delta = \frac{\sum variance}{3}$$

Equation 1.18

Δ is the average variance of three *bcc* unit cells within the "shifted" region.

1.2.3 Microwave Materials

Although microwave materials have been in use since the 1940s[35] it was not until the early 1970s when the first major breakthrough in microwave ceramic technology occurred. $BaTi_4O_9$ was established as one of the first microwave ceramics to fulfil the desired dielectric requirements, with ε_r = 38, $TCF \approx$ 15 ppm / °C and $Q \approx$ 5000 at 2 GHz. During the 1980s $Ba_2Ti_9O_{20}$ was shown to possess even better properties (ε_r = 40, $TCF \approx$ 2 ppm / °C and $Q \approx$ 15000 at 2 GHz[47]), and along with other materials

24

including (Mg,Ca)TiO$_3$ and ZrTiO$_4$, formed the first generation of ceramic resonators. At the start of the 1990s due to the rapid advancement of mobile telecommunications technology, the requirements for dielectric ceramics used as resonators and filters for base stations and handsets changed. Base stations require higher Q ceramics, 40000 GHz $< Q \times f_0 <$ 250000 GHz to prevent heat and interference between signals in high power processing combined with moderate relative permittivity (25 $< \varepsilon_r <$ 50). Conversely the evolution of microwave ceramics required for handsets was driven by the need for miniaturisation and negative-positive zero (NP0) chips, with high relative permittivity (70 $< \varepsilon_r <$ 120). **Table 1.2** lists current ceramics used as microwave resonators in base stations, with the exception of Ba$_4$Nd$_{9.33}$Ti$_{18}$O$_{54}$ ceramics which are utilised as materials for digital television receivers.

It can be noted that as ε_r increases, Q decreases, hence there is a significant lack of higher ε_r ceramics with appropriate Q (48000 GHz). Therefore, the problem of a trade off between miniaturisation, high ε_r and low losses is an ongoing issue with current zero TCF compounds.[23]

Material	ε_r	$Q \times f_0$ (GHz)	Structure
$BaMg_{1/3}Ta_{2/3}O_3$	24	250000	Complex perovskite
$BaZn_{1/3}Ta_{2/3}O_3$	29	150000	Complex perovskite
$Ba(Co,Zn)_{1/3}Ta_{2/3}O_3$	34	90000	Complex perovskite
$SrTiO_3$-$LaAlO_3$	39	60000	Simple perovskite
$CaTiO_3$-$NdAlO_3$	45	48000	Simple perovskite
$ZrTiO_4$-$ZnNb_2O_6$	44	48000	α PbO_2
$Ba_4Nd_{9.33}Ti_{18}O_{54}$	80	10000	Perovskite/TTB (TTB=tetragonal tungsten bronze structure)

Table 1.2: Current ceramics in use as microwave resonators in base stations, (all zero TCF) reproduced from Reaney *et al*.[23]

1.2.4 Hexagonal B-site Deficient Perovskite Microwave Dielectrics

1.2.4.1 $A_5B_4O_{15}$

Due to the drive for miniaturisation of devices B-site deficient hexagonal perovskites have become an area of growing research for their dielectric properties and application in this area, as they display promising properties. The majority of research conducted in this area concentrates on the n=5 layered structures, and in 1961 Galasso and Katz[48] reported the existence of the B-cation deficient ceramics $Ba_5Ta_4O_{15}$, $Ba_5Nb_4O_{15}$ and $Sr_5Ta_4O_{15}$. These oxides have since been well studied[49, 50] and were found to have hexagonal symmetry and crystallise in space group, $P\bar{3}m1$. Furthermore, $Sr_5Nb_4O_{15}$, which is isostructural with the tantalum analogue, was reported by Whiston and Smith[51]. All demonstrate promising dielectric properties, listed in **table 1.3**.

Compound	$\varepsilon_{\mathbf{r}}$	$Q \times f_0$	TCF (ppm / °C)
$Ba_5Ta_4O_{15}$	28	31600	12
$Ba_5Nb_4O_{15}$	39	23700	78
$Sr_5Ta_4O_{15}$	41	2400	Too large to measure
$Sr_5Nb_4O_{15}$	40	19400	55

Table 1.3: Some $A_5B_4O_{15}$ type perovskites and their dielectric properties.

However spectroscopic studies by Massa *et al.*[52] have shown that the lattice of $Ba_5Ta_4O_{15}$ is stable whereas that of $Ba_5Nb_4O_{15}$ on the verge of collapsing to a lower symmetry state, and hence there may be increased lattice anharmonicity in the compound. It is postulated that this may be the reason for the higher $\varepsilon_{\mathbf{r}}$ of $Ba_5Nb_4O_{15,}$ although on another note, the presence of tantalum as opposed to niobium seems to improve the *TCF* of the Ba-based compounds.[53]

Further studies have been carried out by Sebastian *et al.*[53] on the n=5 layered compounds, varying the cation substitutions further (where A = Ba, Sr, Mg, Ca, Zn; B = Nb, Ta). The ceramics have $\varepsilon_{\mathbf{r}}$ in the range 11-51, $Q \times f_0$ in the range 2400 - 88000 GHz, and *TCF* in the range -73 - +232 ppm / °C. Single phase compounds could not be formed for $Ca_5Nb_4O_{15}$, $Ca_5Ta_4O_{15}$ and $Zn_5Nb_4O_{15}$, however it was found that due to the presence of secondary phases $\varepsilon_{\mathbf{r}}$ increased which subsequently affected the Q, which was then decreased. Sebastian *et al.*[54] have further expanded on their findings, examining the dielectric properties of $Ba_{5-x}Sr_xTa_4O_{15,}$ $Ba_5Nb_xTa_{4-x}O_{15}$ and $Sr_5Nb_xTa_{4-x}O_{15.}$ It was found that all solid-solution members have hexagonal symmetry, and the substitution of Sr^{2+} at the Ba^{2+} site in $Ba_{5-x}Sr_xTa_4O_{15}$ increases the $\varepsilon_{\mathbf{r}}$ as the value of x is raised. The dielectric loss is also very high when x > 3. The $Ba_5Nb_xTa_{4-x}O_{15}$ system shows intermediate dielectric properties of the end-members, the $Sr_5Nb_xTa_{4-x}O_{15}$ solid-solutions show a lower $\varepsilon_{\mathbf{r}}$ than the parent oxides, and the dielectric loss increases drastically when x nears 4, by substitution at both the A- and B-site.

Further studies by Lee *et al.*[43] confirmed these findings after investigation of the system $(Ba_{1-x}Sr_x)_5Nb_4O_{15}$, where it was found that considerable distortion of the NbO_6 octahedra was observed, indicating that lattice anharmonicity exists within the structure. The symmetry of the crystal structure changed from P$\bar{3}$m1 to P$\bar{3}$c1 with Sr^{2+} substitution. The Ba-rich compounds demonstrated a linear increase of ε_r and *TCF* and an increase of the lattice parameter (*c/a*) ratio, whereas the Sr-rich compounds exhibited a decrease in the (*c/a*) ratio and ionic polarisability, resulting in the gradual decrease of ε_r with Sr^{2+} substitution. Tilting of the octahedra due to a change of symmetry from P$\bar{3}$m1 to P$\bar{3}$c1 in Sr-rich compounds is observed, thus coinciding with the findings of Reaney *et al.*[39], which in turn caused an abrupt decrease of *TCF*.

Other studies have been performed with a variety of substitutions on the A- and B-site in the n= 5 series.[42, 55-63] Rare earth elements are co-substituted on the A-site along with an alkaline earth ion such as Ba^{2+} or Sr^{2+} in addition to various co-substitutions of transition metals, such as Ti^{4+}, Ta^{5+}, Nb^{5+} and Sn^{4+}, on the B-site. It is these multiple substitutions that facilitate the fine tuning of the dielectric properties. In particular Fang *et al.*[64] have demonstrated how this co-substitution can improve dielectric properties in particular *TCF*, which is one of the more difficult properties to optimise. This is demonstrated by the n=5 oxides $Ba_4NdTiNb_3O_{15}$ and $Ba_3Nb_2Ti_2Nb_2O_{15}$ with *TCF*s of +12 ppm / °C and +28 ppm / °C respectively whilst still possessing a respectable ε_r and Q.[65] Further studies on the compounds $Ba_3La_2Ti_2Nb_2O_{15}$ and $Ba_2La_3Ti_3NbO_{15}$ exhibited *TCF*s of +4 ppm / °C and -8 ppm / °C respectively with a good ε_r and Q.

1.2.4.2 $A_6B_5O_{18}$

Fewer reports published in the scientific literature exist for the n= 6 layered materials where the dielectric properties have been defined. $Ba_2La_4Ti_5O_{18}$ was investigated[33, 66] and was found to possess a high ε_r 46, a good Q, 31839 GHz and a negative *TCF* of -36.4 ppm / °C. Zhang *et al.*[67-69] have investigated the $BaO-La_2O_3-TiO_2-Nb_2O_5$ system for n=6 layered structures and found that $Ba_4La_2Ti_3Nb_2O_{18}$ once again possessed promising dielectric properties with a high ε_r of 55.1, a Q of 21273 GHz,

and a positive TCF of +61 ppm / °C. Therefore it was thought that with further studies within the n=6 homologous analogues from this system with intermediate compositions may potentially reveal useful materials with a TCF close to zero, as the TCF decreases gradually with an increase in B-site bond valence due to the decrease in unit-cell volumes with increasing content of La^{3+} and Ti^{4+} ions. However further studies in the system still failed to yield a close to zero TCF compound.

Sebastian *et al.*[70] expanded on the number of structures studied in the n=6 layered structures and their microwave dielectric properties (where A = Ba, Sr, La; B = Nb / Ta, Ti / Zr, and Mg / Zn) and it was found that these materials have relatively high Q values, upto 51000 GHz and a high ε_r of 26 - 48, and the TCF varies from -39 to +83 ppm / °C. The La-based compounds have a negative TCF whilst Ba-based compounds have a positive TCF. ε_r is largely influenced by the ionic polarisabilities and TCF values showed significant change with structure and composition. Similar observations were made to what was found by Kuang *et al.*[42] for n=5 layered structures where the TCF can be tuned to some extent by controlling the size of A- and B-cations and hence the tolerance factor. Therefore by adjusting the ratio of Ba^{2+} and Sr^{2+} on the A-site it may be possible to tune the TCF close to zero.

1.2.4.3 $A_8B_7O_{24}$

A meagre amount of literature exists for structures with higher values of n, and in particular their respective dielectric properties. The n=8 layered structures have been investigated however many studies concentrate solely on the structural properties[71-73]. In 2006 Rawal *et al.*[18] examined the dielectric properties of the less common twinned structure of $Ba_8Nb_4Ti_3O_{24}$. They demonstrated that the rarer twinned perovskites possess encouraging microwave dielectric properties, in particular the ε_r is higher than those of many shifted perovskites and the Q is comparable with many of the shifted perovskites. This in itself is interesting as the B-site cation distribution is very different for shifted and twinned hexagonal perovskites[17]. Other examples of $A_8B_7O_{24}$ perovskites are known which also possess promising dielectric properties,[74, 75] as do a few materials with higher values of n. It is worthwhile mentioning that the general trend witnessed is that for B-site deficient hexagonal

perovskites the ε_r and TCF gradually increase whilst Q decreases, as n increases. Types of ceramics with n<5 may therefore have superior properties if the correct substitutions of ions can be found to provide suitable ε_r and TCF values whilst maintaining a high Q.[76]

1.2.4.4 A$_4$B$_3$O$_{12}$

Of particular interest in this study are A$_4$B$_3$O$_{12}$ n=4 layered B-cation deficient perovskites. Only a small selection of data exist on the dielectric properties of these n=4 layered oxides, there are however several studies on the structural properties of these compounds.[77-79] The selection of compositions studied for their dielectric properties generally consist of Ba^{2+} / Sr^{2+} / La^{3+} on the A-site and d^0 transition metal(s) on the B-site, as this combination seems to result in the best dielectric properties by selective tuning of these cations. However from the variety of these n=4 materials that have been synthesised, still only a few exist where the dielectric properties may be suitable for commercial application.

The existence of Sr$_3$LaNb$_3$O$_{12}$ has been established since 1987 by Sirotinkin *et al.*[80], as has the crystal structure of Ba$_3$LaNb$_3$O$_{12}$ which was reported in 1980 by Rother *et al.*[81] Both phases have since been re-investigated for their dielectric properties by Fang *et al.*[82] and Rawal *et al.*[20] respectively. These isostructural compounds are quoted as crystallising in space group R-3m, but recently Rawal *et al.*[83] showed that both structures are better described in space group R-3, and not R-3m as previously quoted. Therefore tilting of the NbO$_6$ octahedra is present within the structure, and it is this tilting which influences the dielectric properties of the compound, in particular the TCF. It was postulated that the presence of a tilt transition in the structures from R-3 to R-3m at temperatures of ~465 K and ~720 K for Ba$_3$LaNb$_3$O$_{12}$ and Sr$_3$LaNb$_3$O$_{12}$ respectively could be responsible for the TCF values witnessed (for the Ba-rich oxide -100 ppm / °C and for the Sr-rich oxide -5 ppm / °C). The difference is attributed to the closer proximity of the tilt transition temperature to room temperature for Ba$_3$LaNb$_3$O$_{12}$ than that of Sr$_3$LaNb$_3$O$_{12}$. It is therefore proposed that TCF in these 12R-type hexagonal perovskites can be tuned by controlling the tolerance factor, and consequently the tilt transition temperature, in a manner similar to that used for many Ba- and Sr-based 3C-type ABO$_3$ perovskites.

Furthermore Hu *et al.*[76] investigated the $Ba_{3-x}Sr_xLaNb_3O_{12}$ system, (where x = 0 – 3) and found that the substitution of Sr^{2+} for Ba^{2+} effectively enhances the Q and controls *TCF*. With increasing Sr^{2+} content the Q changed from 12000 to 45327 GHz, *TCF* improved from -93 to -9 ppm / °C, and ε_r decreased. This decrease in ε_r was explained by the ionic polarisabilities of the ions, the increase in Q was suggested to be due to the size distribution of the A-site cations, since as the Sr-content is increased the size difference between the A-site cations is reduced. Finally the increase in *TCF* was attributed to the link between tolerance factor and *TCF* as established by Reaney *et al.*[39] for complex perovskites. However this study still quotes all structures in the system as untilted, in space group R-3m, which is contrary to that quoted for the end members by Rawal *et al.*[83] Due to the lack of in depth structural study of the compounds, there are questions that still remain unanswered regarding this $Ba_{3-x}Sr_xLaNb_3O_{12}$ series of phases. Therefore further investigation of the electrical properties is warranted to gain more a more accurate understanding of the structure-property relationships.

Another study of niobium based $A_4B_3O_{12}$ perovskites, where Sr^{2+} is substituted for Ba^{2+} is that by Sithara *et al.*[84], concentrating on the system $Ba_{3-x}Sr_xYNb_3O_{12}$. The results show there is a second phase present in the system and it is this second phase that influences the *TCF*, especially in $BaSr_2YNb_3O_{12}$ which has the greatest proportion of secondary phase giving it the best *TCF* in the system (+8 ppm / °C). ε_r increases as Sr^{2+} content increases, but conversely Q decreases as Sr^{2+} content increases. The powder diffraction studies show when Ba^{2+} is completely replaced by Sr^{2+} the compound undergoes a structural transition, and hence possesses a *TCF* different to the other members of the system. This suggests that analogues with a composition close to the onset of a structural transition may allow the *TCF* to be tuned to zero.

Fang *et al.* have gone on to study the $Ba_{3-n}La_{1+n}Ti_nNb_{3-n}O_{12}$ system[85, 86] where it was found that as the content of La^{3+} and Ti^{4+} was raised, ε_r decreased. This is as would be expected due to the ionic polarisabilities of La^{3+} and Ti^{4+}. The *TCF* of the compounds improved with increasing La^{3+} and Ti^{4+} content, from -40 ppm / °C for

$Ba_3LaNb_3O_{12}$ to +6 ppm / °C for $BaLa_3NbTi_2O_{12}$, however the value quoted for $Ba_3LaNb_3O_{12}$ is slightly different to that quoted by Rawal et al.[83] at -100 ppm / °C. It is suggested by Fang et al. that TCF may be controlled by tolerance factor, as, tolerance factor gradually decreases as TCF increases and a near zero TCF may be obtainable by synthesising intermediate compositions between $Ba_2La_2TiNb_2O_{12}$ and $BaLa_3NbTi_2O_{12}$. All compounds of the system display a good ε_r and Q, however once again the space group is quoted as R-3m, which has been proven by Rawal et al.[83] to be incorrect.

Conversely, there are very few reports of Ta-based $A_4B_3O_{12}$ perovskites and their dielectric properties. In 2008 Fang et al.[87] and Zhang et al.[88] examined the dielectric properties of $Ba_3LaTa_3O_{12}$, since Shannon's effective ionic radii and charge are the same for Nb^{5+} and Ta^{5+}, it is worthwhile to investigate whether Ta^{5+} based $A_4B_3O_{12}$ hexagonal perovskites might have equivalent or superior qualities to those of the Nb-analogues. The ceramic was found to exhibit a ε_r of 36.8, a Q of 21965 GHz, and a negative TCF of -49.6 ppm / °C. $Sr_3LaTa_3O_{12}$ was first investigated structurally in 1987 by Sirotinkin et al.[80] and then later by Antinov et al.[89], but it was not until very recently that the dielectric properties of the compound were discussed.[90] $Sr_3LaTa_3O_{12}$ is reported to have a ε_r of 30.1, a Q of 16050 GHz and a TCF of -43 ppm / °C. This material is the m=1 member of the system $Sr_{4-m}La_mTi_{m-1}Ta_{4-m}O_{12}$ (where m = 1 - 3) and the study proceeded to show that as m increases the dielectric properties were improved. The microwave properties could be adjusted by varying the composition; $SrLa_3Ti_2TaO_{12}$ in particular exhibited Q and ε_r values comparable with those of existing microwave materials, at 40.1 and 42130 GHz respectively. Although the TCF value is small at -8 ppm / °C, it still needs reduction in magnitude for practical application in base stations, and the substitution of Ta^{5+} for Nb^{5+} for these purposes is under consideration.

The symmetry and crystal structure of the Ta-based n=4 layered compounds need to be verified before a fuller understanding of properties, and effective tuning can be obtained. Comparing the Sr-rich and Ba-rich tantalum $A_4B_3O_{12}$ perovskites, it is evident that the Ba-based compound exhibits a slightly better ε_r and Q but a slightly

worse TCF compared to the Sr-based compound. Neither of the compounds possess dielectric properties comparable to commercially available microwave dielectrics, and significant cation substitutions on the A- and B-site are required to improve these physical properties.

Yu *et al.*[91] have recently investigated $Ba_2La_2TiTa_2O_{12}$, with an aim to synthesise a compound with a commercially viable Q (> 48000 GHz) proposing that the substitution of Ta^{5+} for Nb^{5+} may improve the Q in particular.[53] Nevertheless with a Q of 36188 GHz, a ε_r of 37.8 and a TCF of -52 ppm / °C, further substitutions are required to achieve properties suitable for use as a dielectric resonator, and further structural studies are required to accurately establish the space group.

Very recently Fang *et al.*[92] have studied the first system to incorporate Ta^{5+} and Nb^{5+} on the B-site, $Ba_4LiNb_{3-x}Ta_xO_{12}$ and examined whether n=4 layered structures of the rarer twinned variety exhibit superior properties to those of the shifted variety, as demonstrated in the $A_8B_7O_{24}$.[18] Adequate ε_r values were obtained for series in the range, 28-37, and a TCF in the range of +25 – +65 ppm / °C which at present is not suitable for commercial use. However it is the Q values that are impressive with the x=3 member $Ba_4LiTa_3O_{12}$ displaying a Q of 104000 GHz, therefore further studies are required to control the TCF values.

1.2.4.5 Intergrowth Compounds

As previously described in **section 1.1.6**, intergrowth compounds consist of perovskite slabs of varying thicknesses that are ordered over a long periodicity along the *z*-axis of the hexagonal unit cell. Very few intergrowth phases are known and their potential for use as microwave dielectric resonators and filters has rarely been considered.

To date only two examples of the $4^1 5^1$ stacking type sequence compounds exist, $La_4Ti_3O_{12}$–$LaTiO_3$ and $La_4Ti_3O_{12}$–$BaTiO_3$, however no electrical properties are defined for these structures. This type of stacking sequence is extremely rare and it is more usual to find that intergrowth compounds crystallise in stacking sequence $5^x 6^y$. As there are only Ti^{4+} ions on the B-site, this gives rise to problems as it is

easily reduced to Ti^{3+}, therefore the presence of a d^0 M^{5+} ion which is much more stable in this electronic configuration is better. HRTEM (high-resolution transmission electron microscopy) studies were carried out on the $Ba_5Nb_4O_{15}$–$BaTiO_3$ system and it appeared that intergrowth stability seems to be highly sensitive to the difference in average size of the A-cation between the two parent compounds.[93] Therefore the $Ba_5Nb_4O_{15}$–$BaTiO_3$ system seems a favourable area of study as there is only one A-cation present which is the same in both parent compounds. It was found that intergrowth structures could be formed within this system and that the ability to form intergrowths depends on the structural compatibility between the two parent compounds. One of the main criteria that govern the ability to form these super-lattices is the accordance of the anionic lattices which is itself dependent on the average size of the A-cation. Furthermore Boullay et al.[94] demonstrated that the superspace group approach can be used to describe intergrowth structures.

To date the only published study on the dielectric properties of intergrowth structures is that by Zhao et al.[46] where it is suggested that the TCF can be improved upon by the formation of intergrowths, in comparison to the TCF of the parent compounds. The $Ba_5Nb_4O_{15}$–$BaTiO_3$ system[19, 94] was the focus of this study and the 5^16^1, 5^26^1 and 5^36^1 structures were then examined for their dielectric properties. Since the intergrowth compounds allow the extent of atomic displacements of cations and anions along the z-axis to be reduced, the TCF is subsequently improved by the formation of intergrowths. The change in TCF was thus evaluated by the degree of atomic displacements using the parameter d, TCF increased with increasing d value. The 5^16^1 crystal structure was determined using neutron powder diffraction (NPD), but the presence of stacking faults makes this impossible for the 5^26^1 and 5^36^1 compounds.[19, 95] However similar regularisation of the thickness of the octahedral layers may also occur in the 5^26^1 and 5^36^1 intergrowths because the stability of the intergrowths mainly results from the simultaneous regularisation of both anionic and cationic sublattices.[19] For all structures, modest Q and ε_r values were exhibited.

No evidence of Ta-based intergrowth compounds exist and since Ta^{5+} and Nb^{5+} are both pentavalent and have equivalent ionic radii, then the formation of Ta-based

intergrowths is a real possibility. In general tantalate compounds give lower permittivity than their niobate counterparts, but on the other hand they give rise to substantially higher values of Q,[92] and this may be significant in applications where a high Q as opposed to high ε_r is the key to improvement to the dielectric properties.

1.3 Objectives

The objective of this study is to structurally characterise various series of B-site deficient hexagonal perovskites and consider how assorted A- and B-site substitutions influence and correlate to the electrical properties displayed.

The effect of substituting Sr^{2+} for Ba^{2+} on the A-site is investigated in the solid solution series $Ba_{3-x}Sr_xLaNb_3O_{12}$ (when x = 1, 2, 3). The structural properties are assessed at variable temperatures to aid in the interpretation of electrical properties displayed. This work is presented in **Chapter 3**.

The effect of introducing Ta^{5+} on to the B-site in the series $Ba_{3-x}Sr_xNb_{1-y}Ta_yO_{12}$ (when x = 0, 1, 2, 3 and y = 1, 2) is researched. This is of interest as previous studies have shown the introduction of Ta^{5+} can improve Q values in particular[53]. However Nb^{5+} and Ta^{5+} ions are the same size therefore the structural consequences of this substitution are also probed to establish structure-property correlations. This work is presented in **Chapter 4**.

Intergrowth structures are investigated, to further improve upon microwave dielectric properties established in **Chapter 3** and **4**, by fine-tuning structural characteristics. This is achieved by combining parent structures with particularly favourable microwave dielectric properties, with an aim to produce an intergrowth compound with superior properties. This work is presented in **Chapter 5**.

1.4 References

1.   Muller, U., *Ionic Compounds*, in *Inorganic Structural Chemistry*. (Wiley, Chichester, 2007)

2.   Venkatesh, J. and Murthy, V.R.K., *Materials Chemistry and Physics*. **58**, 3 276-279 (1999)

3.   Pauling, L., *Journal of the American Chemical Society*. **51**, 4 1010-1026 (1929)

4.   Tilley, R., *The Depiction of Crystal Structures*, in *Crystals and Crystal Structures*. (Wiley, Chichester, 2006)

5.   Shannon, R.D., *Acta Crystallographica Section A*. **32**, Sep1 751-767 (1976)

6.   Wells, A.F., *Ionic Crystals*, in *Structural Inorganic Chemistry*. (Oxford University Press, 1962)

7.   West, A.R., *Basic Solid State Chemistry* (Wiley, Chichester, 1999)

8.   Glazer, A.M., *Acta Crystallographica Section B-Structural Science*. 3384-3392 (1972)

9.   Woodward, P.M., *Acta Crystallographica Section B-Structural Science*. **53**, 32-43 (1997)

10.   Kuang, X., Allix, M. M. B., Claridge, J. B., Niu, H. J., Rosseinsky, M. J., Ibberson, R. M. And Iddles, D. M., *Journal of Materials Chemistry*. **16**, 11 1038-1045 (2006)

11.   Mitchell, R.H., *Perovskites : modern and ancient.* (Ontario: Thunder Bay, 2002)

12.   Jagodzinski, H., *Acta Crystallographica*. **2**, 4 201-207 (1949)

13.   Kuroda, K., Ishizawa, N., Mizutani, N., and Kato, M., *Journal of Solid State Chemistry*. **38**, 297-299 (1981)

14.   Burbank, R.D. and Evans, H.T., Jr., *Acta Crystallographica*. **1**, 330-336 (1948)

15.   Donohue, P.C., Katz, L., and Ward, R., *Inorganic Chemistry*. **4**, 306-310 (1965)

16.   Negas, T., Roth, R.S., Parker, S., and Brower, W.S., *Journal of Solid State Chemistry*. **8**, 1-13 (1973)

17.   Trolliard, G., Teneze, N., Boullay, P., and Mercurio, D., *Journal of Solid State Chemistry*. **177**, 4-5 1188-1196 (2004)

18. Rawal, R., Feteira, A., Flores, A.A., Hyatt, N.C., West, A.R., Sinclair, D.C., Sarma, K., and Alford, N.M., *Journal of the American Ceramic Society*. **89**, 1 336-339 (2006)

19. Teneze, N., Boullay, P., Trolliard, G., and Mercurio, D., *Solid State Sciences*. **4**, 9 1119-1128 (2002)

20. Rawal, R., Feteira, A., Hyatt, N.C., Sinclair, D.C., Sarma, K., and Alford, N.M., *Journal of the American Ceramic Society*. **89**, 1 332-335 (2006)

21. William D. Callister, J., *Fundamentals Of Materials Science and Engineering, An integrated Approach* (John Wiley & Sons, Inc., 2005)

22. Moulson, A.J. and Herbert., J.M., *Electroceramics, Materials, Properties and Applications* (Wiley, Chichester, 2008)

23. Reaney, I.M. and Iddles, D., *Journal of the American Ceramic Society*. **89**, 7 2063-2072 (2006)

24. Herbert, A.J.M.A.J.M., *Electroceramics, Materials, Properties, Applications* (Wiley, 2008)

25. Fang, L., Zhang, H., Huang, T. H., Yuan, R. Z. And Dronskowski, R., *Materials Research Bulletin*. **39**, 11 1649-1654 (2004)

26. Vineis, C., Davies, P. K., Negas, T. And Bell, S., *Materials Research Bulletin*. **31**, 5 431-437 (1996)

27. Jawahar, I.N., Santh, N. I., Sebastian, M. T., Mohanan, P., *Journal of Materials Research*. **17**, 12 3084-3089 (2002)

28. Fang, L., Zhang, H., Yuan, R. Z. And Liu, H. X., *Materials Letters*. **59**, 4 535-538 (2005)

29. Fang L., Z.H., Hong X., Meng F., Yang J., Huang T., *Materials Letters*. **58**, 3884-3887 (2004)

30. Fang, L., Meng, S., Zhang, H. And Liu, Z., *Materials Letters*. **60**, 1147-1150 (2006)

31. Lee, C., Ou, C., Lin, Y., Huang, C., Su, C., *Journal of European Ceramic Society*. **27**, 5 2273-2280 (2007)

32. Shannon, R.D., *Journal of Applied Physics*. **73**, 1 348-366 (1993)

33. Vineis, C., Davies, P.K., Negas, T., and Bell, S., *Materials Research Bulletin*. **31**, 5 431-437 (1996)

34. Shannon, R., *Acta Crystallographica Section A*. **32**, 5 751-767 (1976)

35.   Wersing, W., *Current Opinion in Solid State and Materials Science*. **1**, 5 715-731 (1996)

36.   Johnsson, M. and Lemmens, P., *Crystallography and chemistry of perovskites* (Wiley, New York, 2006)

37.   Harrop, P.J., *Journal of Materials Science*. **4**, 4 370-374 (1969)

38.   Colla, E.L., Reaney, I.M., and Setter, N., *Journal of Applied Physics*. **74**, 5 3414-3425 (1993)

39.   Reaney, I.M., Colla, E.L., and Setter, N., *Japanese Journal of Applied Physics Part 1-Regular Papers Short Notes & Review Papers*. **33**, 7A 3984-3990 (1994)

40.   Lufaso, M.W., *Chemistry of Materials*. **16**, 11 2148-2156 (2004)

41.   Ferreira, V.M., Baptista, J.L., Kamba, S., and Petzelt, J., *Journal of Materials Science*. **28**, 21 5894-5900 (1993)

42.   Kuang, X., Allix, M.M.B., Claridge, J.B., Niu, H.J., Rosseinsky, M.J., Ibberson, R.M., and Iddles, D.M., *Journal of Materials Chemistry*. **16**, 11 1038-1045 (2006)

43.   Lee, C.-T., Ou, C.-C., Lin, Y.-C., Huang, C.-Y., and Su, C.-Y., *Journal of the European Ceramic Society*. **27**, 5 2273-2280 (2007)

44.   Zhao, F., Yue, Z., Pei, J., Gui, Z., and Li, L., *Applied Physics Letters*. **90**, 14 142908-3 (2007)

45.   Zhao, F., Yue, Z.X., Pei, J., Gui, Z.L., and Li, L.T., *Applied Physics Letters*. **90**, 14 142908-3 (2007)

46.   Zhao, F., Yue, Z., Pei, J., Zhuang, H., Gui, Z., and Li, L., *Applied Physics Letters*. **89**, 20 202901-3 (2006)

47.   Masse, D.J., Pucel, R.A., Readey, D.W., Maguire, E.A., and Hartwig, C.P., *Proceedings of the Institute of Electrical and Electronic Engineers*. **59**, 11 1628 (1971)

48.   Galasso, F. and Katz, L., *Acta Crystallographica*. **14**, 6 647-650 (1961)

49.   Shannon, J. and Katz, L., *Acta Crystallographica Section B*. **26**, 2 102-105 (1970)

50.   Hutchison, J.L. and Jacobson, A.J., *Acta Crystallographica Section B*. **31**, 5 1442-1444 (1975)

51.   Whiston, C.D. and Smith, A.J., *Acta Crystallographica*. **23**, 1 82-84 (1967)

52. Massa, N.E., Pagola, S., and Carbonio, R., *Physical Review B*. **53**, 13 8148 (1996)

53. Jawahar, I.N., Mohanan, P., and Sebastian, M.T., *Materials Letters*. **57**, 24-25 4043-4048 (2003)

54. Jawahar, I.N., Sebastian, M.T., and Mohanan, P., *Materials Science and Engineering B-Solid State Materials for Advanced Technology*. **106**, 2 207-212 (2004)

55. Zheng, H., Woodward, D.I., Gillie, L., and Reaney, I.M., *Journal of Physics: Condensed Matter*. 31 7051 (2006)

56. Fang, L., Zhang, G.L., Hu, C.Z., and Zhang, H., *Materials Letters*. **62**, 4-5 670-672 (2008)

57. Gui, D.Y., Zhang, H., Fang, L., and Xue, L.H., *Journal of Materials Science-Materials in Electronics*. **19**, 6 543-546 (2008)

58. Fang, L., Men, S.S., Zhang, H., Liu, Z.Q., and Liu, H.F., *Journal of Electroceramics*. **21**, 1-4 137-140 (2008)

59. Fang, L., Su, H.P., Yu, Q., Zhang, H., and Cui, X.M., *Materials Letters*. **62**, 25 4121-4123 (2008)

60. Pei, J., Yue, Z.X., Zhao, F., Gui, Z.L., and Li, L.T., *Journal of Alloys and Compounds*. **459**, 1-2 390-394 (2008)

61. Fang, L., Zhang, H., Huang, T.H., Yuan, R.Z., and Dronskowski, R., *Materials Research Bulletin*. **39**, 11 1649-1654 (2004)

62. Fang, L., Su, H.P., Yu, Q., Zhang, H., and Wu, B.L., *Journal of the American Ceramic Society*. **91**, 8 2769-2771 (2008)

63. Rejini, R. and Sebastian, M.T., *International Journal of Applied Ceramic Technology*. **3**, 3 230-235 (2006)

64. Fang, L., Zhang, H., Hong, X.K., Meng, F.C., Yang, J.F., and Huang, T.H., *Materials Letters*. **58**, 30 3884-3887 (2004)

65. Fang, L., Diao, C.L., Zhang, H., Yuan, R.Z., Dronskowski, R., and Liu, H.X., *Journal of Materials Science-Materials in Electronics*. **15**, 12 803-805 (2004)

66. Teneze, N., Mercurio, D., Trolliard, G., and Frit, B., *Materials Research Bulletin*. **35**, 10 1603-1614 (2000)

67. Zhang, H., Fang, L., Dronskowski, R., Muller, P., and Yuan, R.Z., *Journal of Solid State Chemistry*. **177**, 11 4007-4012 (2004)

68. Fang, L., Zhang, H., Yuan, R.Z., and Dronskowski, R., *Journal of Materials Science*. **39**, 23 7093-7095 (2004)

69. Zhang, H., Fang, L., Elsebrock, R., and Yuan, R.Z., *Materials Chemistry and Physics*. **93**, 2-3 450-454 (2005)

70. Santha, N.I. and Sebastian, M.T., *Journal of the American Ceramic Society*. **90**, 2 496-501 (2007)

71. Abakumov, A.M., Van Tendeloo, G., Scheglov, A.A., Shpanchenko, R.V., and Antipov, E.V., *Journal of Solid State Chemistry*. **125**, 1 102-107 (1996)

72. Shpanchenko, R.V., Nistor, L., Van Tendeloo, G., Van Landuyt, J., Amelinckx, S., Abakumov, A.M., Antipov, E.V., and Kovba, L.M., *Journal of Solid State Chemistry*. **114**, 2 560-574 (1995)

73. Teneze, N., Boullay, P., Petricek, V., Trolliard, G., and Mercurio, D., *Solid State Sciences*. **4**, 9 1129-1136 (2002)

74. Davies, P.K., Borisevich, A., and Thirumal, M., *Journal of the European Ceramic Society*. **23**, 14 2461-2466 (2003)

75. Mallinson, P., Claridge, J.B., Iddles, D., Price, T., Ibberson, R.M., Allix, M., and Rosseinsky, M.J., *Chemistry of Materials*. **18**, 26 6227-6238 (2006)

76. Hu, C., Fang, L., Su, H., Liu, L., and Wu, B., *Journal of Alloys and Compounds*. **487**, 1-2 504-506 (2009)

77. Collins, B.M., Jacobson, A.J., and Fender, B.E.F., *Journal of Solid State Chemistry*. **10**, 1 29-35 (1974)

78. Konstantinov, P., Krezhov, K., Sváb, E., Mészáros, G., and Török, G., *Physica B: Condensed Matter*. **276-278**, 260-261 (2000)

79. Li, Z.F., Sun, J.L., You, L.P., Wang, Y.X., and Lin, J.H., *Journal of Alloys and Compounds*. **379**, 1-2 117-121 (2004)

80. Sirotinkin, V.P., Averkova, O.E., Starikov, A.M., and Evdokimov, A.A., *Zhurnal Neorganicheskoi Khimii*. **32**, 1 262-263 (1987)

81. Von Rother, H.J., Kemmler-Sack, S., Treiber, U., and Cyris, W.R., *Z. Anorg, Allg. Chem. .* **466**, 131-138 (1980)

82. Fang, L., Zhang, H., Yu, Q., Su, H.P., Wu, B.L., and Cui, X.M., *Journal of the American Ceramic Society*. **92**, 2 556-558 (2009)

83. Rawal, R., et al., **94**, 19 192904 (2009)

84. Sithara, S.P., Rajesh, S., Rajani, K.V., Murali, K.P., and Ratheesh, R., *Scripta Materialia*. **59**, 4 424-427 (2008)

85. Fang, L., Meng, S.-S., Zhang, H., and Liu, Z.-Q., *Materials Letters*. **60**, 9-10 1147-1150 (2006)

86. Fang, L., Meng, S.-S., Zhang, H., and Wu, B.-L., *Transactions of Nonferrous Metals Society of China*. **16**, Supplement 2 s521-s523 (2006)

87. Fang, L., Wu, Y., Hu, C.Z., Chen, P., and Zhang, H., *Materials Letters*. **62**, 4-5 594-596 (2008)

88. Zhang, H., Wu, Y., Meng, S., and Fang, L., *Journal of Alloys and Compounds*. **460**, 1-2 460-463 (2008)

89. Antonov, V.A., Arsenev, P.A., and Kopylova, E.K., *Kristallografiya*. **35**, 3 630-633 (1990)

90. Fang, L., Li, C., Peng, X., Hu, C., and Wu, B., *Journal of the American Ceramic Society*. **93**, 7 1884-1887 (2010)

91. Yu, Q., Fang, L., Zhang, H., and Su, H.P., *Journal of Materials Science-Materials in Electronics*. **20**, 7 671-674 (2009)

92. Fang, L., Li, C., Peng, X., Hu, C., Wu, B., and Zhou, H., *Journal of the American Ceramic Society*. **93**, 5 1229-1231 (2010)

93. Trolliard, G., Harre, N., Mercurio, D., and Frit, B., *Journal of Solid State Chemistry*. **145**, 2 678-693 (1999)

94. Boullay, P., Ténèze, N., Trolliard, G., Mercurio, D., and Perez-Mato, J.M., *Journal of Solid State Chemistry*. **174**, 1 209-220 (2003)

95. Trolliard, G., Teneze, N., Boullay, P., Manier, M., and Mercurio, D., *Journal of Solid State Chemistry*. **173**, 1 91-100 (2003)

Chapter 2

2. Experimental Techniques

2.1 Sample Synthesis

All samples were synthesised *via* the standard ceramic route. Stoichiometric amounts of dried starting materials, usually oxides and carbonates, were mixed in a pestle and mortar with acetone as a homogenising medium. The samples were then heated to reaction temperature in an alumina crucible in a furnace, until a single phase material was obtained. For larger batches of samples, *i.e.* > 10 g the ball milling technique was used, which allows for a better mixing of the sample and a powder with a finer particle size for making denser pellets suitable for electrical measurements.

2.2 Structural Characterisation Techniques

Two complementary diffraction techniques have been employed for the structural characterisation of samples, X-ray powder diffraction (XRPD) and neutron powder diffraction (NPD). XRPD allowed preliminary structural characterisation to be performed, and the assessment of phase purity. NPD allowed for the definitive assignment of the positions of the oxygen atoms, which is of particular importance when considering the tilting of octahedra in the systems investigated.
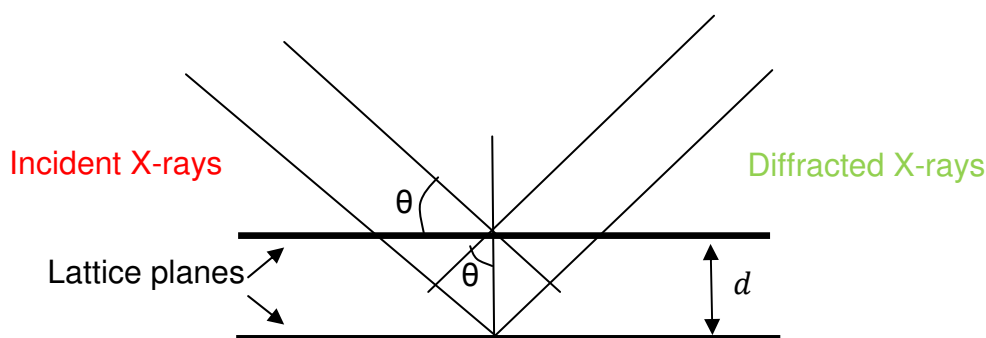
2.2.1 Powder Diffraction

Three types of radiation are generally utilised for powder diffraction studies, X-rays, neutrons and electrons. XRPD and NPD are governed by Braggs law[1], defined in ***equation 2.0***:

$$2d \sin \theta = n\lambda \qquad\qquad\qquad \textbf{\textit{Equation 2.0}}$$

Bragg's approach to diffraction regards crystals as built up of layers or planes. Each plane acts as a semi-transparent mirror, and the majority of the impinging radiation is diffracted off a plane at a specific angle that is equal to the angle of incidence. Ideally a powder sample has crystals randomly arranged in every possible orientation[2] thus

maximising the likelihood of the radiation striking every crystal plane. This concept is depicted in **figure 2.0**.

Figure 2.0: Derivation of Bragg's law.

Two types of powder diffraction exist for sample characterisation, constant wavelength and energy dispersive.

- Constant wavelength – A fixed wavelength monochromatic beam of X-rays or neutrons is diffracted by a powder sample. The different *d*-spacings for reflections are measured by moving the detector.

- Energy dispersive – The wavelength is varied using a polychromatic beam of radiation and the detector is fixed at angle θ. An energy dispersive detector measures the *d*-spacings for reflections related to certain wavelengths.

The X-ray wavelength commonly employed is characteristic of Kα radiation, λ = 1.5418 Å, emitted by copper. This radiation is scattered upon interaction with the electrons of an atom. The strength of scattering is dependent on the structure factor, F which is proportional to the atomic number of the element, *Z.* Therefore scattering increases steadily as atomic number increases. A gradual decrease in scattering intensity is witnessed with increasing angle 2θ, because distances between electrons within atoms are short, leading to destructive interference of the diffracted beams when the X-rays are scattered by electrons from different parts of the atom. Another consequence of the reduction of scattering intensity with decreasing atomic number *Z*, is the difficulty in locating lighter atoms such as hydrogen and oxygen, especially in the presence of heavier atoms. Therefore it is sometimes advantageous

to use NPD as scattering of neutrons is not just a simple function of atomic number and hence light atoms are often strong neutron scatterers, *figure 2.1*.
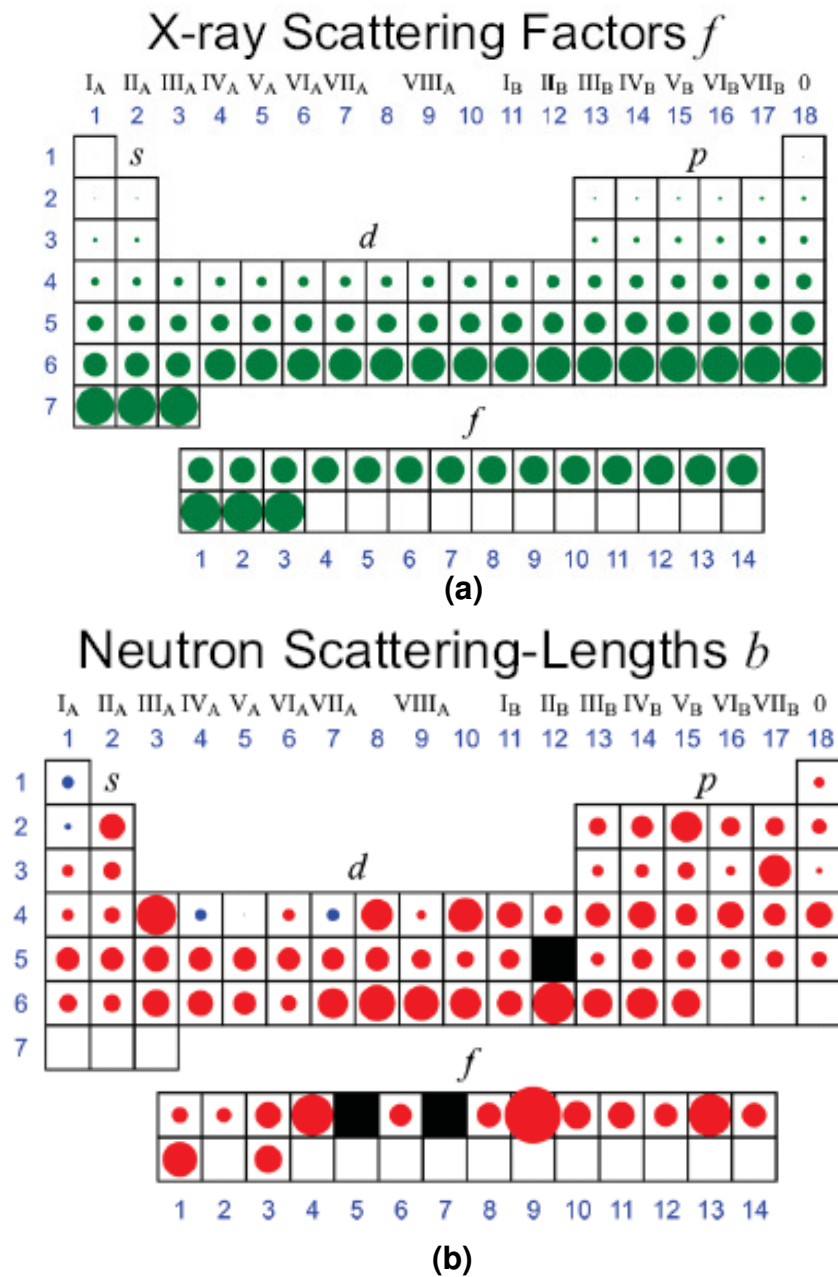
Figure 2.1: (a) X-ray scattering strength; **(b)** Neutron scattering lengths, the larger the dot the more intense the scattering, [3] (blue dots indicate negative scattering lengths).

Neutrons that are used for diffraction have a wavelength of the order of 0.5 to 3 Å. The neutron wavelength depends on velocity and can be described by the de Broglie relation.[4] The scattering power of neutrons is not simply determined by atomic number as with X-rays, as it is the atomic nuclei, rather than electrons that are responsible for the scattering. The strength of scattering is represented by the scattering length b and since neutrons and nuclei are extremely small, significant scattering takes place only when a neutron passes close to a nucleus. Hence the scattering length is not related to atomic number and neutron scattering powers vary erratically across the periodic table, often with large differences between adjacent elements. Heavy elements do not always dominate lighter ones as with X-rays and even different isotopes of the same element can have different neutron scattering powers. The intensity of neutron scattering does not fall off at higher angles like that of X-rays, and lower intensities at higher angles are due entirely to atomic vibrations. Consequently NPD is an extremely useful tool for structure determination as it allows elements of similar atomic number to be distinguished from each other.[5]

2.2.2 Diffraction Instrumentation

2.2.2.1 Constant Wavelength XRPD

X-ray diffraction experiments were conducted on a STOE STADI-P Powder Diffractometer (University of Sheffield) operating with Cu Kα_1 radiation (λ=1.5406 Å). Data were obtained over the 2θ range 10 to 110 ^{o} with a detector step-size of 0.1 ^{o}, hence a 0.02° step in 2θ. A Bruker D8 Advance Diffractometer, operating with Cu Kα radiation (λ=1.5418 Å), with a position sensitive detector, in reflection mode was used for assessment of phase purity. Scans were usually 45 minutes long over an angular range of 10 to 90° 2θ.

Diffraction patterns were analysed using a variety of computer programs, including the Fullprof suite[6], STOE WinXPow, and Chekcell[7]. The database of reported diffraction profiles published by the Joint Committee of Powder Diffraction Standards (JCPDS) was used for comparison of samples with known materials.

2.2.2.2 Constant Wavelength NPD

The D2B instrument at the Institut Laue-Langevin (ILL) in Grenoble, France was used for the collection of constant wavelength data. D2B is a high resolution two-axis powder diffractometer using neutrons from a reactor source, that are tuned to a wavelength of 1.594 Å using a Ge monochromator [hkl = 335]. Data were collected over an angular range of 5 - 165° 2θ measured at a step size of 0.005°. There are 128 ^{3}He detectors spaced at intervals of 1.25°, and a variety of sample environments can be used, including a furnace to obtain variable temperature neutron data up to 900 °C.
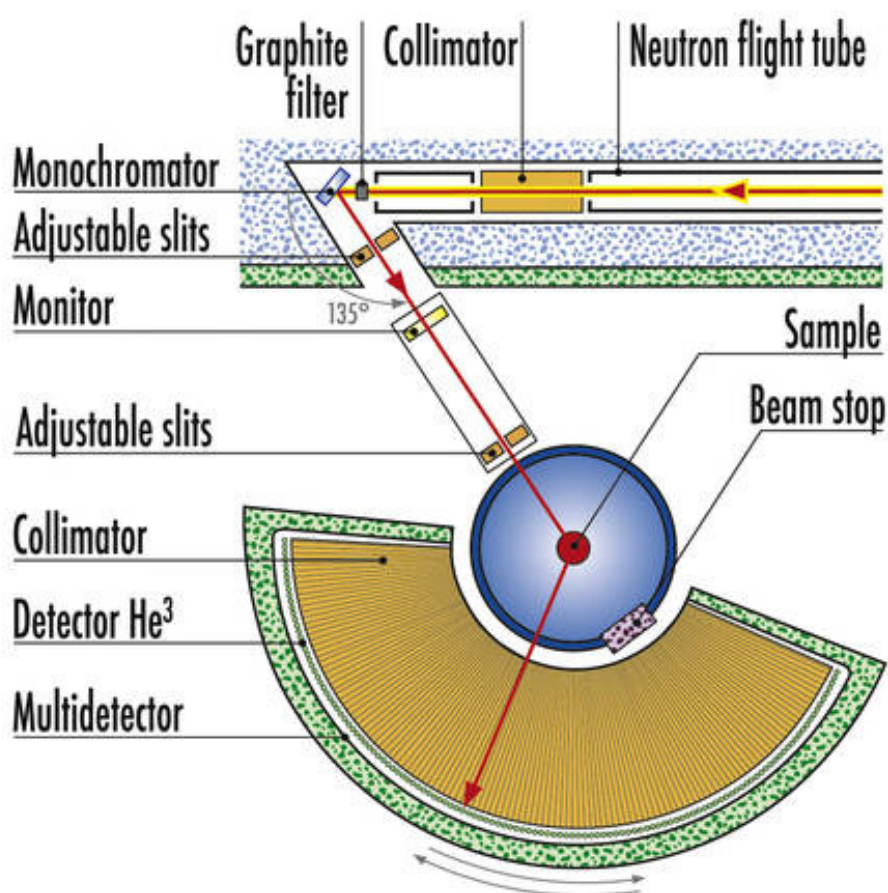
Figure 2.2: Labelled schematic of the D2B instrument.[8]

2.2.2.3 Variable Wavelength NPD

Variable wavelength NPD is more commonly referred to as *time of flight*, where neutrons are obtained by a spallation process, and the entire neutron spectrum is used with a fixed diffraction angle, θ. The detectors are situated at a known distance from the neutron source and the diffracted radiation that arrives at the detector is separated according to its time of flight and wavelength. The wavelength, which depends on velocity, is governed by the de Broglie relation, ***equation 2.1***:[9, 10]

$$\lambda = \frac{h}{mv}$$
Equation 2.1

where,

$h = 6.626 \times 10^{-34}$, the Planck constant

$m = 1.675 \times 10^{-27}$Kg, the mass of the neutron

$v = $ Velocity

From Bragg's Law (defined in ***equation 2.0***) a relationship between *time of flight* and *d*-spacing can be defined:

$$2dsin\theta = \lambda$$
Equation 2.2

$$2dsin\theta = \frac{h}{mv}$$
Equation 2.3

Therefore:

$$d \propto t$$
Equation 2.4

Three *time of flight* diffractometers were employed for collection of data, GEM, POLARIS and HRPD, all at the ISIS facility in Oxfordshire, United Kingdom.

- GEM can be used to perform high intensity, high resolution experiments to study the structure of disordered materials and crystalline powders. The GEM detector array has 7270 elements (not including monitors) in 86 modules and these detectors cover a scattering angle range from 1.1 to 169.3° 2θ. The GEM instrument is depicted in **figure 2.3**.


Figure 2.3: GEM instrument at target station 1, ISIS.[11]

- POLARIS is a high intensity, medium resolution powder diffractometer. It has a total of 434 ^{3}He gas and ZnS scintillator detectors arranged into four separate banks, two at low angles, one at 2θ ~ 90° and one at backscattering angles. These are referred to as the A, B, E and C banks respectively. Detector banks utilised in this study are C and E with d-spacings ranging from 0.2 - 3.2 and 0.2 - 4.0 correspondingly. The POLARIS instrument can be seen in *figure 2.4*.
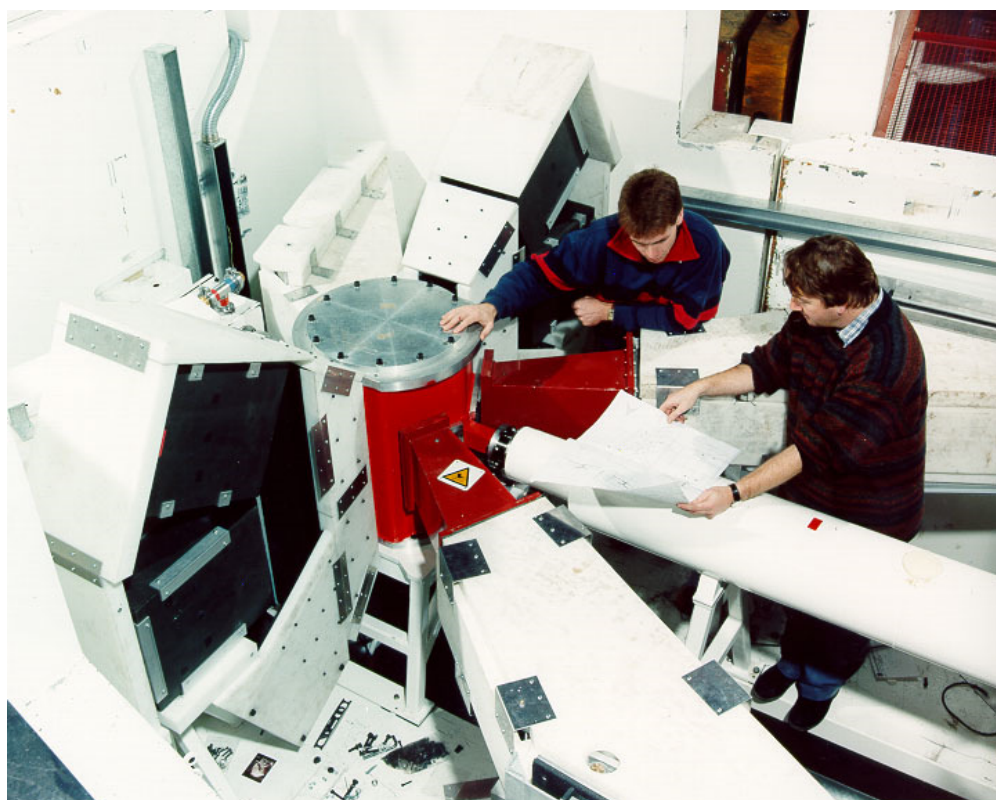
Figure 2.4: POLARIS instrument at target station 1, ISIS.[12]

- HRPD is the highest resolution neutron powder diffractometer of its type in the world. It is composed of three detectors, a ZnS Scintillator, backscattering and 90° detector and a ^{3}He low angle detector. These are used to collect data over a range of d-spacings, ~0.6 - 4.6 Å, ~0.9 - 6.6 Å and ~2.2 - 16.5 Å for backscattering, 90° and low angle respectively. The HRPD instrument can be seen in *figure 2.5*.
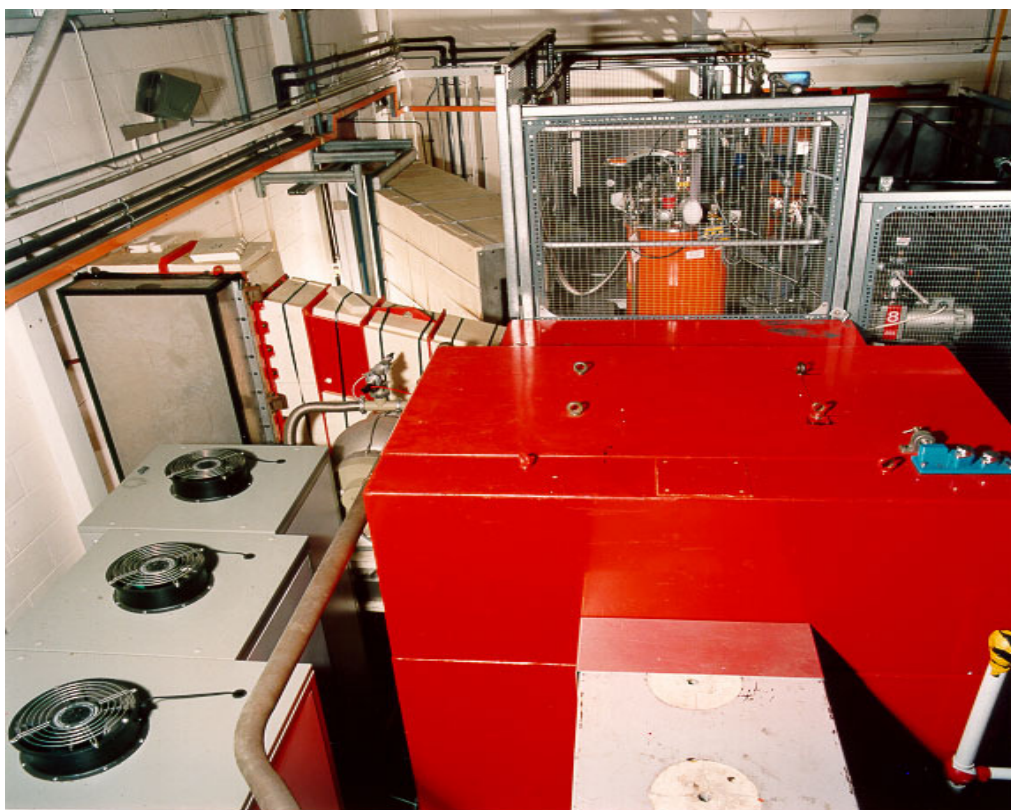
Figure 2.5: View of the HRPD instrument enclosure.[13]

2.3 Rietveld Structural Refinement

Rietveld refinement is a widely used tool for the structural refinement of polycrystalline materials. The refinement process uses a well-established mathematical procedure called least squares analysis, which defines the 'best fit' of two sets of data and allows strongly overlapping reflections to be resolved. The technique therefore requires a diffraction data file where intensity has been recorded at well defined steps and a model structure / approximate solution. The least squares analysis process aims for a 'best fit' of data by minimising the difference between all of the observed intensity points (experimental data) and the calculated intensities (model data). To achieve this certain variables are adjusted, which are related to the crystal structure, such as lattice parameters, atomic coordinates, thermal parameters and fractional occupancies. Variables related to the instrument can also be adjusted.

The intensity of the diffracted beam, I_{hkl} is proportional to the structure factor, F_{hkl} by the relationship defined in **equation 2.5**:

$$I_{hkl} \propto |F_{hkl}|^2$$
<div align="right">**Equation 2.5**</div>

The quantity minimised in the least squares refinement is the residual S_y:[14]

$$S_y = \sum_i \{w_i(y_i(obs) - y_i(calc))\}^2$$
<div align="right">**Equation 2.6**</div>

where,

$y_i(obs)$ = observed (gross) intensity at the ith step

$y_i(calc)$ = calculated intensity at the ith step, the sum is over all data points

w_i is a weighting factor, usually taken as, $w_i = 1/y_i(obs)$

Several R values are used, known as reliability factors, to assess the correlation between the calculated and observed models; these are R_{wp} (weighted pattern), R_p (pattern), R_e (expected) and a value of χ^2 is used to describe the "goodness of fit" of the overall refinement. The equations below describe these different parameters:

$$R_{wp} = \left\{ \frac{\sum w_i (y_i(obs) - y_i(calc))^2}{\sum w_i (y_i(obs))^2} \right\}^{1/2}$$

Equation 2.7

$$R_p = \frac{\sum |y_i(obs) - y_i(calc)|}{\sum y_i(obs)}$$

Equation 2.8

$$R_e = \left\{ \frac{(n-p+c)}{\sum w_i y_i(obs)^2} \right\}^{1/2}$$

Equation 2.9

where,

n = number of points

p = number of variables

c = number of constraints applied.

$$\chi^2 = \frac{R_{wp}}{R_e}$$

Equation 2.10

The GSAS suite of programs[15] (General Structure Analysis System) is used for all Rietveld refinements detailed in this thesis.

2.5 Dielectric Properties

2.5.1 Microwave Dielectric Resonance Measurement

There are two main microwave dielectric resonance measurement techniques in common use, the post resonance technique also known as the Hakki and Coleman method[16], and the cylinder cavity resonance technique.[17, 18] The difference between the two techniques is based on different geometrical arrangements of metal shields; these shields are introduced to prevent radiation loss. For both techniques a relatively large sample volume is required as the resonance is basically supported by the dielectric itself. The lowest transverse electric (TE) mode of a cylindrical dielectric sample is always used in both techniques for measurements as it makes it easier to

identify the resonance peak, and the equations for the dielectric properties are more easily derived than those of other modes.

- Hakki and Coleman first suggested the post resonance technique in 1960[16]; this is the most popular and widely used dielectric resonance method for measurement of dielectric properties. A cylindrical dielectric rod is placed between two parallel metal plates, which are larger than the dielectric rod, and two coupling antennae are used to connect power in and out which are loosely electromagnetically coupled to the system. The TE_{011} mode is adopted for measurements and the resonant frequency f_o, the half power bandwidth Δf_{3dB}, the insertion loss S_{21}, the diameter D = 2a, and thickness L of the specimen are recorded for the calculation of dielectric properties.

- In the cylinder cavity resonance technique the sample is put inside a cylindrical cavity with diameter *d* and height *h*, and sat on a quartz support, *figure 2.6*. The $TE_{01\delta}$ mode is used for measurements and values of the same parameters are recorded, as per the Hakki and Coleman method. However a more accurate dielectric loss value is provided and it requires a slightly smaller sample size than that of the Hakki and Coleman method.
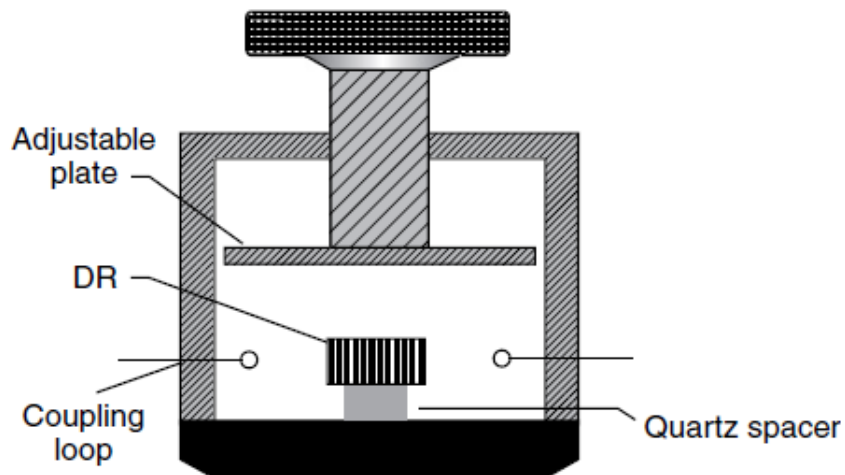
Figure 2.6: Schematic of the set-up for the cylinder cavity resonance technique[19]

Essentially ε_r is determined from the resonance frequency f_0, and Q from $f_0 / \Delta f$, where Δf is the 3 dB bandwidth. The temperature coefficient of resonant frequency (TCF) is calculated by measuring the resonant frequency of the material over a range of temperatures, using **equation 2.11**:

$$TCF = \frac{1}{f_0} \times \frac{\Delta f_0}{\Delta T}$$

<div align="right">*Equation 2.11*</div>

where,

f_0 is the resonance frequency at 320 K,

Δf_0 is the change in frequency

ΔT is the change in temperature

This coefficient is expressed as parts per million per degrees Celsius (ppm / °C) by multiplying the results by 1,000,000.

Measurements for the current project were performed using the cylinder cavity technique at the Department of Engineering Materials at the University of Sheffield.

2.5.2 Impedance Spectroscopy

Impedance spectroscopy is a technique used for the electrical characterisation of materials, where the response of a dielectric material to an applied voltage is plotted as a function of frequency at set temperatures. It aids in the identification of observed relaxation effects with processes at both the atomic and microstructural levels.[20] Therefore ac impedance measurements allow the different regions of the material to be characterised according to their relaxation times or time constants. The impedance of the sample is measured over a wide range of frequency, typically 10^{-2} to 10^7 Hz. Different regions of a ceramic sample are characterised by a resistance and a capacitance, usually placed in parallel. The characteristic relaxation time, or time constant τ, of each 'parallel RC element' is given by the product of R and C, $\tau = RC$. The RC elements are separable due to the relation, $\omega_{max} RC = 1$, which holds at the maximum loss ω_{max}, in the impedance spectrum.
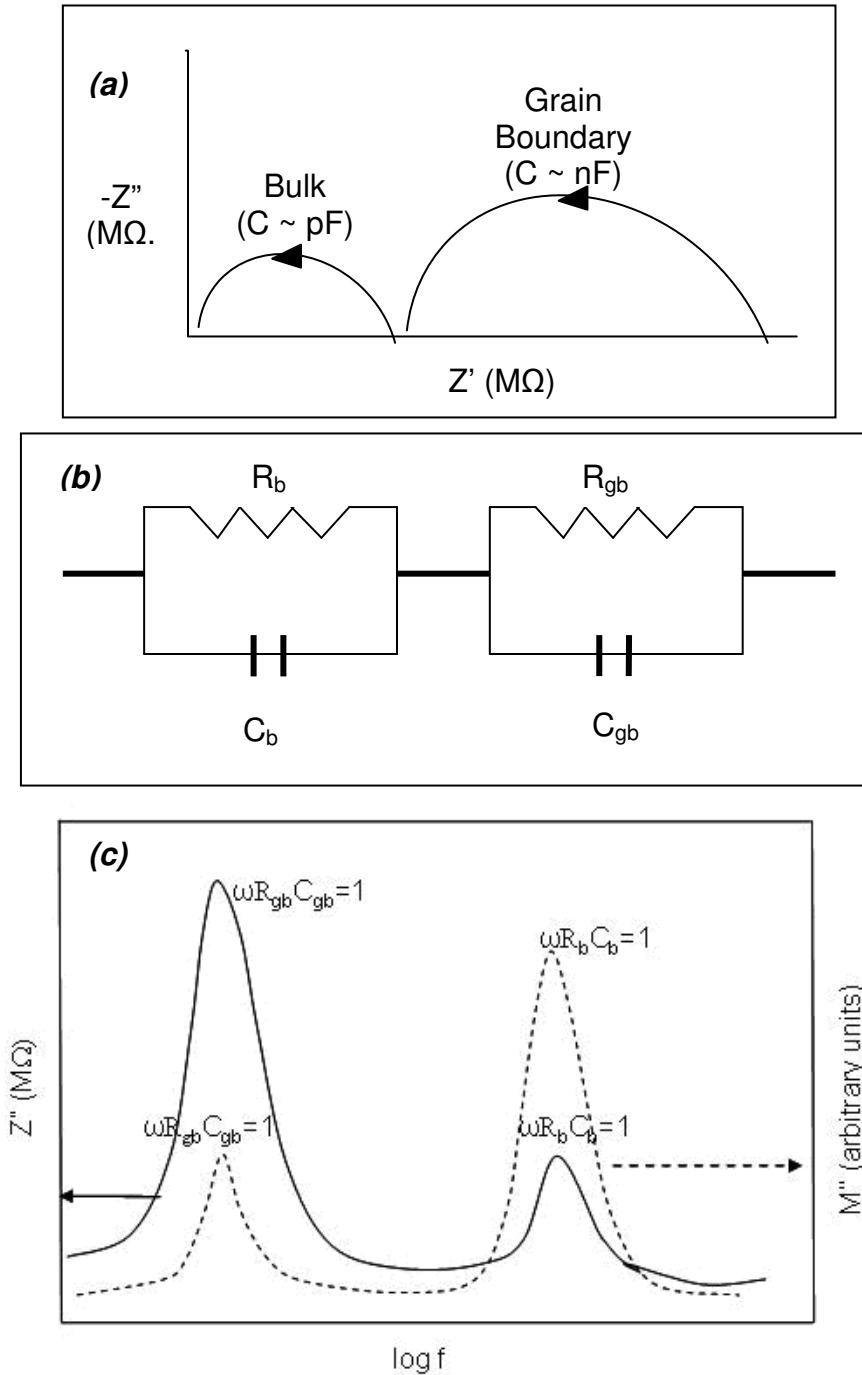
Impedance data are presented in the form of a Z* plot of imaginary Z" (capacitive) against real Z' (resistive) impedances, **figure 2.5** (a). Each parallel RC element, **figure 2.5** (b), gives rise to a semi-circle in the impedance plot, with the R values acquired from the intercepts on the Z' axis, and the C values are obtained by applying the equation, $\omega_{max} RC = 1$ to the frequency at the maximum of each semi-circle. Once R and C values have been defined, these can be assigned to regions of the sample. The assignment is based on the magnitudes of the capacitances as described in **table 2.1**.

Capacitance (F)	Phenomenon Responsible
10^{-12}	Bulk
10^{-11}	Minor, second phase
10^{-11}-10^{-8}	Grain boundary
10^{-10}-10^{-9}	Bulk ferroelectric
10^{-9}-10^{-7}	Surface layer
10^{-7}-10^{-5}	Sample-electrode interface
10^{-4}	Electrochemical reactions

**Table 2.1**: Capacitance values and their possible interpretation[20]

In an ideal situation this form of data representation would yield enough information, however sometimes particular features of the sample can dominate the response and a Z* plot can often show a singular unresolved semi-circle. In this case M* plots or -Z", M" spectroscopic plots are utilised (where $M^* = j \omega C_o Z^*$, $j = \sqrt{-1}$, and C_o is the vacuum capacitance of the cell) can be used to extract R and C values. The values are calculated from the Debye peaks which occur at $\omega_{max} RC = 1$ for the different electroactive regions in combined spectroscopic plots of the imaginary components of impedance and electric modulus, -Z" (MΩ), M" (arbitrary units), as shown in **figure 2.5** (c). In this particular case where the grain boundary and the bulk regions

have very different time constants, each region can be clearly distinguished by visual inspection of -Z" and M" spectroscopic plots. Each spectrum contains two Debye peaks, and ω_{max} in -Z" and M" spectroscopic plots occurs at a similar frequency for each region.


Figure 2.5: (a) Schematic representation of Impedance data presented in the form of a Z* plot for the circuit shown in (b). (b) A typical equivalent circuit used to analyse impedance spectroscopy data of electroceramics. (c) A typical combined -Z",M" spectroscopic plot for the circuit shown in (b), reproduced from[21].

A ceramic which is electrically homogeneous, shows only a single semicircular arc in Z* plots and therefore demonstrates evidence for only a bulk component. -Z" and M" spectroscopic plots for a homogeneous ceramic show a single Debye peak occurring at very similar frequencies in each spectrum, *figure 2.6*. The bulk response can therefore be modelled on a single parallel RC element. An electrically inhomogeneous ceramic, however, consists of either, a rather broad and depressed single-arc in Z* plots, which could in some cases, be interpreted as two poorly-resolved overlapping semicircles. Such non-ideal responses are indicative of either an electrically heterogeneous bulk response or overlapping bulk and grain boundary responses with similar time constants. The -Z" and M" spectroscopic plots for heterogeneous ceramics have single but broadened Debye peaks that occur at different frequencies, *figure 2.7*.
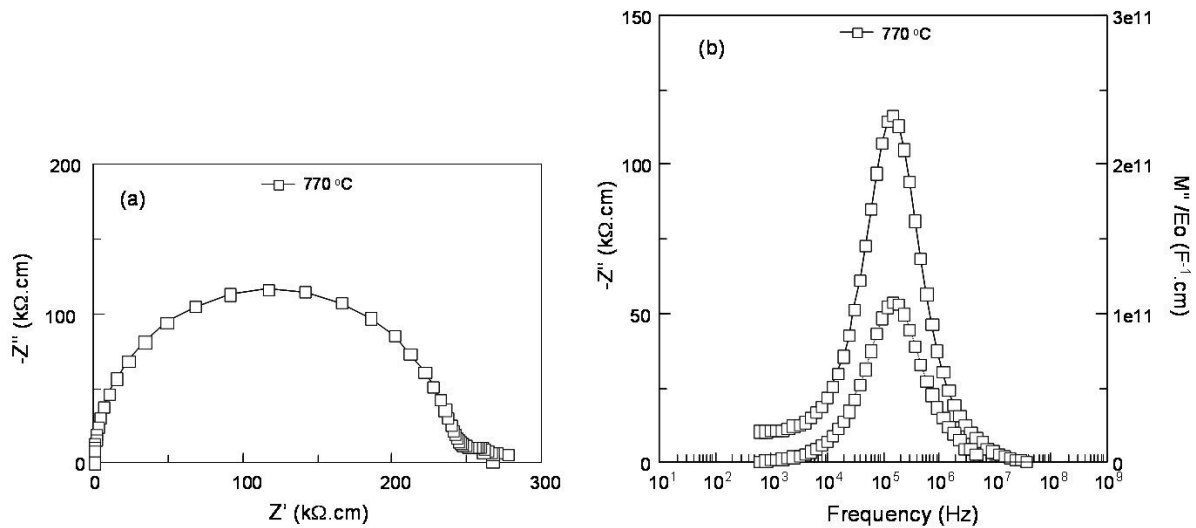
Figure 2.6: (a) Z* plot and (b) a combined -Z",M" spectroscopic plot for a homogeneous ceramic recorded at 770 °C.
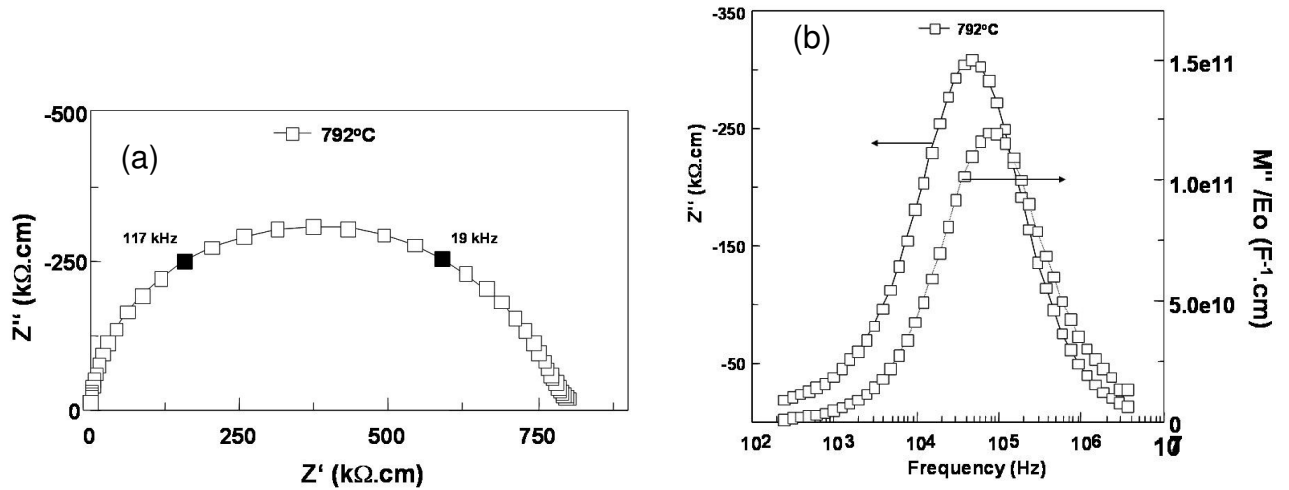
Figure 2.7: (a) Z* plot and, (b) combined -Z", M" spectroscopic plot for a heterogeneous ceramic recorded at 792 °C.

The temperature dependence of resistance is plotted in the Arrhenius format, from which activation energies associated with bulk and grain boundary conduction processes can be established. The slope of the straight line is usually proportional to the band gap.

Therefore impedance spectroscopy is useful because it can be used to indicate whether the overall resistance of a material is dominated by bulk or grain boundary components, to assess the quality and electrical homogeneity of an electroceramic, since there is generally link between microstructure and ac response, and finally to measure the values of the component resistances and capacitances.

Impedance measurements were performed at the Department of Engineering Materials at the University of Sheffield by Mr Andrew Mould. Measurements were performed on two sets of equipment, a Hewlett Packard 4192A Impedance analyser (5 Hz - 40 MHz) and an Agilent 4294A (40 Hz -100 MHz). In both cases, the applied voltage was 100 mV.

2.5.3 Fixed frequency capacitance measurement

Fixed frequency complex capacitance measurements were performed using an LCR meter at the Department of Engineering Materials at the University of Sheffield by Mr Andrew Mould. In simple terms, if impedance spectroscopy is a frequency sweep at particular temperatures, then the fixed frequency complex capacitance measurements are a temperature sweep at particular frequencies.

2.5.4 Density calculations

The density of pellets was calculated using Archimedes principle, whereby:

$$\rho = {}^{m}\!/_{V} \hspace{6cm} \textbf{\textit{Equation 2.12}}$$

Where, ρ is density, m is the mass, and V is the volume of the pellet.

2.6 References

1.   Bragg, W.L., *Proceedings of the Royal Society of London. Series A, Containing Papers of a Mathematical and Physical Character.* **89**, 613 468-489 (1914)

2.   West, A.R., *Basic Solid State Chemistry* (Wiley, Chichester, 1999)

3.   Cockcroft, J.K. *Peak Intensities in Powder Diffraction.* in *PCG Rietveld school.* 2008. Durham.

4.   Furrer, A., Mesot, J., and Strassle, T., *Neutron Scattering in Condensed Matter Physics* (World Scientific, Singapore, 2009)

5.   Clegg, W., *Crystal Structure Determination* (Oxford University Press, 1998)

6.   Rodriguez-Carvajal, J., *Physica B.* **192**, 55 (1993)

7.   Laugier., J. and Bochu., B. *CHEKCELL Graphical indexing and spacegroup assignment helper tool* [Accessed, 2010] Available from: http://www.ccp14.ac.uk/ccp/web-mirrors/lmgp-laugier-bochu/.

8.   Ill.,*D2B*[Accessed,28/08/2010]Availablefrom:http://www.ill.eu/html/instruments-support/instruments-groups/instruments/d2b/.

9.   Bacon, G.E., *Neutron Physics* (Clarendon Press, Oxford, 1955)

10.   Bacon, G.E., *Neutron Diffraction* (Clarendon Press, Oxford, 1973)

11.   Isis. *http://www.isis.stfc.ac.uk/instruments/gem/* [Accessed, 28/08/2010].

12.   Isis. *http://www.isis.stfc.ac.uk/instruments/polaris/* [Accessed, 28/08/2010].

13.   Isis. *http://www.isis.stfc.ac.uk/instruments/hrpd/* [Accessed, 28/08/2010].

14.   Lee, C., Ou, C., Lin, Y., Huang, C., Su, C., *Journal of European Ceramic Society.* **27**, 5 2273-2280 (2007)

15.   Larson, A.C. and Von Dreele, R.B., *General Structure Analysis System (GSAS)*, in *Los Alamos National Laboratory Report* 1994.

16.   Hakki, B.W. and Coleman, P.D., *Microwave Theory and Techniques, IRE Transactions on.* **8**, 4 402-410 (1960)

17.   Krupka, J., *Measurement Science and Technology.* **9**, 10 1751 (1998)

18.   Krupka, J., *Measurement Science and Technology.* **17**, 6 R55 (2006)

19.   Mailadil, T.S., *Dielectric Materials for Wireless Communication* (Elsevier Science, Amsterdam, 2008)

20.   Moulson, A.J. and Herbert., J.M., *Electroceramics, Materials, Properties and Applications* (Wiley, Chichester, 2008)

21. Keith, G.M., *Synthesis and Characterisation of Transition Metal Doped Hexagonal BaTiO₃*, in *Department of Engineering Materials*. 2003, University of Sheffield: Sheffield.

Chapter 3

Synthesis and Characterisation of B-cation deficient Series $Ba_{3-x}Sr_xLaNb_3O_{12}$ (x = 1 - 3)

3.1 Introduction

The $Ba_{3-x}Sr_xLaNb_3O_{12}$ series can be described as 12R-type B-cation deficient "shifted" structures[1] of the n=4 layered variety, previously described in **section 1.1.5**. As the structures are "shifted" there is a resulting periodic shift between the corner-sharing octahedral blocks a vector of ⅓<01-10>$_H$.

$Sr_3LaNb_3O_{12}$ was first synthesised in 1987 by Sirotinkin *et al.*[2] and $Ba_3LaNb_3O_{12}$ in 1980 by Rother *et al.*[3] The end members have been quoted as crystallising in space group R-3m[2-5] but recently Rawal *et al.*[6] demonstrated that both structures are better described in space group R-3, and not R-3m as previously quoted, therefore tilting of the NbO_6 octahedra is present within the structure. The study also investigated the relationship between the structural features and the dielectric properties exhibited by the materials $Ba_3LaNb_3O_{12}$ and $Sr_3LaNb_3O_{12}$. It was postulated that the tilted octahedra within the structure influence the dielectric properties of the compound, more specifically the *TCF*. Furthermore it was suggested that a tilt transition occurs within the structures from tilted to untilted (from space group R-3 to R-3m) at temperatures of ~ 192 °C and ~ 447 °C for $Ba_3LaNb_3O_{12}$ and $Sr_3LaNb_3O_{12}$ respectively. This is reflected in the *TCF* values witnessed (for the Ba-rich oxide -100 ppm / °C and for the Sr-rich oxide -5 ppm / °C) implying that the *TCF* value is dependent on the proximity to room temperature of the tilt transition temperature. It was therefore hypothesised that in these 12*R*-type hexagonal perovskites, *TCF* can be tuned by controlling the tolerance factor, and consequently the tilt transition temperature, in a manner similar to that used for many Ba- and Sr-based 3*C*-type ABO_3 perovskites.

Of late Hu *et al.*[7] investigated the $Ba_{3-x}Sr_xLaNb_3O_{12}$ system, (where x= 0 − 3) this is the only published evidence quoting the synthesis of the intermediate compositions $Ba_2SrLaNb_3O_{12}$ and $BaSr_2LaNb_3O_{12}$. This study found that on increasing the Sr^{2+} content the Q changed from 12000 to 45327 GHz, *TCF* improved from -93 to -9 ppm

/ °C, and ε_r decreased, although this study still quotes all structures in space group R-3m, which is contrary to that quoted for the end members by Rawal *et al.*[8]

Therefore further investigation of the $Ba_{3-x}Sr_xLaNb_3O_{12}$ series of phases is warranted to gain a more accurate understanding of the structure-property relationships.

3.2 Synthesis

All materials in the series were synthesised *via* the standard ceramic route. Stoichiometric amounts of dried high purity reagents, $BaCO_3$, $SrCO_3$, La_2O_3 and Nb_2O_5 were hand ground using a pestle and mortar. They were then heated at a rate of 300 °C per hour, to reaction temperature, 1400 °C for $Sr_3LaNb_3O_{12}$, and 1360 °C for $Ba_3LaNb_3O_{12}$, $Ba_2SrLaNb_3O_{12}$ and $BaSr_2LaNb_3O_{12}$. Each ceramic was heated for 120 hours, with intermediate grindings every 24 hours. The materials were allowed to cool to room temperature.

3.3 Structural Characterisation

3.3.1 X-ray Powder Diffraction (XRPD) and Neutron Powder Diffraction (NPD)

X-ray powder diffraction (XRPD) patterns were collected on a STOE STADI P X-ray powder diffractometer at the University of Sheffield. The scans were over the range 5 - 100 degrees 2theta (scan length 14 hours 35 minutes, detector step size of 0.01°, time / step of 50 seconds). Neutron powder diffraction data were collected on the HRPD instrument at ISIS, Oxford (room temperature (RT), for $Ba_2SrLaNb_3O_{12}$, and $BaSr_2LaNb_3O_{12}$) and on the D2B diffractometer at the Institut Laue-Langevin (λ = 1.594), Grenoble, France (variable temperature for $Sr_3LaNb_3O_{12}$, $Ba_2SrLaNb_3O_{12}$, and $BaSr_2LaNb_3O_{12}$). Details of each data collection source are listed in **table 3.00**. Data were refined using the Rietveld method with the GSAS suite of programs.[9] Variable temperature NPD data have already been published for $Ba_3LaNb_3O_{12}$[8], therefore all refinement data quoted for this composition is from published values, just for the purpose of providing a complete set of data for the $Ba_{3-x}Sr_xLaNb_3O_{12}$ series.

	RT	320°C	600°C	900°C
$Ba_2SrLaNb_3O_{12}$	HRPD D2B	D2B	-	D2B
$BaSr_2LaNb_3O_{12}$	HRPD	-	-	D2B
$Sr_3LaNb_3O_{12}$	D2B	-	D2B	D2B

Table 3.00*: Details of NPD collection sources.*

A two-step approach to the refinement of the model against the diffraction data was required for the intermediate structures due to the presence of three A-site cations. The model was refined against the XRPD data solely to establish the Sr^{2+} occupancy in the structure over the two available A-sites. The Ba^{2+} and La^{3+} ions were entered as one element, as Ba^{2+} and La^{3+} are essentially indistinguishable with X-rays. This approach allows the Sr^{2+} fractional occupancy to be established. In the next step several approaches were investigated: (i) a joint refinement using XRPD and NPD data with the Sr^{2+} occupancies fixed from the XRPD refinement (ii) a joint XRPD and

NPD refinement with each element allowed to vary separately with constraints and (iii) NPD refinement with the Sr^{2+} occupancy values fixed from the XRPD refinement.

Using method (i), the Ba^{2+} and La^{3+} occupancies were refined with constraints thus ensuring the overall occupancy of the A-sites remained at 100%. Similar constraints were applied for method (iii). For method (iii) an alternate refinement was performed where all A-site elements were allowed to vary separately with constraints applied only to each element, method (ii), to assess the validity of the refinement approach. Occupancy values within 3% of the values obtained for method (i) were obtained, therefore the fixing of the Sr^{2+} occupancy values from the XRPD refinement was deemed acceptable (however in some cases when using method (i) the A-site occupancies were slightly above or below 100 % due to rounding up). Method (iii) was considered to be the most appropriate giving more reliable, unbiased statistics. An example of all of these varying approaches is presented for $Ba_2SrLaNb_3O_{12}$ in **section 3.3.1.1**.

During variable temperature NPD refinements for $Ba_2SrLaNb_3O_{12}$ and $BaSr_2LaNb_3O_{12,}$ each elemental A-site occupancy was allowed to vary individually with constraints, method (ii), this meant that A-site occupancy sometimes showed a minor deviation from 100 %, but gave an unbiased assessment of the structure. For example, for the RT data for $Ba_2SrLaNb_3O_{12}$ (D2B) refinement method (iii) was used, but for the higher temperature refinements method (ii) was required as no comparable XRPD data were available. For the $Sr_3LaNb_3O_{12}$ NPD refinements, constraints could be applied to the A-sites as Sr^{2+} and La^{3+} have discernible neutron scattering lengths b (Ba: b=0.525 fm, Sr: b=0.702 fm, La: b=0.827 fm) and only two A-cations are present. Variable temperature NPD data were necessary to study structural changes as a function of increasing temperature, with an aim to use these data to aid the interpretation of electrical measurements.
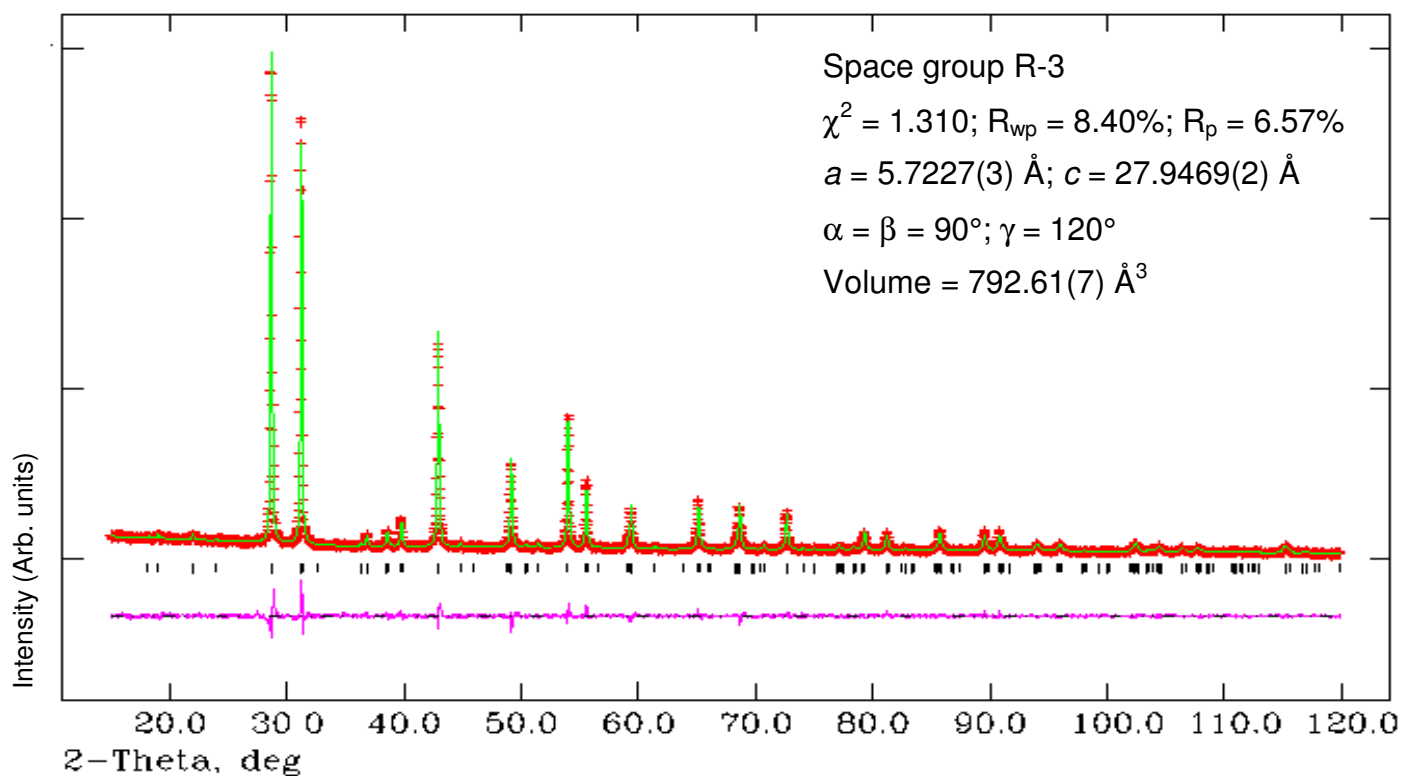
3.3.1.1 Ba$_2$SrLaNb$_3$O$_{12}$

Fitted diffraction profiles and refined parameters from each refinement approach are presented to both illustrate the differences and provide evidence for the final refinement method choice.

3.3.1.1.1 XRPD refinement

The refinement results are summarised below in **figure 3.00** and **table 3.01**. Refinement statistics and lattice parameters are given in **figure 3.00**.

Figure 3.00: Calculated (green), experimental (red) and difference (pink) profile plot for $Ba_2SrLaNb_3O_{12}$ XRPD data. Tick marks represent Bragg peak positions.
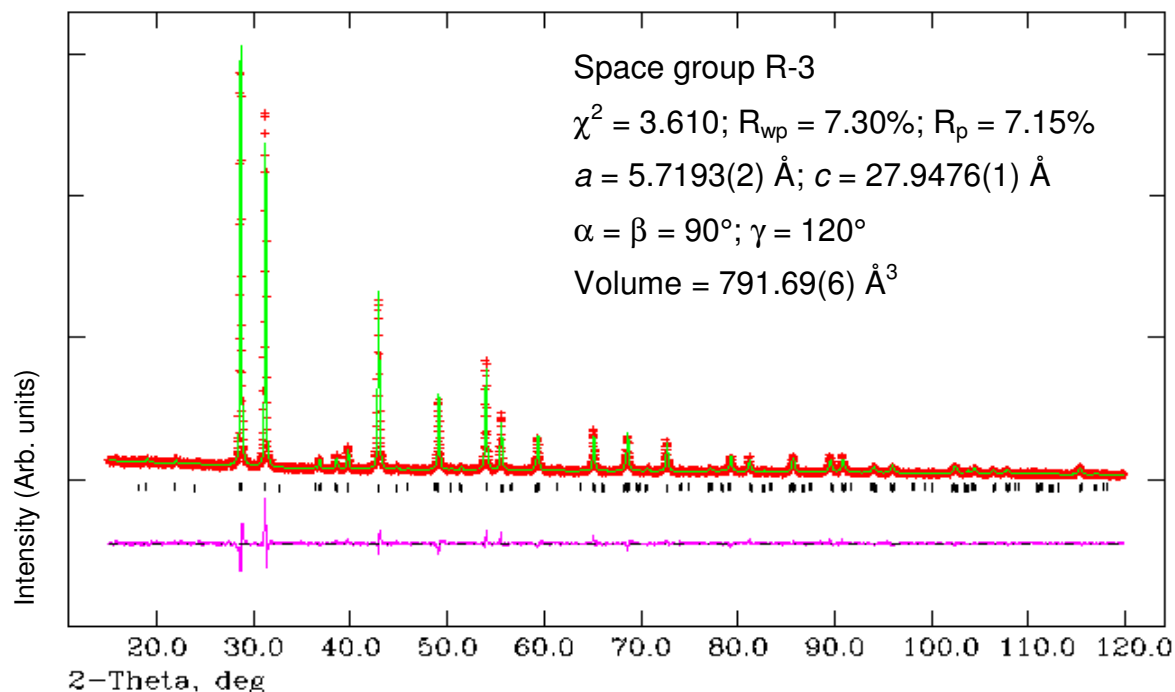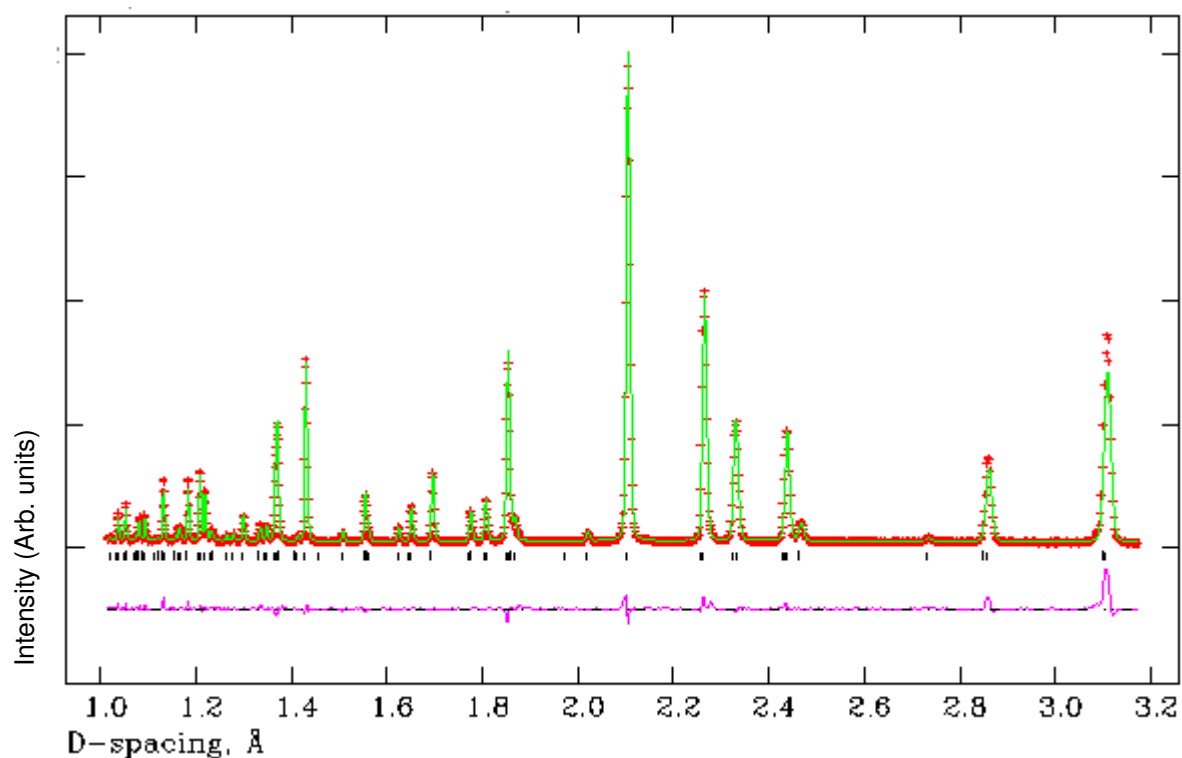
Atom	Wyckoff	x	y	z	U_{iso}*100 ($\AA^2$)	Frac.
Ba/Sr1	6c	0	0	0.2878(2)	2.81(2)	0.71(2)*/0.30(2)**
Ba/Sr2	6c	0	0	0.1354(2)	1.40(2)	0.80(2)*/0.21(2)**
Nb1	6c	0	0	0.4232(2)	1.26(2)	1
Nb2	3a	0	0	0	1.12(2)	1
O1	18f	0.142(1)	0.813(4)	0.6267(8)	4.2(8)	1
O2	18f	0.152(1)	0.791(1)	0.4530(5)	2.7(7)	1

Ba^{2+} and La^{3+} are entered as one element. **Due to rounding up the overall A-site occupancies are slightly over 100%, and thus slightly over the stated composition, but are within experimental error.*

Table 3.01: Refinement results for $Ba_2SrLaNb_3O_{12}$ (XRPD RT data)

3.3.1.1.2 Method (i)

The refinement results are summarised below in *figures 3.01, 3.02, 3.03* and *table 3.02*. Refinement statistics and lattice parameters are given in *figure 3.01*.

Space group R-3

$\chi^2 = 3.610$; $R_{wp} = 7.30\%$; $R_p = 7.15\%$

$a = 5.7193(2)$ Å; $c = 27.9476(1)$ Å

$\alpha = \beta = 90°$; $\gamma = 120°$

Volume $= 791.69(6)$ Å^3

Figure 3.01: Calculated (green), experimental (red) and difference (pink) profile plot for $Ba_2SrLaNb_3O_{12}$ XRPD data. Tick marks represent Bragg peak positions.
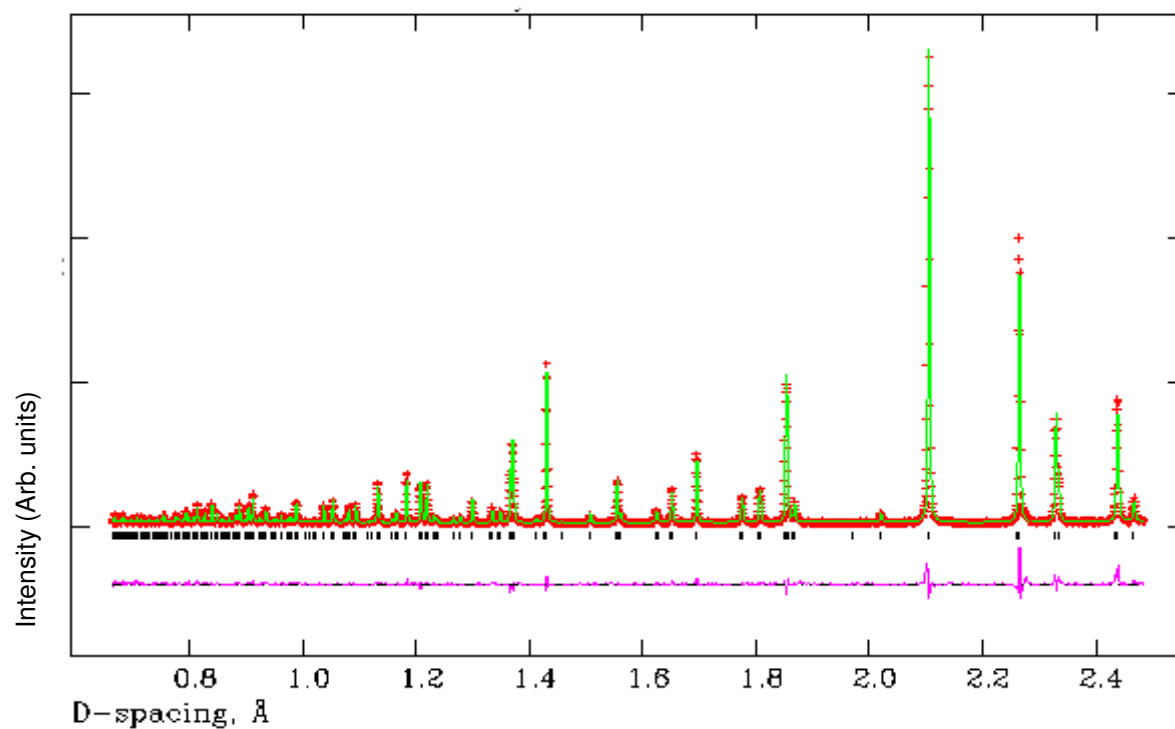
Figure 3.02: Calculated (green), experimental (red) and difference (pink) profile plot for $Ba_2SrLaNb_3O_{12}$ NPD data from HRPD backscattering bank (bank 1). Tick marks represent Bragg peak positions.

Figure 3.03: Calculated (green), experimental (red) and difference (pink) profile plot for $Ba_2SrLaNb_3O_{12}$ NPD data from HRPD 90NS bank (bank 2). Tick marks represent Bragg peak positions.
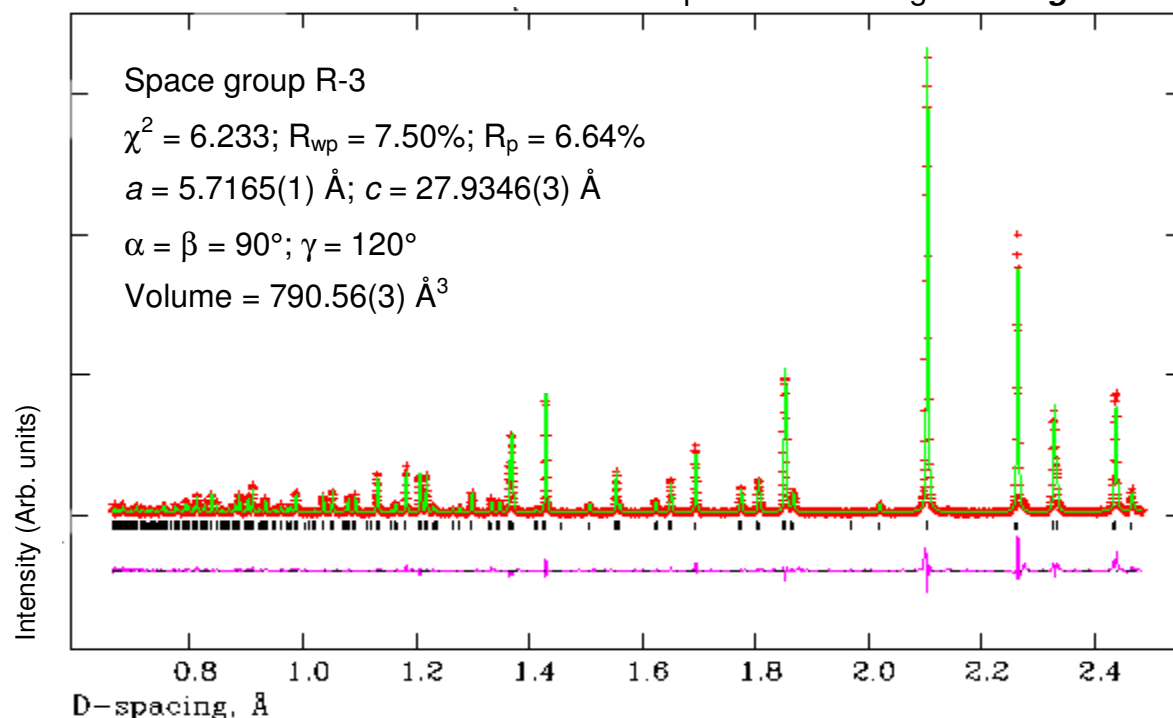
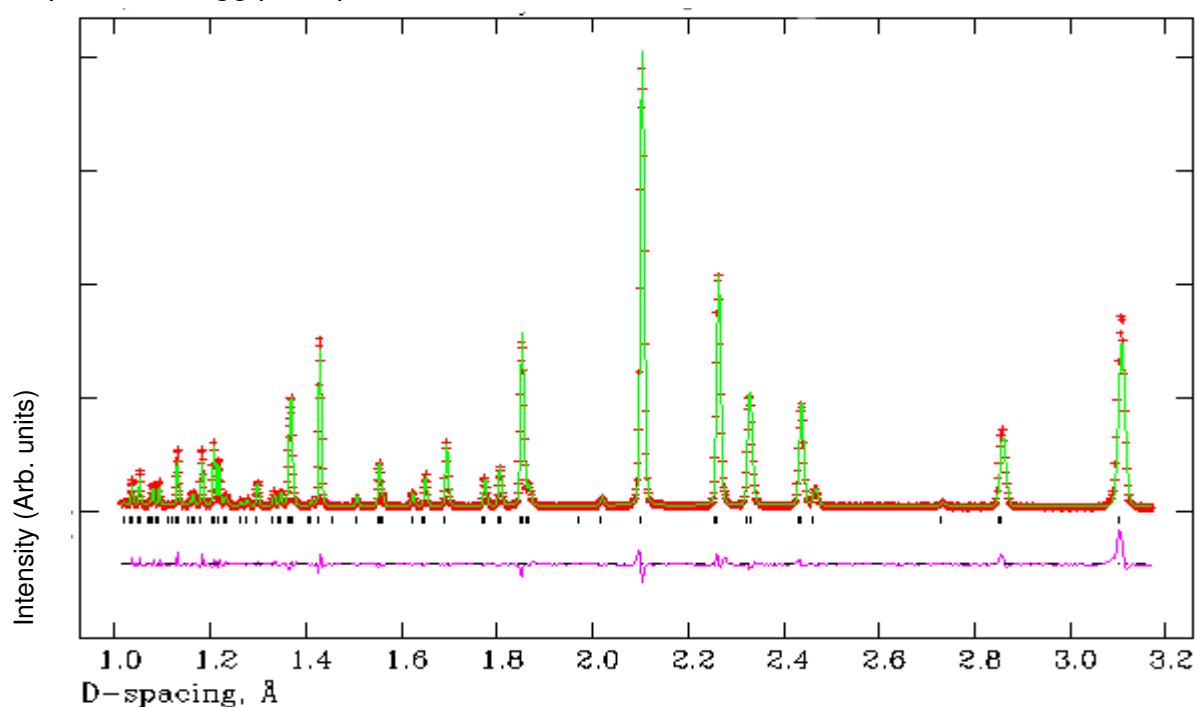| Atom	Wyckoff	x	y	z	$U_{iso}*100$ ($Å^2$)	Frac.
Ba/Sr/La1	6c	0	0	0.2867(1)	1.32(7)	0.24(1)/0.30*/0.46(1)
Ba/Sr/La2	6c	0	0	0.1369(1)	2.11(1)	0.76(1)/0.20*/0.04(1)
Nb1	6c	0	0	0.4222(1)	1.70(5)	1
Nb2	3a	0	0	0	1.53(7)	1
O1	18f	0.6701(5)	0.7968(4)	0.6288(5)	2.88(4)	1
O2	18f	0.1948(4)	0.8622(4)	0.4518(4)	2.35(4)	1

*Sr^{2+} occupancies fixed from XRPD refinement.

Table 3.02: Refinement results for $Ba_2SrLaNb_3O_{12}$ (XRD & HRPD RT data)

3.3.1.1.3 Method (ii)

The refinement results are summarised below in *figures 3.04, 3.05, 3.06* and *table 3.03*. Refinement statistics and lattice parameters are given in *figure 3.04*.

Space group R-3

$\chi^2 = 3.867$; $R_{wp} = 7.55\%$; $R_p = 7.78\%$

$a = 5.7166(1)$ Å; $c = 27.9344(6)$ Å

$\alpha = \beta = 90°$; $\gamma = 120°$

Volume = 790.976(3) Å^3
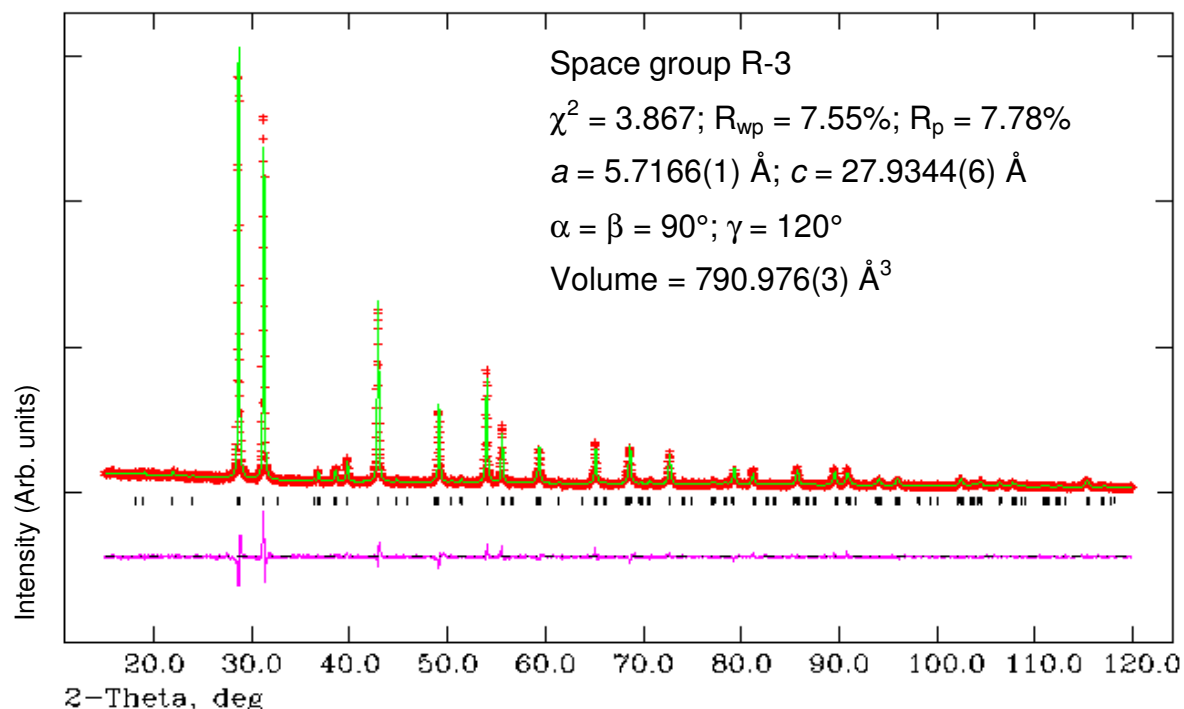
Figure 3.04: Calculated (green), experimental (red) and difference (pink) profile plot for Ba$_2$SrLaNb$_3$O$_{12}$ XRPD data. Tick marks represent Bragg peak positions.
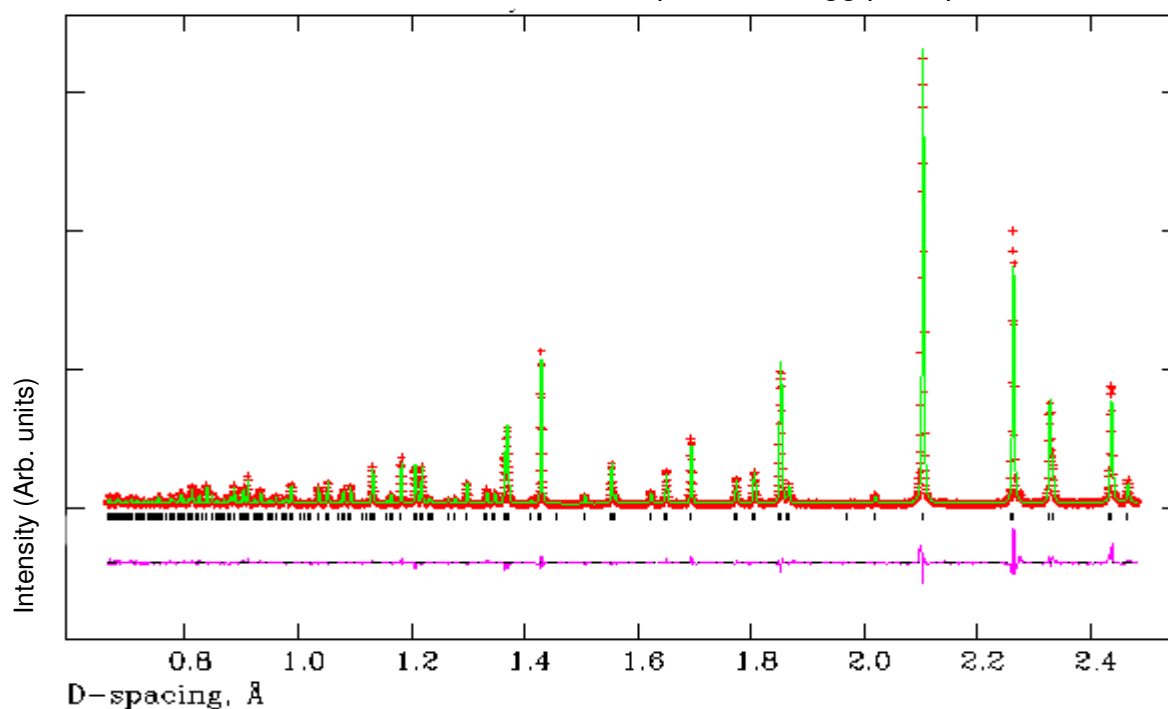
Figure 3.05: Calculated (green), experimental (red) and difference (pink) profile plot for Ba$_2$SrLaNb$_3$O$_{12}$ NPD data from HRPD backscattering bank (bank 1). Tick marks represent Bragg peak positions.

69
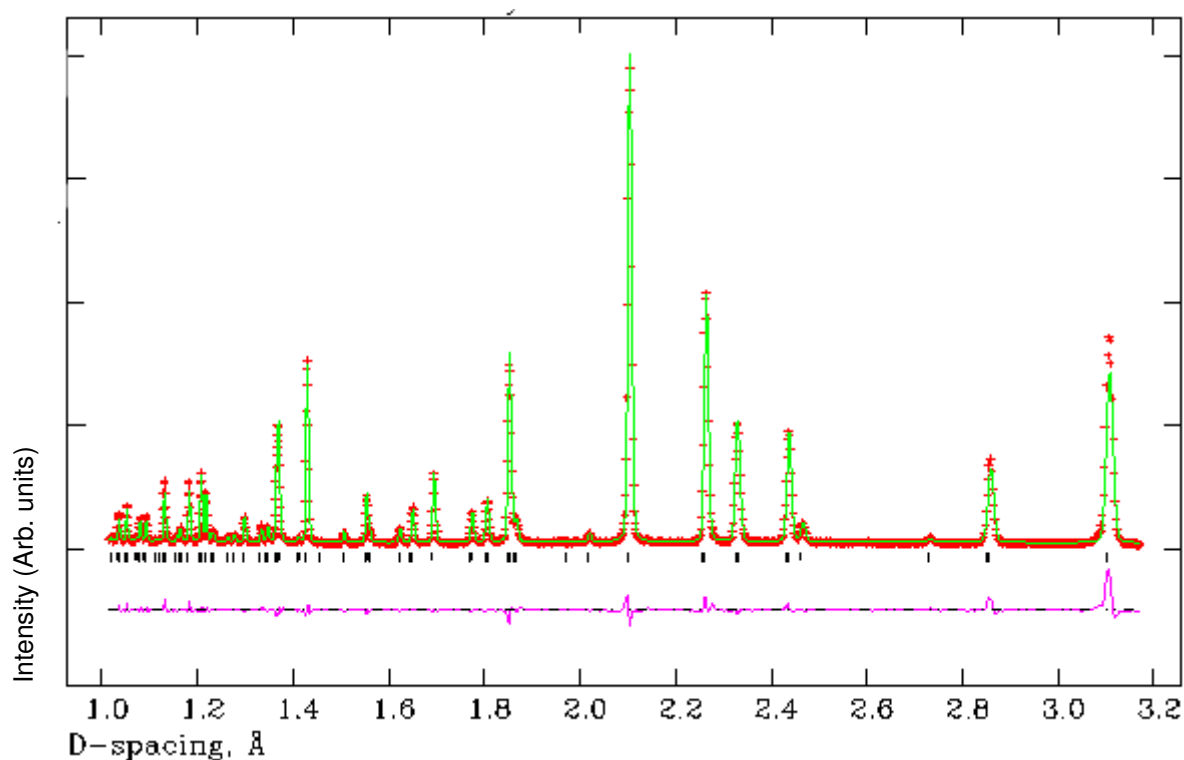
Figure 3.06: Calculated (green), experimental (red) and difference (pink) profile plot for $Ba_2SrLaNb_3O_{12}$ NPD data from HRPD 90NS bank (bank 2). Tick marks represent Bragg peak positions.

Atom	Wyckoff	x	y	z	$U_{iso}*100$ $(Å^2)$	Frac.
Ba/Sr/La1	6c	0	0	0.2867(1)	1.14(5)	0.22(1)/0.30(1)/0.46(1)*
Ba/Sr/La2	6c	0	0	0.1369(1)	2.37(7)	0.79(1)/0.19(1)/0.04(1)*
Nb1	6c	0	0	0.4222(1)	1.72(5)	1
Nb2	3a	0	0	0	1.54(7)	1
O1	18f	0.6701(6)	0.7970(4)	0.6288(5)	2.90(4)	1
O2	18f	0.1949(4)	0.8623(4)	0.4518(4)	2.36(4)	1

A-site occupancies are not exactly 100% as each element was allowed to vary independently.

Table 3.03: Refinement results for $Ba_2SrLaNb_3O_{12}$ (XRD & HRPD RT data)

3.3.1.1.4 Method (iii)

The refinement results are summarised below in *figures 3.07* and *3.08* and *tables 3.03* and *3.04*. Refinement statistics and lattice parameters are given in *figure 3.07*.

Space group R-3

$\chi^2 = 6.233$; $R_{wp} = 7.50\%$; $R_p = 6.64\%$

$a = 5.7165(1)$ Å; $c = 27.9346(3)$ Å

$\alpha = \beta = 90°$; $\gamma = 120°$

Volume = 790.56(3) Å^3

Figure 3.07: Calculated (green), experimental (red) and difference (pink) profile plot for $Ba_2SrLaNb_3O_{12}$ NPD data from HRPD backscattering bank (bank 1). Tick marks represent Bragg peak positions.

Figure 3.08: Calculated (green), experimental (red) and difference (pink) profile plot for $Ba_2SrLaNb_3O_{12}$ NPD data from HRPD 90NS bank (bank 2). Tick marks represent Bragg peak positions.

Atom	Wyckoff	x	y	z	$U_{iso}*100$ (Å^2)	Frac.
Ba/Sr/La1	6c	0	0	0.2867(1)	1.00(9)	0.27(2)/0.30/0.44(2)*
Ba/Sr/La2	6c	0	0	0.1371(1)	2.21(1)	0.74(2)/0.20/0.06(2)
Nb1	6c	0	0	0.4221(1)	1.55(6)	1
Nb2	3a	0	0	0	1.39(1)	1
O1	18f	0.1271(6)	0.7971(5)	0.6287(1)	2.72(6)	1
O2	18f	0.1379(5)	0.8052(5)	0.4517(1)	2.23(5)	1

A-site occupancies are over 100% due to rounding, but values are within experimental error.

Table 3.04: Refinement results for $Ba_2SrLaNb_3O_{12}$ (HRPD RT data)

Bond lengths (Å)			Bond Angles (°)		
Ba/Sr/La(1)-O(1) =	2.882(3)	(x3)	O(1)-Nb(1)-O(1) =	82.1(1)	(x3)
Ba/Sr/La(1)-O(1) =	3.085(2)	(x3)	O(1)-Nb(1)-O(2) =	165.8(1)	(x3)
Ba/Sr/La(1)-O(1) =	2.653(3)	(x3)	O(1)-Nb(1)-O(2) =	86.2(1)	(x3)
Ba/Sr/La(1)-O(2) =	2.604(2)	(x3)	O(1)-Nb(1)-O(2) =	88.4(1)	(x3)
			O(2)-Nb(1)-O(2) =	101.5(1)	(x3)
Ba/Sr/La(2)-O(1) =	3.239(3)	(x3)			
Ba/Sr/La(2)-O(2) =	3.066(3)	(x3)	O(1)-Nb(2)-O(1) =	94.2(1)	(x6)
Ba/Sr/La(2)-O(2) =	2.746(3)	(x3)	O(1)-Nb(2)-O(1) =	85.8(1)	(x6)
Ba/Sr/La(2)-O(2) =	2.736(3)	(x3)	O(1)-Nb(2)-O(1) =	180.0	(x3)
Nb(1)-O(1) =	2.174(4)	(x3)			
Nb(1)-O(2) =	1.851(2)	(x3)			
Nb(2)-O(1) =	1.987(3)	(x6)			

Table 3.05: Bond lengths and angles from refinement results for $Ba_2SrLaNb_3O_{12}$

(HRPD RT data)

The comparative methods are summarised in **table 3.06**.

| Refinement Type	χ^2	R_{wp} (%)	R_p (%)	A-site occupancies	
XRPD	1.310	8.40	6.57	Ba*/Sr1	0.71(2)/0.30(2)
				Ba*/Sr2	0.80(2)/0.21(2)
Method (i)	3.610	7.30	7.15	Ba/Sr/La1	0.24(1)/0.30/0.46(1)
				Ba/Sr/La2	0.76(1)/0.20/0.04(1)
Method (ii)	3.867	7.55	7.78	Ba/Sr/La1	0.22(1)/0.30(1)/0.46(1)
				Ba/Sr/La2	0.79(1)/0.19(1)/0.04(1)
Method (iii)	6.233	7.50	6.64	Ba/Sr/La1	0.27(2)/0.30/0.44(2)
				Ba/Sr/La2	0.74(2)/0.20/0.06(2)

Ba^{2+} and La^{3+} entered as one element.

Table 3.06: Summary of the different refinement methods for $Ba_2SrLaNb_3O_{12}$.

Method (iii) was deemed the most appropriate method as it was found to give A-site fractional occupancies within 3% of the joint refinement method and it allowed for an unbiased refinement. Although the χ^2 value is somewhat higher for this approach than for method (i), the exemption of XRPD data overall provided a more consistent approach when the same methods were also trialled for the $BaSr_2LaNb_3O_{12}$ room temperature HRPD data.

Rietveld refinement of $Ba_2SrLaNb_3O_{12}$ following method (iii) proceeded smoothly in space group R-3. Details of the refinement can be found in, **figures 3.07** and **3.08** and **tables 3.04** and **3.05**. The refinement converged with χ^2 = 6.233; R_{wp} = 7.50%; R_p = 6.64%, with lattice parameters a = 5.7165(1) Å; c = 27.9346(3) Å. The resulting structure of $Ba_2SrLaNb_3O_{12}$ can be seen in **figure 3.09**.
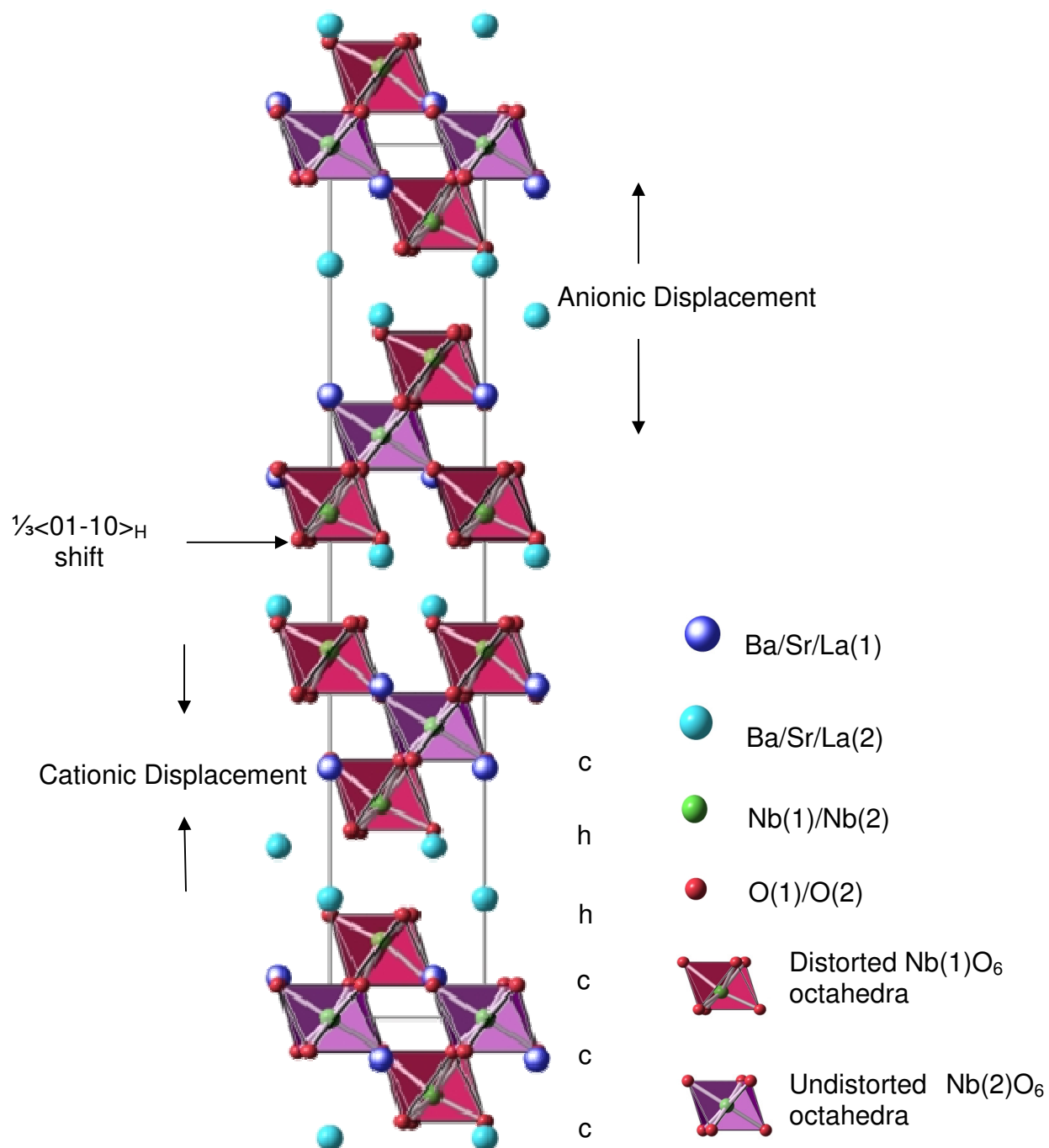
Figure 3.09: Structure of $Ba_2SrLaNb_3O_{12}$ viewed along the *x*-axis.

There are two sites available for the B-cations. B(1) is adjacent to the "shifted" region within a distorted octahedron, the Nb^{5+} ions are displaced towards one triangular octahedron face pointing towards the shifted region. B(2) is within the perovskite block in a regular undistorted octahedron, in the centre of a triple layer of corner-sharing octahedra, **figure 3.10** and **figure 3.11**. The associated distortion values (described previously in **section 1.1.2**) for the two B-site environments are $\Delta d = 0$ and $\Delta d = 63.97$ for B(1) and B(2) respectively. The NbO_6 octahedra are antiphase tilted ($a^- a^- a^-$) about the c-axis by 7.5°, **figure 3.12**.

There is a definite preference for the Ba^{2+} ions in the "shifted" region, A(2), with an occupancy of 74% compared to 27% in the perovskite block. This is expected as the Ba^{2+} ions are larger than Sr^{2+} ions (ionic radii of 1.61 Å and 1.44 Å respectively) and the "shifted" region provides a larger cavity than the perovskite block to accommodate the ions. La^{3+} and Sr^{2+} can fit in both sites, but due to the Ba^{2+} preference for A(2) the majority of both, 44% and 30% respectively, reside in A(1) in the perovskite block.

The cubo-octahedral environment of the A-cations can be seen in **figures 3.13** and **3.14**. There are 3 x A(1)-O bonds of 2.882(3) Å and 3 x A(1)-O bonds of 2.604(2) Å pointing towards neighbouring octahedral layers of B-site cations (along the direction of the z-axis) and 3 x A(1)-O bonds of 2.653(3) Å and 3 x A(1)-O bonds of 3.085(2) Å parallel to the xy-plane pointing towards NbO_6 units in the same octahedral layer.

For the A(2) cations there are 3 x A(2)-O bonds of 2.736(3) Å pointing into vacant shifted region and 3 x A(2)-O bonds of 3.239(3) Å pointing towards triple layers of B-site cations and 3 x A(2)-O bonds of 3.066(3) Å and 3 x A(2)-O bonds of 2.746(3) Å bonds parallel to xy-plane pointing towards NbO_6 units in the same octahedral layer. The A(2) cations are displaced into shifted region and the degree of shift for both A-cations can be seen in **figure 3.17**.

The AO_{12} polyhedra reveal a more distorted environment in the "shifted" region, A(2) than in the perovskite block, A(1) with distortion values $\Delta d = 53.07$ and $\Delta d = 46.94$ correspondingly. This can be seen more clearly in **figures 3.15** and **3.16**, where the distorted A-O lattices are viewed along the z-axis.

Bond valence sums (BVS) were performed for the structure (refer to **section 1.1.1**, **equations 1.2** and **1.3**), the values obtained are listed in **table 3.07**. Overall the BVS calculations performed for the structure imply that the bond lengths obtained for the structure are sensible, and that therefore the refinement is reasonable.

Cation	Theoretical BVS	Calculated BVS	Status
A(1)	2.46	2.61	Over-bonded
A(2)	2.20	2.14	Under-bonded
B(1)	5.00	5.00	-
B(2)	5.00	4.88	Under-bonded

Table 3.07: BVS calculation results for $Ba_2SrLaNb_3O_{12}$

3 x Nb(1)-O(2) = 1.851(2) Å

3 x Nb(1)-O(1) = 2.174(4) Å

6 x Nb(2)-O(1) = 1.987(3) Å
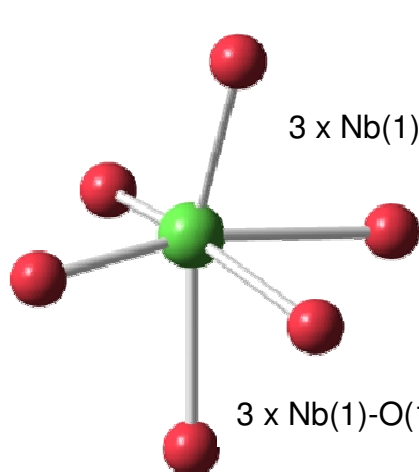
Figure 3.10: Distorted NbO$_6$ octahedron adjacent to "shifted" region (red spheres O^{2-}; green sphere Nb^{5+}). Associated bond lengths labelled.
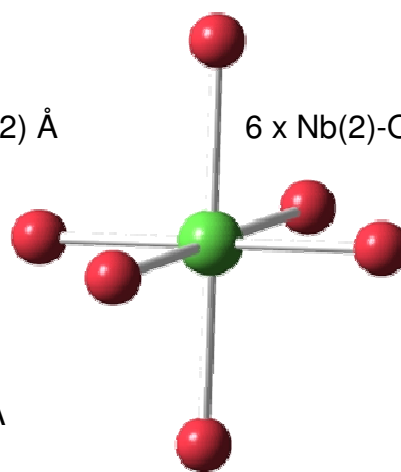
Figure 3.11: Undistorted NbO$_6$ octahedron in the centre of a triple layer of corner-sharing octahedra (red spheres O^{2-}; green sphere Nb^{5+}). Associated bond lengths labelled.
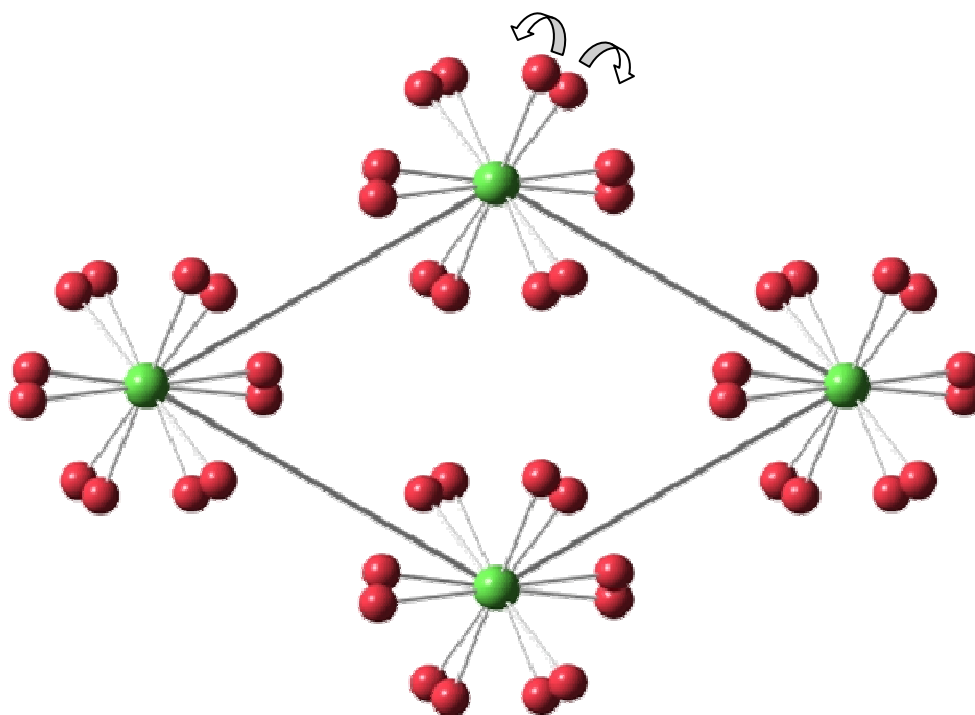
Figure 3.12: View of Ba$_2$SrLaNb$_3$O$_{12}$ structure along the z-axis showing tilting of the octahedra, tilt angle 7.5° [a$^-$ a$^-$ a$^-$] (octahedra omitted for clarity). Arrow indicate direct ion of tilting (red spheres O^{2-}; green spheres Nb^{5+}).
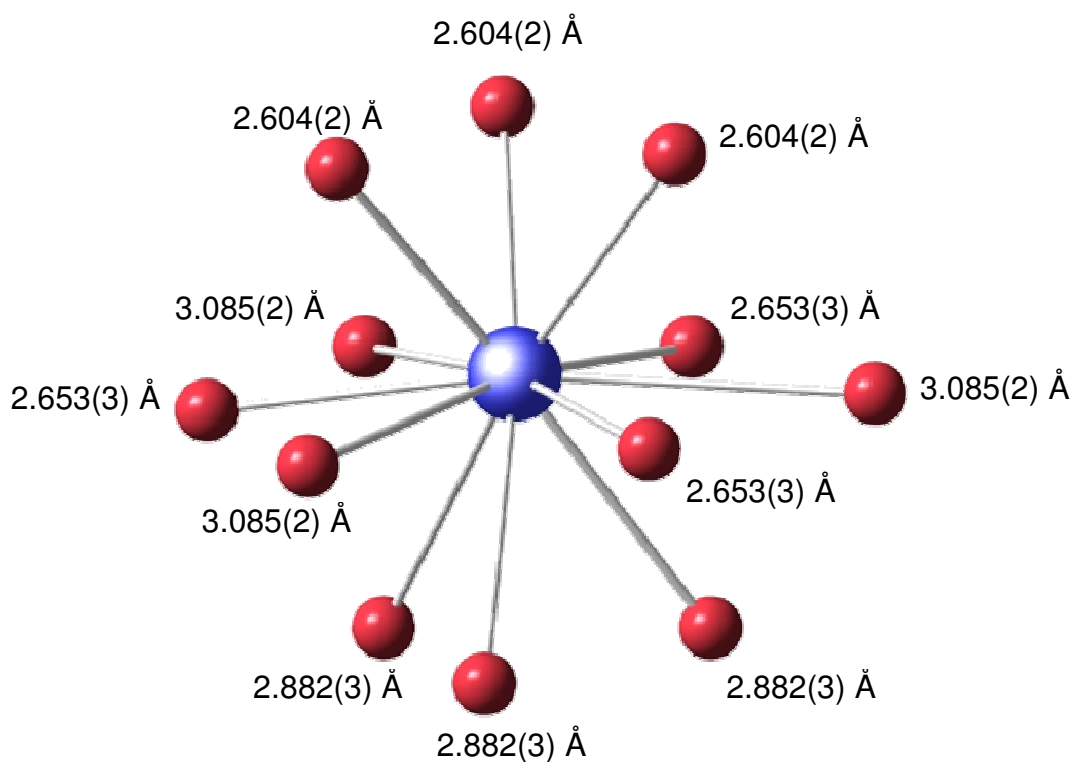
Figure 3.13: Cubo-octahedral environment of A(1) cations located within the triple layer of NbO_6 octahedra with a Ba / Sr / La distribution of 0.27 / 0.30 / 0.44. (Red spheres O^{2-}; blue sphere Ba^{2+} / Sr^{2+} / La^{3+}). Bond lengths are labelled.
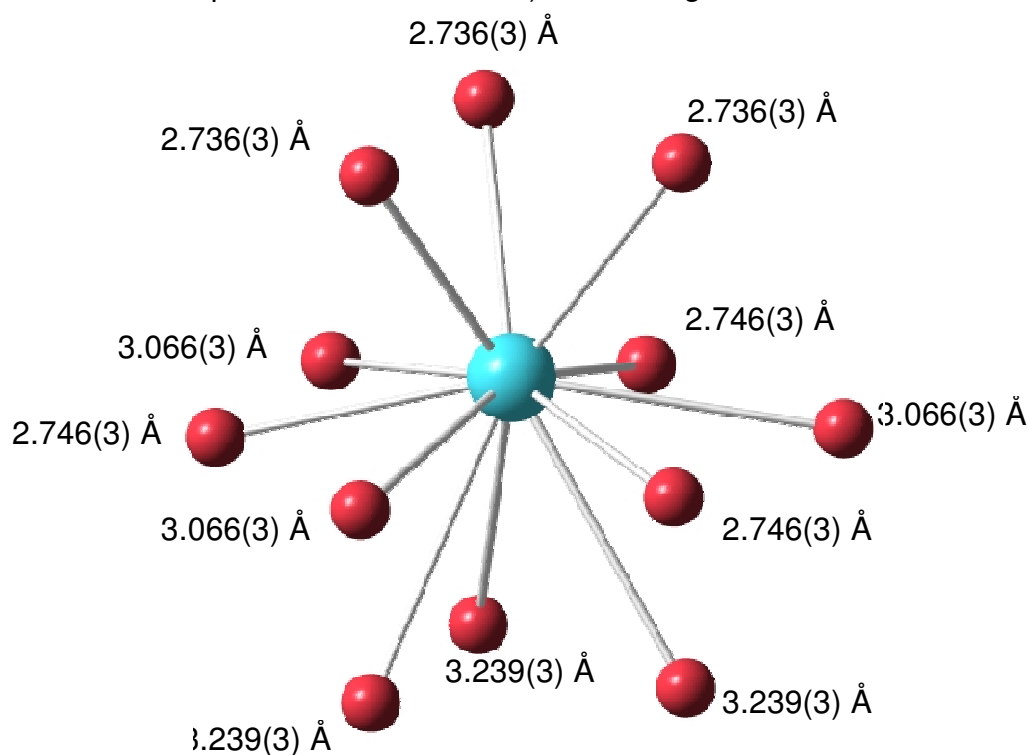
Figure 3.14: Cubo-octahedral environment of A(2) cations located in the shifted region, with a Ba / Sr / La distribution of 0.74 / 0.20 / 0.06. (Red spheres O^{2-}; blue sphere Ba^{2+} / Sr^{2+} / La^{3+}). Bond lengths are labelled
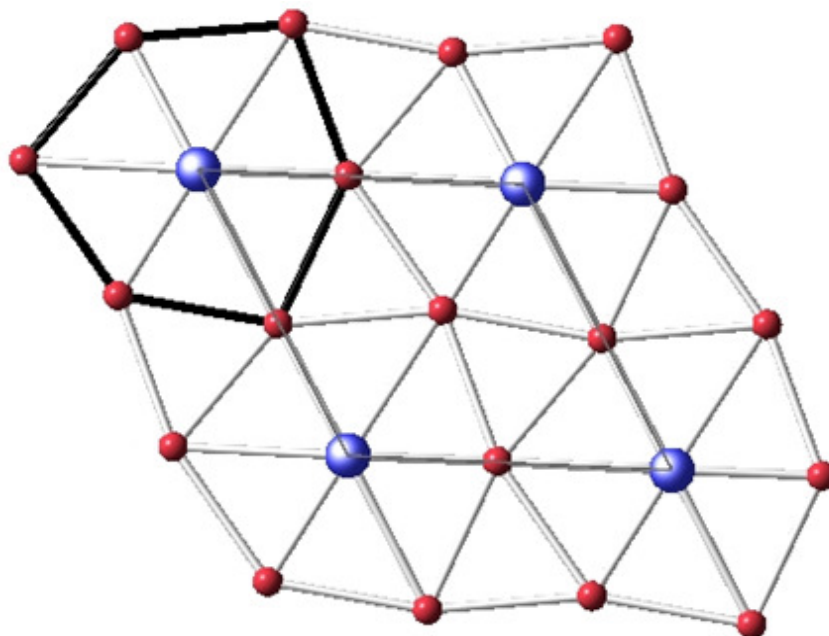
Figure 3.15: View of the distorted A(1)-O lattice along the *z*-axis, O^{2-} ions not parallel to the *xy*-plane are omitted for clarity. Black outline shows a "slice" through the AO_{12} polyhedra, 3 x A(1)-O bonds of 2.563(3) Å and 3 x A(1)-O bonds of 3.085(2) Å parallel to the *xy*-plane. A-cations located on the corners of the unit cell (outlined in grey). (Red spheres O^{2-}; blue sphere Ba^{2+} / Sr^{2+} / La^{3+})
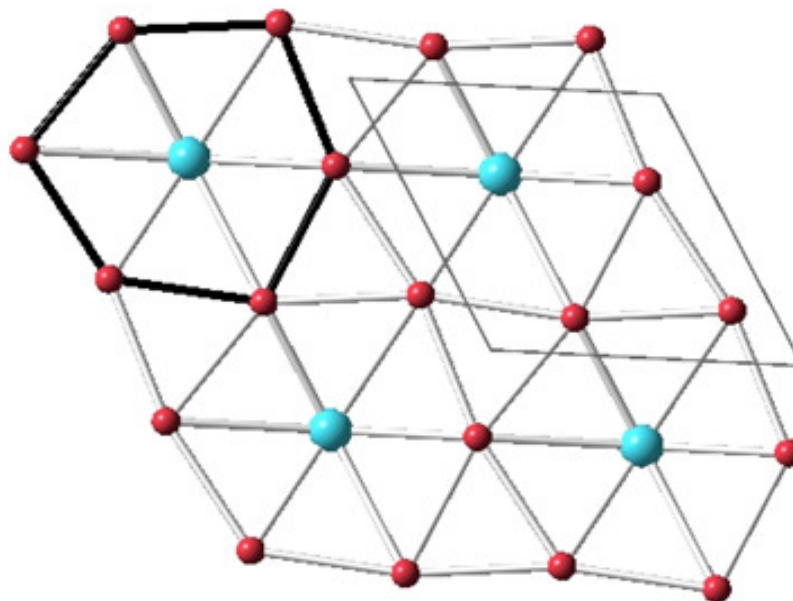
Figure 3.16: View of the distorted A(2)-O lattice along the *z*-axis, O^{2-} ions not parallel to the *xy*-plane are omitted for clarity. Black outline shows a "slice" through the AO_{12} polyhedra, 3 x A(2)-O bonds of 3.066(3) Å and 3 x A(2)-O bonds of 2.746(3) Å parallel to the *xy*-plane. (Unit cell outlined in grey). (Red spheres O^{2-}; blue sphere Ba^{2+} / Sr^{2+} / La^{3+})
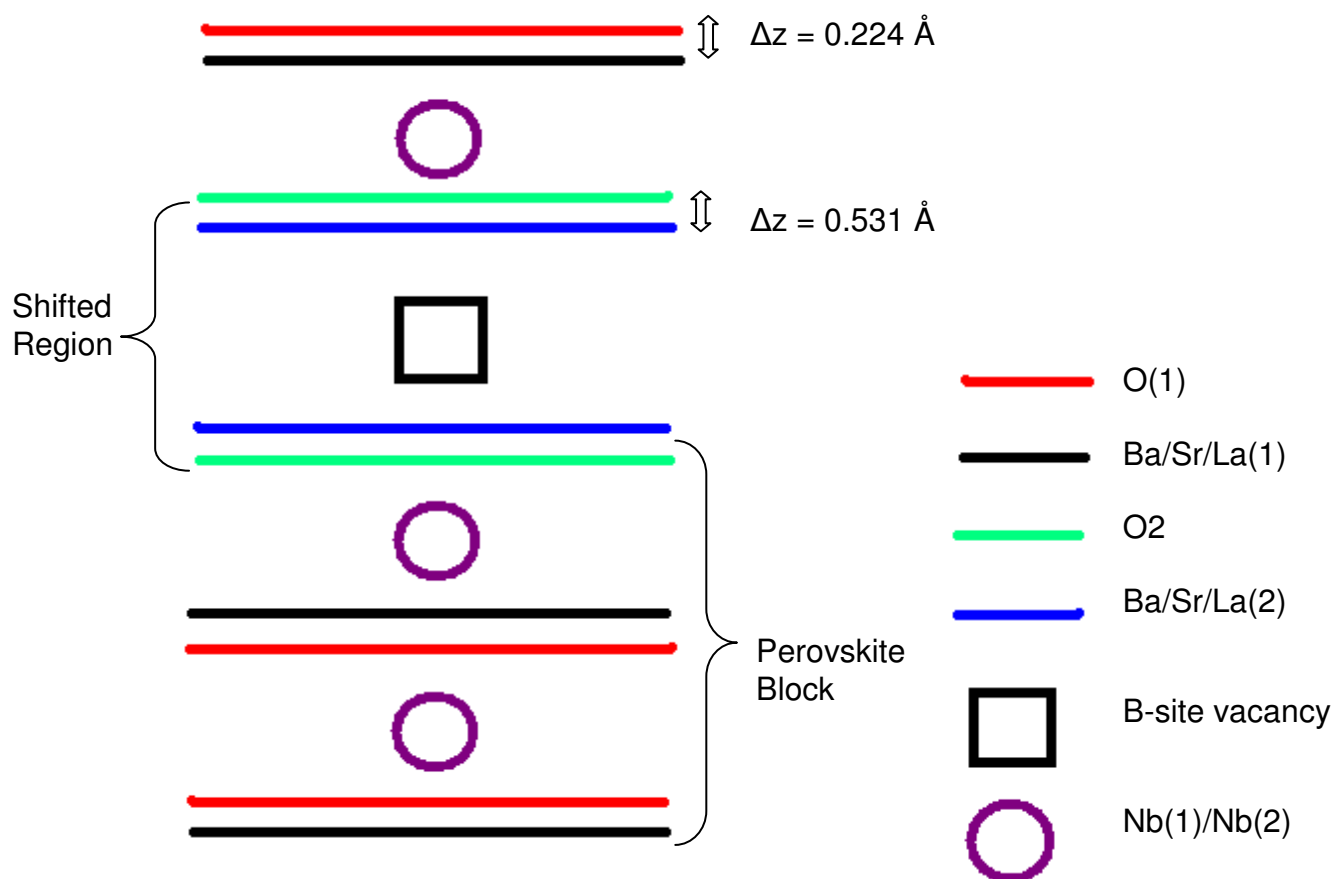
Figure 3.17: A schematic diagram showing A-O displacement along the *z*-axis (Δz) for $Ba_2SrLaNb_3O_{12}$ (not to scale).

Since the majority of the distortion within the structure occurs within the "shifted" region, a parameter known as the variance (Δ) was introduced (**section 1.2.2.2**, **equation 1.12** and **1.13**). This parameter allows the degree of distortion occurring to be compared in different compounds. $Ba_2SrLaNb_3O_{12}$ was found to possess a variance of 14.05×10^{-4} as shown in **figure 3.18**. (For clarity, Δ values are quoted in figures omitting the factor 10^{-4}).

(a)	**(b)**
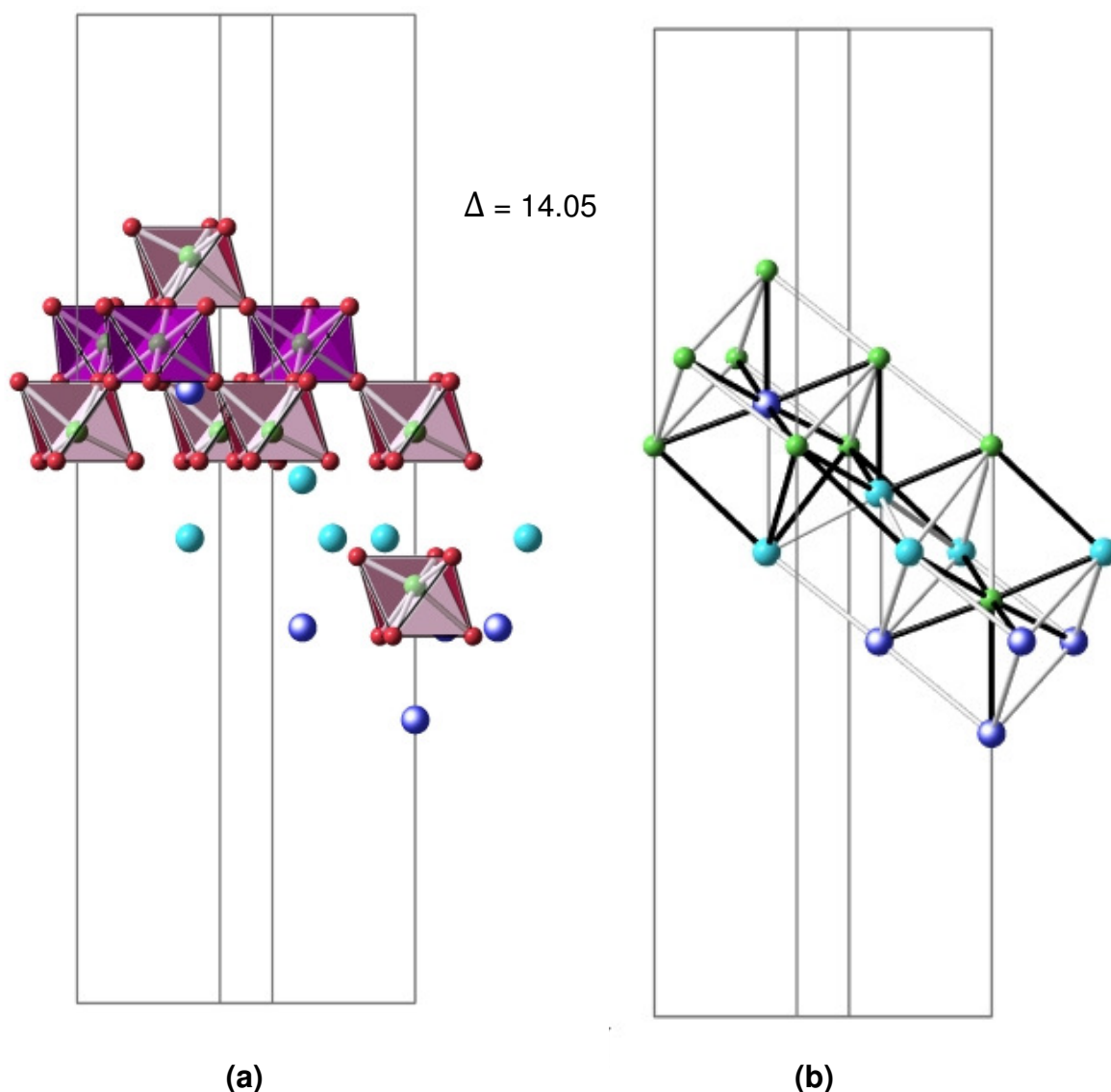
Figure 3.18: **(a)** A- and B-cations involved in the three *bcc* unit cells (O^{2-} ions shown not involved in the *bcc* lattice) **(b)** Structural view of the *bcc* lattice along the *xy*-direction, for $Ba_2SrLaNb_3O_{12}$. Black bonds highlight the A-B distances (bond lengths) selected for calculation of the variance. (Red spheres O^{2-}; blue sphere Ba^{2+} / Sr^{2+} / La^{3+}, green spheres Nb^{5+})

3.3.1.1.5 Variable Temperature Neutron Data

Variable temperature neutron data were collected on the D2B diffractometer at the Institut Laue-Langevin, Grenoble, France. Data were collected at room temperature, 320 °C and 900 °C in order to investigate structural changes with increasing temperature, more specifically the evolution of tilt angle and the rearrangement of A-cations.

3.3.1.1.5.1 Room Temperature NPD data

The refinement results are summarised below in *figure 3.19* and *tables 3.08* and *3.09*. Refinement statistics and lattice parameters are given in *figure 3.19*. It must be noted that the $Ba_2SrLaNb_3O_{12}$ sample used for collection of RT D2B data is different to the sample used for collection of RT HRPD data.

Space group R-3

$\chi^2 = 5.332$; $R_{wp} = 5.00\%$; $R_p = 3.93\%$

$a = 5.7182(1)$ Å; $c = 27.9351(8)$ Å

$\alpha = \beta = 90°$; $\gamma = 120°$

Volume $= 791.05(4)$ Å^3
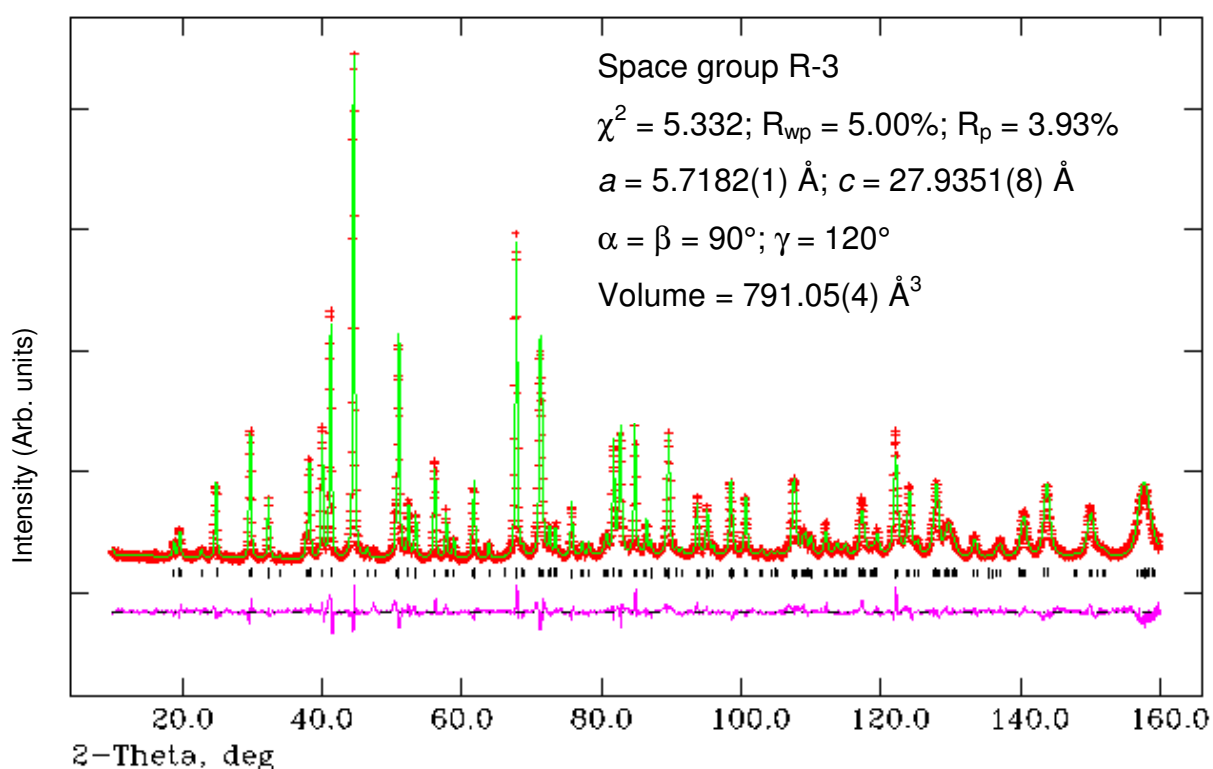
Figure 3.19: Calculated (green), experimental (red) and difference (pink) profile plot for $Ba_2SrLaNb_3O_{12}$ variable temperature NPD data collected from D2B at room temperature. Tick marks represent Bragg peak positions.

Atom	Wyckoff	x	y	Z	$U_{iso}*100$ $(\mathring{A}^2)$	Frac.
Ba/Sr/La1	6c	0	0	0.2869(1)	0.73(1)	0.20(3)/0.30(3)/0.5*
Ba/Sr/La2	6c	0	0	0.1366(2)	0.60(1)	0.80(3)/0.20(3)/0.0*
Nb1	6c	0	0	0.4221(1)	0.15(7)	1
Nb2	3a	0	0	0	0.71(1)	1
O1	18f	0.1306(8)	0.7999(8)	0.6287(1)	1.75(8)	1
O2	18f	0.1394(7)	0.8049(8)	0.4522(1)	1.26(7)	1

*Sr^{2+} values were fixed from XRPD refinement, however, La^{3+} values then refined to 0.5/0.0 and were therefore fixed. Sr^{2+}/Ba^{2+} occupancies were then subsequently allowed to refine with constraints. The $U_{iso}*100$ $(\mathring{A}^2)$ values for this material are different to those of $Ba_2SrLaNb_3O_{12}$ (HRPD RT data) due to the use of different samples.

Table 3.08: Refinement results for $Ba_2SrLaNb_3O_{12}$ (D2B RT data)

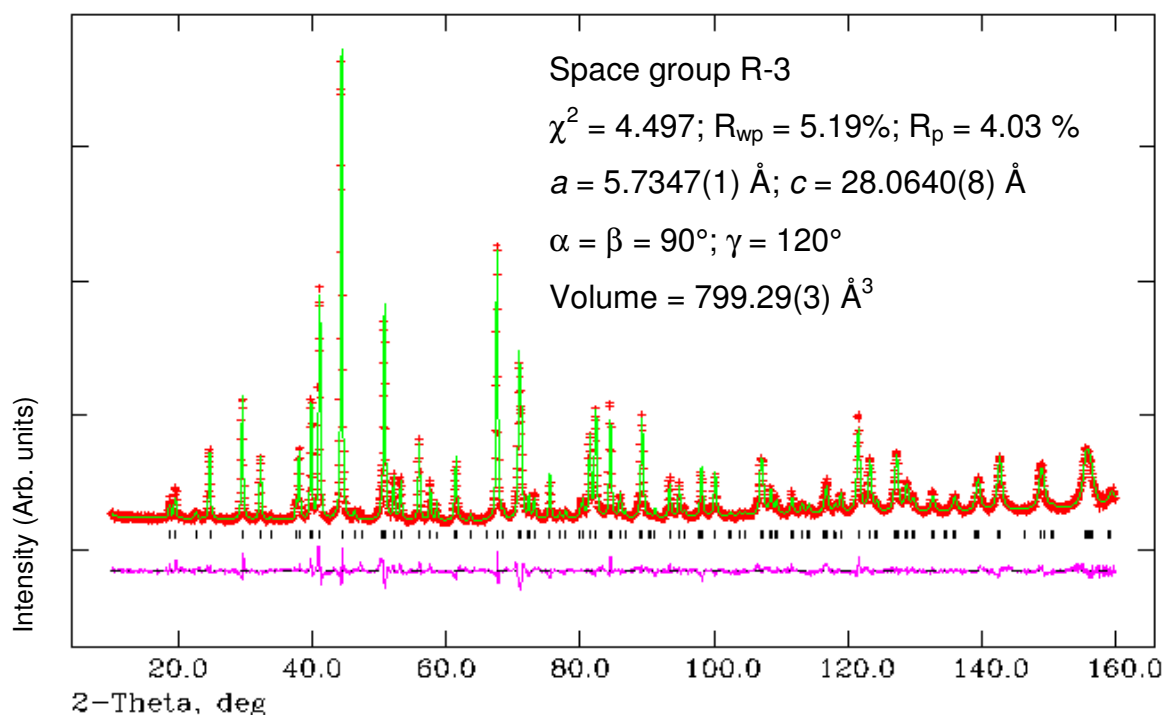| Bond lengths (Å)		Bond Angles (°)	
Ba/Sr/La(1)-O(1) =	2.878(4) (x3)	O(1)-Nb(1)-O(1) =	82.1(2) (x3)
Ba/Sr/La(1)-O(1) =	3.067(4) (x3)	O(1)-Nb(1)-O(2) =	166.1(2) (x3)
Ba/Sr/La(1)-O(1) =	2.671(4) (x3)	O(1)-Nb(1)-O(2) =	86.7(2) (x3)
Ba/Sr/La(1)-O(2) =	2.612(4) (x3)	O(1)-Nb(1)-O(2) =	88.3(2) (x3)
		O(2)-Nb(1)-O(2) =	101.2(2) (x3)
Ba/La(2)-O(1) =	3.225(4) (x3)		
Ba/La(2)-O(2) =	3.059(4) (x3)	O(1)-Nb(2)-O(1) =	94.1(2) (x6)
Ba/La(2)-O(2) =	2.745(4) (x3)	O(1)-Nb(2)-O(1) =	85.9(2) (x6)
Ba/La(2)-O(2) =	2.731(5) (x3)	O(1)-Nb(2)-O(1) =	180.0 (x3)
Nb(1)-O(1) =	2.175(4) (x3)		
Nb(1)-O(2) =	1.865(3) (x3)		
Nb(2)-O(1) =	1.983(4) (x6)		

Table 3.09: Bond lengths and angles from refinement results for $Ba_2SrLaNb_3O_{12}$

(D2B RT data)
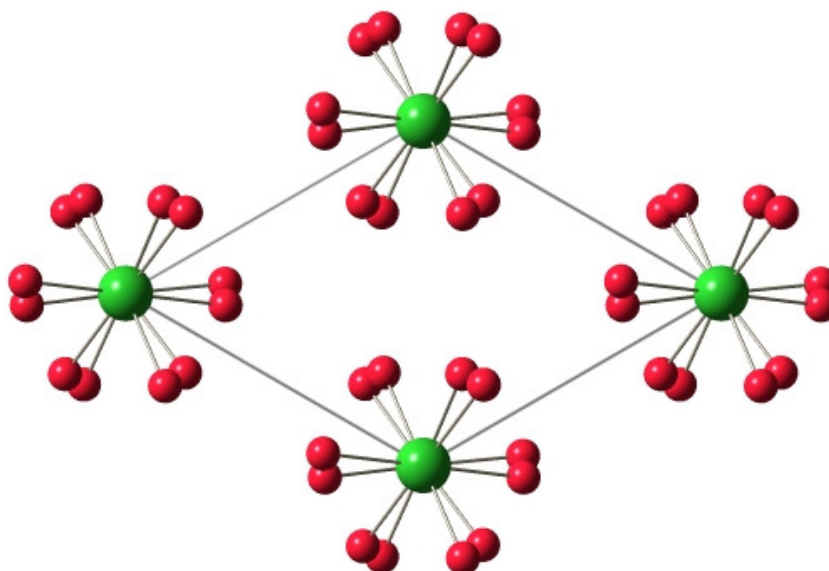
Figure 3.20: View of $Ba_2SrLaNb_3O_{12}$ structure along the z-axis from RT D2B data, showing tilting of the octahedra, tilt angle 7.5° [a^- a^- a^-] (octahedra omitted for clarity). (Red spheres O^{2-}; green spheres Nb^{5+}.)

3.3.1.1.5.2 NPD data at 320 °C

The refinement results are summarised below in **figure 3.21** and **tables 3.10** and **3.11**. Refinement statistics and lattice parameters are given in **figure 3.21**.


Space group R-3

χ^2 = 4.497; R_{wp} = 5.19%; R_p = 4.03 %

a = 5.7347(1) Å; c = 28.0640(8) Å

$\alpha = \beta = 90°$; $\gamma = 120°$

Volume = 799.29(3) $Å^3$

Figure 3.21: Calculated (green), experimental (red) and difference (pink) profile plot for $Ba_2SrLaNb_3O_{12}$ variable temperature NPD data collected from D2B at 320 °C. Tick marks represent Bragg peak positions.

84

Atom	Wyckoff	x	Y	z	$U_{iso}*100$ $(Å^2)$	Frac.
Ba/Sr/La1	*6c*	0	0	0.2869(2)	1.87(1)	0.2(1)/0.3(4)/0.5(3)
Ba/Sr/La2	*6c*	0	0	0.1362(2)	1.23(2)	0.8(1)/0.2(4)/0.0(3)
Nb1	*6c*	0	0	0.4221(1)	0.61(8)	1
Nb2	*3a*	0	0	0	0.92(2)	1
O1	*18f*	0.1379(1)	0.8079(1)	0.6290(2)	2.76(1)	1
O2	*18f*	0.1483(1)	0.8145(1)	0.4520(1)	2.23(8)	1

Table 3.10: Refinement results for $Ba_2SrLaNb_3O_{12}$ (D2B 320°C data)

Bond lengths (Å)			Bond Angles (°)		
Ba/Sr/La(1)-O(1) =	2.877(5)	(x3)	O(1)-Nb(1)-O(1) =	81.6(2)	(x3)
Ba/Sr/La(1)-O(1) =	3.032(7)	(x3)	O(1)-Nb(1)-O(2) =	165.7(2)	(x3)
Ba/Sr/La(1)-O(1) =	2.723(7)	(x3)	O(1)-Nb(1)-O(2) =	86.7(3)	(x3)
Ba/Sr/La(1)-O(2) =	2.619(4)	(x3)	O(1)-Nb(1)-O(2) =	88.7(3)	(x3)
			O(2)-Nb(1)-O(2) =	101.2(2)	(x3)
Ba/Sr/La(2)-O(1) =	3.234(5)	(x3)			
Ba/Sr/La(2)-O(2) =	3.014(7)	(x3)	O(1)-Nb(2)-O(1) =	94.2(2)	(x6)
Ba/Sr/La(2)-O(2) =	2.804(7)	(x3)	O(1)-Nb(2)-O(1) =	85.8(2)	(x6)
Ba/Sr/La(2)-O(2) =	2.756(5)	(x3)	O(1)-Nb(2)-O(1) =	180.0	(x3)
Nb(1)-O(1) =	2.183(5)	(x3)			
Nb(1)-O(2) =	1.861(4)	(x3)			
Nb(2)-O(1) =	1.985(5)	(x6)			

Table 3.11: Bond lengths and angles from refinement results for $Ba_2SrLaNb_3O_{12}$

(D2B 320°C data)
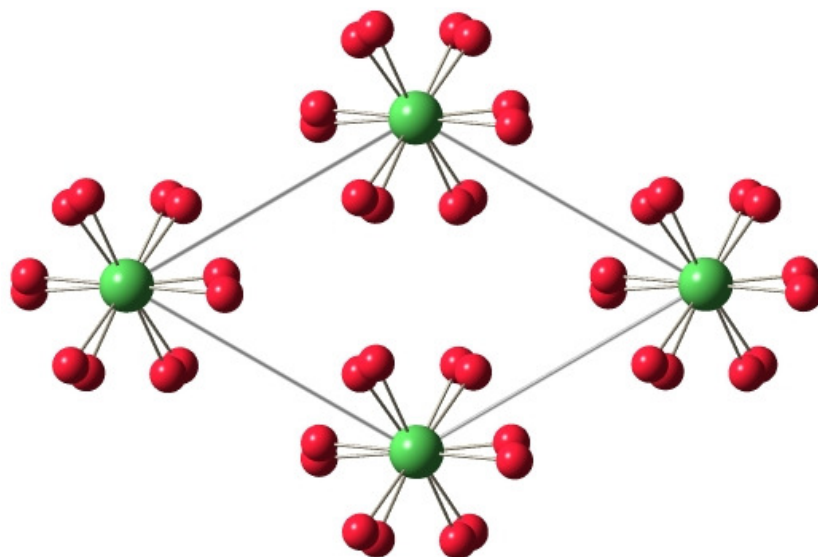
Figure 3.22: View of $Ba_2SrLaNb_3O_{12}$ structure along the z-axis from 320 °C D2B data, showing tilting of the octahedra, tilt angle 4.5° [a^- a^- a^-] (octahedra omitted for clarity). (Red spheres O^{2-}; green spheres Nb^{5+}.)

3.3.1.1.4.3 NPD data at 900 °C

The refinement results are summarised below in **figure 3.23** and **tables 3.12** and **3.13**. Refinement statistics and lattice parameters are given in **figure 3.23**.

Space group R-3

$\chi^2 = 9.885$; $R_{wp} = 5.72\%$; $R_p = 4.12\%$

$a = 5.7807(2)$ Å; $c = 28.346(1)$ Å

$\alpha = \beta = 90°$; $\gamma = 120°$

Volume = 820.31(5) $Å^3$
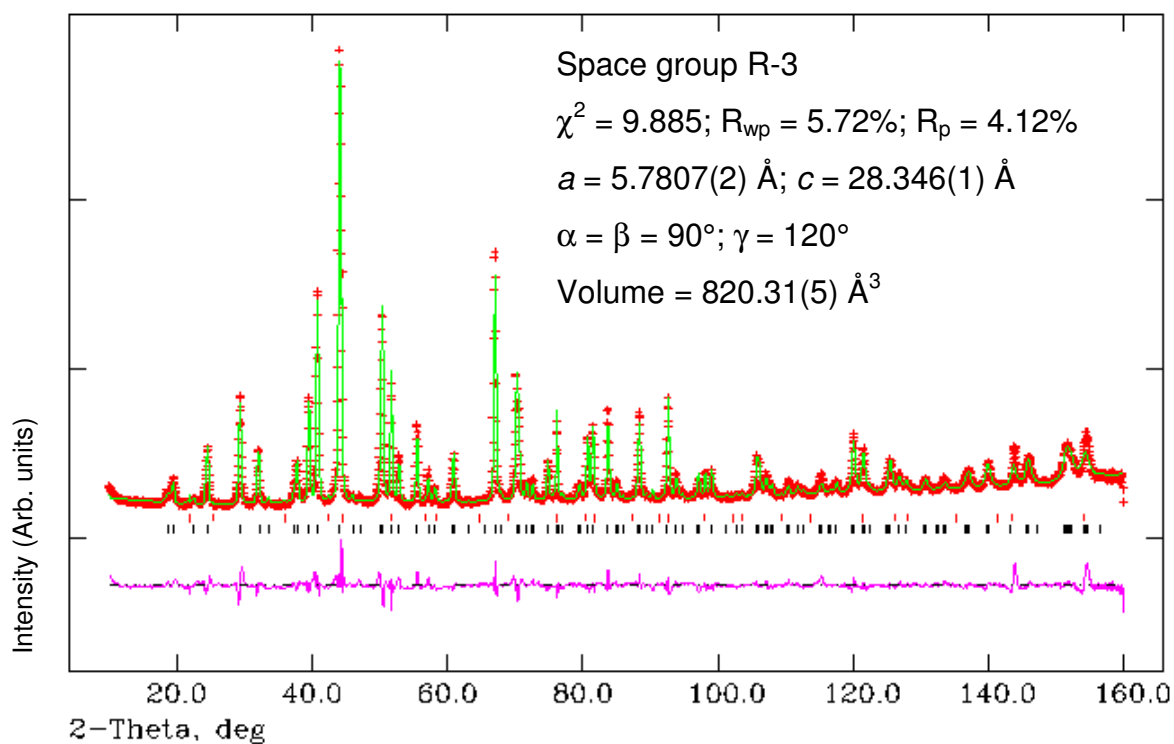
Red tick marks for second phase (steel from sample can lid).
Figure 3.23: Calculated (green), experimental (red) and difference (pink) profile plot for $Ba_2SrLaNb_3O_{12}$ variable temperature NPD data collected from D2B at 900 °C. Tick marks represent Bragg peak positions.

Extra sharp reflections are witnessed in these data due to the expansion of the steel cap of the vanadium can at high temperature. The steel was modelled as a second phase, as indicated by the red tick marks.

Atom	Wyckoff	x	y	z	$U_{iso}*100$ $(Å^2)$	Frac.
Ba/Sr/La1	6c	0	0	0.2874(3)	3.62(2)	0.2(7)/0.3(5)/0.49(1)*
Ba/Sr/La2	6c	0	0	0.1348(3)	1.83(2)	0.8(7)/0.2(5)/0.01(1)*
Nb1	6c	0	0	0.4225(2)	1.27(1)	1
Nb2	3a	0	0	0	1.44(2)	1
O1	18f	0.1479(2)	0.8141(2)	0.6295(2)	3.77(1)	1
O2	18f	0.1703(2)	0.8343(2)	0.4516(1)	3.82(1)	1

*A-site occupancies slightly over/under 100% due to rounding up.

Table 3.12: Refinement results for $Ba_2SrLaNb_3O_{12}$ (D2B 900 °C data)

Bond lengths (Å)			Bond Angles (°)		
Ba/Sr/La(1)-O(1) =	2.891(8)	(x3)	O(1)-Nb(1)-O(1) =	81.1(3)	(x3)
Ba/Sr/La(1)-O(1) =	3.010(1)	(x3)	O(1)-Nb(1)-O(2) =	164.4(9)	(x3)
Ba/Sr/La(1)-O(1) =	2.791(1)	(x3)	O(1)-Nb(1)-O(2) =	84.9(3)	(x3)
Ba/Sr/La(1)-O(2) =	2.635(7)	(x3)	O(1)-Nb(1)-O(2) =	89.8(4)	(x3)
			O(2)-Nb(1)-O(2) =	102.1(3)	(x3)
Ba/La(2)-O(1) =	3.230(8)	(x3)			
Ba/La(2)-O(2) =	2.915(1)	(x3)	O(1)-Nb(2)-O(1) =	94.1(3)	(x6)
Ba/La(2)-O(2) =	2.941(1)	(x3)	O(1)-Nb(2)-O(1) =	85.9(3)	(x6)
Ba/La(2)-O(2) =	2.816(7)	(x3)	O(1)-Nb(2)-O(1) =	180.0	(x3)
Nb(1)-O(1) =	2.230(7)	(x3)			
Nb(1)-O(2) =	1.873(5)	(x3)			
Nb(2)-O(1) =	1.975(7)	(x6)			

Table 3.13: Bond lengths and angles from refinement results for $Ba_2SrLaNb_3O_{12}$
(D2B 900 °C data)
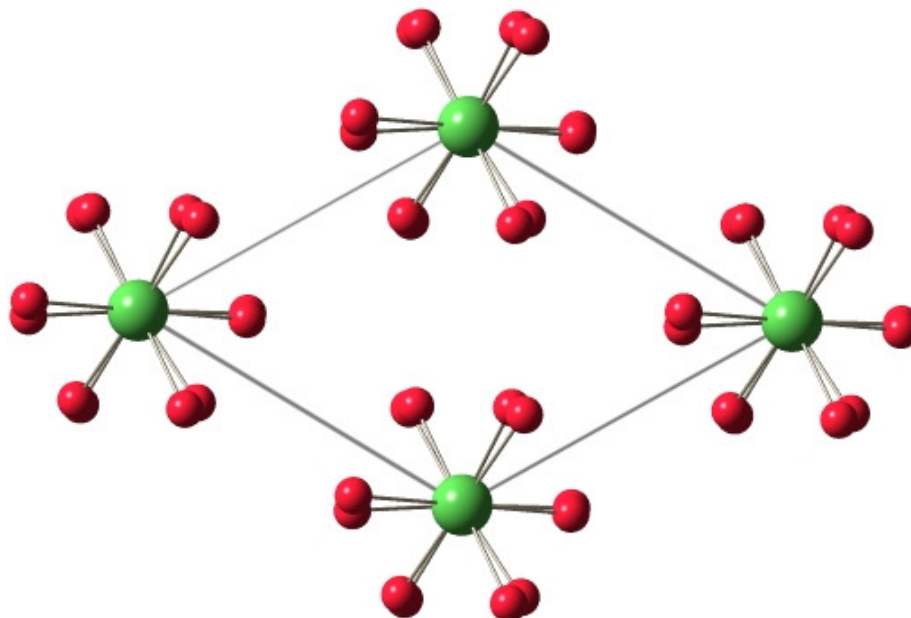
Figure 3.24: View of $Ba_2SrLaNb_3O_{12}$ structure along the z-axis from 900°C D2B data, showing tilting of the octahedra, tilt angle 4° [a⁻ a⁻ a⁻] (octahedra omitted for clarity). (Red spheres O^{2-}; green spheres Nb^{5+}.)
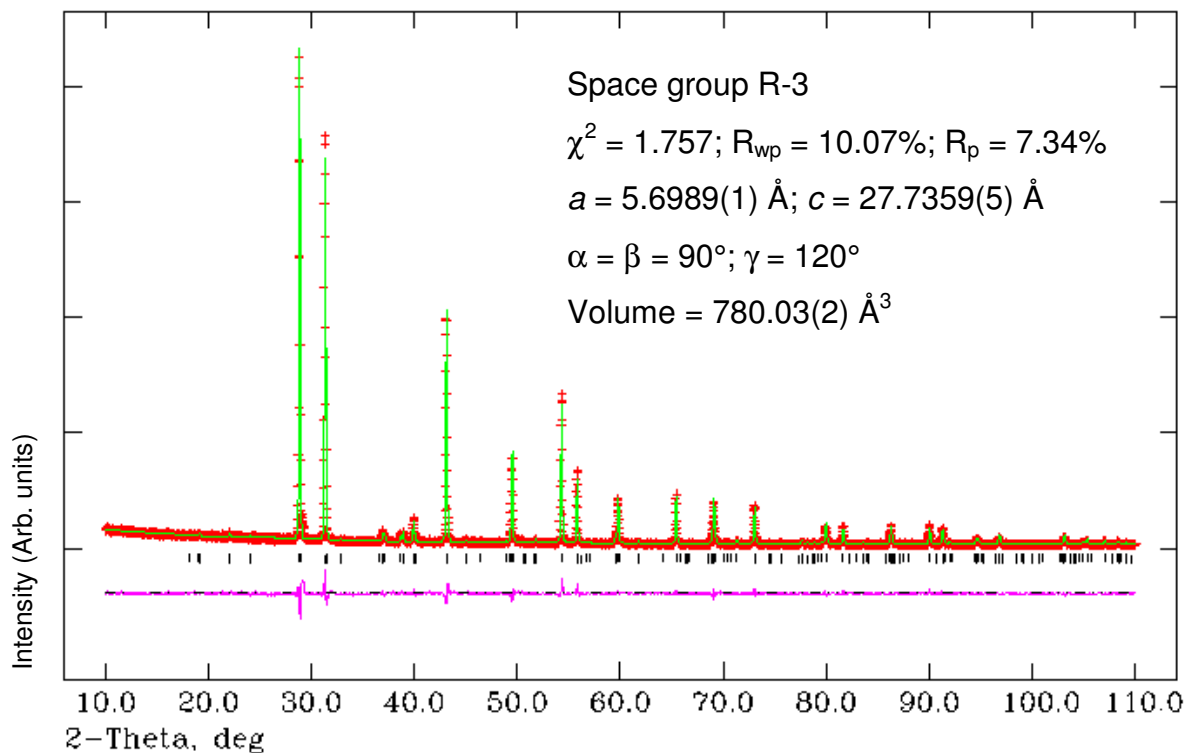
The variable temperature neutron data for $Ba_2SrLaNb_3O_{12}$ showed a decrease in tilt angle as the temperature increased, (7.5°, 4.5° and 4° at room temperature, 320°C and 900°C respectively) however even at 900°C the tilt angle is still significantly greater than zero. Therefore a tilted to untilted (R-3 to R-3m) structural transition has yet to occur.

The room temperature refinement showed that the majority of Ba^{2+} ions prefer to occupy the "shifted" region. However variable temperature refinements at 320°C and 900°C could suggest a redistribution to accommodate more of this cation in the "shifted" region, dependent upon how the estimated standard deviations associated with the fractional occupancies are viewed. It is not known how this movement would be feasible at these temperatures. Therefore although this phenomena has been considered the only conclusion that can be drawn from the variable temperature neutron data is that Ba^{2+} cations prefer to occupy the "shifted" region.

3.3.1.2 BaSr₂LaNb₃O₁₂

3.3.1.2.1 XRPD Refinement

The refinement results are summarised below in *figure 3.25* and *tables 3.14* and *3.15*. Refinement statistics and lattice parameters are given in *figure 3.25*.

Space group R-3

$\chi^2 = 1.757$; $R_{wp} = 10.07\%$; $R_p = 7.34\%$

$a = 5.6989(1)$ Å; $c = 27.7359(5)$ Å

$\alpha = \beta = 90°$; $\gamma = 120°$

Volume = $780.03(2)$ Å³

Figure 3.25: Calculated (green), experimental (red) and difference (pink) profile plot for BaSr₂LaNb₃O₁₂ XRPD data. Tick marks represent Bragg peak positions.

Atom	Wyckoff	x	y	z	U_{iso}*100 (Å²)	Frac.
Ba/Sr1	6c	0	0	0.2874(2)	2.74(2)	0.46(2)*/0.54(2)
Ba/Sr2	6c	0	0	0.1368(2)	2.56(2)	0.54(2)*/0.46(2)
Nb1	6c	0	0	0.4224(2)	2.57(2)	1
Nb2	3a	0	0	0	2.81(3)	1
O1	18f	0.126(5)	0.792(5)	0.6283(5)	1.9(5)	1
O2	18f	0.135(5)	0.780(5)	0.4510(4)	1.8(5)	1

*Ba^{2+} and La^{3+} entered as one element, Ba^{2+}.

Table 3.14: Refinement results for BaSr₂LaNb₃O₁₂ (XRPD RT data)

Bond lengths (Å)			Bond Angles (°)		
Ba/Sr/La(1)-O(1) =	2.872(2)	(x3)	O(1)-Nb(1)-O(1) =	83.0(7)	(x3)
Ba/Sr/La(1)-O(1) =	3.092(2)	(x3)	O(1)-Nb(1)-O(2) =	164.1(7)	(x3)
Ba/Sr/La(1)-O(1) =	2.622(2)	(x3)	O(1)-Nb(1)-O(2) =	85.0(1)	(x3)
Ba/Sr/La(1)-O(2) =	2.527(1)	(x3)	O(1)-Nb(1)-O(2) =	85.3(1)	(x3)
			O(2)-Nb(1)-O(2) =	104.4(5)	(x3)
Ba/Sr/La(2)-O(1) =	3.191(2)	(x3)			
Ba/Sr/La(2)-O(2) =	3.137(3)	(x3)	O(1)-Nb(2)-O(1) =	93.5(6)	(x6)
Ba/Sr/La(2)-O(2) =	2.664(3)	(x3)	O(1)-Nb(2)-O(1) =	86.5(6)	(x6)
Ba/Sr/La(2)-O(2) =	2.685(1)	(x3)	O(1)-Nb(2)-O(1) =	180.0	(x3)
Nb(1)-O(1) =	2.179(2)	(x3)			
Nb(1)-O(2) =	1.940(1)	(x3)			
Nb(2)-O(1) =	1.970(2)	(x6)			

Table 3.15: Bond lengths and angles from refinement results for $BaSr_2LaNb_3O_{12}$

(XRPD RT data)

3.3.1.2.2 NPD Refinement (method (ii))

The refinement results are summarised below in **figures 3.26** and **3.27** and **tables 3.16** and **3.17**. Refinement statistics and lattice parameters are given in **figure 3.26**.

Space group R-3

$\chi^2 = 9.984$; $R_{wp} = 8.85\%$; $R_p = 7.80\%$

$a = 5.6865(2)$ Å; $c = 27.597(1)$ Å

$\alpha = \beta = 90°$; $\gamma = 120°$

Volume = 772.83(4) $Å^3$
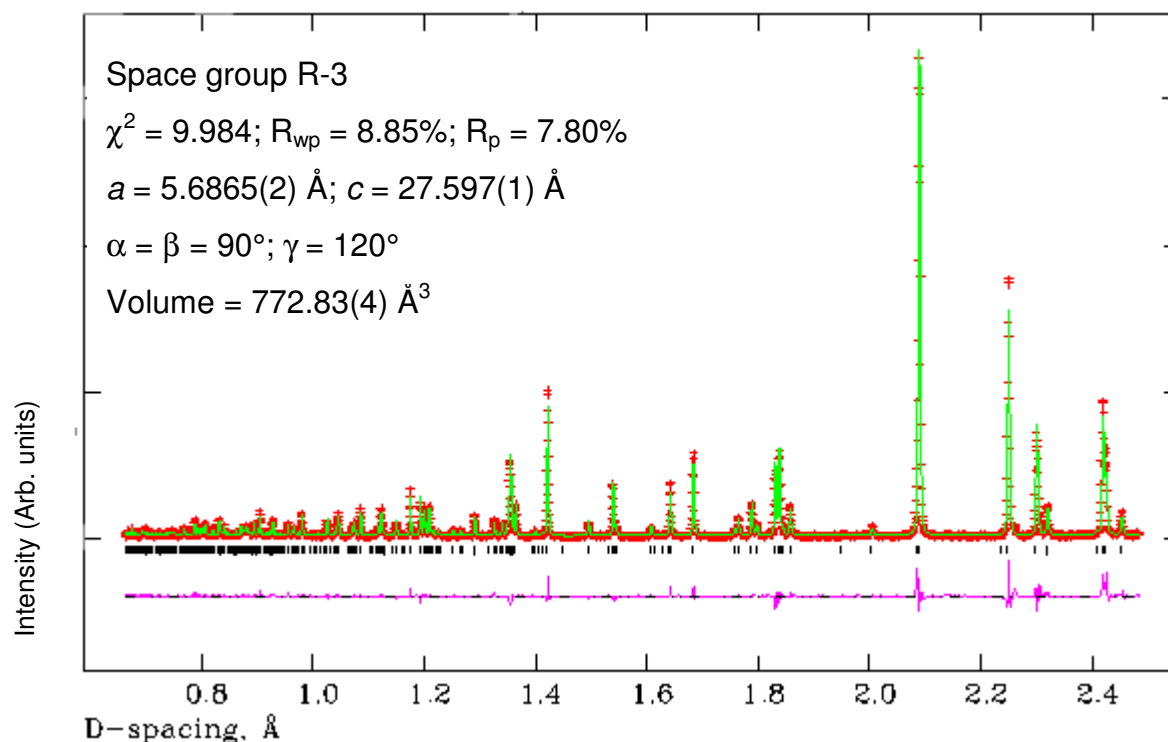
Figure 3.26: Calculated (green), experimental (red) and difference (pink) profile plot for $BaSr_2LaNb_3O_{12}$ NPD data from HRPD backscattering bank (bank 1). Tick marks represent Bragg peak positions.
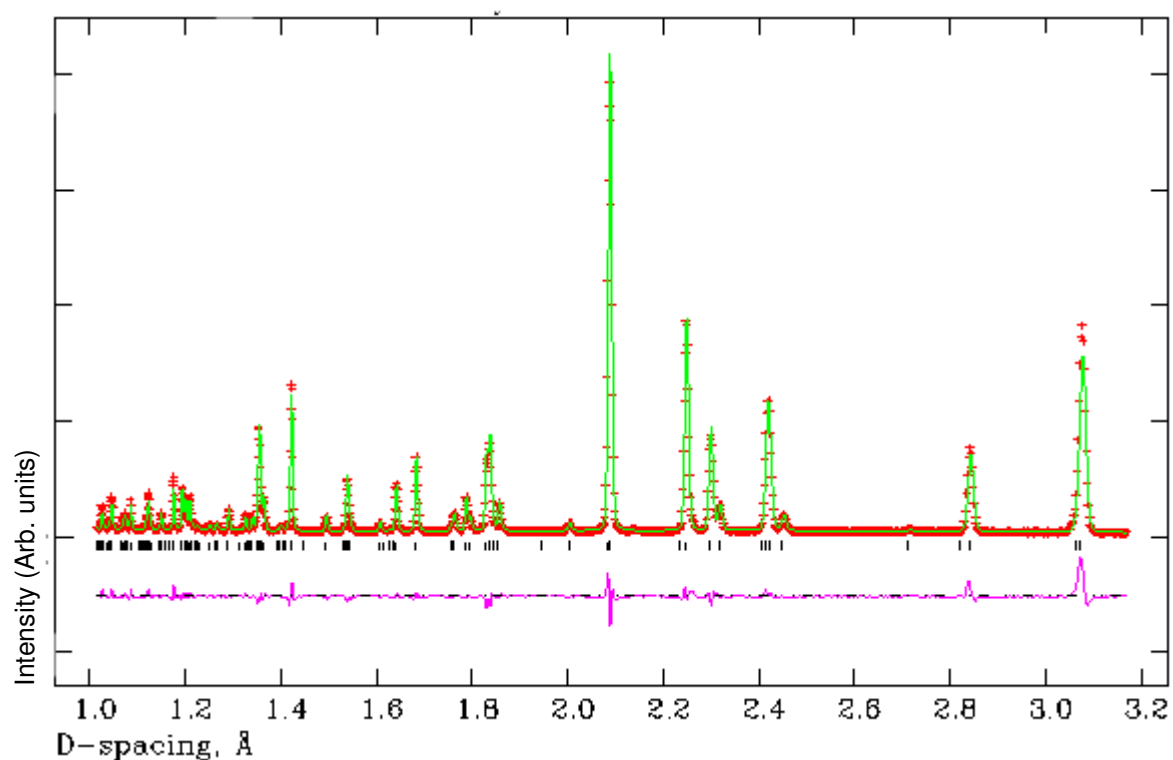
Figure 3.27: Calculated (green), experimental (red) and difference (pink) profile plot for $BaSr_2LaNb_3O_{12}$ NPD data from HRPD 90NS bank (bank 2). Tick marks represent Bragg peak positions.

Atom	Wyckoff	X	y	z	$U_{iso}*100$ $(Å^2)$	Frac.
Ba/Sr/La1	6c	0	0	0.2862(1)	0.83(1)	0.17(2)**/0.54*/0.29(2)**
Ba/Sr/La2	6c	0	0	0.1386(1)	2.96(1)	0.35(2)**/0.46*/0.19(2)**
Nb1	6c	0	0	0.4229(1)	1.59(7)	1
Nb2	3a	0	0	0	2.01(1)	1
O1	18f	0.1194(5)	0.7892(5)	0.6281(1)	2.70(5)	1
O2	18f	0.1221(4)	0.7893(4)	0.4526(1)	2.57(5)	1

*Sr^{2+} occupancies fixed from XRPD refinement. **Composition slightly over/under that stated, due to rounding up.

Table 3.16: Refinement results for $BaSr_2LaNb_3O_{12}$ (HRPD RT data)

Bond lengths (Å)			Bond Angles (°)		
Ba/Sr/La(1)-O(1) =	2.882(3)	(x3)	O(1)-Nb(1)-O(1) =	82.3(1)	(x3)
Ba/Sr/La(1)-O(1) =	3.112(2)	(x3)	O(1)-Nb(1)-O(2) =	165.8(1)	(x3)
Ba/Sr/La(1)-O(1) =	2.594(2)	(x3)	O(1)-Nb(1)-O(2) =	86.8(1)	(x3)
Ba/Sr/La(1)-O(2) =	2.584(2)	(x3)	O(1)-Nb(1)-O(2) =	87.2(1)	(x3)
			O(2)-Nb(1)-O(2) =	101.9(1)	(x3)
Ba/Sr/La(2)-O(1) =	3.230(3)	(x3)			
Ba/Sr/La(2)-O(2) =	3.141(2)	(x3)	O(1)-Nb(2)-O(1) =	94.0(1)	(x6)
Ba/Sr/La(2)-O(2) =	2.646(2)	(x3)	O(1)-Nb(2)-O(1) =	86.0(1)	(x6)
Ba/Sr/La(2)-O(2) =	2.666(3)	(x3)	O(1)-Nb(2)-O(1) =	180.0	(x3)
Nb(1)-O(1) =	2.166(4)	(x3)			
Nb(1)-O(2) =	1.849(2)	(x3)			
Nb(2)-O(1) =	1.987(3)	(x6)			

Table 3.17: Bond lengths and angles from refinement results for $BaSr_2LaNb_3O_{12}$
(HRPD RT data)

The $BaSr_2LaNb_3O_{12}$ Rietveld refinement using method (iii) proceeded effortlessly in space group R-3. Details of the refinement can be found in **figures 3.26** and **3.27** and **tables 3.15** and **3.16**. The ceramic had lattice parameters a = 5.6865(2) Å; c = 27.597(1) Å and the refinement converged with associated statistics χ^2 = 9.984, R_{wp} = 8.85%, and R_p = 7.80%. The resultant structure can be seen in **figure 3.28**.
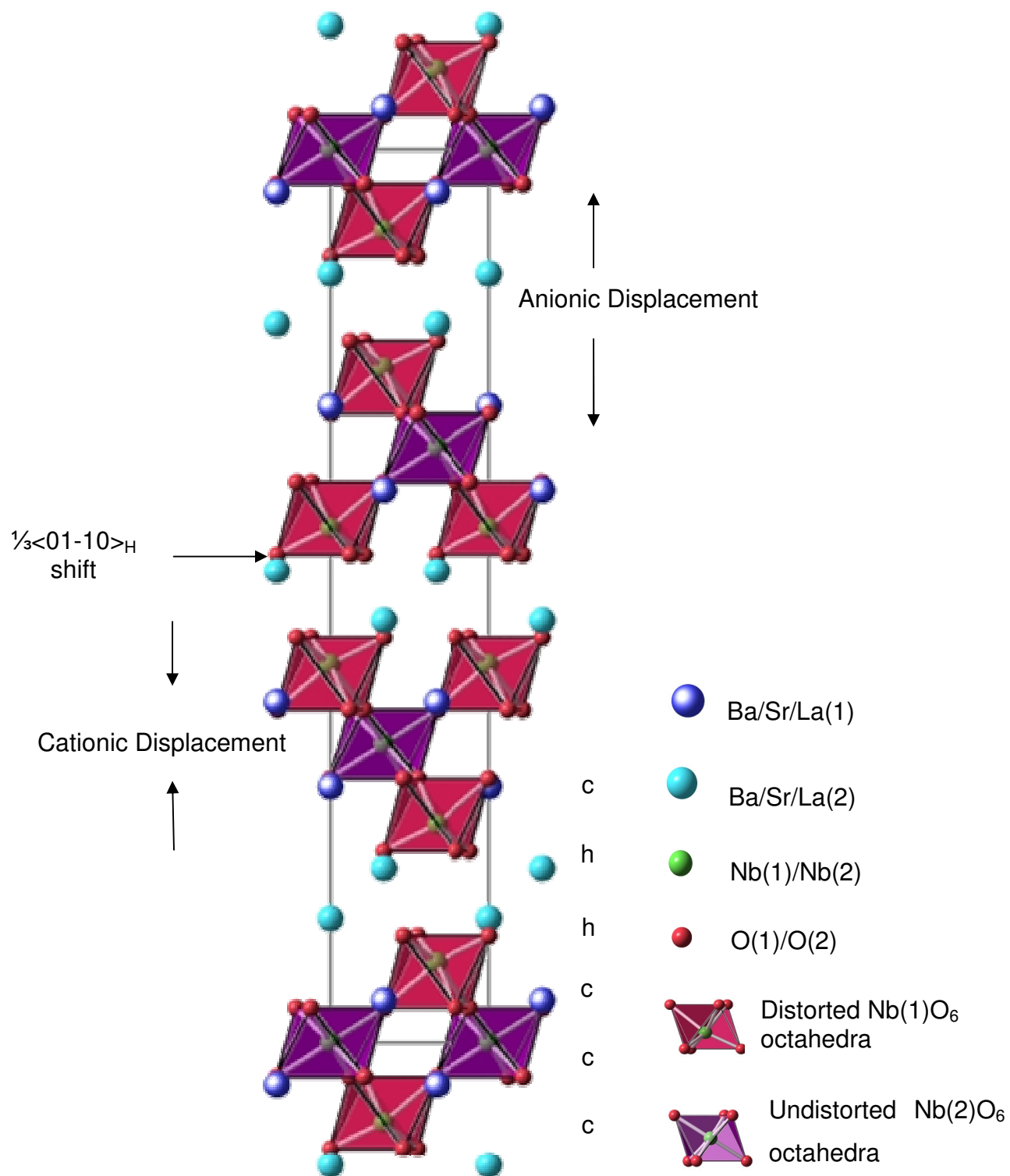
Figure 3.28: Structure of $BaSr_2LaNb_3O_{12}$ viewed along the *x*-axis.

The two B-site environments can be seen in **figures 3.29** and **3.30**. The associated distortion values (described previously in **section 1.1.2**) for the two B-site environments are $\Delta d = 0$ and $\Delta d = 62.31$ for B(1) and B(2) respectively. The NbO_6 octahedra are tilted about the *z*-axis by an angle of 8.5° with Glazer notation a$^-$ a$^-$ a$^-$, **figure 3.31**.

The dominant divalent A-cation in the structure, Sr^{2+} shows no particular preference for either A-site at room temperature with an approximate 50:50 split over the two sites (54% perovskite block; 46% "shifted" region). Ba^{2+} the larger of the two divalent A-cations shows a preference for A(2) in the shifted region, (35% compared to 17% in A(1) where there is more room for this larger cation. La^{3+} demonstrates a slight preference for A(1) in the perovskite block. This again can be explained due to its radius being smaller than that of Ba^{2+}, therefore allowing it to be comfortably accommodated in the perovskite block.

The A-cation environments can be seen in **figures 3.32** and **3.33**. The $A(1)O_{12}$ polyhedra consist of 3 x A(1)-O bonds of 2.594(2) Å and 3 x A(1)-O bonds of 3.112(2) Å parallel to the *xy*-plane pointing towards NbO_6 units in the same octahedral layer, and 3 x A(1)-O bonds of 2.584(2) Å and 3 x A(1)-O bonds of 2.882(3) Å pointing towards neighbouring octahedral layers of B-site cations (along the direction of the *z*-axis).

Within the $A(2)O_{12}$ polyhedra there are 3 x A(2)-O bonds of 2.666(3) Å pointing into vacant shifted region and 3 x A(2)-O) bonds of 3.230(3) Å pointing towards triple layers of B-site cations, and 3 x A(2)-O bonds of 3.141(2) Å and 3 x A(2)-O bonds of 2.646(2) Å bonds parallel to *xy*-plane. The A(2) cations are displaced into shifted region and the degree of shift for both A-cations can be seen in **figure 3.36**.

The AO_{12} polyhedra reveal a more distorted environment in the "shifted" region, A(2) than in the perovskite block, A(1) with distortion values $\Delta d = 83.37$ and $\Delta d = 61.84$ correspondingly. This can be seen more clearly in **figures 3.34** and **3.35** where the distorted A-O lattices can be seen along the *z*-axis.

Bond valence sums (BVS) were performed for the structure (referred to in **section 1.1.1, equations 1.2** and **1.3**), the values are listed in **table 3.18**. Overall the BVS

calculations performed for the structure imply that the bond lengths obtained for the structure are sensible and that the resulting refinement data are acceptable.

Cation	Theoretical BVS	Calculated BVS	Status
A(1)	2.29	2.59	Over-bonded
A(2)	2.19	2.14	Under-bonded
B(1)	5.00	5.05	Over-bonded
B(2)	5.00	4.88	Under-bonded

Table 3.18: BVS calculation results for $BaSr_2LaNb_3O_{12}$
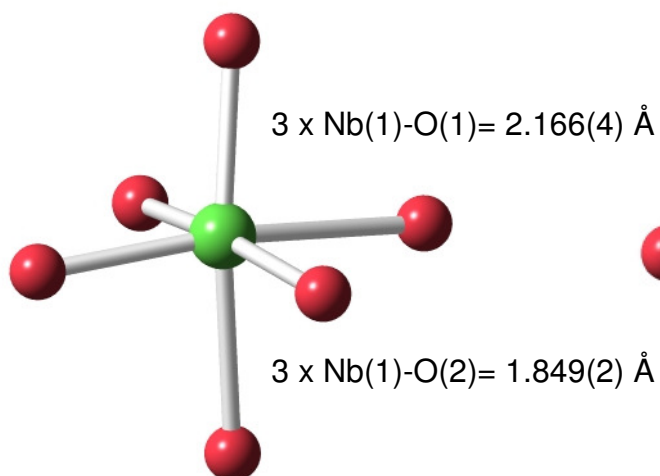
Figure 3.29: Distorted NbO$_6$ octahedron adjacent to "shifted" region (red spheres O^{2-}; green sphere Nb^{5+}). Associated bond lengths labelled.

3 x Nb(1)-O(1)= 2.166(4) Å

3 x Nb(1)-O(2)= 1.849(2) Å
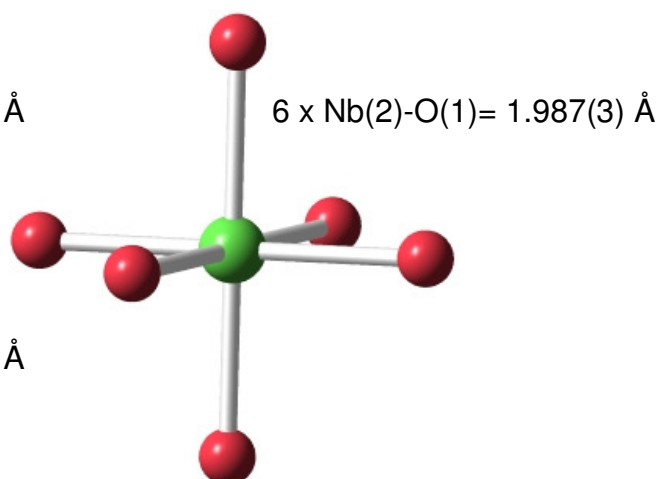
Figure 3.30: Undistorted NbO$_6$ octahedron in the centre of a triple layer of corner-sharing octahedra (red spheres O^{2-}; green sphere Nb^{5+}). Associated bond lengths labelled.

6 x Nb(2)-O(1)= 1.987(3) Å
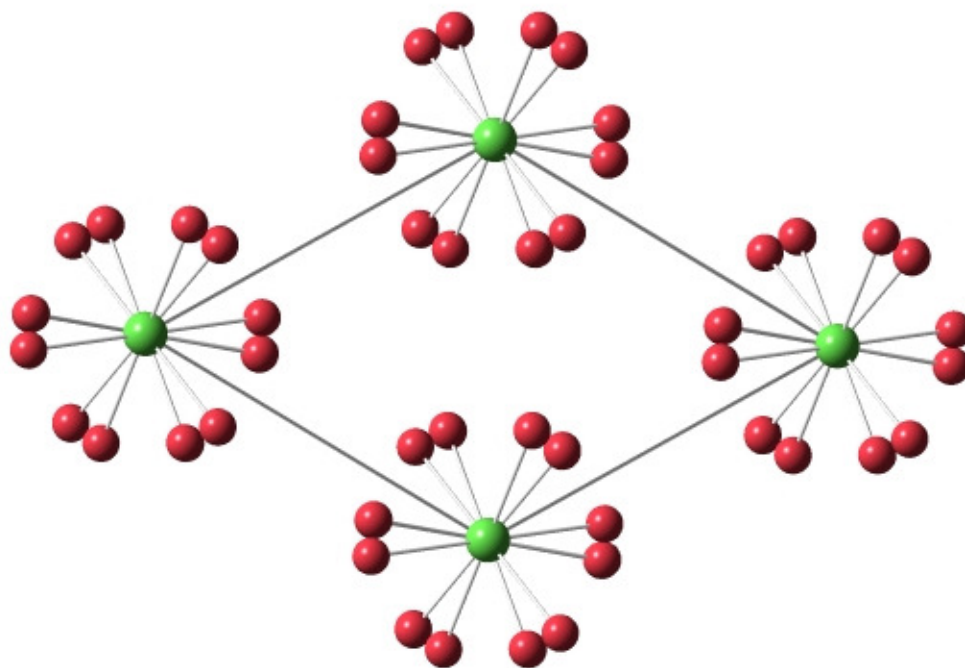
Figure 3.31: View of BaSr$_2$LaNb$_3$O$_{12}$ structure along the z-axis showing tilting of the octahedra, tilt angle 8.5° [a$^-$ a$^-$ a$^-$] (octahedra omitted for clarity). (Red spheres O^{2-}; green spheres Nb^{5+}.)
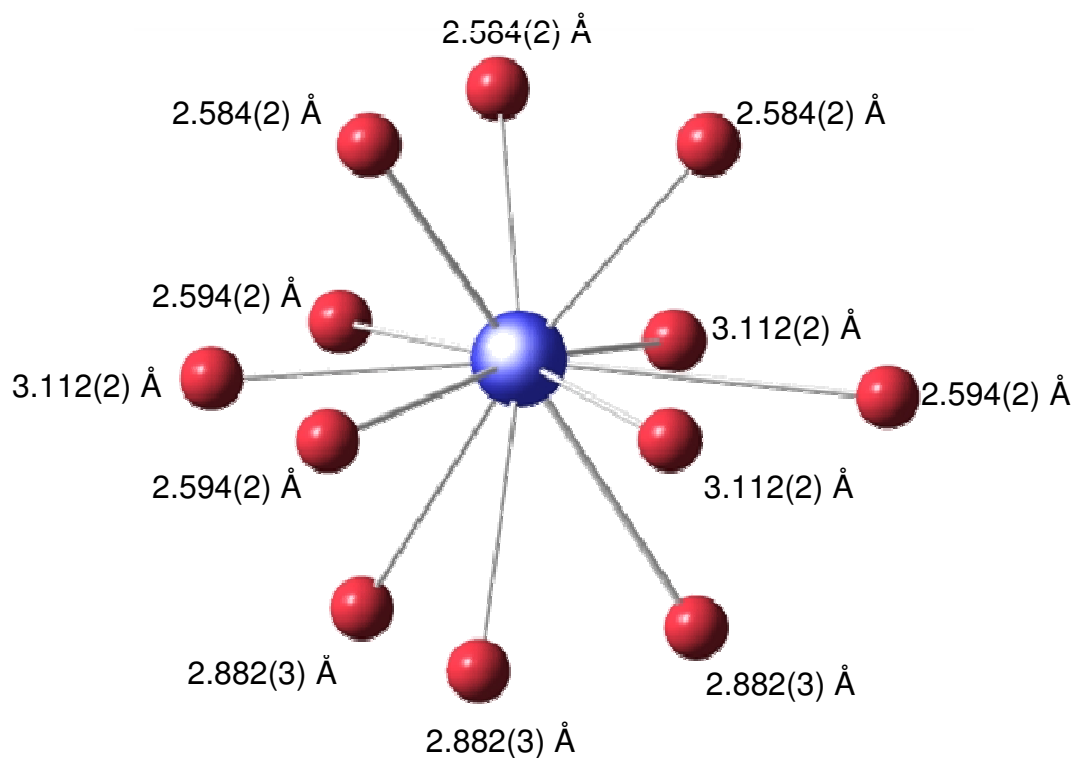
Figure 3.32: Cubo-octahedral environment of A(1) cations located within the triple layer of NbO_6 octahedra with a Ba / Sr / La distribution of 0.17 / 0.54 / 0.29. (Red spheres O^{2-}; blue sphere Ba^{2+} / Sr^{2+} / La^{3+}). Bond lengths are labelled.
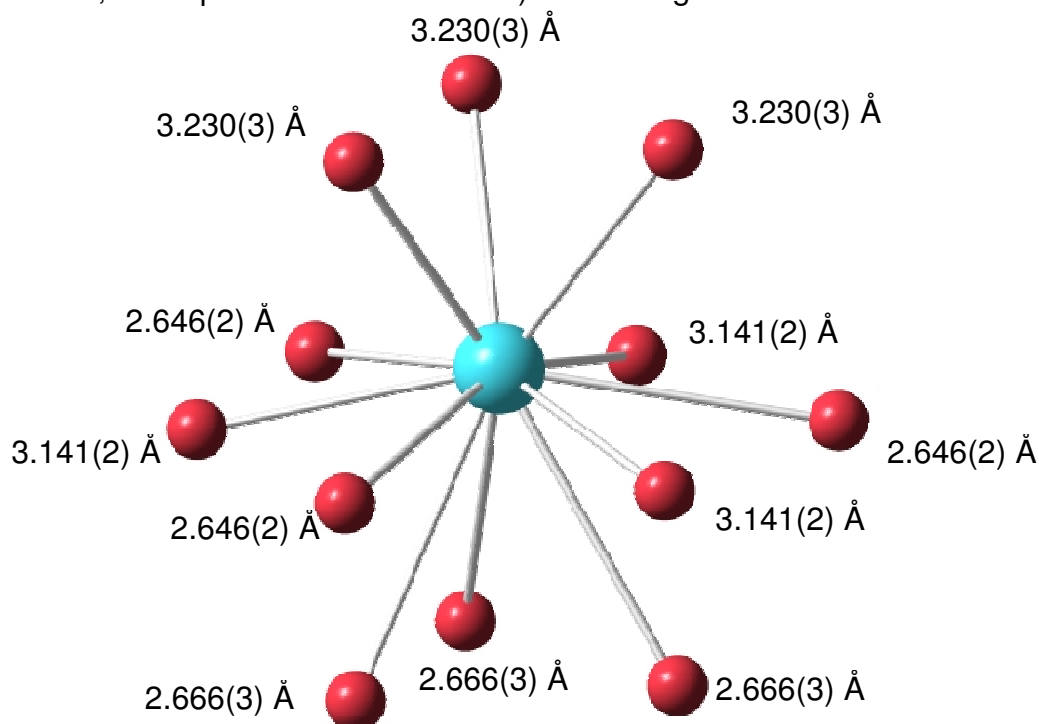
Figure 3.33: Cubo-octahedral environment of A(2) cations located in the shifted region, with a Ba / Sr / La distribution of 0.35 / 0.46 / 0.19. (Red spheres O^{2-}; blue sphere Ba^{2+} / Sr^{2+} / La^{3+}). Bond lengths are labelled.
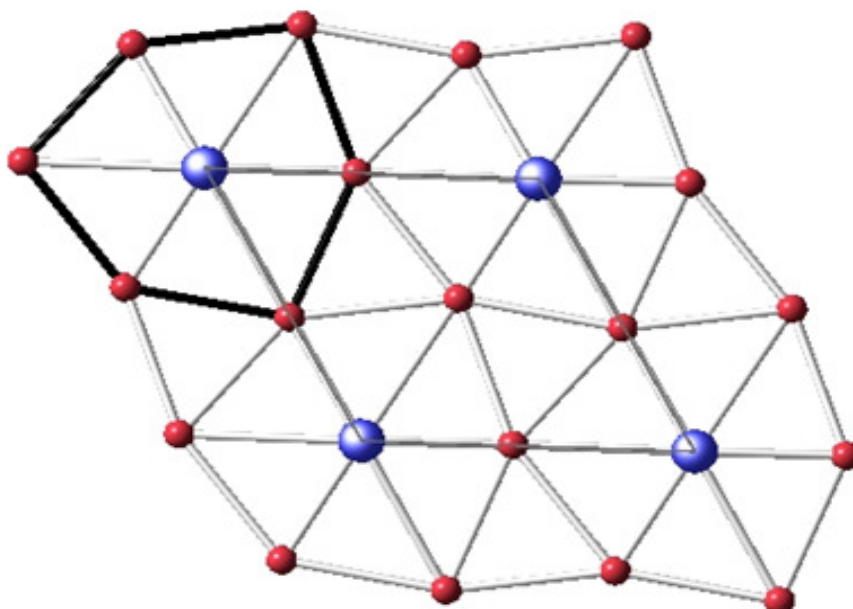
Figure 3.34: View of the distorted A(1)-O lattice along the *z*-axis, O^{2-} ions not parallel to the *xy*-plane are omitted for clarity. Black outline shows a "slice" through the AO_{12} polyhedra, 3 x A(1)-O bonds of 2.594(2) Å and 3 x A(1)-O bonds of 3.112(2) Å parallel to the *xy*-plane. The A-cations are on the corners of the unit cell, outlined in grey. (Red spheres O^{2-}; blue sphere Ba^{2+} / Sr^{2+} / La^{3+})
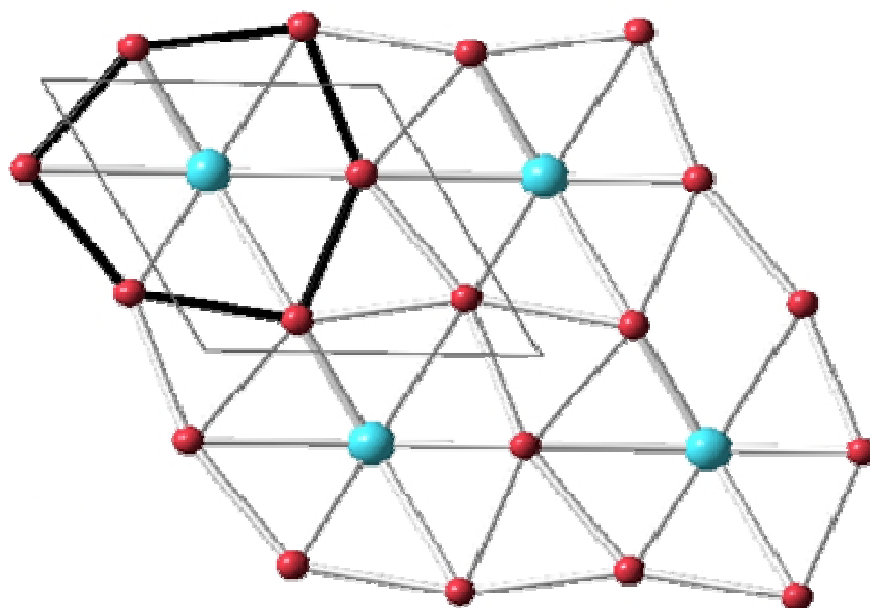
Figure 3.35: View of the distorted A(2)-O lattice along the *z*-axis, O^{2-} ions not parallel to the *xy*-plane are omitted for clarity. Black outline shows a "slice" through the AO_{12} polyhedra, 3 x A(2)-O bonds of 3.141(2) Å and 3 x A(2)-O bonds of 2.646(2) Å parallel to the *xy*-plane. The unit cell is outlined in grey. (Red spheres O^{2-}; blue sphere Ba^{2+} / Sr^{2+} / La^{3+})
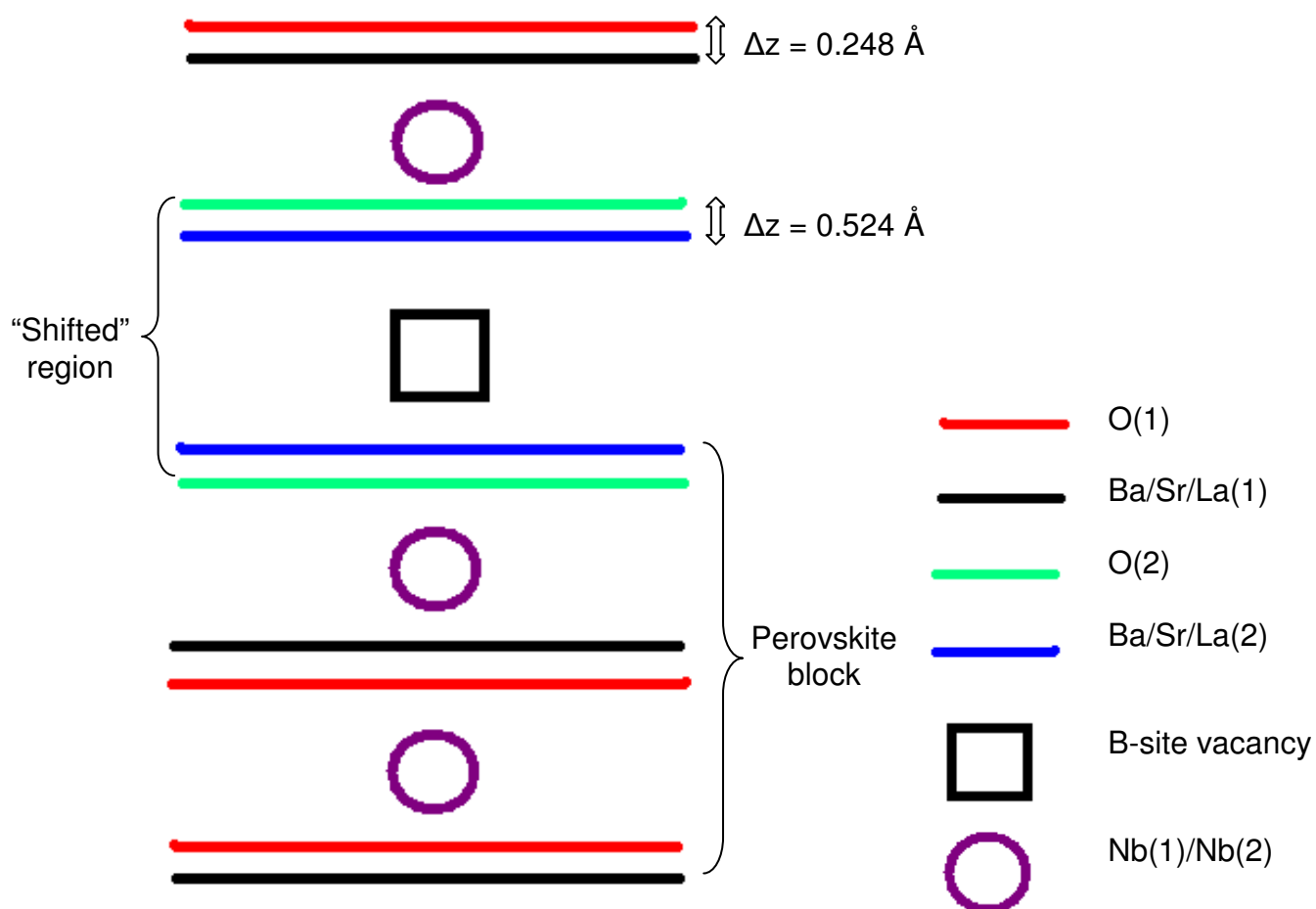
Figure 3.36: A schematic diagram showing A-O displacement along the *z*-axis (Δz) for $BaSr_2LaNb_3O_{12}$ (not to scale).

$BaSr_2LaNb_3O_{12}$ was found to possess a variance of 12.16×10^{-4} this can be seen in **figure 3.37**. (For clarity, Δ values are quoted in figures omitting the factor 10^{-4}).

$\Delta = 12.16$

(a)　　　　　　　　　　　(b)
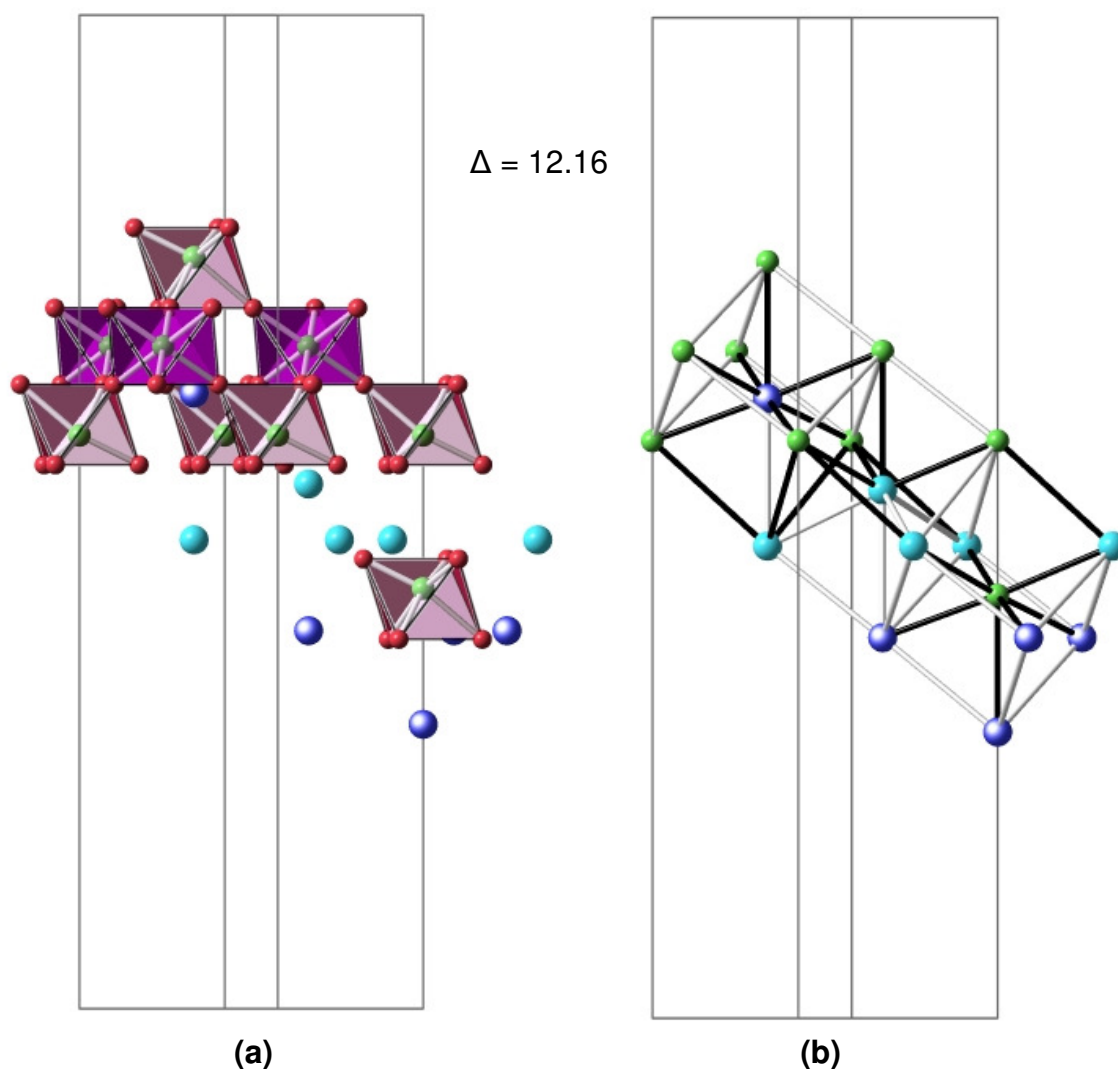
Figure 3.37: (a) A- and B-cations involved in the three *bcc* unit cells (O^{2-} ions shown not involved in the *bcc* lattice) **(b)** Structural view of the *bcc* lattice along the *xy*-direction, for $BaSr_2LaNb_3O_{12}$. Black bonds highlight the A-B distances (bond lengths) selected for calculation of the variance. (Red spheres O^{2-}; blue sphere Ba^{2+} / Sr^{2+} / La^{3+}, green spheres Nb^{5+})

3.3.1.2.3 Variable Temperature Neutron Data

Variable temperature neutron data were collected on the D2B diffractometer. Data were only collected at 900 °C for $BaSr_2LaNb_3O_{12}$ due to time limitations, however this, along with room temperature data from HRPD, is sufficient to investigate structural changes with increasing temperature.

3.3.1.2.3.1 NPD data at 900 °C

The data were initially refined using method (ii); this meant that the A-site occupancies deviated very slightly from 100%. The extent of the difference between the two sites was too large to be within the range of acceptable experimental error, and therefore different approaches were investigated. Three separate refinements were performed wherein each time one elements' occupancy was fixed at the value reached when using method (ii), and constraints were subsequently applied to the two remaining elements to ensure the overall site occupancies were 100%. The results from the different refinement approaches are listed in **table 3.19**.

Refinement Type	χ^2	R_{wp} (%)	R_p (%)	A-site occupancies	
Method (ii)	5.566	8.62	6.05	Ba/Sr/La1	0.4(8)/0.49(1)/0.3(5)
				Ba/Sr/La2	0.1(8)/0.51(1)/0.2(5)
La^{3+} occupancies fixed	5.562	8.62	6.05	Ba/Sr/La1	-0.12(6)/0.84(6)/0.28*
				Ba/Sr/La2	0.62(6)/0.16(6)/0.22*
Ba^{2+} occupancies fixed	5.562	8.62	6.05	Ba/Sr/La1	0.37*/-0.44(1)/1.07(1)
				Ba/Sr/La2	0.13*/1.44(1)/-0.57(1)
Sr^{2+} occupancies fixed	5.562	8.62	6.05	Ba/Sr/La1	0.01(4)/0.49*/0.50(4)
				Ba/Sr/La2	0.49(4)/0.51*/0.00(4)

*fixed occupancy value

Table 3.19: Summary of different refinement approaches for $BaSr_2LaNb_3O_{12}$ 900 °C D2B data.

It can be seen from the refinement results in **table 3.19** that the high temperature data for $BaSr_2LaNb_3O_{12}$ have a high associated margin of error for the A-site fractional occupancies, this can be partially attributed to the increased temperature. Consequently the fractional occupancies are unstable, and from the three fixed

occupancy refinements performed it appears that fixing the Sr^{2+} occupancy values yields the most sensible results. Whilst the statistics for all three approaches are comparable when the Sr^{2+} occupancies are fixed, the values also seem to be the most logical when compared to the room temperature data, and when taking into consideration all of the structural aspects. This is the same approach as used in refinement method (iii) however in previous cases XRPD data were also available to give a definitive assignment of the Sr^{2+} occupancies. Therefore when three A-cations are present, comparable XRPD data are required at the same temperature to allow an accurate appointment of fractional occupancies. Consequently the resulting occupancy values and any conclusions drawn from them should be interpreted with care, and this problem in mind.

The refinement results are summarised below in **figure 3.38** and **tables 3.20** and **3.21**. Refinement statistics and lattice parameters are given in **figure 3.38**.

Space group R-3

χ^2 = 5.562; R_{wp} = 8.62%; R_p = 6.05%

a = 5.7529(1) Å; c = 28.1165(8) Å

$\alpha = \beta = 90°$; $\gamma = 120°$

Volume = 805.87(3) $Å^3$
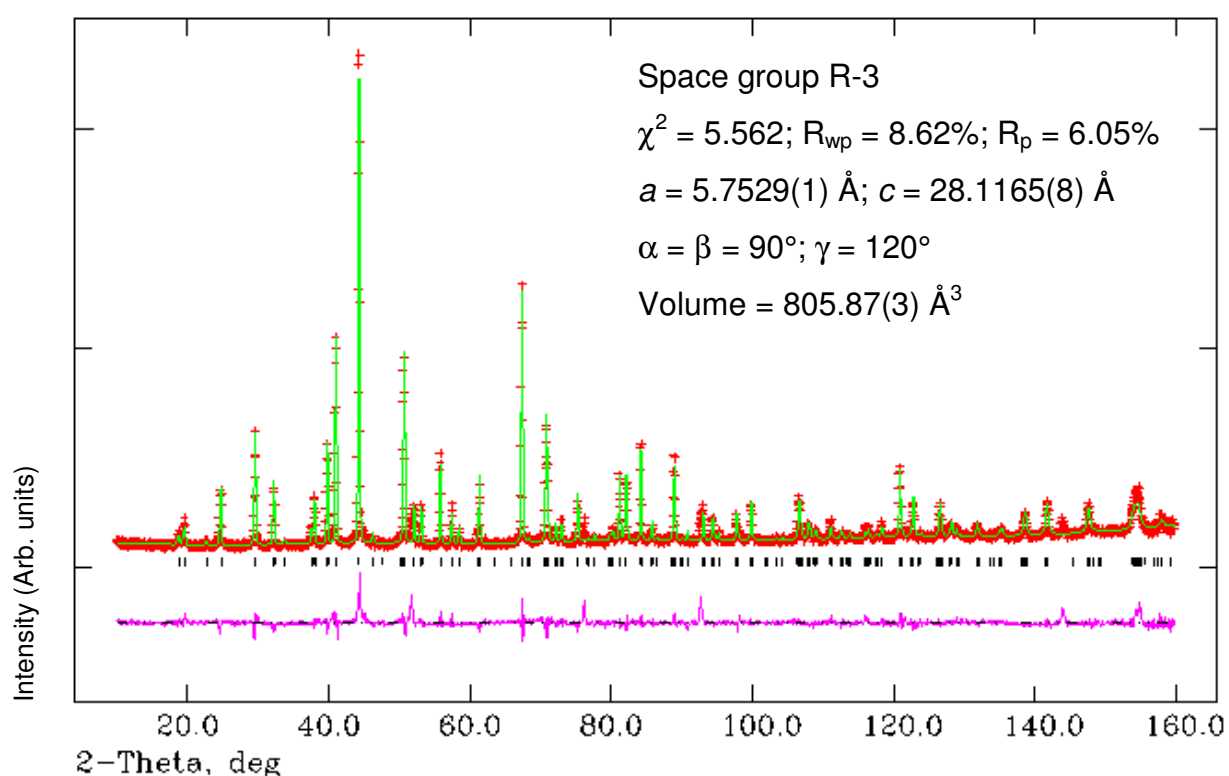
Figure 3.38: Calculated (green), experimental (red) and difference (pink) profile plot for $BaSr_2LaNb_3O_{12}$ variable temperature NPD data collected from D2B at 900 °C. Tick marks represent Bragg peak positions.

Atom	Wyckoff	x	Y	z	$U_{iso} \times 100$ (Å^2)	Frac.
Ba/Sr/La1	6c	0	0	0.2870(3)	3.48(3)	0.01(4)/0.49*/0.5(4)
Ba/Sr/La2	6c	0	0	0.1370(4)	3.26(3)	0.49(4)/0.51*/0.0(4)
Nb1	6c	0	0	0.4220(2)	1.28(1)	1
Nb2	3a	0	0	0	1.12(2)	1
O1	18f	0.1437(2)	0.8143(2)	0.6280(3)	4.59(2)	1
O2	18f	0.1684(2)	0.8344(2)	0.4523(2)	3.93(1)	1

*Sr^{2+} occupancy values fixed.

Table 3.20: Refinement results for $BaSr_2LaNb_3O_{12}$ (D2B data, 900 °C)

Bond lengths (Å)			Bond Angles (°)		
Ba/Sr/La(1)-O(1) =	2.902(9)	(x3)	O(1)-Nb(1)-O(1) =	82.3(4)	(x3)
Ba/Sr/La(1)-O(1) =	3.005(1)	(x3)	O(1)-Nb(1)-O(2) =	166.1(4)	(x3)
Ba/Sr/La(1)-O(1) =	2.764(1)	(x3)	O(1)-Nb(1)-O(2) =	85.0(4)	(x3)
Ba/Sr/La(1)-O(2) =	2.629(8)	(x3)	O(1)-Nb(1)-O(2) =	90.3(4)	(x3)
			O(2)-Nb(1)-O(2) =	100.9(3)	(x3)
Ba/La(2)-O(1) =	3.238(9)	(x3)			
Ba/La(2)-O(2) =	2.913(1)	(x3)	O(1)-Nb(2)-O(1) =	93.4(3)	(x6)
Ba/La(2)-O(2) =	2.928(1)	(x3)	O(1)-Nb(2)-O(1) =	86.6(3)	(x6)
Ba/La(2)-O(2) =	2.735(9)	(x3)	O(1)-Nb(2)-O(1) =	180.0	(x3)
Nb(1)-O(1) =	2.165(9)	(x3)			
Nb(1)-O(2) =	1.869(6)	(x3)			
Nb(2)-O(1) =	2.004(8)	(x6)			

Table 3.21: Bond lengths and angles from refinement results for $BaSr_2LaNb_3O_{12}$

(D2B 900 °C data)
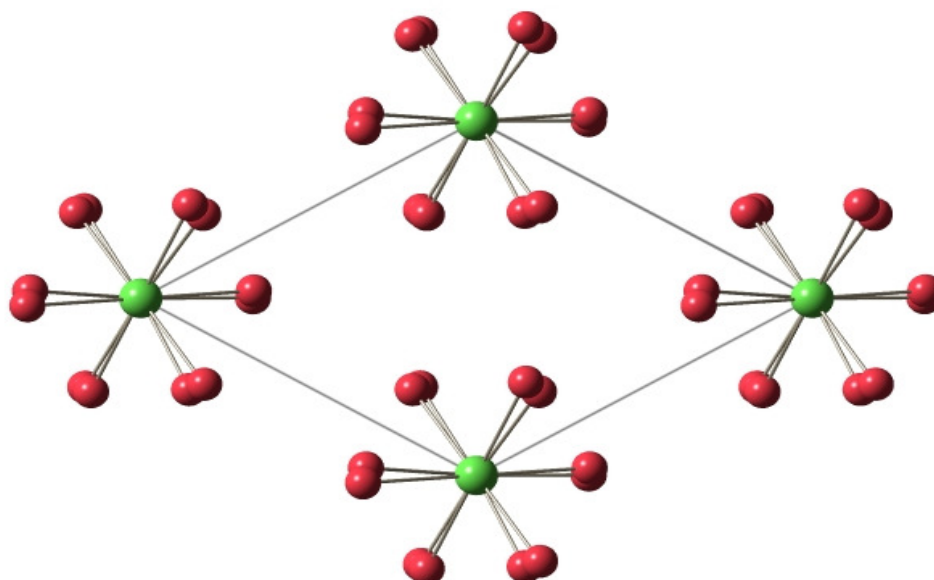
Figure 3.39: View of $BaSr_2LaNb_3O_{12}$ structure along the z-axis from 900 °C D2B data, showing tilting of the octahedra, tilt angle 5° [a⁻ a⁻ a⁻] (octahedra omitted for clarity). (Red spheres O^{2-}; green spheres Nb^{5+}.)

When the 900 °C variable temperature NPD data for $BaSr_2LaNb_3O_{12}$ are compared to the room temperature HRPD data, it could be considered that there is a rearrangement of the dominant divalent cation Sr^{2+} when the temperature is increased. However, once again, there is not enough evidence to support this theory as the movement of cations at this temperature is not entirely feasible. The tilt angle of the octahedra decreases (from 9° at RT to 5° at 900 °C), although, the tilt angle is still significantly above zero and the structure is still best described in space group R-3, and is therefore still not untilted at 900 °C (the refinement results can be seen in **figure 3.38** and **tables 3.20** and **3.21**).

3.3.1.3 $Sr_3LaNb_3O_{12}$

3.3.1.3.1 Variable Temperature NPD Data

Variable temperature neutron data were collected on the D2B diffractometer. Data were collected at room temperature, 600 °C and 900 °C to study structural changes with increasing temperature.

3.3.1.3.1.1 Room Temperature NPD data

The refinement results are summarised below in **figure 3.40** and **tables 3.22** and **3.23**. Refinement statistics and lattice parameters are given in **figure 3.40**.

Space group R-3

$\chi^2 = 3.681$; $R_{wp} = 7.52\%$; $R_p = 5.93\%$

$a = 5.6556(1)$ Å; $c = 27.1756(4)$ Å

$\alpha = \beta = 90°$; $\gamma = 120°$

Volume = 752.79(2) Å^3
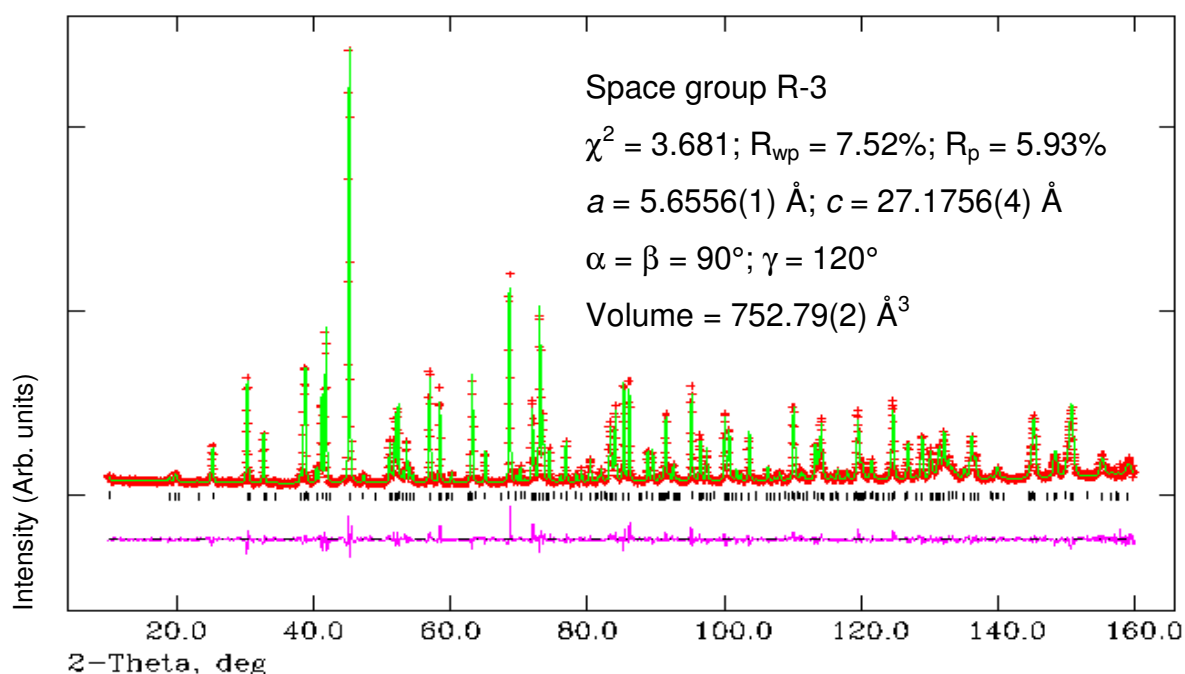
Figure 3.40: Calculated (green), experimental (red) and difference (pink) profile plot for $Sr_3LaNb_3O_{12}$ variable temperature NPD data collected from D2B RT. Tick marks represent Bragg peak positions.

Atom	Wyckoff	x	y	z	$U_{iso}*100$ ($\mathring{A}^2$)	Frac.
Sr/La1	6c	0	0	0.2863(1)	0.71(9)	0.56(6)/0.44(6)
Sr/La2	6c	0	0	0.1391(2)	0.76(9)	0.94(6)/0.06(6)
Nb1	6c	0	0	0.4239(1)	0.15(7)	1
Nb2	3a	0	0	0	0.50(1)	1
O1	18f	0.1149(5)	0.7849(6)	0.6270(1)	1.03(5)	1
O2	18f	0.1088(5)	0.7729(7)	0.4541(1)	0.97(6)	1

Table 3.22: Refinement results for $Sr_3LaNb_3O_{12}$ (D2B data, RT)

Bond lengths (Å)		Bond Angles (°)	
Sr/La(1)-O(1) =	2.872(4) (x3)	O(1)-Nb(1)-O(1) =	83.0(2) (x3)
Sr/La(1)-O(1) =	3.118(2) (x3)	O(1)-Nb(1)-O(2) =	165.9(2) (x3)
Sr/La(1)-O(1) =	2.552(2) (x3)	O(1)-Nb(1)-O(2) =	87.5(1) (x3)
Sr/La(1)-O(2) =	2.599(3) (x3)	O(1)-Nb(1)-O(2) =	85.6(1) (x3)
		O(2)-Nb(1)-O(2) =	102.1(2) (x3)
Sr/La(2)-O(1) =	3.178(4) (x3)		
Sr/La(2)-O(2) =	3.201(2) (x3)	O(1)-Nb(2)-O(1) =	93.4(1) (x6)
Sr/La(2)-O(2) =	2.543(2) (x3)	O(1)-Nb(2)-O(1) =	86.6(1) (x6)
Sr/La(2)-O(2) =	2.592(4) (x3)	O(1)-Nb(2)-O(1) =	180.0 (x3)
Nb(1)-O(1) =	2.146(4) (x3)		
Nb(1)-O(2) =	1.869(3) (x3)		
Nb(2)-O(1) =	1.991(4) (x6)		

Table 3.23: Bond lengths and angles from refinement results for $Sr_3LaNb_3O_{12}$ (D2B RT data)

The $Sr_3LaNb_3O_{12}$ room temperature NPD Rietveld refinement proceeded with ease in space group R-3. Details of the refinement can be found in **figure 3.40** and **tables 3.22** and **3.23.** The material was found to have lattice parameters a = 5.6556(1) Å; c = 27.1756(4) Å with associated statistics χ^2 = 3.681, R_{wp} = 7.52%; and R_p = 5.93%. The ensuing structure can be seen in **figure 3.41**.
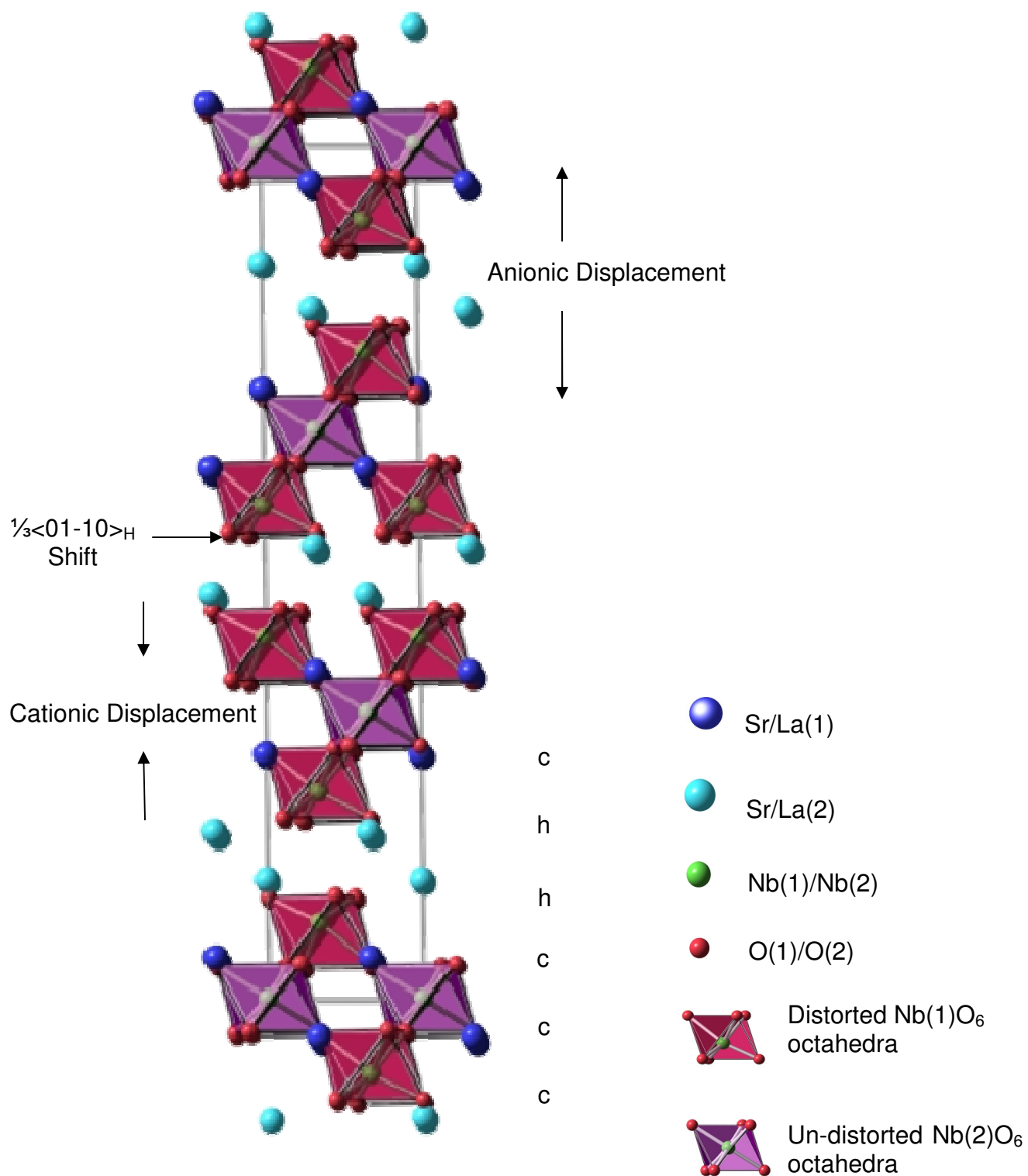
Figure 3.41: Structure of $Sr_3LaNb_3O_{12}$ viewed along the *x*-axis.

The two B-site locations can be seen in *figures 3.42* and *3.43*. The NbO_6 octahedra are tilted about the *c*-axis by an angle of 11° with Glazer notation a⁻ a⁻ a⁻, *figure 3.44*. The distortion values for the BO_6 octahedra in the two B-site environments are $\Delta d = 0$ and $\Delta d = 47.61$ for B(1) and B(2) correspondingly.

The Sr^{2+} cations display a preference for A(2) at room temperature with an occupancy of 94% compared to 56% in A(1). This preference forces the majority of La^{3+} cations (44%) into A(1) in the perovskite block. As La^{3+} is the smaller of the two A-cations, the larger occupancy in the perovskite block is logical, this being the smaller of the two A-sites.

The A-cation environments can be seen in *figures 3.45* and *3.46*. 3 x A(1)-O bonds of 2.599(3) Å and 3 x A(1)-O bonds of 2.872(4) Å are pointing towards neighbouring octahedral layers of B-site cations (along the direction of the *z*-axis). 3 x A(1)-O bonds of 2.552(2) Å and 3 x A(1)-O bonds of 3.118(2) Å are parallel to the *xy*-plane pointing towards BO_6 octahedra in the same perovskite block.

For the A(2) cations there are 3 x A(2)-O bonds of 2.592(4) Å pointing into the "shifted" region and 3 x A(2)-O bonds of 3.178(4) Å pointing towards the perovskite block and 3 x A(2)-O bonds of 3.201(2) Å, and 3 x A(2)-O bonds of 2.543(2) Å bonds parallel to *xy*-plane pointing towards NbO_6 octahedra in the same octahedral layer. The A(2) cations are displaced into shifted region and the degree of shift for both A-cations can be seen in *figure 3.49*.

A(2) and A(1) distortion values are $\Delta d = 33.81$ and $\Delta d = 28.68$ correspondingly. This can be seen clearer in *figures 3.47* and *3.48* where the distorted A-O lattices can be seen along the *z*-axis.

Bond valence sums (BVS) were performed for the structure (referred to in *section 1.1.1, equations 1.2* and *1.3*), the values are listed in *table 3.24*. Overall the BVS calculations performed for the structure demonstrates that the bond lengths obtained are sensible and that the resulting refinement data are suitable.

Cation	Theoretical BVS	Calculated BVS	Status
A(1)	2.44	2.50	Over-bonded
A(2)	2.14	2.06	Under-bonded
B(1)	5.00	4.95	Under-bonded
B(2)	5.00	4.84	Under-bonded

Table 3.24: BVS calculation results for $Sr_3LaNb_3O_{12}$
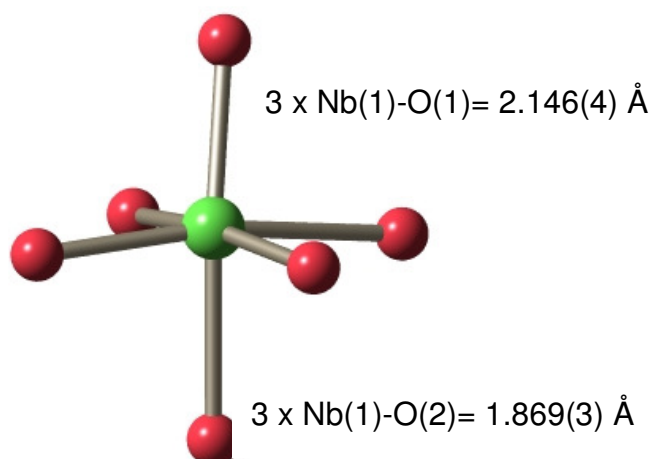
Figure 3.42: Distorted NbO$_6$ octahedron adjacent to "shifted" region (red spheres O^{2-}; green sphere Nb^{5+}). Associated bond lengths labelled.

$3 \times \text{Nb}(1)\text{-O}(1) = 2.146(4)$ Å

$3 \times \text{Nb}(1)\text{-O}(2) = 1.869(3)$ Å
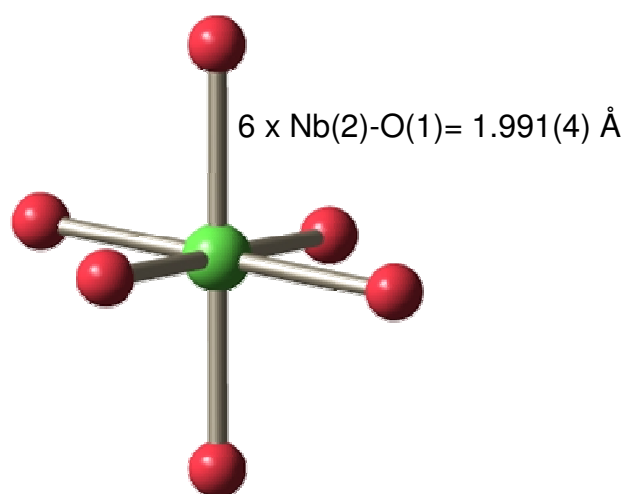
Figure 3.43: Undistorted NbO$_6$ octahedron in the centre of a triple layer of corner-sharing octahedra (red spheres O^{2-}; green sphere Nb^{5+}). Associated bond lengths labelled.

$6 \times \text{Nb}(2)\text{-O}(1) = 1.991(4)$ Å
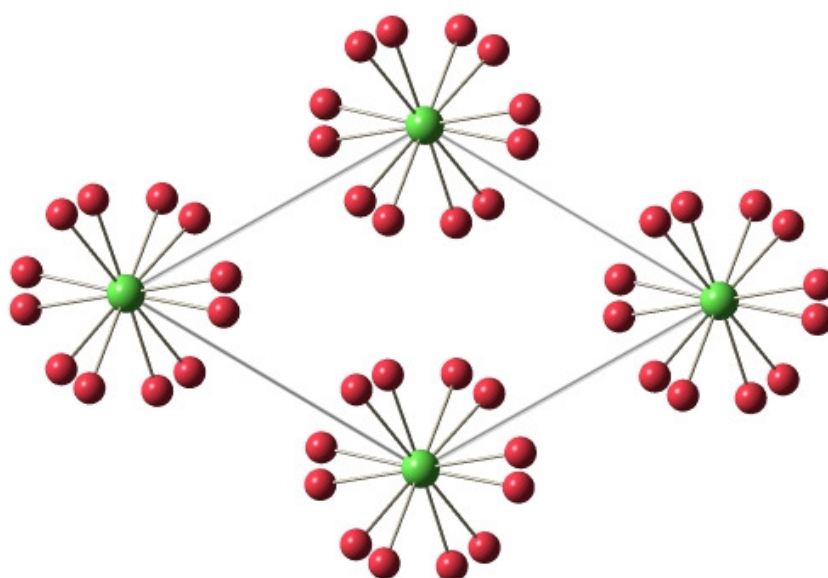
Figure 3.44: View of Sr$_3$LaNb$_3$O$_{12}$ structure along the z-axis showing tilting of the octahedra, tilt angle 11° [a$^-$ a$^-$ a$^-$] (octahedra omitted for clarity). (Red spheres O^{2-}; green spheres Nb^{5+}.)
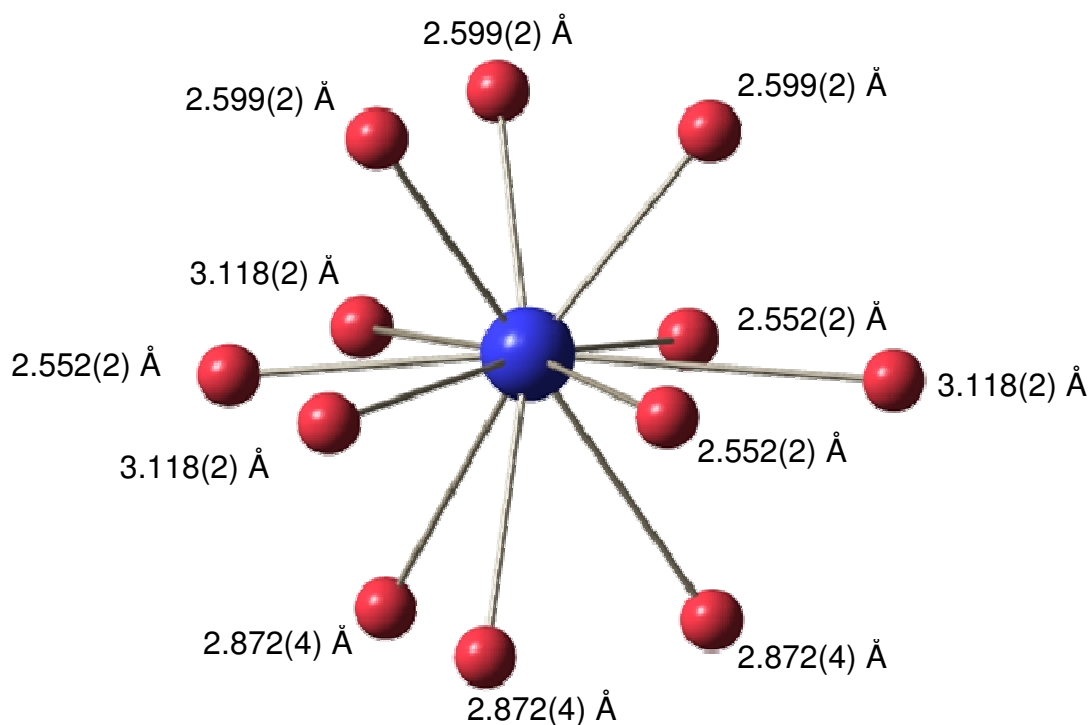
Figure 3.45: Cubo-octahedral environment of A(1) cations located within the triple layer of NbO_6 octahedra with a Sr / La distribution of 0.56 / 0.44. (Red spheres O^{2-}; Blue sphere Sr^{2+} / La^{3+}). Bond lengths are labelled.
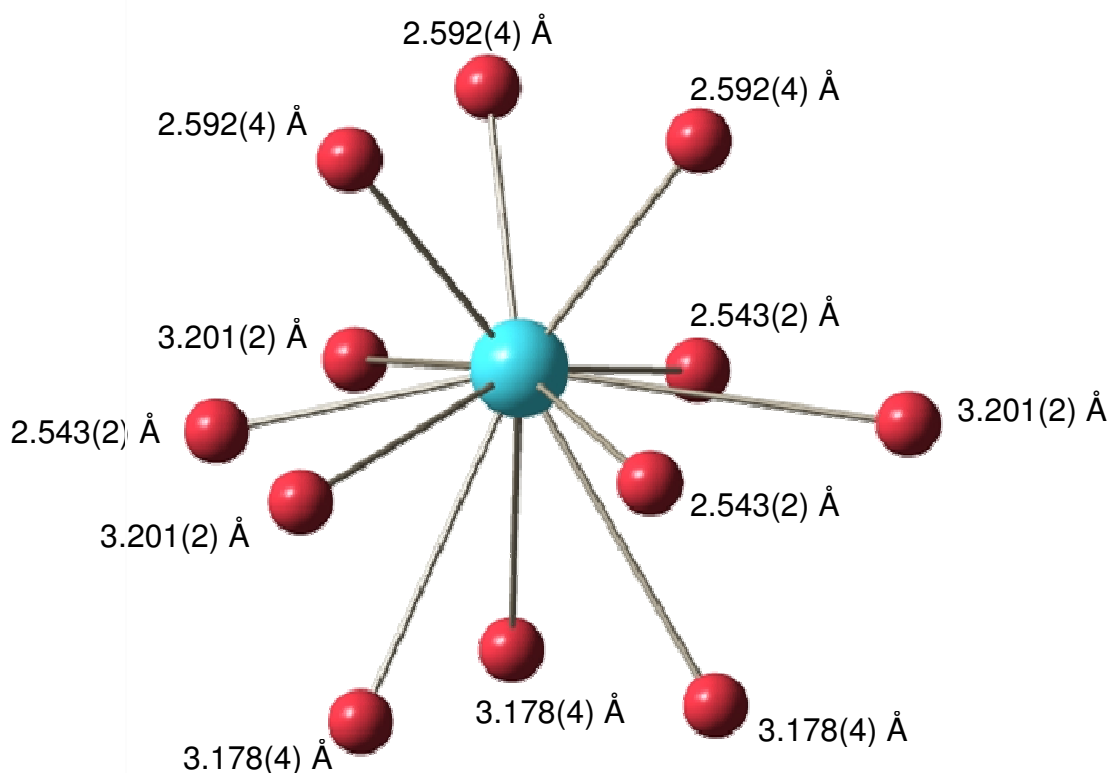
Figure 3.46: Cubo-octahedral environment of A(2) cations located in the "shifted" region, with a Sr / La distribution of 0.94 / 0.06. (Red spheres O^{2-}; blue sphere Sr^{2+} / La^{3+}). Bond lengths are labelled.
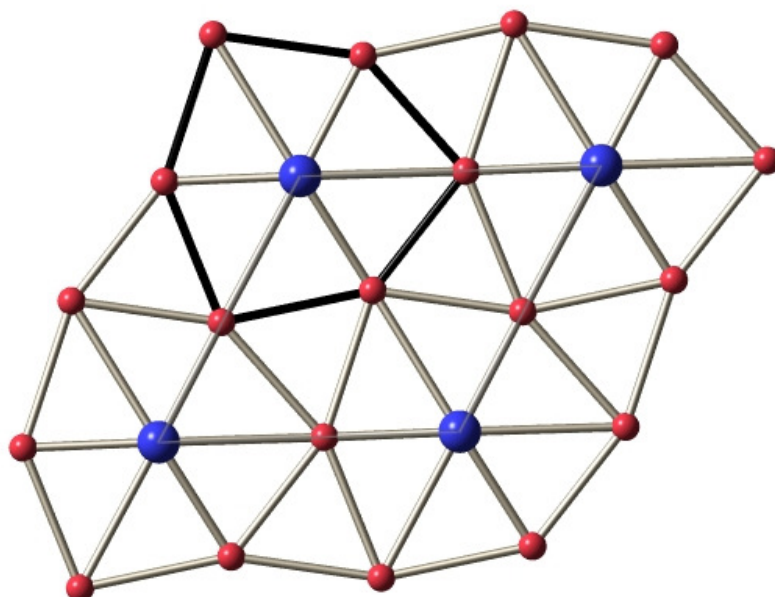
Figure 3.47: View of the distorted A(1)-O lattice along the *z*-axis, O^{2-} ions not parallel to the *xy*-plane are omitted for clarity. Black outline shows a "slice" through the AO_{12} polyhedra, 3 x A(1)-O bonds of 2.552(2) Å and 3 x A(1)-O bonds of 3.118(2) Å parallel to the *xy*-plane. A-cations are located on the corners of the unit cell, outlined in grey. (Red spheres O^{2-}; Blue spheres Sr^{2+} / La^{3+}).
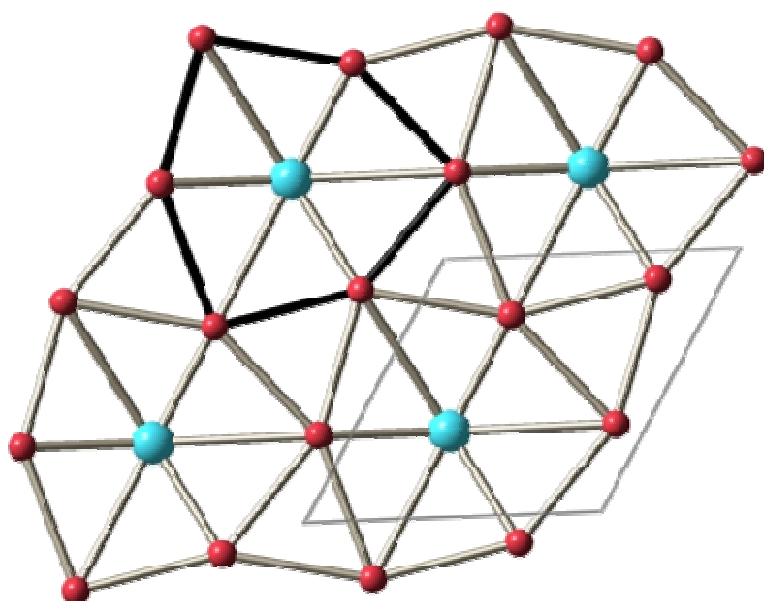
Figure 3.48: View of the distorted A(2)-O lattice along the *z*-axis, O^{2-} ions not parallel to the *xy*-plane are omitted for clarity. Black outline shows a "slice" through the AO_{12} polyhedra, 3 x A(2)-O bonds of 3.201(2) Å and 3 x A(2)-O bonds of 2.543(2) Å bonds parallel to *xy*-plane. The unit cell is outlined in grey. (Red spheres O^{2-}; Blue spheres Sr^{2+} / La^{3+}).

112
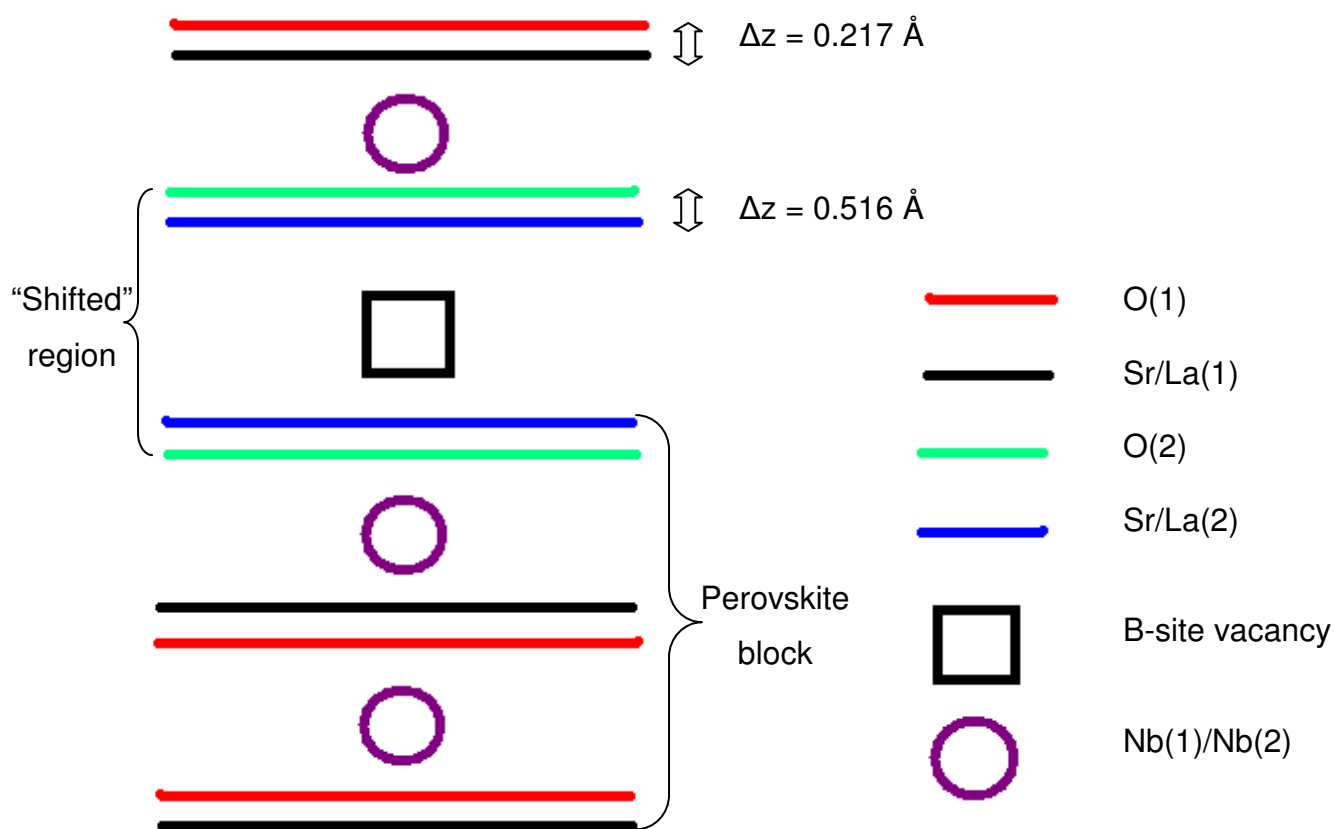
Figure 3.49: A schematic diagram showing A-O displacement along the *z*-axis (Δz) for $Sr_3LaNb_3O_{12}$ (not to scale).

$Sr_3LaNb_3O_{12}$ was found to possess a variance of 10.91 (x 10^{-4}) this can be seen in **figure 3.50**. (For clarity , Δ values are quoted in figures omitting the factor 10^{-4}).

$\Delta = 10.91$

(a)   (b)
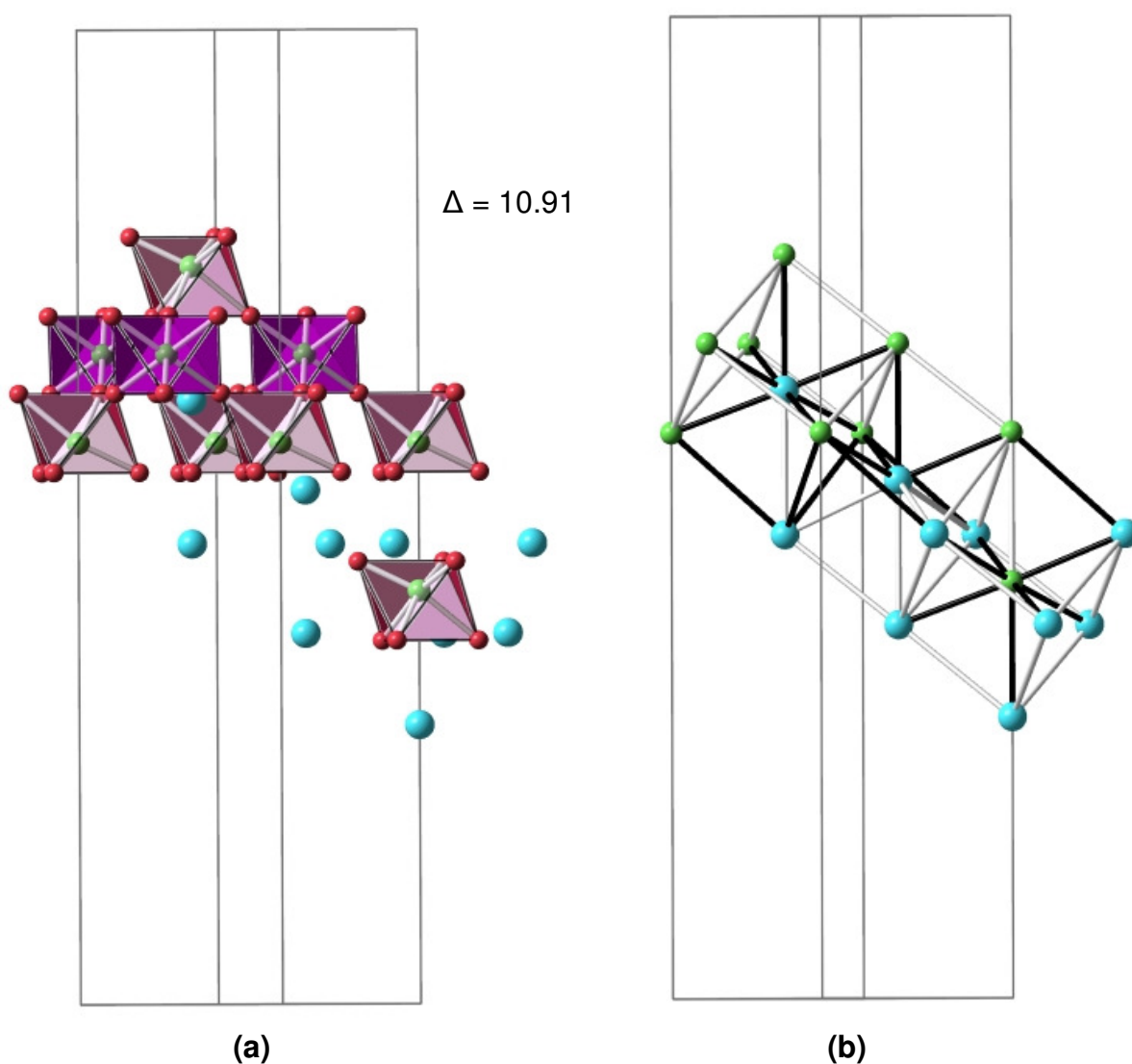
Figure 3.50: (a) A- and B-cations involved in the three *bcc* unit cells (O^{2-} ions shown not involved in the *bcc* lattice) **(b)** Structural view of the *bcc* lattice along the *xy*-direction, for $Sr_3LaNb_3O_{12}$. Black bonds highlight the A-B distances (bond lengths) selected for calculation of the variance. (Red spheres O^{2-}; Blue spheres Sr^{2+} / La^{3+}; Green spheres Nb^{5+}).

3.3.1.3.1.2 NPD data at 600 °C

The refinement results are summarised below in *figure 3.51* and *tables 3.25* and
3.26. Refinement statistics and lattice parameters are given in *figure 3.51*.

Space group R-3

$\chi^2 = 4.064$; $R_{wp} = 7.53\%$; $R_p = 5.64\%$

$a = 5.6870(1)$ Å; $c = 27.4303(5)$ Å

$\alpha = \beta = 90°$; $\gamma = 120°$

Volume = 768.28(2) Å^3
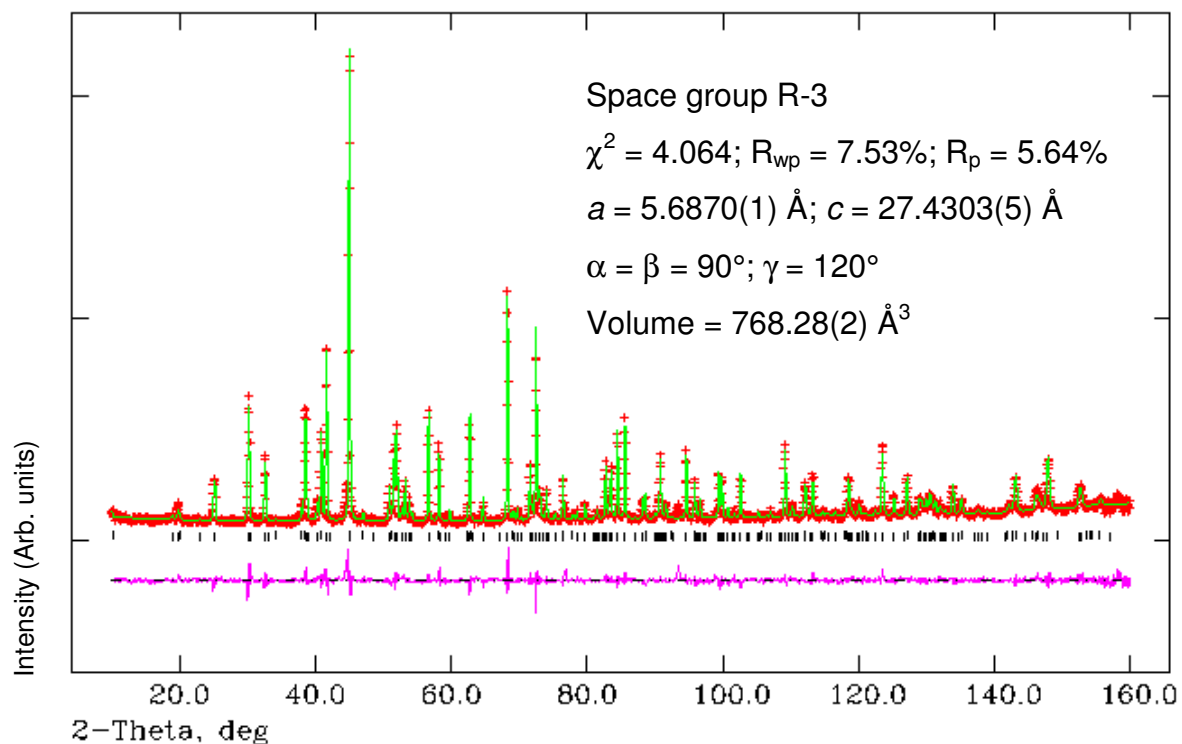
Figure 3.51: Calculated (green), experimental (red) and difference (pink) profile plot
for $Sr_3LaNb_3O_{12}$ variable temperature NPD data collected from D2B at 600 °C. Tick
marks represent Bragg peak positions.

Atom	Wyckoff	x	y	z	$U_{iso}*100$ $(Å^2)$	Frac.
Sr/La1	6c	0	0	0.2860(2)	2.35(1)	0.5/0.5
Sr/La2	6c	0	0	0.1385(2)	2.70(1)	1.0/0.0
Nb1	6c	0	0	0.4241(2)	0.87(1)	1
Nb2	3a	0	0	0	0.75(2)	1
O1	18f	0.1200(9)	0.7930(9)	0.6275(2)	2.66(9)	1
O2	18f	0.1174(8)	0.7822(8)	0.4540(1)	2.85(1)	1

Table 3.25: Refinement results for $Sr_3LaNb_3O_{12}$ (D2B data, 600 °C)

115

Bond lengths (Å)		Bond Angles (°)	
Sr/La(1)-O(1) =	2.878(6) (x3)	O(1)-Nb(1)-O(1) =	81.6(2) (x3)
Sr/La(1)-O(1) =	3.099(4) (x3)	O(1)-Nb(1)-O(2) =	165.0(3) (x3)
Sr/La(1)-O(1) =	2.606(4) (x3)	O(1)-Nb(1)-O(2) =	87.7(2) (x3)
Sr/La(1)-O(2) =	2.606(6) (x3)	O(1)-Nb(1)-O(2) =	86.4(2) (x3)
		O(2)-Nb(1)-O(2) =	102.2(2) (x3)
Sr/La(2)-O(1) =	3.206(7) (x3)		
Sr/La(2)-O(2) =	3.167(4) (x3)	O(1)-Nb(2)-O(1) =	93.9(2) (x6)
Sr/La(2)-O(2) =	2.605(4) (x3)	O(1)-Nb(2)-O(1) =	86.1(2) (x6)
Sr/La(2)-O(2) =	2.625(6) (x3)	O(1)-Nb(2)-O(1) =	180.0 (x3)
Nb(1)-O(1) =	2.158(6) (x3)		
Nb(1)-O(2) =	1.865(5) (x3)		
Nb(2)-O(1) =	2.004(6) (x6)		

Table 3.26: Bond lengths and angles from refinement results for $Sr_3LaNb_3O_{12}$ (D2B 600°C data)
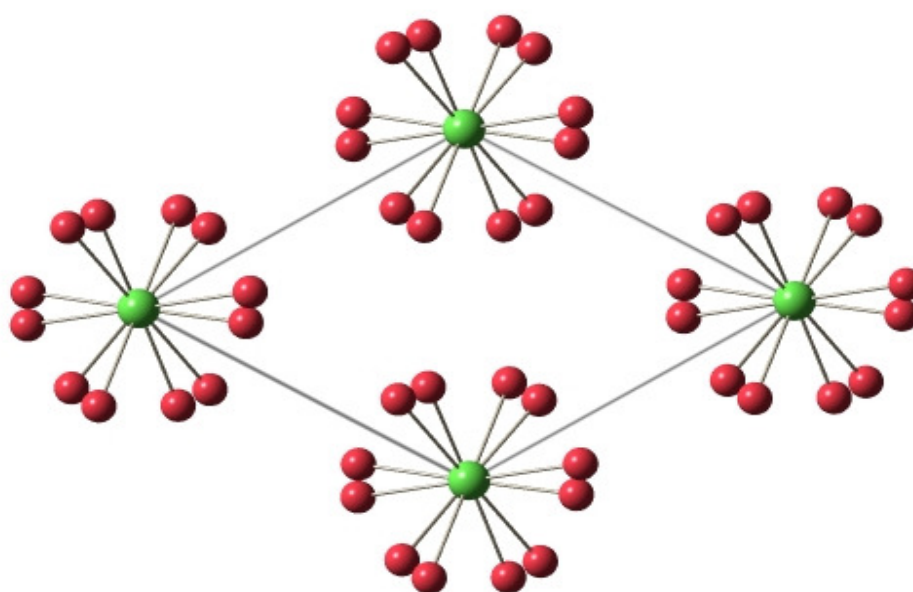
Figure 3.52: View of $Sr_3LaNb_3O_{12}$ structure along the z-axis showing tilting of the octahedra, tilt angle 9° [a⁻ a⁻ a⁻] 600°C (octahedra omitted for clarity). (Red spheres O^{2-}; Green spheres Nb^{5+}).

3.3.1.3.1.3 NPD data at 900 °C

The refinement results are summarised below in **figure 3.53** and **tables 3.27** and **3.28**. Refinement statistics and lattice parameters are given in **figure 3.53**.

Extra sharp reflections are witnessed with this data due to the expansion of the steel cap of the vanadium can at high temperature. The steel was modelled as a second phase, as indicated by the red tick marks.

Space group R-3
$\chi^2 = 6.472$; $R_{wp} = 6.32\%$; $R_p = 4.41\%$
$a = 5.7063(1)$ Å; $c = 27.5726(7)$ Å
$\alpha = \beta = 90°$; $\gamma = 120°$
Volume = 777.53(3) Å^3
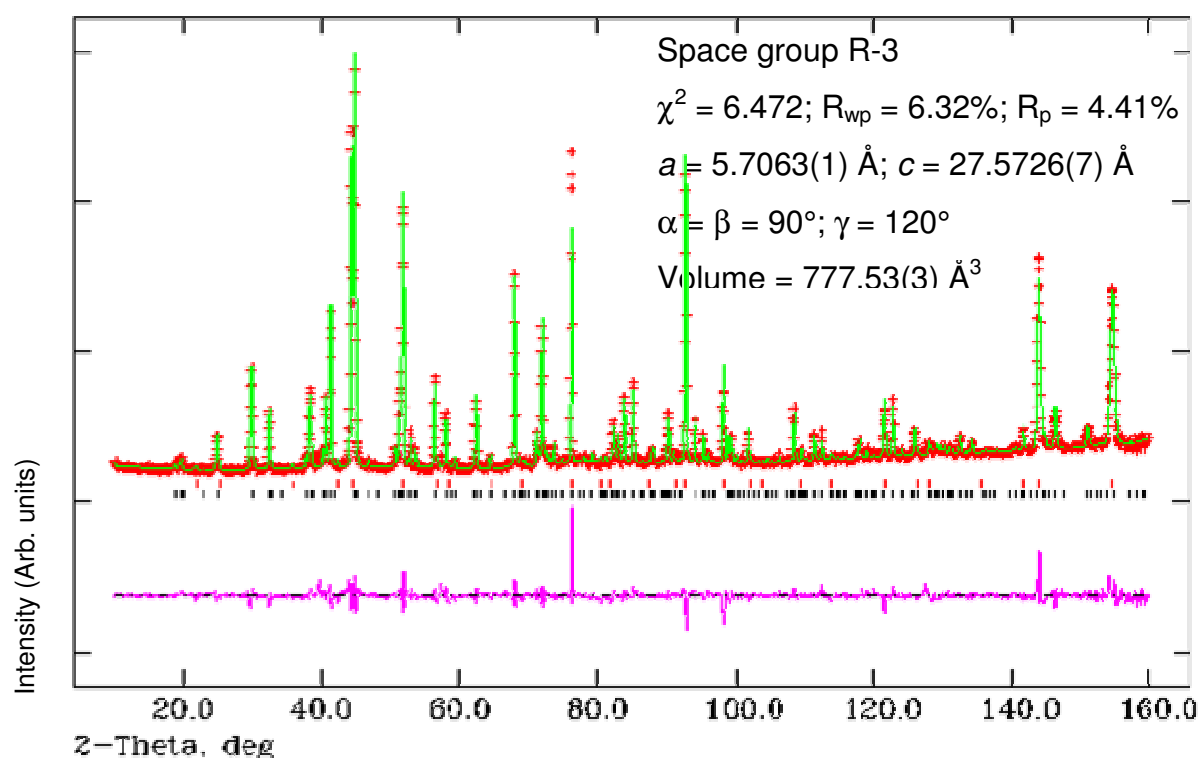
Red tick marks for second phase, steel.

Figure 3.53: Calculated (green), experimental (red) and difference (pink) profile plot for Sr$_3$LaNb$_3$O$_{12}$ variable temperature NPD data collected from D2B at 900 °C. Tick marks represent Bragg peak positions.

Atom	Wyckoff	x	y	z	$U_{iso}*100$ (Å^2)	Frac.
Sr/La1	6c	0	0	0.2862(4)	3.52(2)	0.5/0.5
Sr/La2	6c	0	0	0.1371(3)	3.57(3)	1.0/0.0
Nb1	6c	0	0	0.4241(3)	1.09(2)	1
Nb2	3a	0	0	0	0.88(2)	1
O1	18f	0.1261(2)	0.7967(2)	0.6279(3)	4.14(2)	1
O2	18f	0.1247(1)	0.7912(1)	0.4535(2)	3.78(2)	1

Table 3.27: Refinement results for Sr$_3$LaNb$_3$O$_{12}$ (D2B data, 900 °C)

Bond lengths (Å)		Bond Angles (°)	
Sr/La(1)-O(1) =	2.883(1) (x3)	O(1)-Nb(1)-O(1) =	81.5(4) (x3)
Sr/La(1)-O(1) =	3.082(7) (x3)	O(1)-Nb(1)-O(2) =	164.9(4) (x3)
Sr/La(1)-O(1) =	2.643(7) (x3)	O(1)-Nb(1)-O(2) =	87.4(4) (x3)
Sr/La(1)-O(2) =	2.612(9) (x3)	O(1)-Nb(1)-O(2) =	86.8(4) (x3)
		O(2)-Nb(1)-O(2) =	102.2(3) (x3)
Sr/La(2)-O(1) =	3.190(1) (x3)		
Sr/La(2)-O(2) =	3.128(7) (x3)	O(1)-Nb(2)-O(1) =	93.9(3) (x6)
Sr/La(2)-O(2) =	2.655(7) (x3)	O(1)-Nb(2)-O(1) =	86.1(3) (x6)
Sr/La(2)-O(2) =	2.677(9) (x3)	O(1)-Nb(2)-O(1) =	180.0 (x3)
Nb(1)-O(1) =	2.180(1) (x3)		
Nb(1)-O(2) =	1.853(7) (x3)		
Nb(2)-O(1) =	1.993(1) (x6)		

Table 3.28: Bond lengths and angles from refinement results for $Sr_3LaNb_3O_{12}$ (D2B 900 °C data)
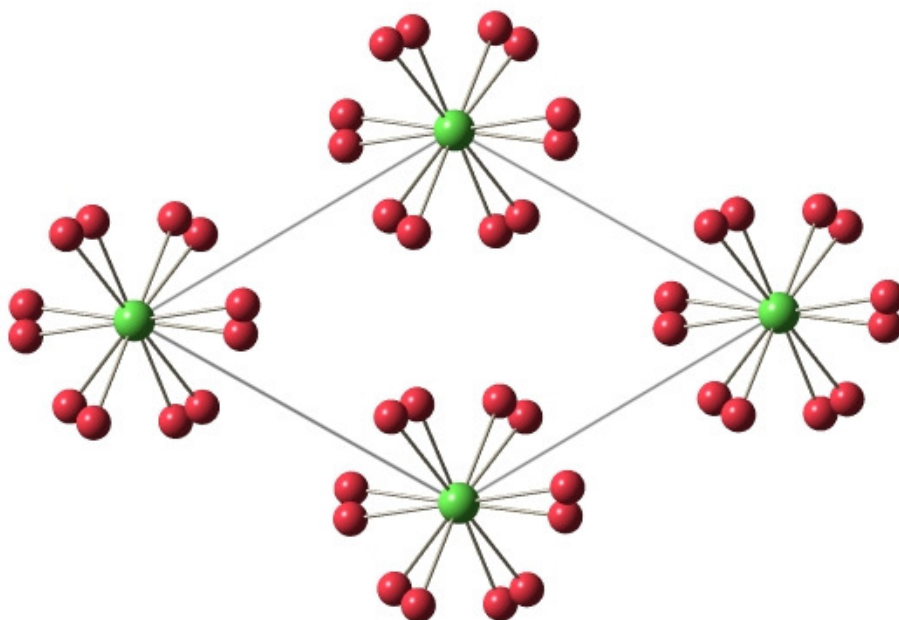
Figure 3.54: View of $Sr_3LaNb_3O_{12}$ structure along the z-axis showing tilting of the octahedra, tilt angle 8° [a⁻ a⁻ a⁻] 900 °C (octahedra omitted for clarity). (Red spheres O^{2-}; Green spheres Nb^{5+}).

The variable temperature neutron data for $Sr_3LaNb_3O_{12}$ display a decrease in tilt angle as the temperature increases (11°, 9° and 8° at room temperature, 600 °C and 900 °C respectively), although even at 900 °C the tilt angle is still significantly greater than zero. No structural transition from tilted to untilted (R-3 to R-3m) therefore occurs up to 900 °C.

After examining the data, it was once again considered that an A-cation distribution occurred to accommodate the majority of Sr^{2+} cations in the "shifted" region. Dependent upon how the estimated standard deviations associated with the fractional occupancies are viewed this theory could be supported. However, as the movement of cations is unlikely at these temperatures this theory is dismissed due to a lack of evidence.

3.3.2 Discussion

3.3.2.1 Variable temperature NPD data

The study of the $Ba_{3-x}Sr_xLaNb_3O_{12}$ series yielded interesting results. As the Sr^{2+} content in the structure increased the tolerance factor was found to decrease, when x = 1, 2 and 3, tolerance factor values of 1.007 0.992 and 0.977 are obtained respectively. As Sr^{2+} cations replace Ba^{2+} cations across the series, the tilt angle of the NbO_6 octahedra at room temperature increases from 7.5° to 8.5° to 11°, for $Ba_2SrLaNb_3O_{12}$, $BaSr_2LaNb_3O_{12}$ and $Sr_3LaNb_3O_{12}$ correspondingly. This increase in tilt angle and decrease in tolerance factor as Sr^{2+} content is increased relates to the size difference between Ba^{2+} and Sr^{2+}. Hence the NbO_6 octahedra rotate about the z-axis to a higher degree as more Sr^{2+} is introduced.

Variable temperature NPD data were collected for the series to investigate how the structures evolve with increasing temperature and to establish if an octahedral tilt transition as witnessed for $Ba_3LaNb_3O_{12}$[8] at ~ 192 °C, was also observed for the other members of the series at elevated temperatures. A structural transition from tilted to an untilted arrangement (Space group R-3 to R-3m) was not observed for the x = 1, 2 and 3 members at temperatures up to 900 °C. However, a reduction in tilt angle with increasing temperature was witnessed for all structures, summarised in *table 3.29*.

Name	Ba$_3$LaNb$_3$O$_{12}$		Ba$_2$SrLaNb$_3$O$_{12}$			BaSr$_2$LaNb$_3$O$_{12}$		Sr$_3$LaNb$_3$O$_{12}$		
Temperature (°C)	RT	300	RT	320	900	RT	900	RT	600	900
Tilt angle (°)	4	0[10]	7.5	4.5	4	9	5	11	8.5	7.5

Table 3.29: Summary of variable temperature NPD data refinement results for the

Ba$_{3-x}$Sr$_x$LaNb$_3$O$_{12}$ series.

Upon examination of the estimated standard deviations associated with the fractional occupancies, it was considered that, with increasing temperature an A-cation rearrangement occurred to accommodate the majority of the dominant divalent cation in the "shifted" region. This theory was dismissed as it was considered unlikely that cations could move at such low temperatures.

Interestingly the average A-cation radius over each A-site remains very stable as seen in **tables 3.30** and **3.31** for Ba$_2$SrLaNb$_3$O$_{12}$ and Sr$_3$LaNb$_3$O$_{12}$ respectively. However not enough variable temperature data were collected for BaSr$_2$LaNb$_3$O$_{12}$ to allow similar conclusions to be drawn.

Temp (°C)	Average A(1) Radius (Å)	Average A(2) Radius (Å)
RT	1.41	1.44
600	1.40	1.44
900	1.40	1.44

Table 3.30: Average A-cation radius over A(1) and A(2) for Ba$_2$SrLaNb$_3$O$_{12}$

Temp (°C)	Average A(1) Radius (Å)	Average A(2) Radius (Å)
RT	1.43	1.58
320	1.43	1.58
900	1.42	1.60

Table 3.31: Average A-cation radius over A(1) and A(2) for Sr$_3$LaNb$_3$O$_{12}$

After collection of variable temperature NPD it was postulated by Rawal *et al.*[8] for Ba$_3$LaNb$_3$O$_{12}$ that at ~ 192 °C an octahedral tilt transition occurs, and the structure becomes completely untilted. This hypothesis was supported by electrical data, where at 1 MHz a peak in ε_r occurred at this temperature. Electrical data were also collected for Sr$_3$LaNb$_3$O$_{12}$, and evidenced an inflection in the curve (as opposed to a clear peak) occurred in ε_r at ~ 447 °C, however no variable temperature NPD data were collected for this structure.

The variable temperature NPD data collected (**section 3.3.1.3.1**) for Sr$_3$LaNb$_3$O$_{12}$ up to 900 °C found the structure was not completely untilted (space group R-3). As no tilt transition has occurred for this structure it is unknown what the peak in permittivity correlates to at this present time. The fact that Ba$_3$LaNb$_3$O$_{12}$ is completely untilted at the same temperature as the peak in electrical data may be attributed to the fact that the dominant divalent A-cation is Ba^{2+}. Since Ba$_3$LaNb$_3$O$_{12}$ has a larger tolerance factor (1.022) than the other members of the series, and hence a smaller tilt angle at room temperature (4°), therefore less movement is required to achieve a tilt angle of 0°, and this can be achieved at a temperature closer to room temperature. As the Sr^{2+} content is increased, the tolerance factor decreases, the tilt angle at room temperature is increased, and therefore more structural adjustment is required to attain a tilt angle of 0°. It is therefore logical that the temperature that this tilt transition occurs at is higher when the room temperature tilt angle is larger. However a direct and unequivocal link between tilt angle and tilt transition temperature is not entirely feasible since the intermediate compositions possess smaller tilt angles than Sr$_3$LaNb$_3$O$_{12}$. Due to equipment limitations it was not possible to attain NPD data above 900 °C, but it is proposed that if data were collected above this temperature tilt transitions to 0° would be witnessed if melting did not occur first.

These data suggest that a link may be made between tolerance factor and a structural transition, and this may be used to explain the observed electrical properties in Ba- and Sr- based B-site deficient perovskites, akin to that used for many Ba- and Sr-based 3*C*-type *AB*O$_3$ perovskites.[11] However, the relationship is more complex and this structural transition is temperature dependent.

The $Sr_3LaNb_3O_{12}$ A(2) occupancy at room temperature obtained from D2B data (96%) varies slightly from the occupancy for this site quoted by Rawal *et al.*[8] (~86%). This difference can be attributed to the data being obtained from two different samples which may possess slight differences due to associated synthesis techniques.

There is a need for comparable XRPD data at the relevant temperatures to give an accurate assessment of the crystal structures. General conclusions can be drawn from the data, that is, a reduction in tilting occurs when heating begins, and that although a peak in permittivity at 1 MHz in LCR data correlates to a tilt transition for $Ba_3LaNb_3O_{12}$, this is not the case for $Sr_3LaNb_3O_{12}$.

3.3.3.2 Room temperature structural data

Members of the $Ba_{3-x}Sr_xLaNb_3O_{12}$ series crystallise with a 12R structure. The anions and cations in the structures are cooperatively displaced in opposite directions along the *z*-axis. This displacement between O^{2-} anions and A-cations is quantified by the Δz shift values seen in ***figures 3.17, 3.36*** and ***3.49***, for $Ba_2SrLaNb_3O_{12}$, $BaSr_2LaNb_3O_{12}$ and $Sr_3LaNb_3O_{12}$ respectively. The Δz shift values, summarised in ***table 3.32***, clearly demonstrate that the A-cations and O^{2-} anions in the "shifted" region are more significantly displaced than in the perovskite block. Across the series a reduction in Δz in the "shifted" region is witnessed as the Sr^{2+} content increases. This reduction can be attributed to the presence of a greater concentration of the smaller A-cation.

Composition	$Ba_2SrLaNb_3O_{12}$	$BaSr_2LaNb_3O_{12}$	$Sr_3LaNb_3O_{12}$
A(1)-O(1) Perovskite block Δz (Å)	0.224	0.248	0.217
A(2)-O(2) "Shifted region" Δz (Å)	0.531	0.524	0.516

Table 3.32: Summary of Δz shift values for $Ba_{3-x}Sr_xLaNb_3O_{12}$ series

As a consequence of the cooperative displacement of anions and cations in opposite directions, the AO_{12} polyhedra become distorted. The distortion within the AO_{12} polyhedra has been quantified by the parameter Δd and the corresponding distortion values for the series are summarised in ***table 3.33***. An increase in Sr^{2+} content

results in a larger value of Δd for the AO_{12} polyhedra, a greater tilt angle, and a more marked distortion of the oxygen sublattice.

Composition	$Ba_2SrLaNb_3O_{12}$	$BaSr_2LaNb_3O_{12}$	$Sr_3LaNb_3O_{12}$
$A(1)O_{12}\,\Delta d$ $(x\ 10^{-4})$	46.94	61.84	66.84
$A(2)O_{12}\,\Delta d$ $(x\ 10^{-4})$	53.07	83.37	117.15

Table 3.33: Summary of the Δd values for the AO_{12} polyhedra.

The AO_{12} polyhedral distortion is larger for the A(2) cations located within the "shifted" region, and the difference between the extent of distortion between A(1) and A(2) cations also increases as the Sr^{2+} content increases. This may be explained by examining the A(2) occupancies for the structures.

The B(1) octahedral environment is distorted and the B(2) octahedral environment is undistorted, for all members of the series. The degrees of distortion for the B(1) sites are summarised in **table 3.34**.

Composition	$Ba_2SrLaNb_3O_{12}$	$BaSr_2LaNb_3O_{12}$	$Sr_3LaNb_3O_{12}$
$B(1)O_6\,\Delta d$ $(x\ 10^{-4})$	63.97	62.31	47.61

Table 3.34: Summary of the Δd values for the $B(1)O_6$ octahedra.

The NbO_6 octahedra in all structures in this series are rotated about the z-axis resulting in anti-phase tilting. The degree of tilting within the structures is quantified by the tilt angle; the tilt angles for the various members of the solid solution are listed in **table 3.35**.

Composition	$Ba_2SrLaNb_3O_{12}$	$BaSr_2LaNb_3O_{12}$	$Sr_3LaNb_3O_{12}$
Tilt Angle (°)	7.5	8.5	11

Table 3.35: Summary of RT tilt angles for $Ba_{3-x}Sr_xLaNb_3O_{12}$ series.

It must be noted that the tilt angle for $Sr_3LaNb_3O_{12}$ is slightly different to that quoted for the same composition by Rawal *et al*. but this again is probably due to the use of different samples.

Due to the vacancies present within the crystal structure, the anion sublattice is under tension, and the cation sublattice is compressed. To overcome these

structural hindrances displacements of both cations and anions are observed. This displacement relieves the strain within the structure and allows relaxation of the cationic sublattice, which subsequently facilitates the reconstruction of the *bcc* cationic sublattice. The reconstruction of the *bcc* cationic sublattice therefore contributes to the stability of the crystal structure.

This distortion exhibited within the "shifted" region, which is present in all "shifted" B-cation deficient hexagonal perovskites, can be compared by considering the *bcc* cationic sublattice, regardless of the number of ccp layers present. In order to do this a parameter known as the variance Δ, has been introduced. This parameter is adapted from theories in current literature and is discussed in more detail in **section 1.2.2.2**.

The variance Δ, for the three compositions can be seen in *figure 3.55*. The variance for $Ba_3LaNb_3O_{12}$ is also included for completeness. As the Sr^{2+} content is increased, the magnitude of the variance decreases.
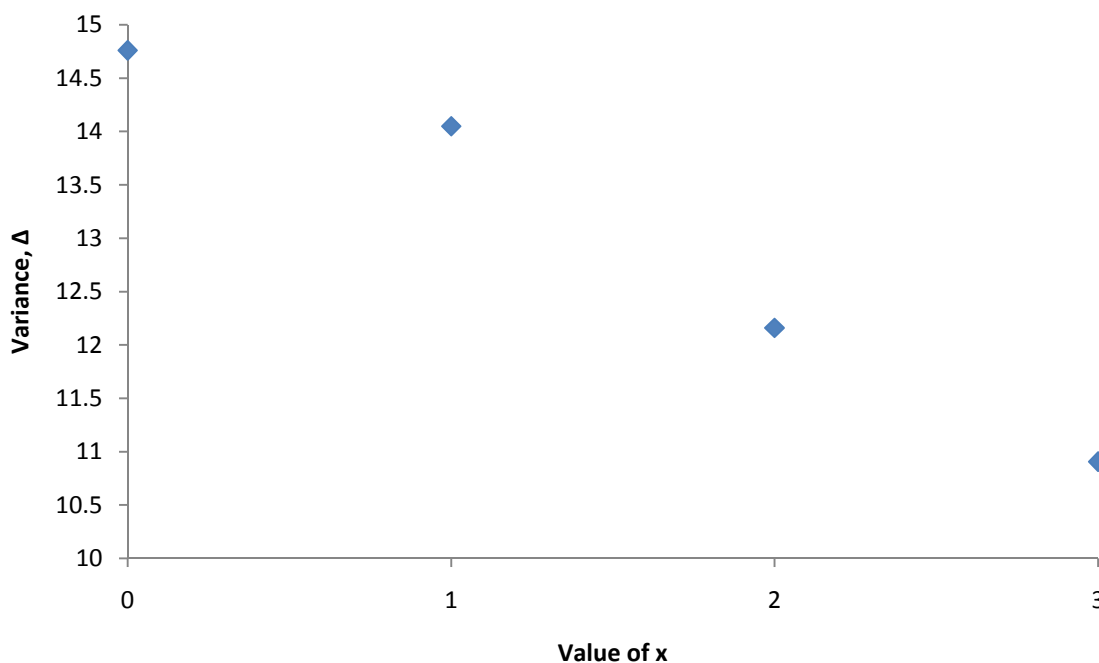
Figure 3.55: Variance Δ, for the $Ba_{3-x}Sr_xLaNb_3O_{12}$ series.

3.4 Electrical characterisation

3.4.1 Impedance Spectroscopy

Impedance spectroscopy measurements for $Sr_3LaNb_3O_{12}$ have previously been performed[12] therefore the data are quoted purely for a comprehensive view, although it must be noted that the measurements were performed on a different sample of $Sr_3LaNb_3O_{12}$, and therefore some slight differences may exist due to synthesis techniques.

$Ba_2SrLaNb_3O_{12}$ and $BaSr_2LaNb_3O_{12}$ were resistive at room temperature and required temperatures above 500 °C to yield data. Plots of impedance data at elevated temperatures for the two compositions implied that the bulk and grain boundary response is being measured. The Arrhenius plot of the bulk and grain boundary conductivity for the two materials, and $Sr_3LaNb_3O_{12}$, can be seen in *figure 3.55*. The Arrhenius plot demonstrates that the data obey the Arrhenius law, with an activation energy E_a of ~1.17 eV for $Ba_2SrLaNb_3O_{12}$, ~1.13 eV for $BaSr_2LaNb_3O_{12}$ and ~ 0.98 eV for $Sr_3LaNb_3O_{12}$. Based on the approximation that the intrinsic band gap $E_g \sim 2E_a$, the conductivity at high temperatures is attributed to intrinsic behaviour, *i.e.* carrier excitation across an intrinsic band gap of >2.0 eV.
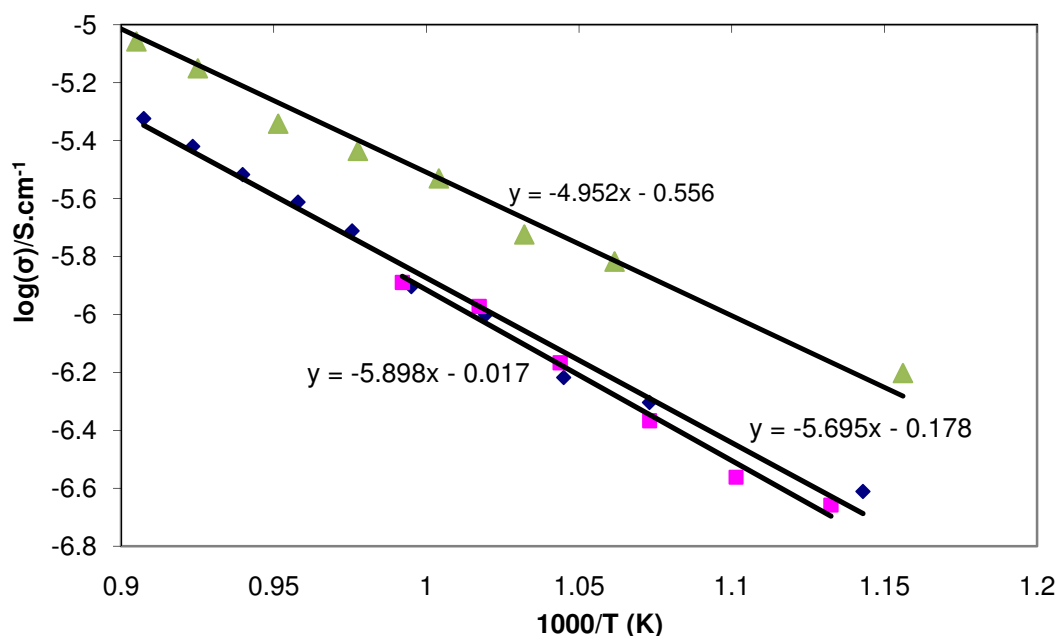
Figure 3.55: Arrhenius plot of bulk and grain boundary conductivity *vs.* reciprocal temperature for $Ba_2SrLaNb_3O_{12}$ (pink); $BaSr_2LaNb_3O_{12}$ (blue); $Sr_3LaNb_3O_{12}$ (green)[12]

3.4.2 Microwave Dielectric Properties

The microwave dielectric properties for the $Ba_{3-x}Sr_xLaNb_3O_{12}$ series are summarised in *table 3.36*. The values for the end members of the series, $Ba_3LaNb_3O_{12}$ and $Sr_3LaNb_3O_{12}$ are quoted from previously measured data.[12] It should be noted the microwave data acquired are for a different sample to that used for variable temperature NPD data therefore slight differences may be present.

The microwave dielectric properties of the series must be interpreted with caution due to the extrinsic effects associated with the low density of some pellets, which is known to influence Q values and to provide unreliable TCF values. The LCR data provided, however, should provide a reasonable idea of behaviour with temperature.

Compositions	ε_r	Q.f. (GHz)	TCF (ppm / $^\circ$C)	Relative Density
$Ba_3LaNb_3O_{12}$[8] (x=0)	44	9047	-100	98%
$Ba_2SrLaNb_3O_{12}$ (x=1)	40	2707	0.003	70%
$BaSr_2LaNb_3O_{12}$ (x=2)	26	15669	12	49%
$Sr_3LaNb_3O_{12}$ (x=3)	36	23532	-5	99%

Table 3.36: Microwave dielectric properties of $Ba_{3-x}Sr_xLaNb_3O_{12}$ series

A previous investigation into this system[7] found slightly different dielectric properties to those quoted in *table 3.36* the difference may be due to suspected complex low temperature behaviour displayed by the compositions which affects the RT properties displayed. If data were to be collected over a larger temperature range a more accurate interpretation of the properties may be possible.

The theoretical values of ε_r calculated using the CM equation are listed in *table 3.37* alongside the experimentally determined values. The theoretical values are slightly different to the experimental values. The deviation of these values from expected could be due to external factors such as the density of the ceramics or microstructure, and also due to structural deviations from the assumptions made in the CM equation.

Composition	Experimental ε_r	Theoretical ε_r*
Ba$_2$SrLaNb$_3$O$_{12}$ (x=1)	40	32
BaSr$_2$LaNb$_3$O$_{12}$ (x=2)	26	46
Sr$_3$LaNb$_3$O$_{12}$ (x=3)	36	39

*Modified αNb^{5+}values were used when, tolerance factor > 1 αNb^{5+} = 3.8 Å^3 [13] and tolerance factor < 1 αNb^{5+} = 4.65 Å^3 [14].

Table 3.37: Comparison of experimental ε_r and theoretical ε_r calculated using the Clausius-Mossotti equation (**section 1.2.1.1**, **equation 1.6**).

A reduction in ε_r is exhibited as the Sr^{2+} content is increased (**figure 3.56**). This is to be expected since Sr^{2+} has a smaller ionic polarisability than Ba^{2+}. Conversely the Q increases as the Sr^{2+} content increases (**figure 3.57**), this can be explained by the reduction in size difference over the A-site as more Sr^{2+} is introduced in place of Ba^{2+}. Anomalies in these trends are seen for the intermediate members of the series, for example in Ba$_2$SrLaNb$_3$O$_{12}$ the Q value drastically drops compared to Ba$_3$LaNb$_3$O$_{12}$, as opposed to increasing like the other members of the series. BaSr$_2$LaNb$_3$O$_{12}$ also displays an anomaly in ε_r wherein it displays a value significantly lower than the end member Sr$_3$LaNb$_3$O$_{12}$, as opposed to slightly larger as would be expected. The behaviour of these intermediate compositions is unpredictable, and from the structural data it is evident that much more is occurring within these structures when three A-cations are present than first thought.

The TCF values exhibited by the series are not highly correlated to the ε_r, as was suggested by Harrop[15] in the 1960s. However it seems there is some relationship between these values and the tolerance factor, and hence the octahedral tilt transition temperature as first suggested by Reaney et al.[11]
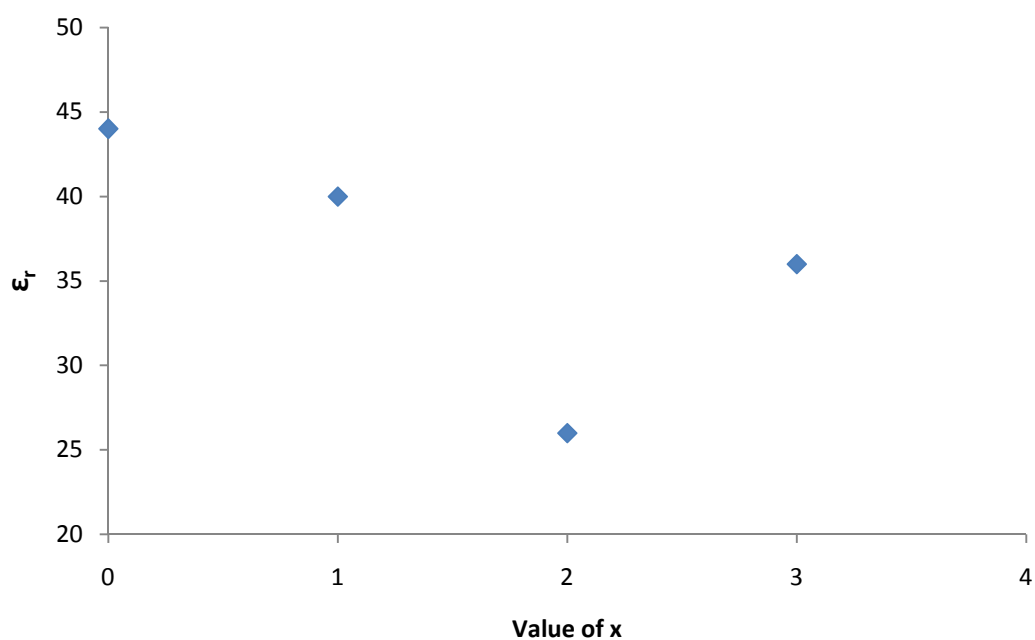
Figure 3.56: Graph to show how ε_r evolves as Sr^{2+} content increases.
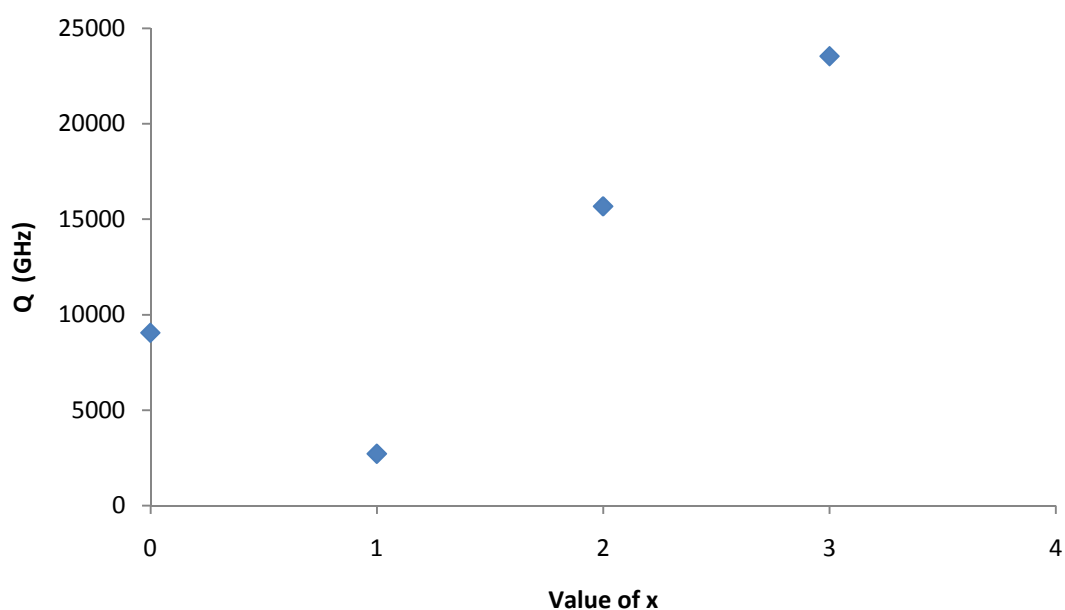
Figure 3.57: Graph to show the evolution of Q as Sr^{2+} content increases.

The structural data suggest evidence of a reduction in tilt angle, with increasing temperature. When three A-cations are present this process becomes more

complicated which is reflected in the TCF values, as opposed to a linear relationship between TCF and tolerance factor **figure 3.58**.
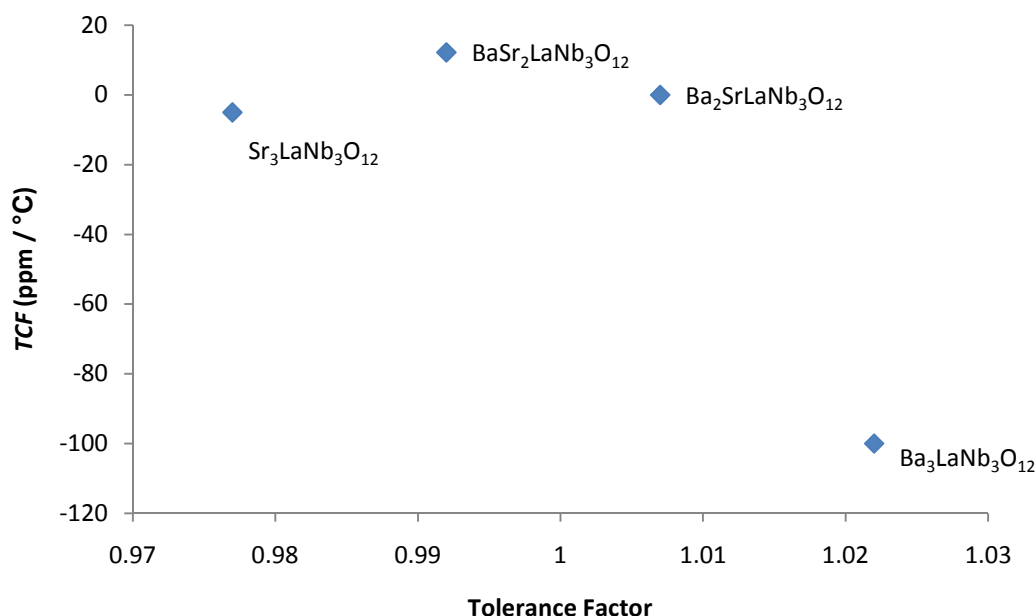
Figure 3.58: TCF *vs*. Tolerance factor for the $Ba_{3-x}Sr_xLaNb_3O_{12}$ series.

It is therefore postulated that the further away from room temperature that the octahedral tilt transition occurs, the closer to zero the TCF value is. The intermediate structures have tolerance factors closest to unity; in fact $Ba_2SrLaNb_3O_{12}$ with a tolerance factor of 1.007 is the closest by 0.001 compared to $BaSr_2LaNb_3O_{12}$ with a tolerance factor of 0.992. This is reflected in the TCF values for the materials with $Ba_2SrLaNb_3O_{12}$ displaying a very promising TCF value of 0.003 ppm / ℃. Usually a positive temperature coefficient of permittivity results in a negative TCF. Anomalies are expected to be due to pellet porosities.

The microwave results show that the material $Ba_2SrLaNb_3O_{12}$ displays the most promising microwave properties with an ε_r of 40 and a TCF value of 0.003 ppm / ℃, however the Q value at 2707 GHz is not large enough to optimise frequency selectivity adequately for commercial application. Therefore the results show that with suitable substitutions on the A-site promising ε_r and TCF values can be

obtained, however further substitutions of cations are required to optimise the Q value.

3.4.3 LCR Data

LCR data have previously been reported for $Ba_3LaNb_3O_{12}$ and $Sr_3LaNb_3O_{12}$[8] with peaks in permittivity at 1 MHz being displayed at ~192 °C and ~447 °C respectively. Variable temperature NPD data reported for $Ba_3LaNb_3O_{12}$ hypothesised that the peak in permittivity correlated to a structural transition at the same temperature. Variable temperature NPD from this study found the peak at ~447 °C for $Sr_3LaNb_3O_{12}$ did not correlate to a tilt transition and it is, as yet, unknown what phenomena this peak correlates to. LCR data are presented for the intermediate compositions $Ba_2SrLaNb_3O_{12}$ and $BaSr_2LaNb_3O_{12}$ in **figures 3.59** and **3.60** correspondingly, to assess whether the results correlate to the variable temperature NPD data collected.
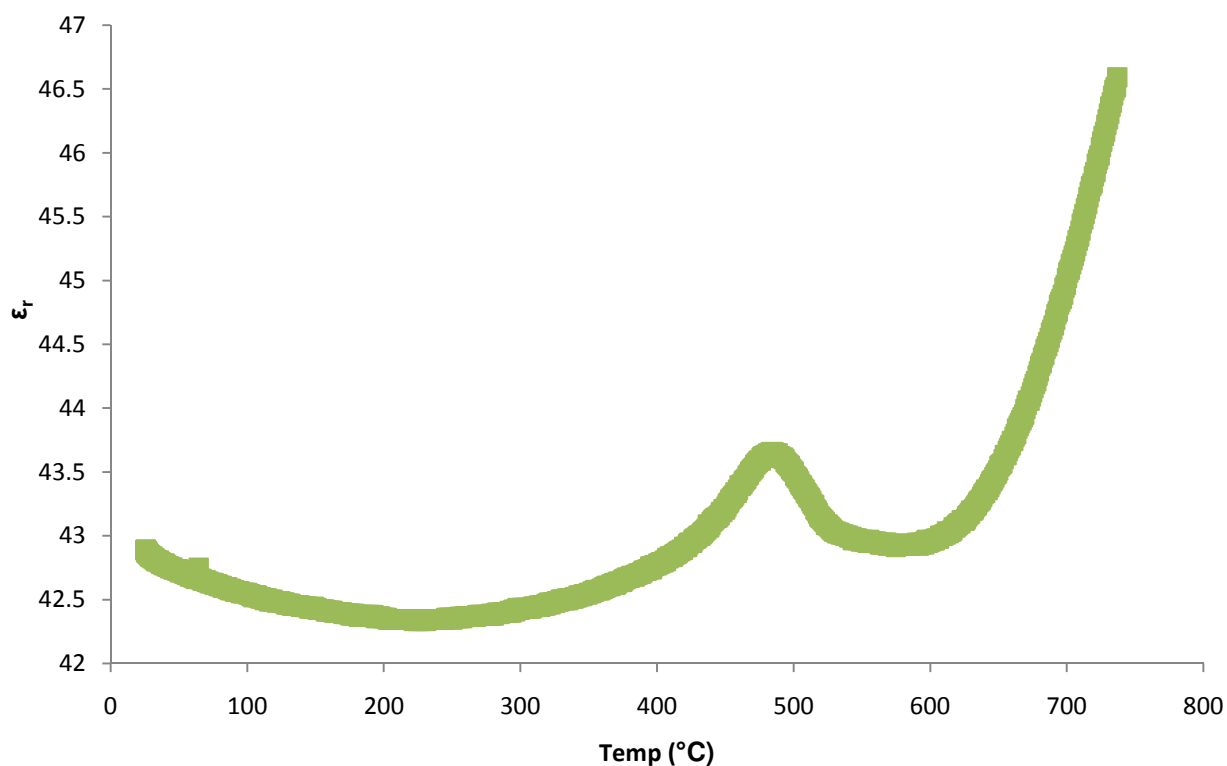
Figure 3.59: Plot of ε_r vs. Temperature for $Ba_2SrLaNb_3O_{12}$ at 1 MHz.
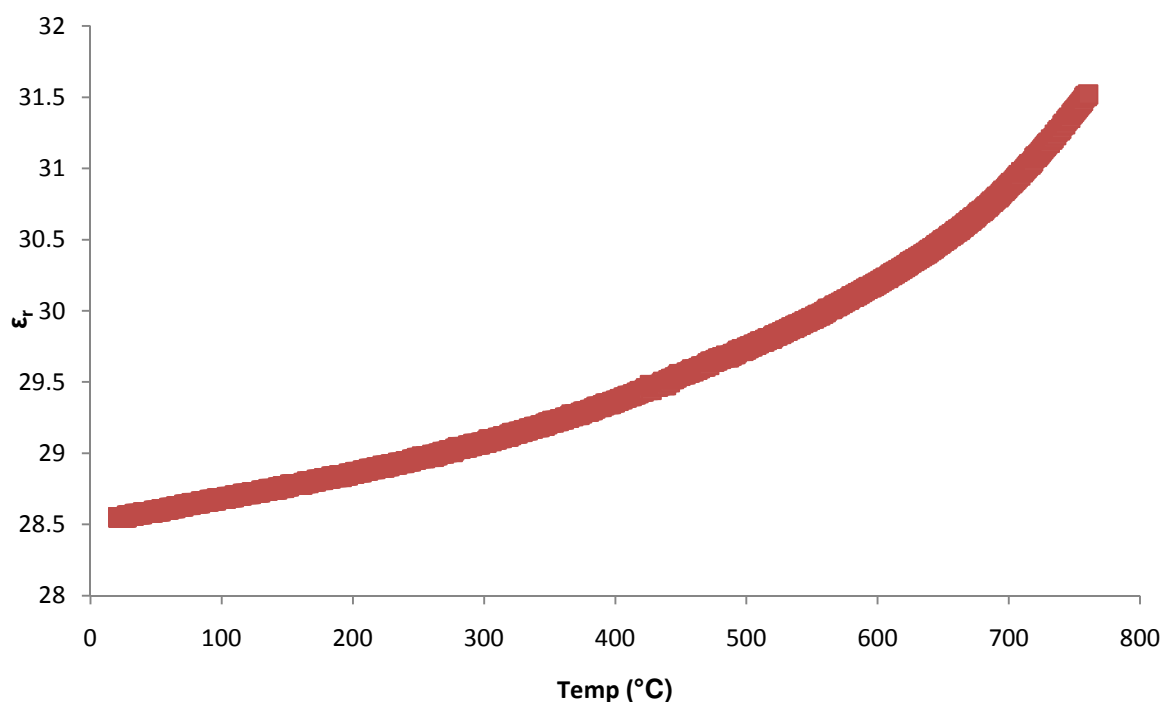
Figure 3.60: Plot of ε_r *vs.* Temperature for $BaSr_2LaNb_3O_{12}$ at 1 MHz.

It can be seen clearly in ***figure 3.59*** that $Ba_2SrLaNb_3O_{12}$ displays an abrupt change in the magnitude of permittivity at 1 MHz at ~490 °C. It was found from variable temperature NPD data that as the temperature is increased the tilt angle of the NbO_6 octahedra decreases, but the octahedra are still tilted up to 900 °C. Therefore as no tilt transition occurred below 900°C, the change in permittivity at ~490 °C does not correlate to the temperature at which a tilt transition occurs and at this stage it is unknown what structural phenomenon this temperature correlates to.

No significant peak, change in magnitude or inflection in permittivity at 1 MHz occurs at any temperature for $BaSr_2LaNb_3O_{12}$, seen in ***figure 3.60***. The reason for this lack of electrical response is unknown but the refinement data suggests something more complicated is occurring with this composition that warrants further investigation, possibly over a larger temperature range.

The study published for $Ba_3LaNb_3O_{12}$ concluded that the peak in permittivity at 1 MHz correlated to a tilt transition, however overall, the LCR data for the other members of the series and the variable temperature NPD data imply the opposite, and it is as yet unknown what the peaks in permittivity correlate to. Refinement data

for $Ba_3LaNb_3O_{12}$ showed that, below 192 °C the tilt angle decreased and above 192 °C there is no difference between space group R-3 and the model and R-3m and the model, and therefore the structure is untilted. However it is not known if the tilt angle is 0° at the maximum of the peak in permittivity, therefore it is feasible to suggest that at the relevant temperature of the peak in permittivity the structure may still be tilted, alternately as this structure has the smallest RT tilt angle of the series it is also possible that the tilt transition does occur at the same temperature as the peak in permittivity because less significant structural rearrangement is required.

Therefore it can be concluded that:

- As soon as heating begins for all compositions, the tilt angle begins to decrease in magnitude.

- For the compositions $Ba_3LaNb_3O_{12}$ and $Sr_3LaNb_3O_{12}$ the process of the tilt transition is less complex as there are only two A-cations which can comfortably co-habit.

- In $Ba_3LaNb_3O_{12}$ the composition has a smaller RT tilt angle, this in turn means the untilted structure can be achieved at a lower temperature.

- In $Sr_3LaNb_3O_{12}$ the structure has further to move to become untilted. It is therefore not surprising that will all occur at a higher temperature.

- Only $Ba_3LaNb_3O_{12}$ manages to achieve an untilted structure below 900°C, all other compositions are still tilted at this temperature. Although, the peak in permittivity in LCR data at 1MHz correlates to a tilt transition for the $Ba_3LaNb_3O_{12}$ structure, this is not the case for the other ceramics. It is as yet unknown the structural relevance of the temperature of the peak in permittivity in LCR data at 1MHz for the other members of the series.

- $BaSr_2LaNb_3O_{12}$ is significantly more complex than the other members of the series. As the dominant divalent cation is much smaller and a reasonable amount of Ba^{2+} is present in the composition, all the A-site cations display a preference for different coordination environments. Therefore there are competing interactions taking place within the structure which inhibit the process of the tilt transition.

132

- For all samples, the LCR data provide a more reasonable reflection of the electrical behaviour as Q and TCF values should be interpreted with caution.

3.5 References

1. Trolliard, G., Teneze, N., Boullay, P., and Mercurio, D., *Journal of Solid State Chemistry*. **177,** 4-5 1188-1196 (2004)

2. Sirotinkin, V. P., Averkova, O. E., Starikov, A. M., and Evdokimov, A. A., *Zhurnal Neorganicheskoi Khimii*. **32,** 1 262-263 (1987)

3. Von Rother, H. J., Kemmler-Sack, S., Treiber, U., and Cyris, W. R., *Z. Anorg, Allg. Chem. .* **466,** 131-138 (1980)

4. Rawal, R., Feteira, A., Hyatt, N. C., Sinclair, D., C., Sarma, K., and Alford, N. M., *Journal of the American Ceramic Society*. **89,** 1 332-335 (2006)

5. Fang, L., Zhang, H., Yu, Q., Su, H. P., Wu, B. L., and Cui, X. M., *Journal of the American Ceramic Society*. **92,** 2 556-558 (2009)

6. Rawal, R., McQueen, A. J., Gillie, L. J., Hyatt, N. C., McCabe, E. E., Samara, K., Alford, N. M., Feteira, A., Reaney, I. M., and Sinclair, D. C., *Applied Physics Letters*. **94,** 19 192904-192904-3 (2009)

7. Hu, C., Fang, L., Su, H., Liu, L., and Wu, B., *Journal of Alloys and Compounds*. **487,** 1-2 504-506 (2009)

8. Rawal, R., McQueen, A., J. , Gillie, L., J., Hyatt, N., C., McCabe, E., E., Samara, K., Alford, N. M., Feteira, A., Reaney, I., M., and Sinclair, D., C. **94,** 19 192904 (2009)

9. Larson, A. C. and Von Dreele, R. B., General Structure Analysis System (GSAS), Los Alamos National Laboratory Report (1994)

10. McQueen, A. J. and Sinclair, D. C., Unpublished Work, University of Sheffield, (2009)

11. Reaney, I. M., Colla, E. L., and Setter, N., *Japanese Journal of Applied Physics Part 1-Regular Papers Short Notes & Review Papers*. **33,** 7A 3984-3990 (1994)

12. Rawal, R., *Synthesis and characterisation of B-site deficient hexagonal perovskites*, Thesis, The University of Sheffield, (Department of Engineering Materials October 2003 – June 2007)

13. Vanderah, T. A., Personal Communication.

14. Lufaso, M. W., *Chemistry of Materials*. **16,** 11 2148-2156 (2004)

15. Harrop, P. J., *Journal of Materials Science*. **4,** 4 370-374 (1969)

Chapter 4

Synthesis and Characterisation of B-cation Deficient Series
$Ba_{3-x}Sr_xLaNb_{3-y}Ta_yO_{12}$ (x = 0 - 3 and y = 1 - 2)
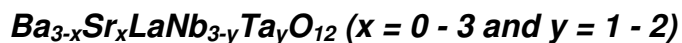
4.1 Introduction

$Ba_3LaTa_3O_{12}$[1, 2] and $Sr_3LaTa_3O_{12}$[3-5] have previously been reported, and their dielectric properties examined to assess whether the Ta-rich phases have superior dielectric properties to those exhibited by their Nb-analogues. Since Nb^{5+} and Ta^{5+} are the same size and charge this is a valid substitution and it has been quoted in the literature that Ta^{5+} is known to improve Q values[1]. The dielectric properties of the two phases are listed alongside the dielectric properties for the Nb-analogues investigated in **Chapter 3**, in **table 4.0**.

Compositions	ε_r	Q.f. (GHz)	TCF (ppm / °C)
$Ba_3LaNb_3O_{12}$	44	9047	-100
$Sr_3LaNb_3O_{12}$	36	23532	-5
$Ba_3LaTa_3O_{12}$ [1, 2]	37	21965	-50
$Sr_3LaTa_3O_{12}$ [3-5]	30	16050	-43

Table 4.00: Microwave dielectric properties of $Ba_3LaTa_3O_{12}$, $Sr_3LaTa_3O_{12}$ and their Nb-analogues.

It can be seen from **table 4.00** that the substitution of Nb^{5+} by Ta^{5+} in the Ba-rich phase results in a marked improvement in the Q and TCF values, but a slight reduction in ε_r. Conversely the Sr-rich phase demonstrates a reduction in all of the dielectric properties when Ta^{5+} is completely substituted for Nb^{5+}. In **Chapter 3** it was found that ε_r and TCF can be effectively tuned by the incorporation of Ba^{2+}, Sr^{2+} and La^{3+} on the A-site. In $Ba_{3-x}Sr_xLaNb_{3-y}Ta_yO_{12}$ therefore it is proposed that by the introduction of Ta^{5+} on the B-site with Nb^{5+}, the dielectric properties may be effectively optimised.

Currently only one example of a mixed B-site Nb^{5+} / Ta^{5+}, n = 4 B-cation deficient perovskite exists,[6] although the phase is not the "shifted" but the "twinned" variant.

This is therefore the first study focussing on n = 4 layered B-cation deficient "shifted" perovskites possessing up to three A-cations and a mixed Nb^{5+} / Ta^{5+} B-site.

4.2 Synthesis

All compositions were synthesised *via* the standard ceramic route. Stoichiometric amounts of dried high purity reagents, $BaCO_3$, $SrCO_3$, La_2O_3, Nb_2O_5 and Ta_2O_5 were hand ground using a pestle and mortar. The materials were then heated to reaction temperature, $1450°C$, at a rate of $300°C$ per hour, for in excess of 120 hours, with intermediate grindings every 48 hours. The materials were allowed to cool to room temperature.

4.3 Structural Characterisation of $Ba_{3-x}Sr_xLaNb_2TaO_{12}$ Series

4.3.1 X-ray Powder Diffraction (XRPD) and Neutron Powder Diffraction (NPD)

XRPD data were collected under the same conditions as described in *section 3.3.1*. Neutron powder diffraction data were collected on the GEM and POLARIS instruments at ISIS, Oxford, UK, and on the D2B diffractometer at the Institut Laue-Langevin, Grenoble, France. Details of the data collection source for each sample are listed in *table 4.01*. Data were refined using the Rietveld method with the GSAS suite of programs.[7]

Joint refinements of XRPD and NPD data against models were required, as the neutrons allowed discrimination between Ba^{2+} and La^{3+}, and the X-rays allowed the location of Sr^{2+} to be determined, and to distinguish between Nb^{5+} and Ta^{5+}. When three A-cations were present the same approach was used as in *Chapter 3*. An XRPD refinement against a model was performed to assign the Sr^{2+} occupancy (Ba^{2+} and La^{3+} were initially entered as one element), then a joint refinement of XRPD and NPD data against a model was performed, with the Sr^{2+} occupancies fixed from the XRPD refinement, however in this case the XRPD histograms were also inserted (method (iv)).

Composition	NPD Collection Source
$Ba_3LaNb_2TaO_{12}$	D2B
$Ba_2SrLaNb_2TaO_{12}$	D2B
$BaSr_2LaNb_2TaO_{12}$	GEM
$Sr_3LaNb_2TaO_{12}$	GEM
$Ba_3LaNbTa_2O_{12}$	POLARIS
$Ba_2SrLaNbTa_2O_{12}$	GEM
$BaSr_2LaNbTa_2O_{12}$	D2B
$Sr_3LaNbTa_2O_{12}$	GEM

Table 4.01: List of NPD collection sources for the $Ba_{3-x}Sr_xLaNb_{3-y}Ta_yO_{12}$ series.

4.3.1.1 $Ba_3LaNb_2TaO_{12}$

4.3.1.1.1 Joint XRPD and NPD refinement

The refinement results are summarised below in **figures 4.00** and **4.01,** and **tables 4.02** and **4.03** Refinement statistics and lattice parameters are given in **figure 4.00**.

Space group R-3

$\chi^2 = 6.212$; $R_{wp} = 6.28\%$; $R_p = 4.89\%$

$a = 5.7437(1)$ Å; $c = 28.1290(3)$ Å

$\alpha = \beta = 90°$; $\gamma = 120°$

Volume = 803.560(2) Å^3
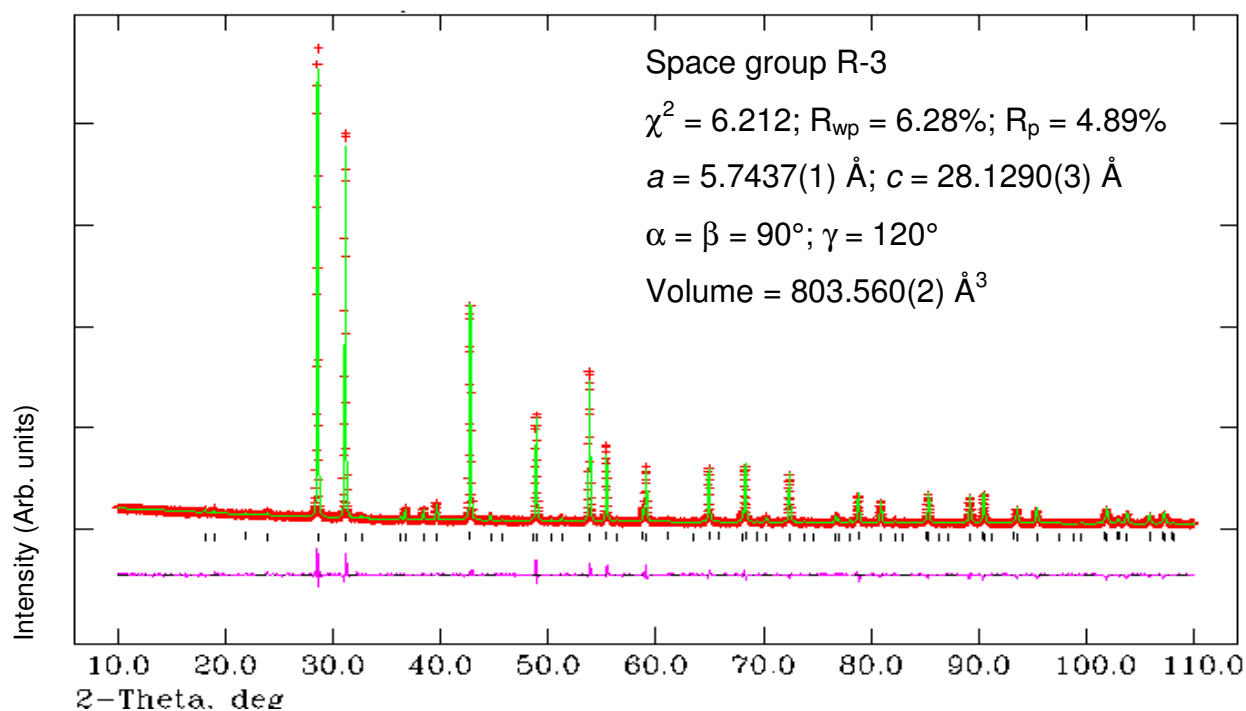
Figure 4.00: Calculated (green), experimental (red) and difference (pink) profile plot for $Ba_3LaNb_2TaO_{12}$ XRPD data. Tick marks represent Bragg peak positions.
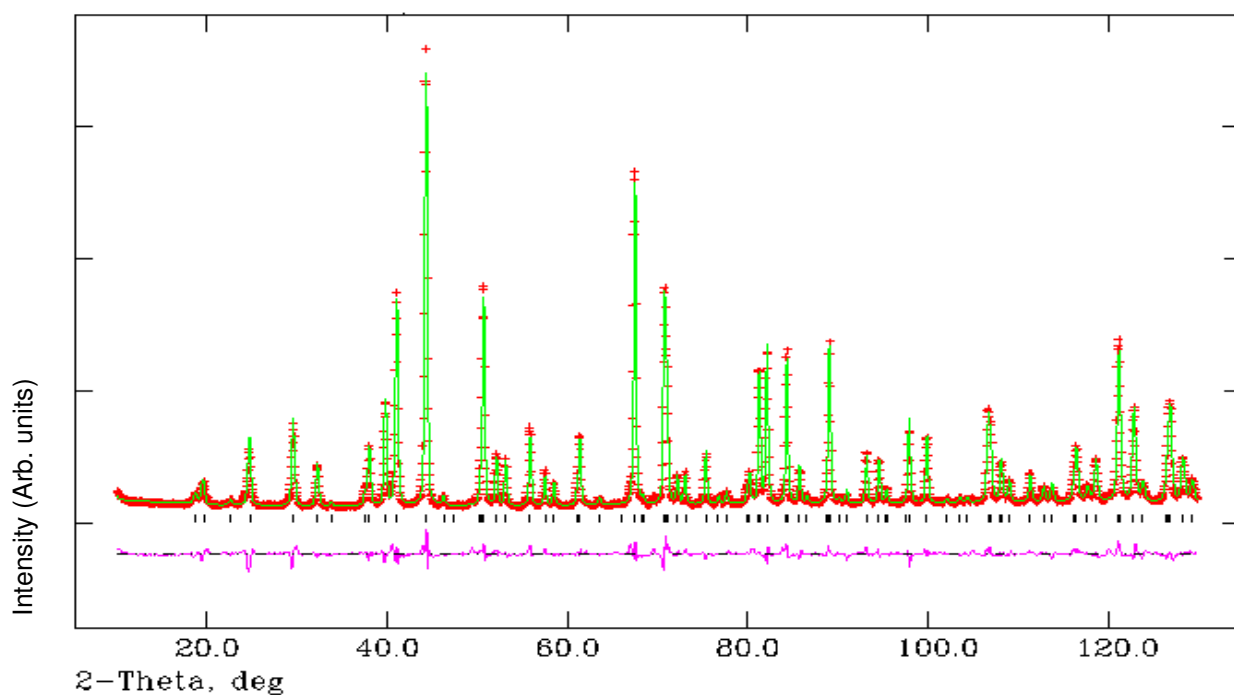
Figure 4.01: Calculated (green), experimental (red) and difference (pink) profile plot for $Ba_3LaNb_2TaO_{12}$ NPD RT data on D2B. Tick marks represent Bragg peak positions.

Atom	Wyckoff	X	y	z	$U_{iso}*100$ $(Å^2)$	Frac.
Ba/La1	*6c*	0	0	0.2868(1)	0.62(5)	0.50/0.50
Ba/La2	*6c*	0	0	0.1365(1)	0.32(6)	1.00/0.00
Nb/Ta1	*6c*	0	0	0.4218(1)	0.05(4)	0.79(1)/0.21(1)
Nb/Ta2	*3a*	0	0	0	0.87(9)	0.42(2)/0.58(2)
O1	*18f*	0.1853(6)	0.8537(6)	0.6284(1)	2.10(4)	1
O2	*18f*	0.1909(5)	0.8571(4)	0.4519(1)	0.72(3)	1

Table 4.02: Refinement results for $Ba_3LaNb_2TaO_{12}$ (XRPD and NPD RT data)

Bond lengths (Å)			Bond Angles (°)		
Ba/La(1)-O(1) =	2.904(3)	(x3)	O(1)-Nb/Ta(1)-O(1) =	82.4(1)	(x3)
Ba/La(1)-O(1) =	2.770(3)	(x3)	O(1)-Nb/Ta(1)-O(2) =	166.5(1)	(x3)
Ba/La(1)-O(1) =	2.993(2)	(x3)	O(1)-Nb/Ta(1)-O(2) =	87.0(1)	(x3)
Ba/La(1)-O(2) =	2.620(3)	(x3)	O(1)-Nb/Ta(1)-O(2) =	88.0(1)	(x3)
			O(2)-Nb/Ta(1)-O(2) =	101.0(1)	(x3)
Ba/La(2)-O(1) =	3.228(3)	(x3)			
Ba/La(2)-O(2) =	2.780(3)	(x3)	O(1)-Nb/Ta(2)-O(1) =	93.4(1)	(x6)
Ba/La(2)-O(2) =	3.051(2)	(x3)	O(1)-Nb/Ta(2)-O(1) =	86.6(1)	(x6)
Ba/La(2)-O(2) =	2.758(3)	(x3)	O(1)-Nb/Ta(2)-O(1) =	180.0	(x3)
Nb/Ta(1)-O(1) =	2.173(3)	(x3)			
Nb/Ta(1)-O(2) =	1.870(2)	(x3)			
Nb/Ta(2)-O(1) =	1.987(3)	(x6)			

Table 4.03: Bond lengths and angles from refinement results for $Ba_3LaNb_2TaO_{12}$
(XRPD and NPD RT data).

The joint XRPD and NPD Rietveld refinement proceeded smoothly showing a distinct preference for the space group R-3. Details of the refinement can be found in ***figures 4.00*** and ***4.01*** and ***tables 4.02*** and ***4.03***. $Ba_3LaNb_2TaO_{12}$ has lattice parameters a = 5.7437(1) Å and c = 28.1290(3) Å, and the refinement converged with associated statistics χ^2 = 6.212, R_{wp} = 6.28% and R_p = 4.89%. The resultant crystal structure is depicted in ***figure 4.02***.
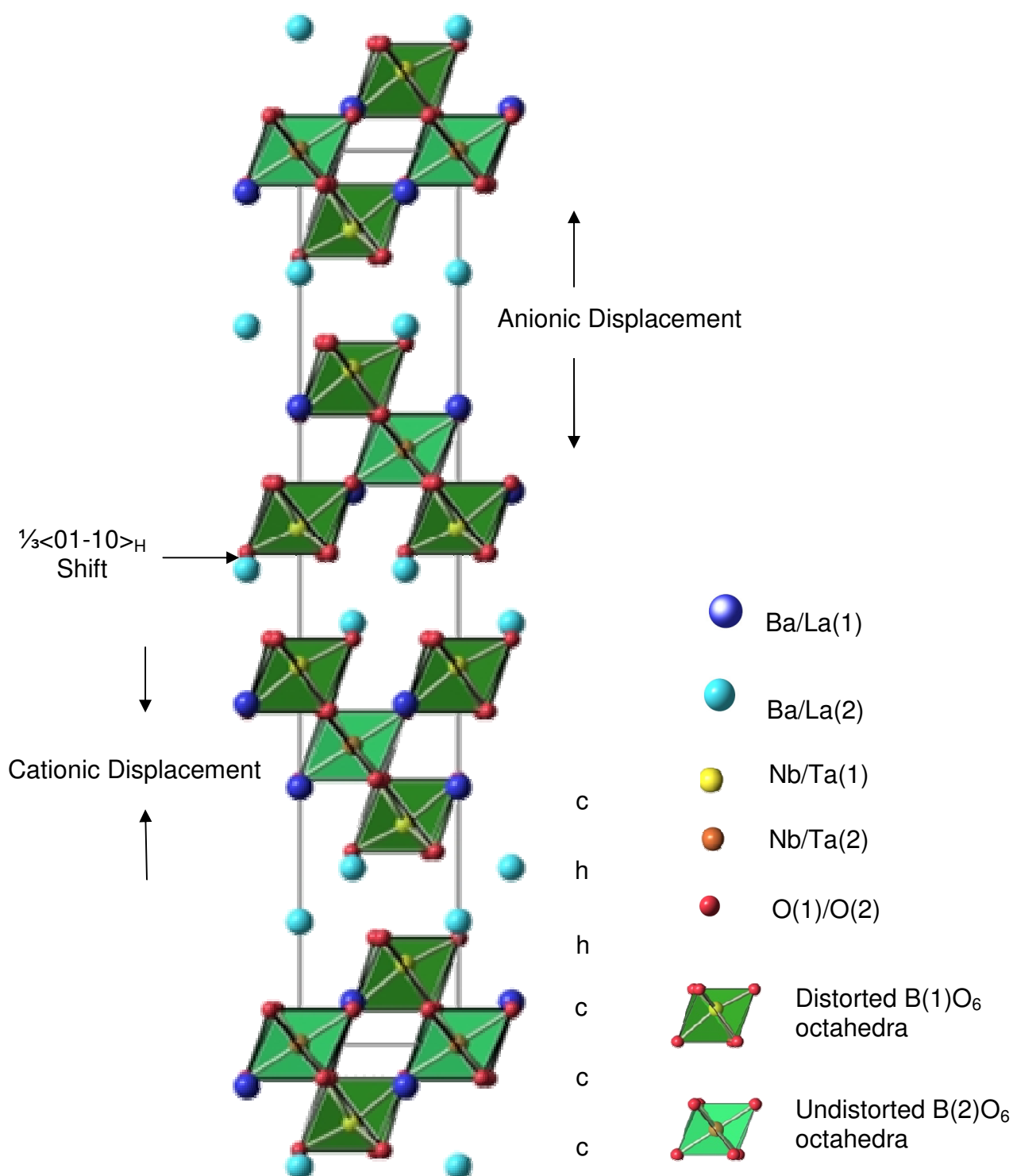
Figure 4.02: Structure of $Ba_3LaNb_2TaO_{12}$ viewed along the *x*-axis.

There are two crystallographically distinct B-site environments in the 12R structure. B(1) is adjacent to the "shifted" region within a distorted octahedron. The B-cations are displaced towards one triangular face of the octahedron, pointing towards the "shifted" region. B(2) is located in the middle of the perovskite block composed of three corner-sharing octahedra. The two different B-cation octahedra can be seen in *figures 4.03* and *4.04* respectively. The Nb^{5+} cations display a preference for B(1) with an occupancy of 79%. There is then an approximate 2:3 distribution of Nb^{5+} / Ta^{5+} across B(2) (42% and 58% respectively) within the undistorted octahedra. It is interesting that when two pentavalent B-ions are present, the Nb^{5+} cations display a preference to inhabit the distorted environment of B(1). It would be assumed that since both Nb^{5+} and Ta^{5+} possess the same charge and are the same size (0.64 Å), that no preference would be displayed by either cation. Therefore, something more unusual is occurring when both Nb^{5+} and Ta^{5+} are present on the B-site together, with Nb^{5+} exhibiting a marked preference for the distorted environment.

Distortion values were calculated for the two types of BO_6 octahedra. The Δd value for the $B(1)O_6$ octahedra is 56.17, with three bonds of 2.173(3) Å and three bonds of 1.870(2) Å, and the the Δd value for $B(2)O_6$ is 0 as the octahedra are undistorted. BO_6 octahedra are antiphase tilted about the *z*-axis by an angle of 4.5°, *figure 4.05*.

The A-sites within the structure are completely ordered with A(2) being composed of 100% Ba^{2+} and a 50:50 split of Ba^{2+} and La^{3+} across A(1).

The cubo-octahedral environment of the A-cations is shown in *figures 4.06* and *4.07*. There are 3 x A(1)-O bonds of 2.620(2) Å and 3 x A(1)-O bonds of 2.904(3) Å pointing towards neighbouring octahedral layers of B-cations (along the direction of the *z*-axis) and 3 x A(1)-O bonds of 2.770(3) Å and 3 x A(1)-O bonds of 2.993(3) Å parallel to the *xy*-plane pointing towards BO_6 units in the same octahedral layer.

For the A(2) cations there are 3 x A(2)-O) bonds of 2.758(3) Å pointing into vacant shifted region and 3 x A(2-)O bonds of 3.228(3) Å pointing towards triple layers of B-site cations and 3 x A(2)-O bonds of 3.051(2) Å and 3 x A(2)-O bonds of 2.780(3) Å bonds parallel to *xy*-plane pointing towards NbO_6 units in the same octahedral layer. The A(2) cations are displaced into shifted region and the degree of shift for both A-cations can be seen in *figure 4.10.*

Similar to the trend observed for the Nb-analogues, the AO_{12} polyhedra reveal a more distorted environment in the "shifted" region, A(2) than in the perovskite block, A(1) with corresponding distortion values Δd = 43.89 and Δd = 24.95. This can be seen more clearly in **figures 4.08** and **4.09** where the distorted A-O lattices are projected along the z-axis.

Bond valence sums (BVS) were performed for the structure (refer to **section 1.1.1, equation 1.2** and **1.3**), the values are listed in **table 4.04**. Overall the BVS calculations performed suggest the refinement is reasonable, however the values are not in such good agreement for the B-sites possibly due to the structural complexity associated with the site.

Cation	Theoretical BVS	Calculated BVS	Status
A(1)	2.50	2.63	Over-bonded
A(2)	2.23	2.00	Under-bonded
B(1)	5.00	5.19	Over-bonded
B(2)	5.00	5.95	Over-bonded

Table 4.04: BVS calculation results for $Ba_3LaNb_2TaO_{12}$

3 x B(1)-O(2) = 1.870(2) Å

3 x B(1)-O(1) = 2.173(3) Å

6 x B(2)-O(1) = 1.987(3) Å
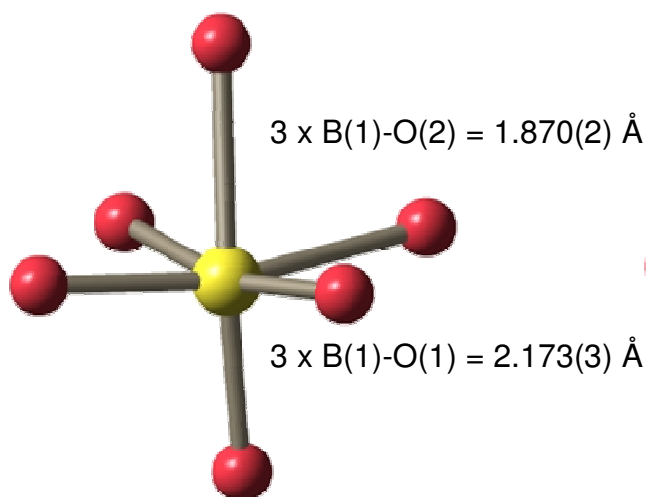
Figure 4.03: Distorted B(1)O$_6$ octahedron adjacent to the "shifted" region (red spheres O^{2-}, yellow sphere B(1) cation). Associated bond lengths labelled.
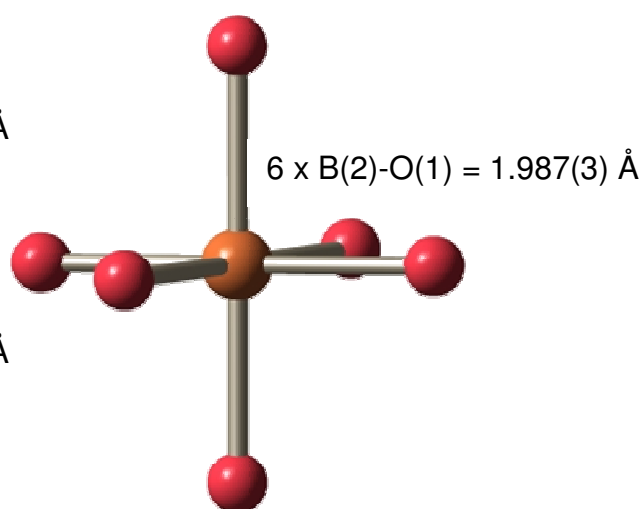
Figure 4.04: Undistorted B(2)O$_6$ octahedron in the centre of the perovskite block (red spheres O^{2-}, orange sphere B(2) cation). Associated bond lengths labelled.
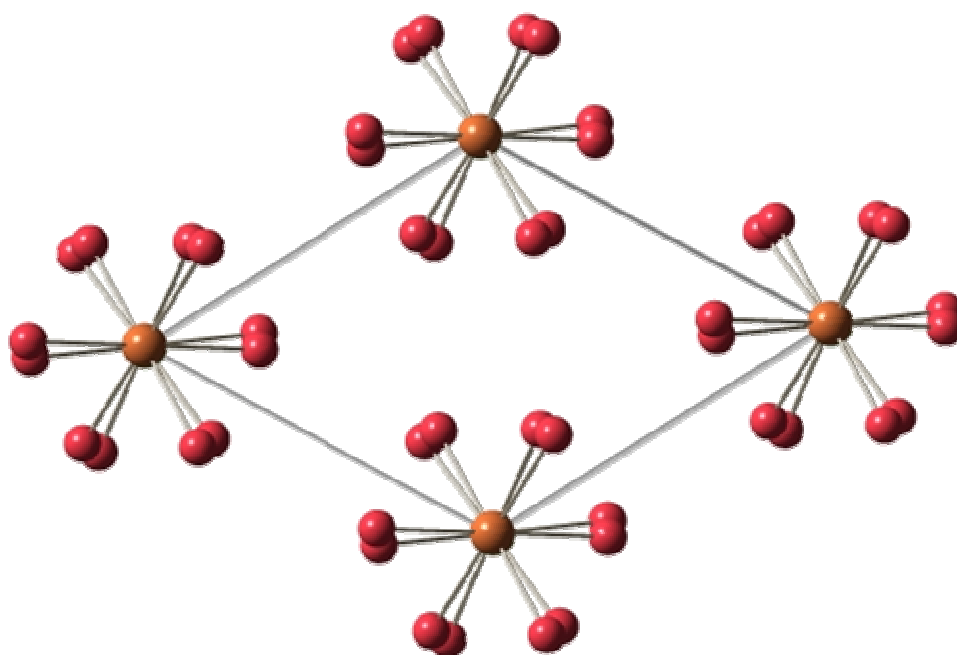
Figure 4.05: View of Ba$_3$LaNb$_2$TaO$_{12}$ structure along the z-axis showing tilting of the octahedra, tilt angle 4.5° [a$^-$ a$^-$ a$^-$] (octahedra omitted for clarity). (Red spheres O^{2-}, Orange spheres Nb^{5+}/Ta^{5+}).
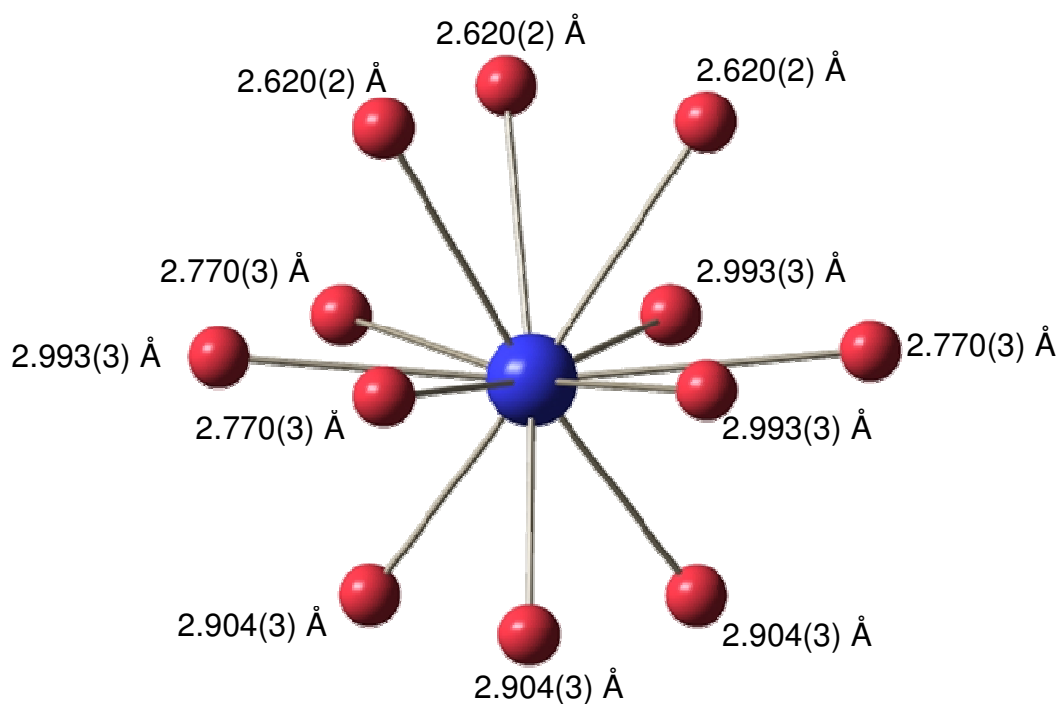
Figure 4.06: Cubo-octahedral environment of A(1) cations located within the triple layer of BO_6 octahedra with Ba^{2+} / La^{3+} distribution of 0.50 / 0.50 (red spheres O^{2-}, blue sphere Ba^{2+} / La^{3+}). Bond lengths are labelled.
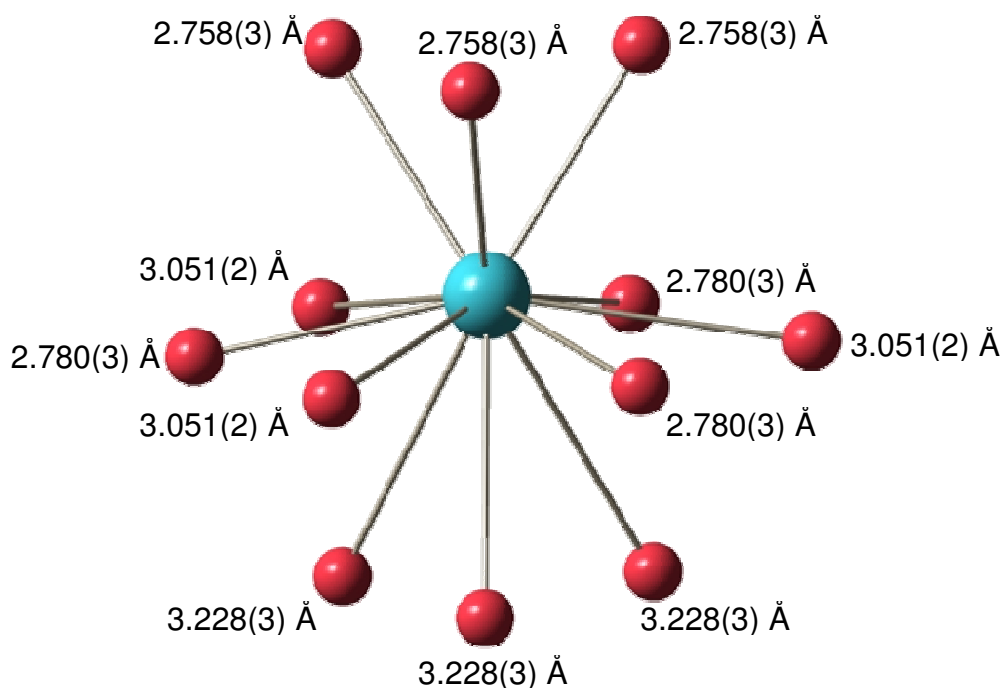
Figure 4.07: Cubo-octahedral environment of A(2) cations located in "shifted" region with a Ba^{2+} / La^{3+} distribution of 1.0 / 0.0 (red spheres O^{2-}, blue sphere Ba^{2+}). Bond lengths are labelled.
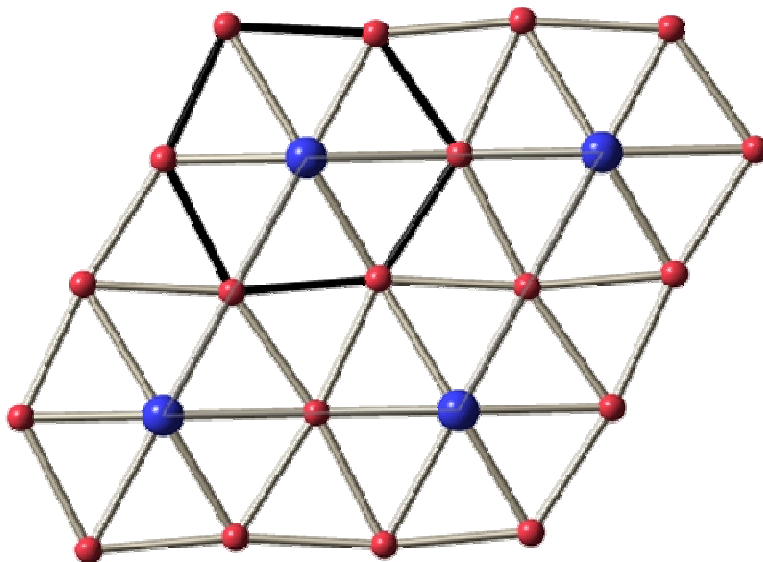
Figure 4.08: View of the distorted A(1)-O lattice along the *z*-axis, O^{2-} ions not parallel to the *xy*-plane are omitted for clarity. Black outline shows a "slice" through the AO_{12} polyhedra, 3 x A(1)-O bonds of 2.620(20 Å and 3 x A(1)-O bonds of 2.770(3) Å parallel to the *xy*-plane. A-cations are on the corners of the unit cell, outlined in grey. (Red spheres O^{2-}, blue spheres Ba^{2+} / La^{3+}).
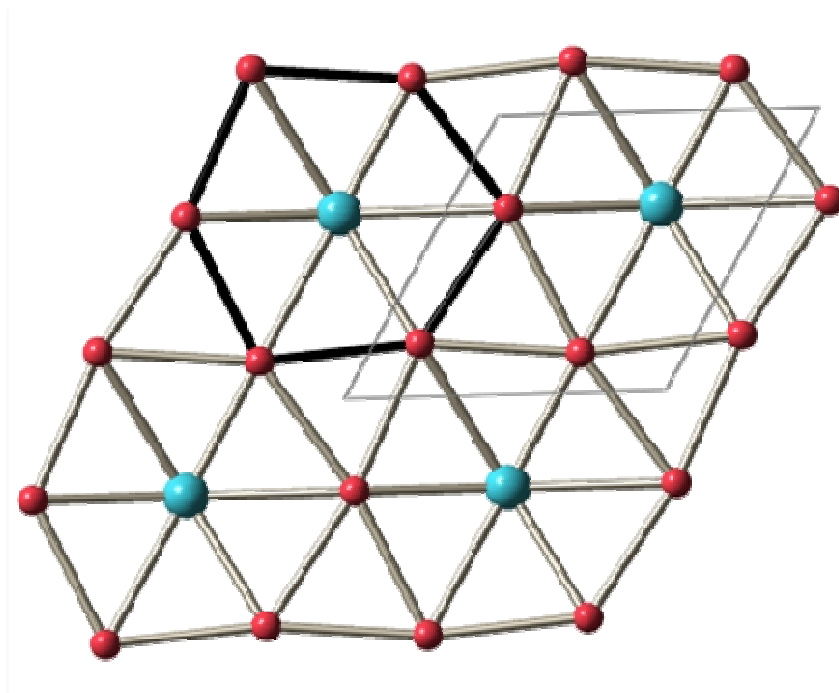
Figure 4.09: View of the distorted A(2)-O lattice along the *z*-axis, O^{2-} ions not parallel to the *xy*-plane are omitted for clarity. Black outline shows a "slice" through the AO_{12} polyhedra, 3 x A(1)-O bonds of 3.051(2) Å and 3 x A(1)-O bonds of 2.780(3) Å parallel to the *xy*-plane. Unit cell is outlined in grey. (Red spheres O^{2-}, blue spheres Ba^{2+} / La^{3+}).
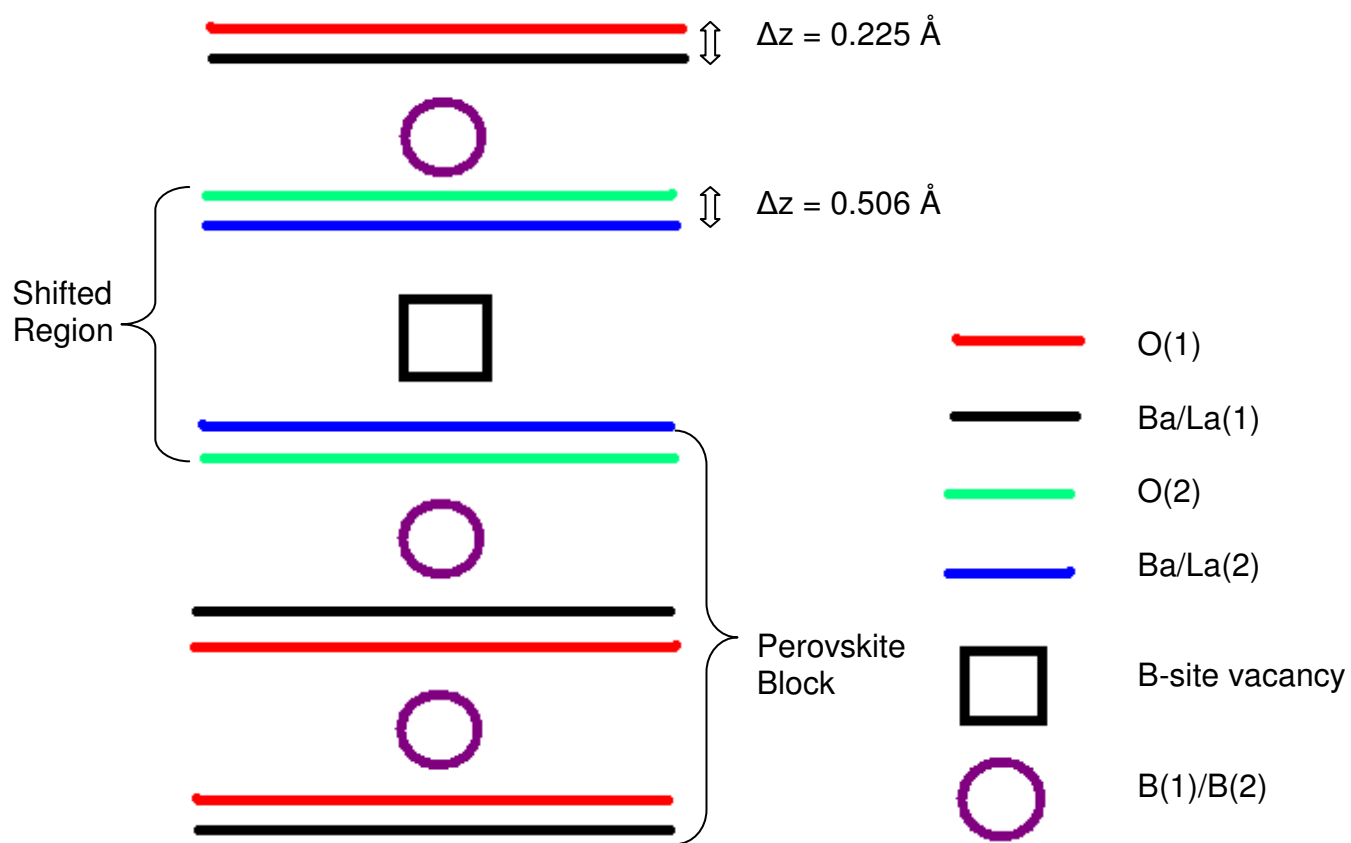
Figure 4.10: A schematic diagram showing A-O displacement along the *z*-axis (Δz) for $Ba_3LaNb_2TaO_{12}$ (not to scale).

The variance of $Ba_3LaNb_2TaO_{12}$ was determined to be 14.89×10^{-4}, this is depicted in *figure 4.11*. (For clarity, Δ values are quoted in figures omitting the factor 10^{-4}).

$\Delta = 14.89$

(a)   **(b)**
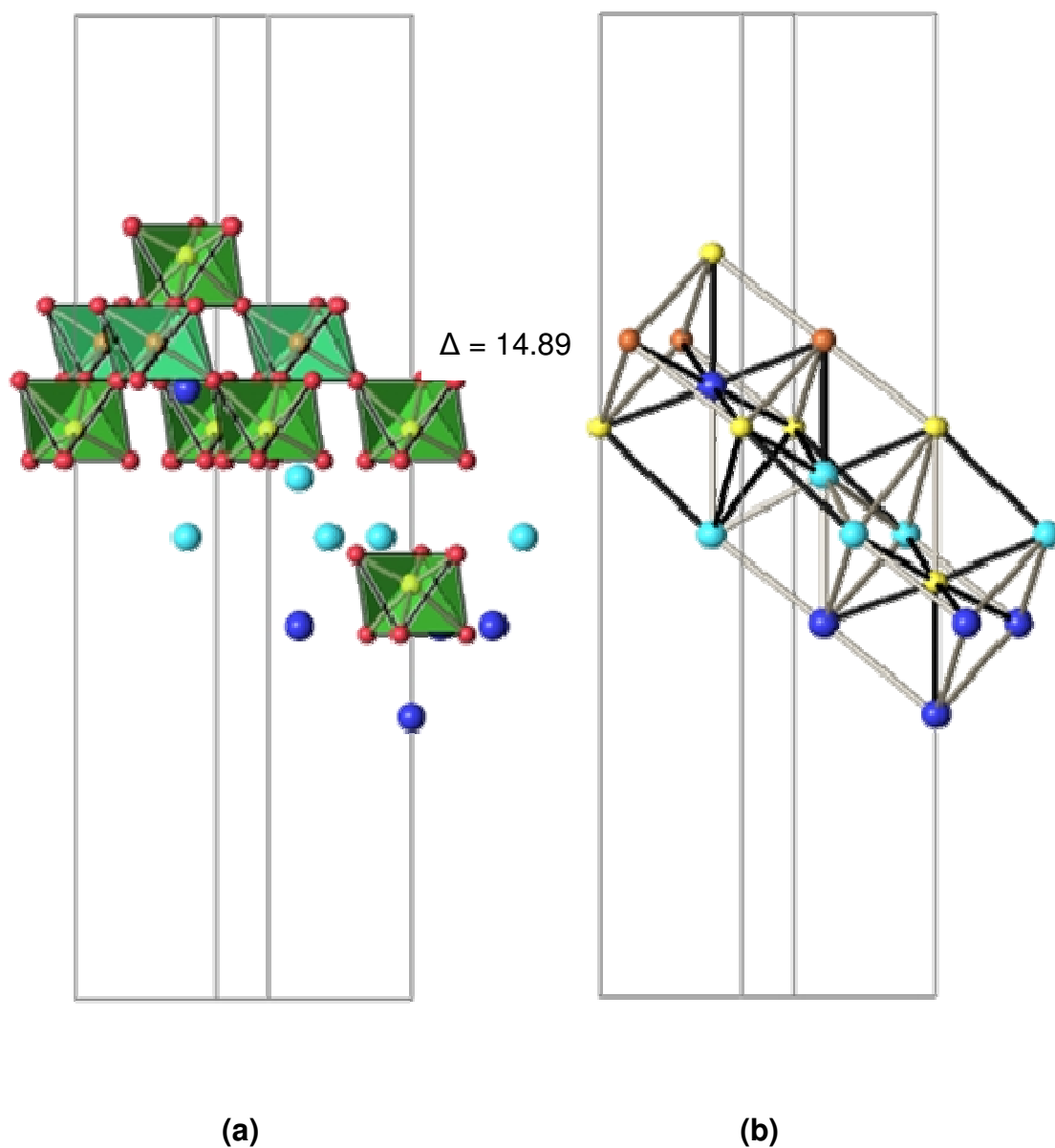
Figure 4.11: ***(a)*** A- and B-cations involved in the three *bcc* unit cells (O^{2-} ions shown not involved in the *bcc* cation sublattice) ***(b)*** Structural view of the *bcc* lattice along the *xy*-direction, for $Ba_3LaNb_2TaO_{12}$. Black bonds highlight the A-B distances (bond lengths) selected for calculation of the variance, Δ. (Red spheres O^{2-}, blue spheres Ba^{2+} / La^{3+}, yellow / orange spheres Nb^{5+}/Ta^{5+})

4.3.1.2 Ba₂SrLaNb₂TaO₁₂

4.3.1.2.1 XRPD Refinement

The refinement results are summarised below in **figure 4.12** and **table 4.05.** Refinement statistics and lattice parameters are given in **figure 4.12**.

Space group R-3

$\chi^2 = 2.224$; $R_{wp} = 13.8\%$; $R_p = 9.49\%$

$a = 5.7197(1)$ Å; $c = 27.9626(5)$ Å

$\alpha = \beta = 90°$; $\gamma = 120°$

Volume = 792.25(2) Å³
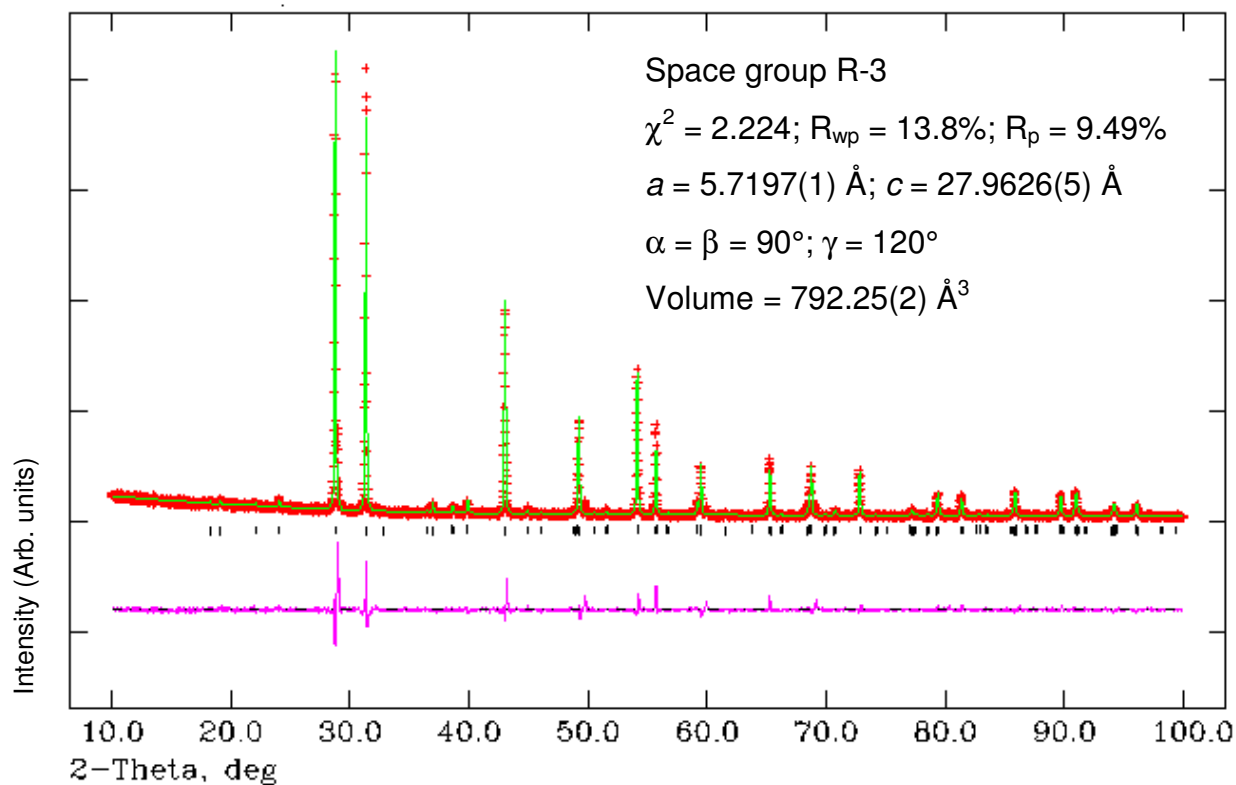
Figure 4.12 Calculated (green), experimental (red) and difference (pink) profile plot for Ba₂SrLaNb₂TaO₁₂ XRPD data. Tick marks represent Bragg peak positions.

Atom	Wyckoff	x	y	z	$U_{iso}*100$ (Å²)	Frac.
Ba/Sr1	6c	0	0	0.2869(2)	1.92(3)	0.64(3)*/0.36(3)
Ba/Sr2	6c	0	0	0.1360(2)	1.19(2)	0.86(3)*/0.14(3)
Nb/Ta1	6c	0	0	0.4222(2)	1.47(3)	0.72(2)/0.28(2)**
Nb/Ta2	3a	0	0	0	1.02(3)	0.57(3)/0.43(3)**
O1	18f	0.126(7)	0.794(7)	0.6259(9)	2.1(8)	1
O2	18f	0.201(1)	0.815(1)	0.4520(7)	4.7(8)	1

*Ba²⁺ and La³⁺ entered as one element, Ba²⁺. **Due to rounding up the overall B-site occupancies are slightly over the stated composition, but are within experimental error.

Table 4.05: Refinement results for Ba₂SrLaNb₂TaO₁₂ (XRPD RT data)

4.3.1.2.2 Method (iv)

The refinement results are summarised below in **figures 4.13** and **4.14** and **tables 4.06** and **4.07**. Refinement statistics and lattice parameters are given in **figure 4.13**.

Space group R-3

$\chi^2 = 4.116$; $R_{wp} = 12.19\%$; $R_p = 10.10\%$

$a = 5.7154(1)$ Å; $c = 27.9493(5)$ Å

$\alpha = \beta = 90°$; $\gamma = 120°$

Volume $= 790.66(2)$ Å^3
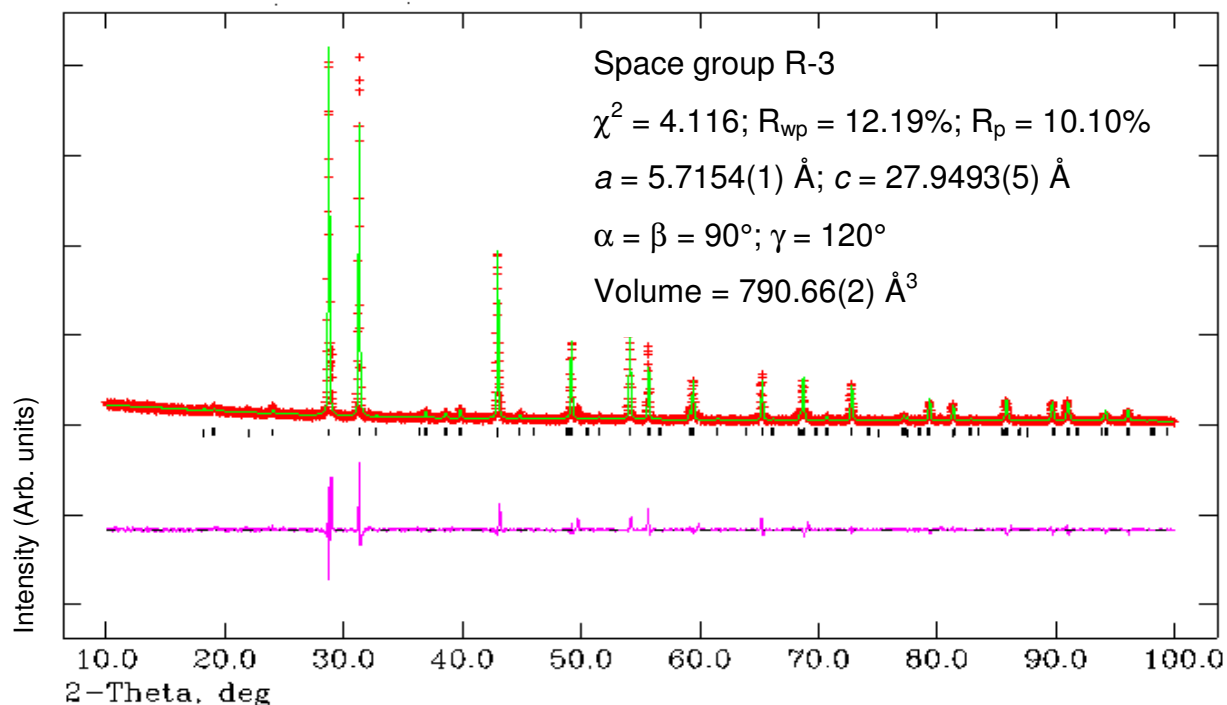
Figure 4.13: Calculated (green), experimental (red) and difference (pink) profile plot for Ba$_2$SrLaNb$_2$TaO$_{12}$ XRPD data. Tick marks represent Bragg peak positions.
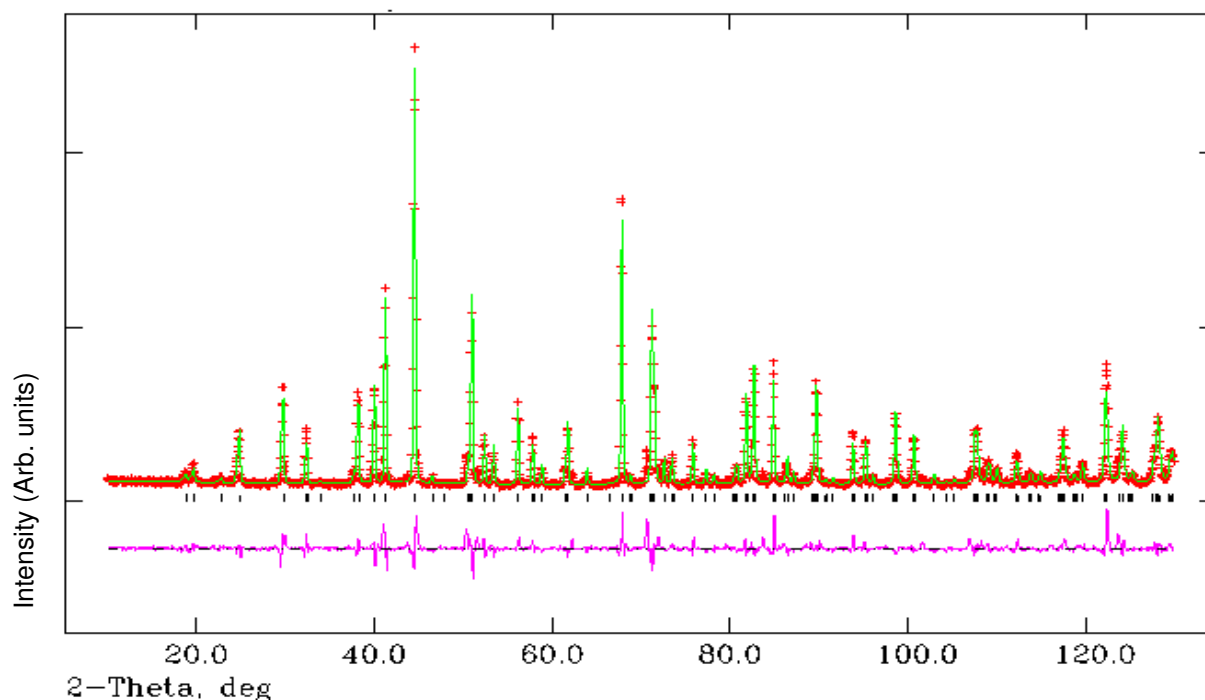
Figure 4.14: Calculated (green), experimental (red) and difference (pink) profile plot for Ba$_2$SrLaNb$_2$TaO$_{12}$ NPD data collected on D2B. Tick marks represent Bragg peak positions.

149

Atom	Wyckoff	x	y	z	$U_{iso}*100$ (Å^2)	Frac.
Ba/Sr/La1	6c	0	0	0.2860(1)	0.60(1)	0.25(2)/0.36*/0.40(2)**
Ba/Sr/La2	6c	0	0	0.1375(2)	1.26(1)	0.76(2)/0.14*/0.11(2)**
Nb/Ta1	6c	0	0	0.4212(1)	0.18(7)	0.80(2)/0.20(2)
Nb/Ta2	3a	0	0	0	2.02(2)	0.40(3)/0.60(3)
O1	18f	0.2020(9)	0.8715(9)	0.6290(1)	1.96(1)	1
O2	18f	0.1976(8)	0.8627(8)	0.4523(1)	1.03(7)	1

*Sr^{2+} occupancies fixed from XRPD refinement. **Composition slightly over/under that stated and overall A-site occupancy slightly over 100% due to rounding up.

Table 4.06: Refinement results for $Ba_2SrLaNb_2TaO_{12}$ (XRPD and NPD RT data)

Bond lengths (Å)		Bond Angles (°)	
Ba/Sr/La(1)-O(1) =	2.893(5) (x3)	O(1)-Nb/Ta(1)-O(1) = 82.5(2) (x3)	
Ba/Sr/La(1)-O(1) =	3.080(4) (x3)	O(1)-Nb/Ta(1)-O(2) = 167.0(2) (x3)	
Ba/Sr/La(1)-O(1) =	2.662(4) (x3)	O(1)-Nb/Ta(1)-O(2) = 88.6(2) (x3)	
Ba/Sr/La(1)-O(2) =	2.593(4) (x3)	O(1)-Nb/Ta(1)-O(2) = 87.0(2) (x3)	
		O(2)-Nb/Ta(1)-O(2) = 100.4(1) (x3)	
Ba/Sr/La(2)-O(1) =	3.255(5) (x3)		
Ba/Sr/La(2)-O(2) =	3.074(4) (x3)	O(1)-Nb/Ta(2)-O(1) = 94.4(2) (x6)	
Ba/Sr/La(2)-O(2) =	2.735(4) (x3)	O(1)-Nb/Ta(2)-O(1) = 85.6(2) (x6)	
Ba/Sr/La(2)-O(2) =	2.711(4) (x3)	O(1)-Nb/Ta(2)-O(1) = 180.0 (x3)	
Nb/Ta(1)-O(1) =	2.166(5) (x3)		
Nb/Ta(1)-O(2) =	1.879(3) (x3)		
Nb/Ta(2)-O(1) =	1.980(5) (x6)		

Table 4.07: Bond lengths and angles from refinement results for $Ba_2SrLaNb_2TaO_{12}$

The refinement using method (ii) proceeded well in space group R-3. Details of the refinement can be found in **figures 4.13** and **4.14** and **tables 4.06** and **4.07**. The refined crystal structure has lattice parameters a = 5.7154(1) Å and c = 27.9493(5) Å and the refinement converged with associated statistics, χ^2 = 4.116, R_{wp} = 12.19% and R_p = 10.10%. The resultant structure can be seen in **figure 4.15**.
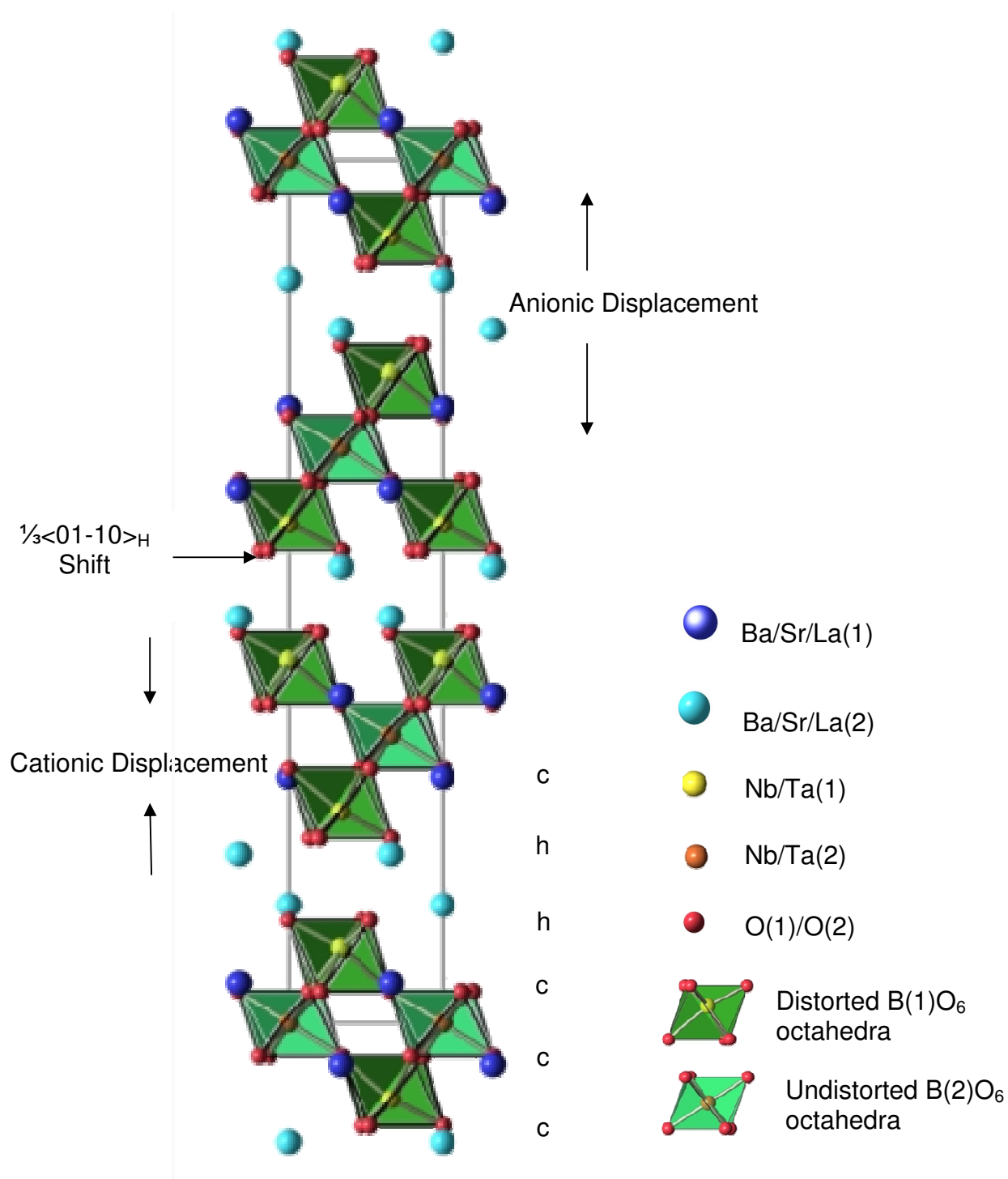
Figure 4.15: Structure of $Ba_2SrLaNb_2TaO_{12}$ viewed along the x-axis.

Again, the Nb^{5+} cations display a preference for B(1) with an occupancy of 80%. There is an 2:3 distribution of Nb^{5+} / Ta^{5+} across B(2) (40% and 60% respectively) again. Similar to the refined crystal structure of $Ba_3LaNb_2TaO_{12}$ it seems that this preference of Nb^{5+} to inhabit the distorted B(1) site is exhibited irrespective of whether there are two or three A-cations present. The two different B-cation environments can be seen in **figures 4.16** and **4.17**.

The Δd value is 50.34 and 0 for B(1) and B(2) respectively. The BO_6 octahedra are antiphase tilted about the z-axis by an angle of 7°, **figure 4.18**.

The dominant divalent A-cation in the structure, Ba^{2+} displays a preference for A(2) with a 76% occupancy, whereas Sr^{2+} and La^{3+} exhibit a preference for A(1) with occupancies in this site of 36% and 40% respectively.

The cubo-octahedral environment of the A-cations can be seen in **figures 4.19** and **4.20**. There are 3 x A(1)-O bonds of 2.593(4) Å and 3 x A(1)-O bonds of 2.893(5) Å pointing towards neighbouring octahedral layers, along the direction of the z-axis and the remaining six bonds labelled are parallel to the xy-plane pointing towards octahedral units in the same octahedral layer.

For the A(2) cations there are 3 x A(2)-O bonds of 2.711(4) Å pointing into vacant shifted region and 3 x A(2)-O bonds of 3.255(5) Å pointing towards triple layers of B-site cations, and the remaining six bonds labelled are parallel to xy-plane. The A(2) cations are displaced into shifted region and the degree of shift for both A-cations can be seen in **figure 4.23.**

The AO_{12} polyhedra again are in a more distorted environment in the "shifted" region, A(2), than in the perovskite block, A(1), with distortion values of Δd = 61.04 and Δd = 45.63 correspondingly. This can be seen more clearly in **figures 4.21** and **4.22** where the distorted A-O lattices are projected along the z-axis.

Bond valence sums (BVS) were performed for the structure (refer to **section 1.1.1, equation 1.2** and **1.3**), values are listed in **table 4.08**. Overall the BVS calculations performed suggest the refinement of the crystal structure is rational, however due to structural complexity associated with the B-sites the values are larger than expected.

Cation	Theoretical BVS	Calculated BVS	Status
A(1)	2.43	2.57	Over-bonded
A(2)	1.86	2.05	Over-bonded
B(1)	5.05	5.18	Over-bonded
B(2)	5.00	6.10	Over-bonded

Table 4.08: BVS calculation results for $Ba_2SrLaNb_2TaO_{12}$
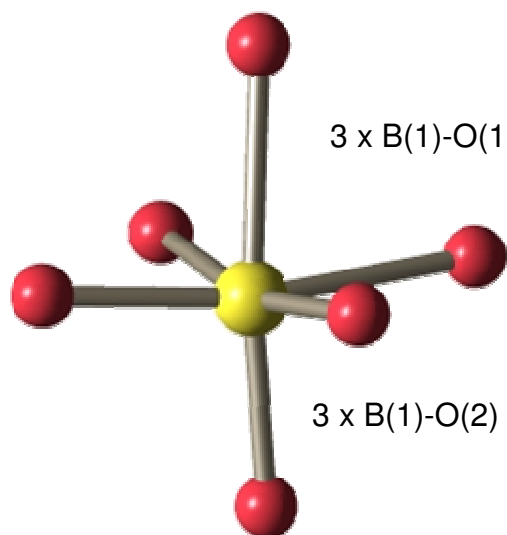
Figure 4.16: Distorted B(1)O$_6$ octahedron adjacent to the "shifted" region (red spheres O^{2-}, yellow sphere B(1) cation). Associated bond lengths labelled.

$3 \times$ B(1)-O(1) = 2.166(5) Å

$3 \times$ B(1)-O(2) = 1.879(3) Å
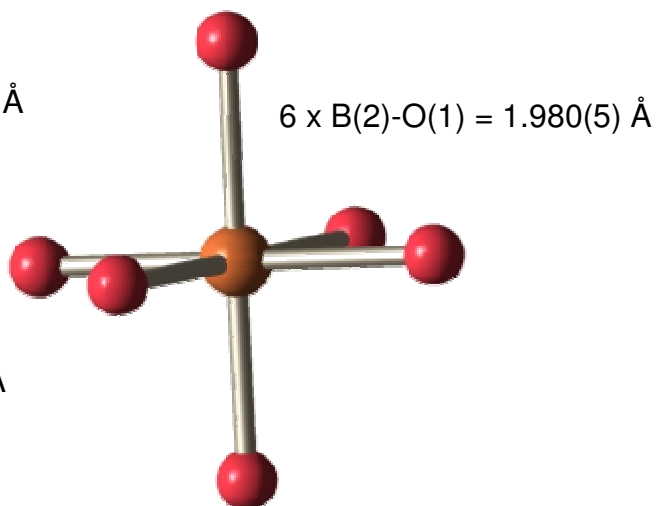
Figure 4.17: Undistorted B(2)O$_6$ octahedron in the centre of the perovskite block (red spheres O^{2-}, orange sphere B(2) cation). Associated bond lengths labelled.

$6 \times$ B(2)-O(1) = 1.980(5) Å
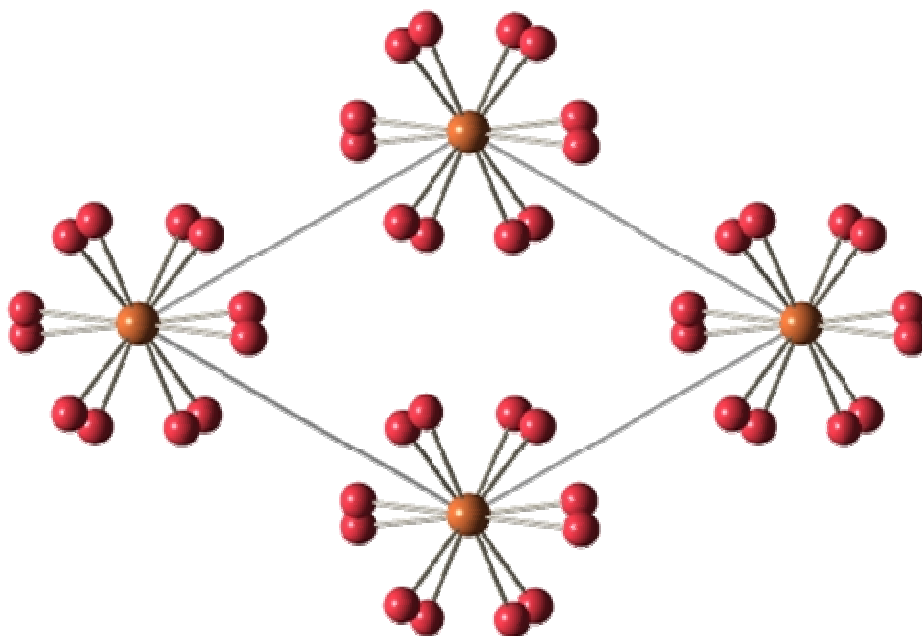
Figure 4.18: View of Ba$_2$SrLaNb$_2$TaO$_{12}$ structure along the *z*-axis showing tilting of the octahedra, tilt angle 7° [a$^-$ a$^-$ a$^-$] (octahedra omitted for clarity). (Red spheres O^{2-}, Orange spheres Nb^{5+}/Ta^{5+}).
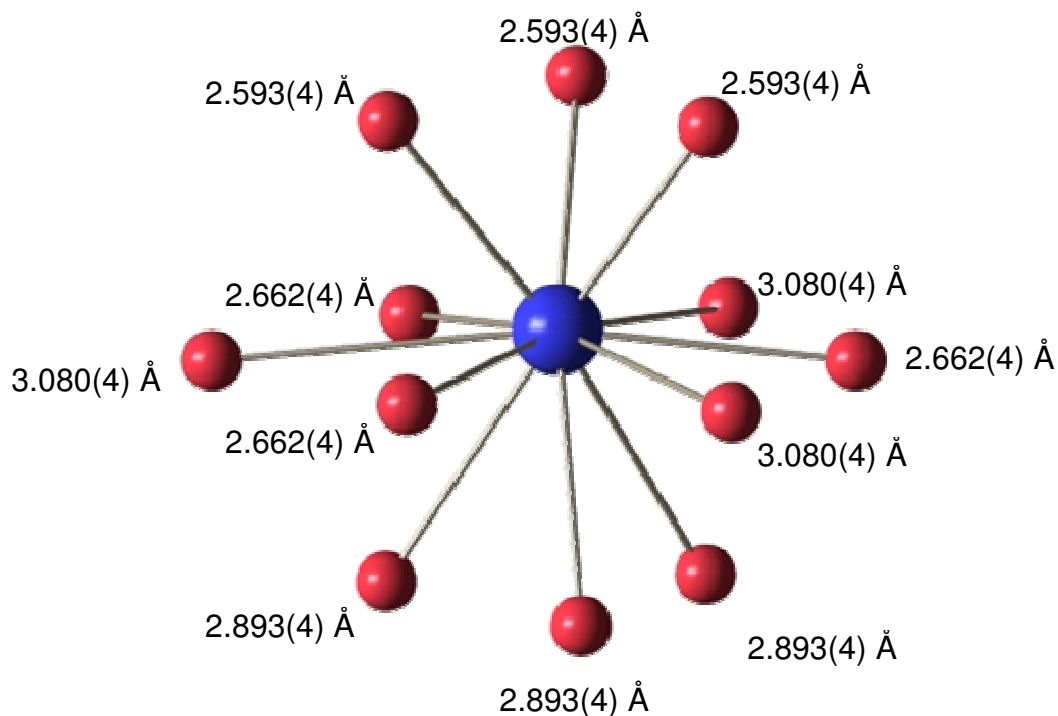
Figure 4.19: Cubo-octahedral environment of A(1) cations located within the triple layer of BO_6 octahedra with Ba^{2+} / Sr^{2+} / La^{3+} distribution of 0.25 / 0.36 / 0.40 (red spheres O^{2-}, blue sphere Ba^{2+} / Sr^{2+} / La^{3+}). Bond lengths are labelled.
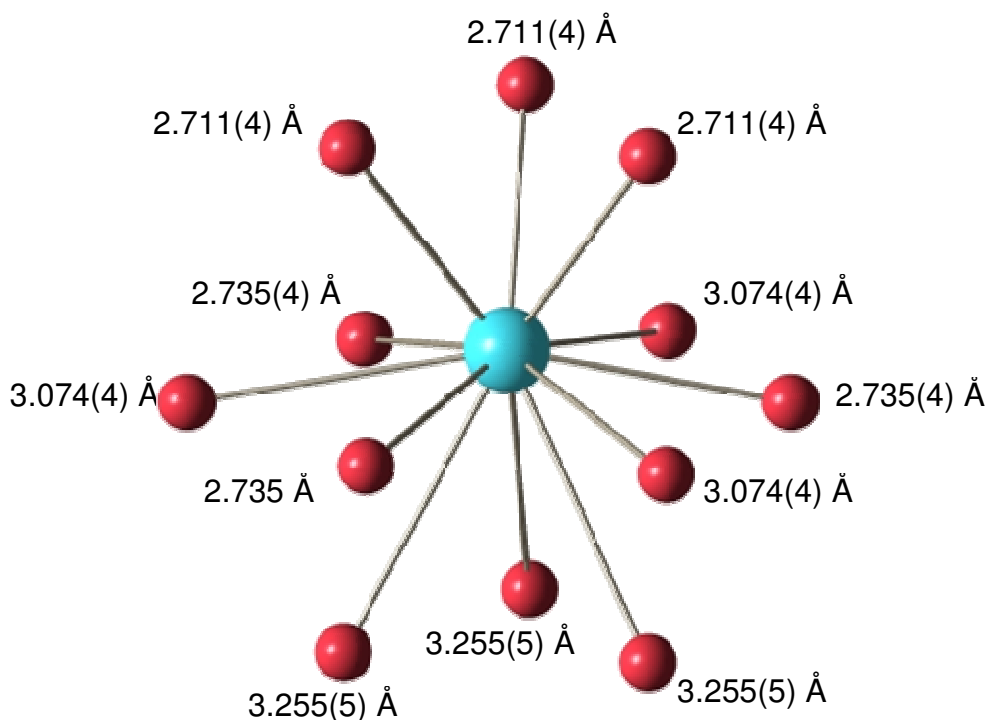
Figure 4.20: Cubo-octahedral environment of A(2) cations located in "shifted" region with a Ba^{2+} / Sr^{2+} / La^{3+} distribution of 0.76 / 0.14 / 0.11 (red spheres O^{2-}, blue sphere Ba^{2+} / Sr^{2+} / La^{3+}). Bond lengths are labelled.
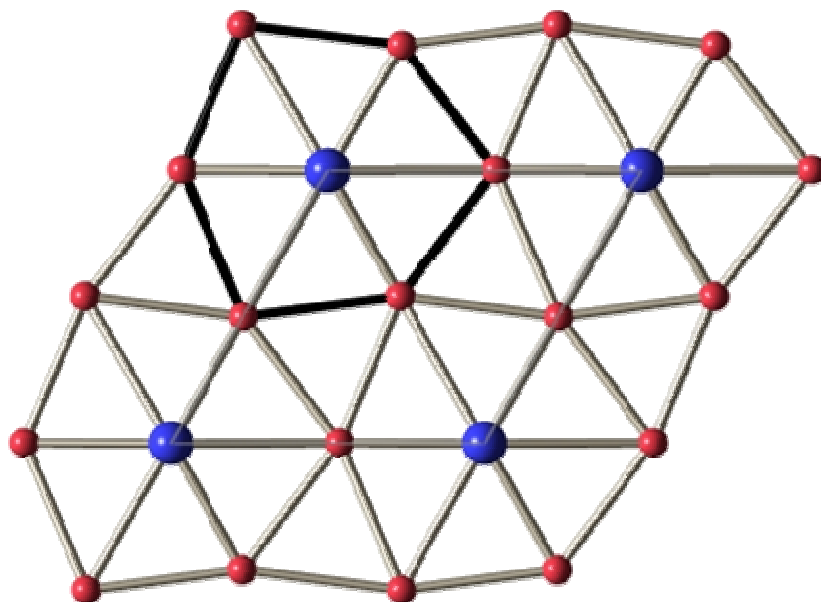
Figure 4.21: View of the distorted A(1)-O lattice along the *z*-axis, O^{2-} ions not parallel to the *xy*-plane are omitted for clarity. Black outline shows a "slice" through the AO_{12} polyhedra, 3 x A(1)-O bonds of 3.080(4) Å and 3 x A(1)-O bonds of 2.662(4) Å parallel to the *xy*-plane. A-cations are located on the corners of the unit cell, outlined in grey. (Red spheres O^{2-}, blue spheres Ba^{2+} / Sr^{2+} / La^{3+}).
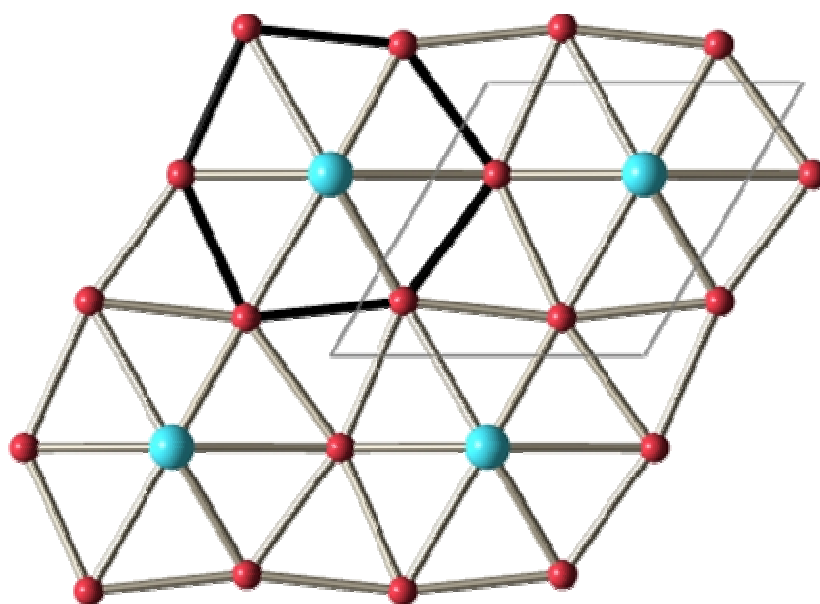
Figure 4.22: View of the distorted A(2)-O lattice along the *z*-axis, O^{2-} ions not parallel to the *xy*-plane are omitted for clarity. Black outline shows a "slice" through the a AO_{12} polyhedra, 3 x A(1)-O bonds of 3.074(4) Å and 3 x A(1)-O bonds of 2.735(4) Å parallel to the *xy*-plane. Unit cell is outlined in grey. (Red spheres O^{2-}, blue spheres Ba^{2+} / Sr^{2+} / La^{3+}).
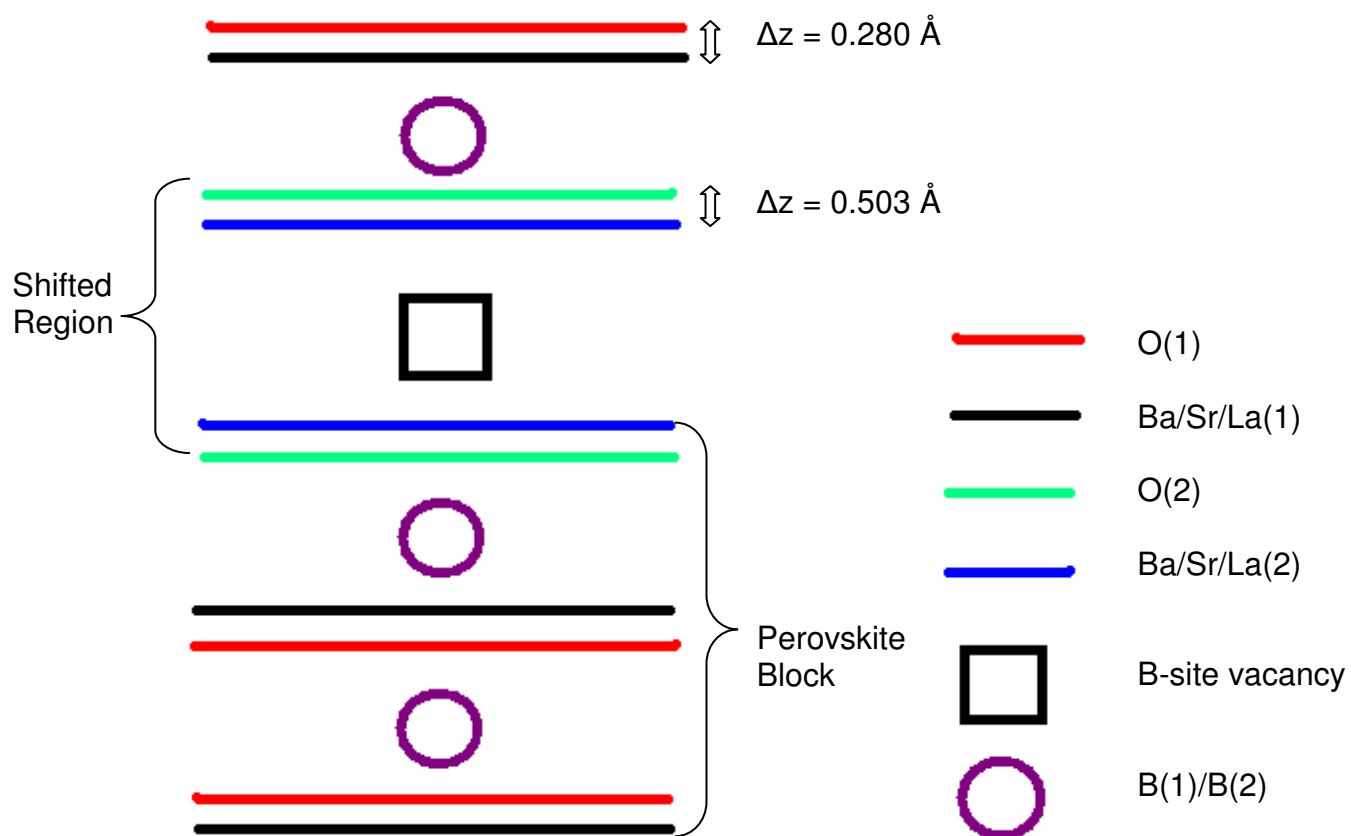
Figure 4.23: A schematic diagram showing A-O displacement along the *z*-axis (Δz) for Ba₂SrLaNb₂TaO₁₂ (not to scale).

The variance of $Ba_2SrLaNb_2TaO_{12}$ was calculated to be 14.23×10^{-4}, as can be seen in *figure 4.24*. (For clarity, Δ values are quoted in figures omitting the factor 10^{-4}).

<div align="center">(a)   (b)</div>
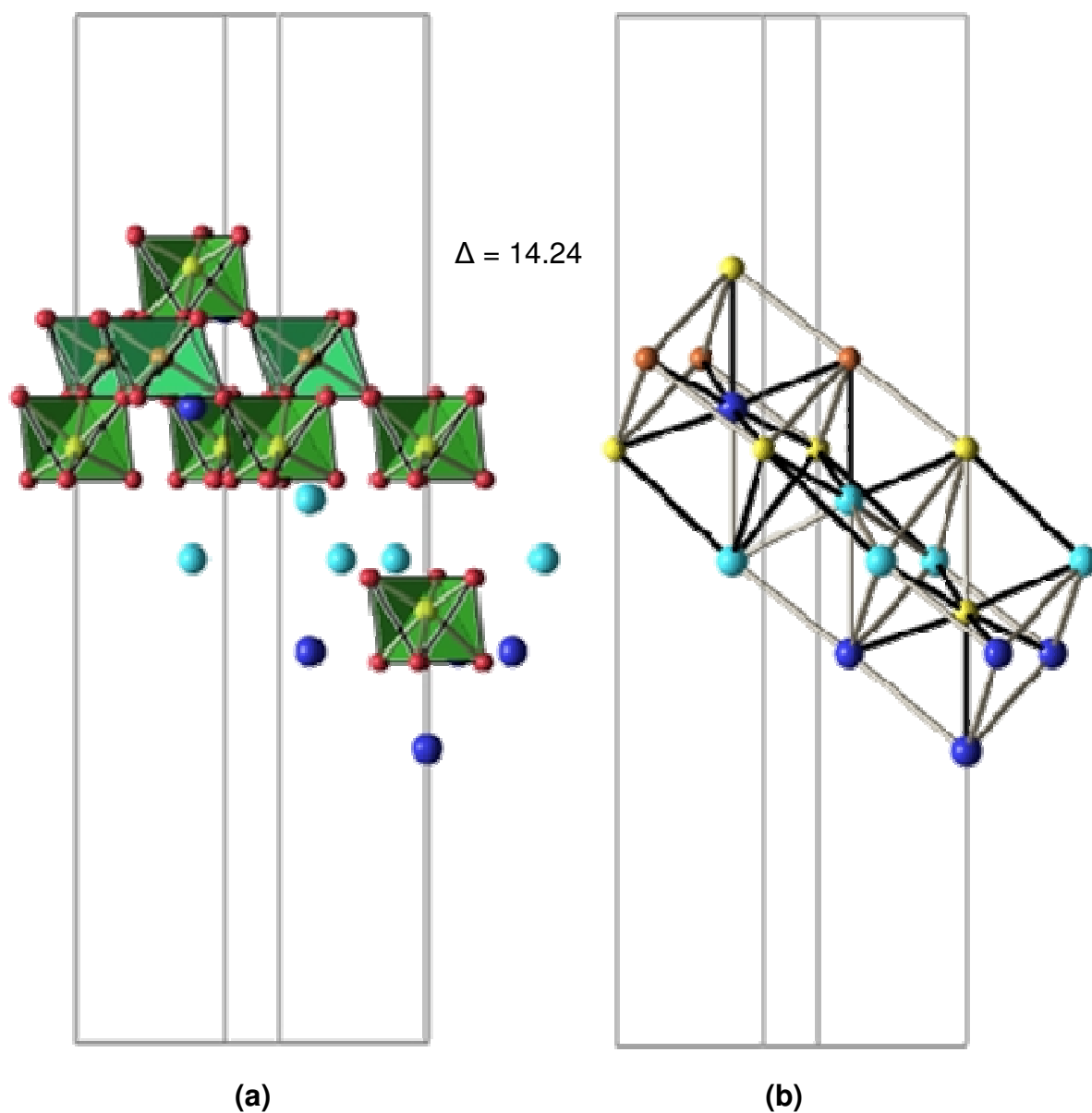
Figure 4.24: (a) A- and B-cations involved in the three bcc unit cells (O^{2-} ions shown not involved in the *bcc* cation sublattice) **(b)** Structural view of the *bcc* lattice along the *xy*-direction, for $Ba_2SrLaNb_2TaO_{12}$. Black bonds highlight the A-B distances (bond lengths) selected for calculation of the variance, Δ. (Red spheres O^{2-}, blue spheres Ba^{2+} / Sr^{2+} / La^{3+}, yellow / orange spheres Nb^{5+}/Ta^{5+}).

4.3.1.3 BaSr$_2$LaNb$_2$TaO$_{12}$

4.3.1.3.1 XRPD Refinement

The refinement results are summarised below in **figure 4.25** and **table 4.09.** Refinement statistics and lattice parameters are given in **figure 4.25**.

Space group R-3

$\chi^2 = 1.564$; R$_{wp}$ = 9.24%; R$_p$ = 6.69%

$a = 5.7013(1)$ Å; $c = 27.6663(3)$ Å

$\alpha = \beta = 90°$; $\gamma = 120°$

Volume = 778.81(1) Å^3
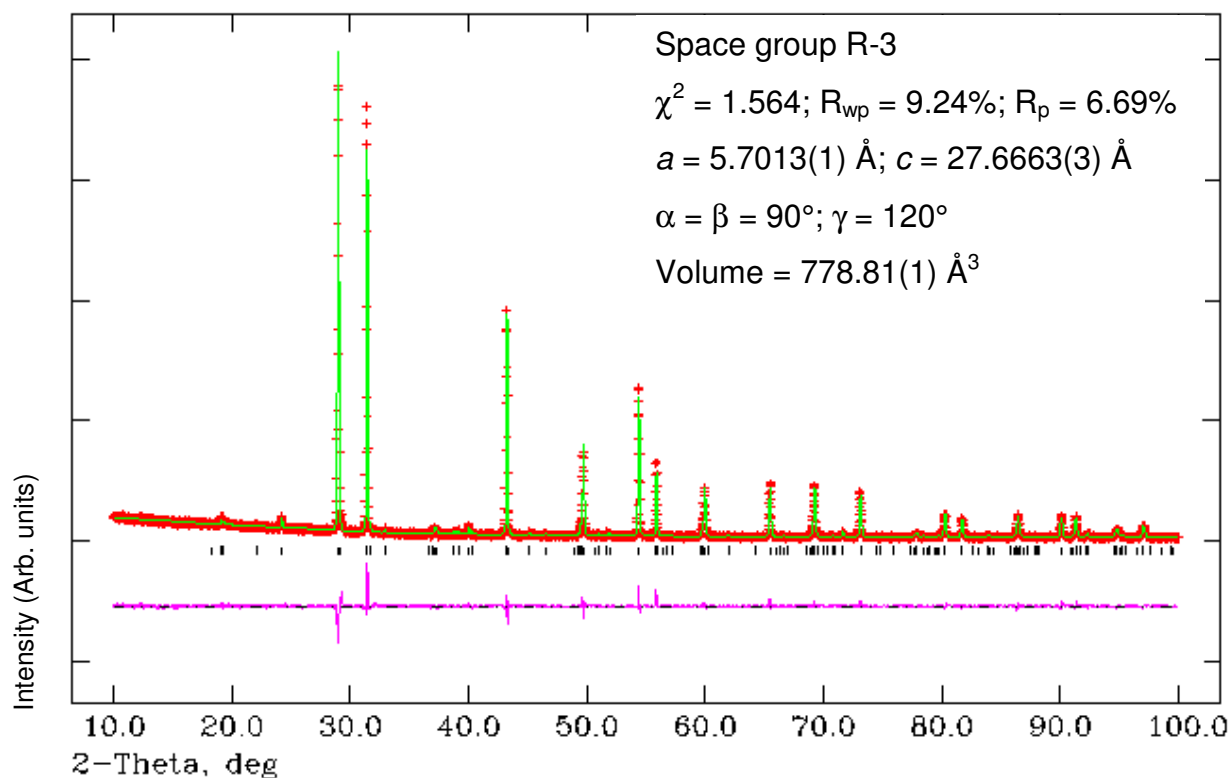
Figure 4.25: Calculated (green), experimental (red) and difference (pink) profile plot for BaSr$_2$LaNb$_2$TaO$_{12}$ XRPD data. Tick marks represent Bragg peak positions.

Atom	Wyckoff	x	y	z	U$_{iso}$*100 (Å^2)	Frac.
Ba/Sr1	6c	0	0	0.2868(1)	1.79(2)	0.57(2)*/0.43(2)
Ba/Sr2	6c	0	0	0.1371(1)	0.63(1)	0.43(2)*/0.57(2)
Nb/Ta1	6c	0	0	0.4226(1)	0.77(1)	0.73(1) /0.27(1)
Nb/Ta2	3a	0	0	0	1.00(2)	0.54(2) /0.46(2)
O1	18f	0.129(4)	0.784 (4)	0.6275(4)	0.0(4)	1
O2	18f	0.145(4)	0.783(4)	0.4522(4)	1.4(4)	1

*Ba^{2+} and La^{3+} are entered as one element, Ba^{2+}

Table 4.09: Refinement results for BaSr$_2$LaNb$_2$TaO$_{12}$ (XRPD RT data)

4.3.1.3.2 Method (iv)

The refinement results are summarised below in **figures 4.26** and **4.27** and **tables 4.10** and **4.11.** Refinement statistics and lattice parameters are given in **figure 4.26**.

Space group R-3

$\chi^2 = 1.807$; $R_{wp} = 7.34\%$; $R_p = 6.85\%$

$a = 5.6993(1)$ Å; $c = 27.6578(4)$ Å

$\alpha = \beta = 90°$; $\gamma = 120°$

Volume $= 778.03(2)$ Å^3
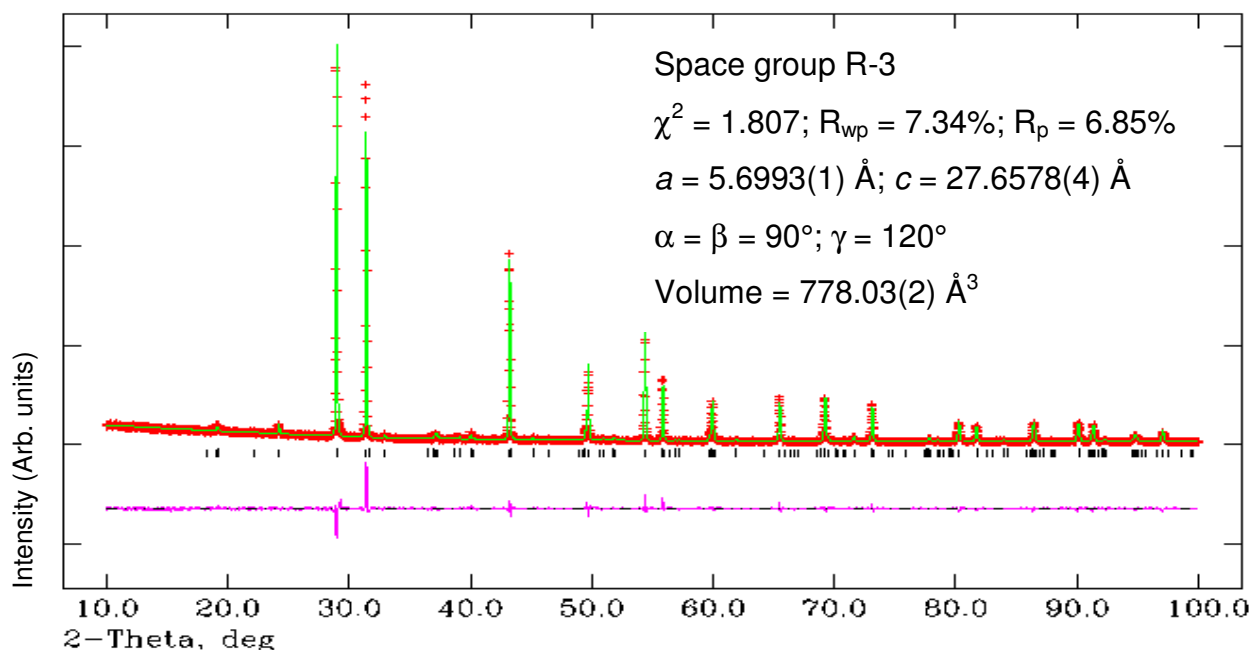
Figure 4.26: Calculated (green), experimental (red) and difference (pink) profile plot for BaSr$_2$LaNb$_2$TaO$_{12}$ XRPD data. Tick marks represent Bragg peak positions.
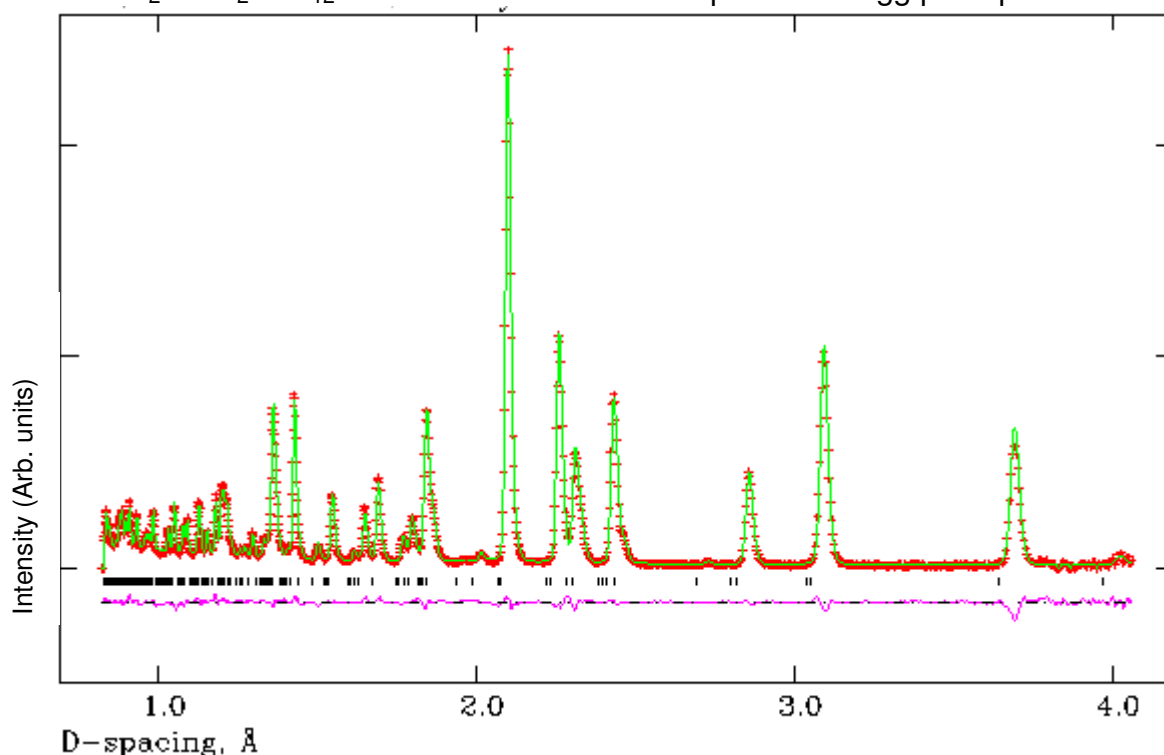
Figure 4.27: Calculated (green), experimental (red) and difference (pink) profile plot for BaSr$_2$LaNb$_2$TaO$_{12}$ NPD data collected on GEM, Bank 4. Tick marks represent Bragg peak positions.

160

Atom	Wyckoff	x	y	z	$U_{iso}*100$ (Å²)	Frac.
Ba/Sr/La1	6c	0	0	0.2863(1)	0.79(7)	0.06(1)/0.44(1)/0.50*
Ba/Sr/La2	6c	0	0	0.1386(1)	1.01(8)	0.44(1)/0.56(1)/0.00*
Nb/Ta1	6c	0	0	0.4219(1)	0.18(5)	0.72(1)/0.28(1)**
Nb/Ta2	3a	0	0	0	1.09(1)	0.57(2)/0.43(2)**
O1	18f	0.1176(5)	0.7912(5)	0.6284(1)	1.49(5)	1
O2	18f	0.1237(4)	0.7891(4)	0.4530(1)	1.28(5)	1

*La^{3+} occupancies were fixed after Sr^{2+} occupancies were fixed from XRPD refinement, and it was found that La^{3+} displays an overall preference for A(1). **Due to rounding up of the B-site a slightly different composition is given to that stated.*

Table 4.10: Refinement results for $BaSr_2LaNb_2TaO_{12}$ (XRPD and NPD RT data)

Bond lengths (Å)			Bond Angles (°)		
Ba/Sr/La(1)-O(1) =	2.870(3)	(x3)	O(1)-Nb/Ta(1)-O(1) =	82.4(1)	(x3)
Ba/Sr/La(1)-O(1) =	3.119(2)	(x3)	O(1)-Nb/Ta(1)-O(2) =	166.7(1)	(x3)
Ba/Sr/La(1)-O(1) =	2.601(2)	(x3)	O(1)-Nb/Ta(1)-O(2) =	87.3(1)	(x3)
Ba/Sr/La(1)-O(2) =	2.603(2)	(x3)	O(1)-Nb/Ta(1)-O(2) =	88.0(1)	(x3)
			O(2)-Nb/Ta(1)-O(2) =	100.8(1)	(x3)
Ba/Sr/La(2)-O(1) =	3.253(3)	(x3)			
Ba/Sr/La(2)-O(2) =	3.142(2)	(x3)	O(1)-Nb/Ta(2)-O(1) =	94.6(1)	(x6)
Ba/Sr/La(2)-O(2) =	2.653(2)	(x3)	O(1)-Nb/Ta(2)-O(1) =	85.4(1)	(x6)
Ba/Sr/La(2)-O(2) =	2.659(3)	(x3)	O(1)-Nb/Ta(2)-O(1) =	180.0	(x3)
Nb/Ta(1)-O(1) =	2.146(3)	(x3)			
Nb/Ta(1)-O(2) =	1.878(2)	(x3)			
Nb/Ta(2)-O(1) =	2.002(3)	(x6)			

Table 4.11: Bond lengths and angles from refinement results for $BaSr_2LaNb_2TaO_{12}$

The refinement using method (iv) progressed well in space group R-3. Once the Sr^{2+} occupancies were fixed, the La^{3+} cations became completely ordered with all the La^{3+} occupying A(1) (50%). Therefore the La^{3+} occupancies were subsequently fixed and the Ba^{2+} / Sr^{2+} occupancies were then allowed to refine, with constraints. Details of the refinement can be found in **figures 4.26** and **4.27** and **tables 4.10** and **4.11**. The refinement converged with lattice parameters a = 5.6993(1) Å and c = 27.6578(4) Å with associated statistics, χ^2 = 1.807, R_{wp} = 7.34% and R_p = 6.85%. The resultant crystal structure can be seen in **figure 4.28**
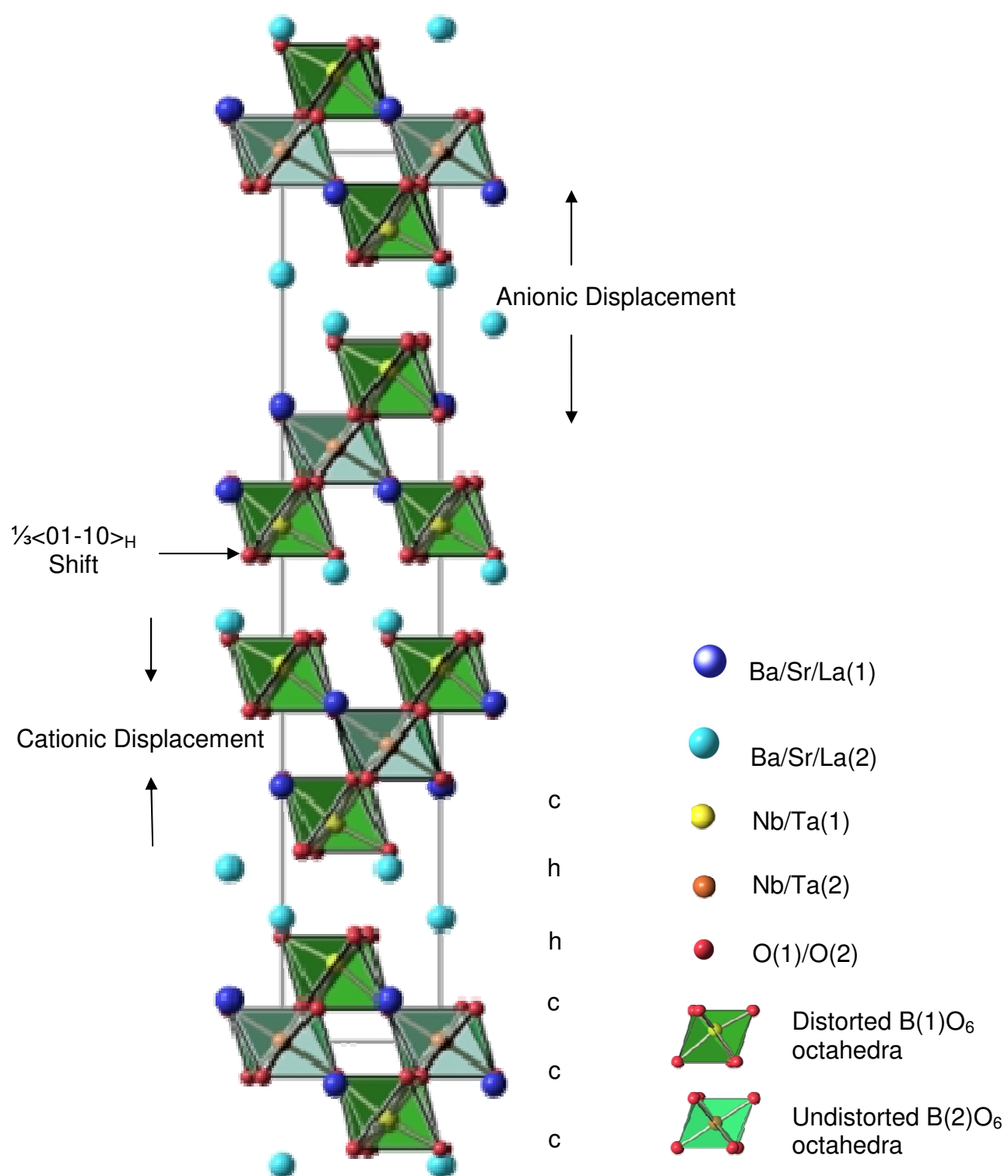
Figure 4.28: Structure of $BaSr_2LaNb_2TaO_{12}$ viewed along the *x*-axis.

Legend:
- Ba/Sr/La(1)
- Ba/Sr/La(2)
- Nb/Ta(1)
- Nb/Ta(2)
- O(1)/O(2)
- Distorted B(1)O$_6$ octahedra
- Undistorted B(2)O$_6$ octahedra

Anionic Displacement

⅓<01-10>$_H$ Shift

Cationic Displacement

c
h
h
c
c
c

The Nb^{5+} cations display a preference for B(1) in the distorted octahedra with an occupancy of 72%. There is an almost 3:2 distribution of Nb^{5+} / Ta^{5+} across B(2) (57% and 43% respectively) located in the undistorted octahedra. This Nb^{5+} preference for B(2) is similar to that displayed by the Ba$_3$LaNb$_2$TaO$_{12}$ and Ba$_2$SrLaNb$_2$TaO$_{12}$ solid solution members. Therefore, it appears that when two pentavalent B-cations are present, the Nb^{5+} cations display a preference to inhabit the distorted environment of B(1) irrespective of whether there are two or three A-cations present. The two different B-cation sites can be seen in **figures 4.29** and **4.30**.

B(1) located adjacent to the "shifted" region possesses a Δd value of 44.36, whereas B(2) in the centre of the perovskite block has a Δd value of 0. The BO$_6$ octahedra are antiphase tilted about the z-axis by an angle of 9°, **figure 4.31**.

The dominant divalent A-cation, Sr^{2+}, displays no particular preference for either A-site with an almost 1:1 distribution across the two sites (44%, A(1) and 56%, A(2)). The La^{3+} cations are completely ordered with an occupancy of 50% in A(1) and 0% in A(2). The Ba^{2+} cations exhibit a preference for A(1) with an occupancy of 44%. As Sr^{2+} is the dominant divalent A-cation there is not enough space to house all of these cations in the perovskite block hence the almost random distribution of this cation across the two sites.

The cubo-octahedral environment of the A-cations can be seen in **figures 4.32** and **4.33**. There are 3 x A(1)-O bonds of 2.603(2) Å and 3 x A(1)-O bonds of 2.870(3) Å pointing towards neighbouring octahedral layers of B-cations (along the direction of the z-axis), and 3 x A(1)-O bonds of 2.601(2) Å and 3 x A(1)-O bonds of 3.119(2) Å parallel to the xy-plane pointing towards BO$_6$ units in the same octahedral layer.

For the A(2) cations there are 3 x A(2)-O bonds of 2.659(3) Å pointing into vacant shifted region and 3 x A(2)-O bonds of 3.253(3) Å pointing towards triple layers of B-site cations, and 3 x A(2)-O bonds of 3.142(2) Å and 3 x A(2)-O bonds of 2.635(2) Å bonds parallel to xy-plane pointing towards NbO$_6$ units in the same octahedral layer. The A(2) cations are displaced into shifted region and the degree of shift for both A-cations can be seen in **figure 4.26.**

Again the AO_{12} polyhedra reveal a more distorted environment in the "shifted" region, than in the perovskite block, with distortion values of $\Delta d = 87.35$ and $\Delta d = 59.09$ correspondingly. This can be seen more clearly in **figures 4.24** and **4.25** where the distorted A-O lattices are projected along the *z*-axis.

Bond valence sums (BVS) were performed for the structure (refer to **section 1.1.1, equations 1.2** and **1.3**), values are listed in **table 4.12**. Overall the BVS calculations performed suggest that the Rietveld refinement is reasonable, however inflated values are witnessed for the B-sites due to the level of structural complexity associated with the site.

Cation	Theoretical BVS	Calculated BVS	Status
A(1)	2.50	2.47	Under-bonded
A(2)	2.00	2.17	Over-bonded
B(1)	5.00	5.46	Over-bonded
B(2)	5.00	5.63	Over-bonded

Table 4.12: BVS calculation results for $BaSr_2LaNb_2TaO_{12}$
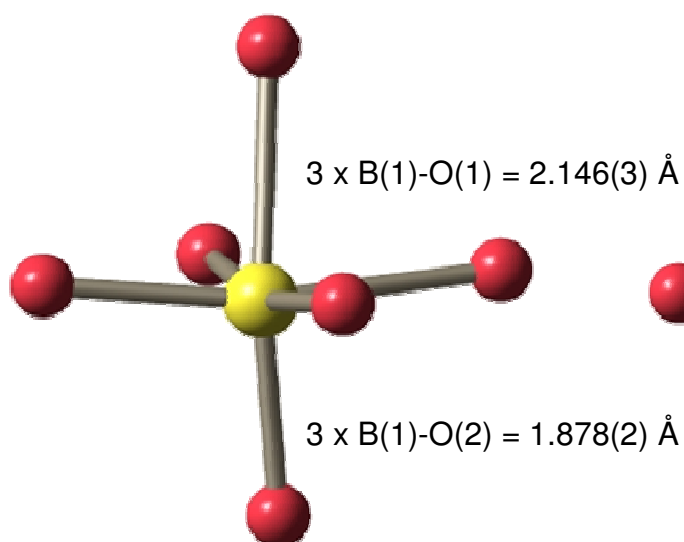
Figure 4.29: Distorted B(1)O6 octahedron adjacent to the "shifted" region (red spheres O^{2-}, yellow sphere B(1) cation). Associated bond lengths labelled.
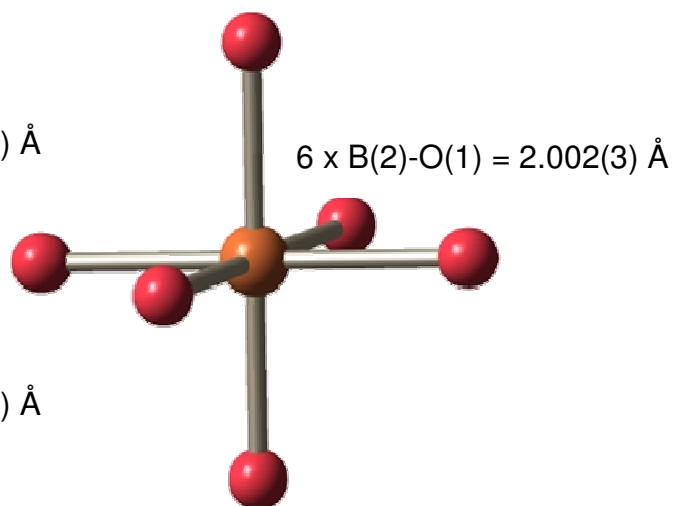
Figure 4.30: Undistorted B(2)O6 octahedron in the centre of the perovskite block (red spheres O^{2-}, orange sphere B(2) cation). Associated bond lengths labelled.
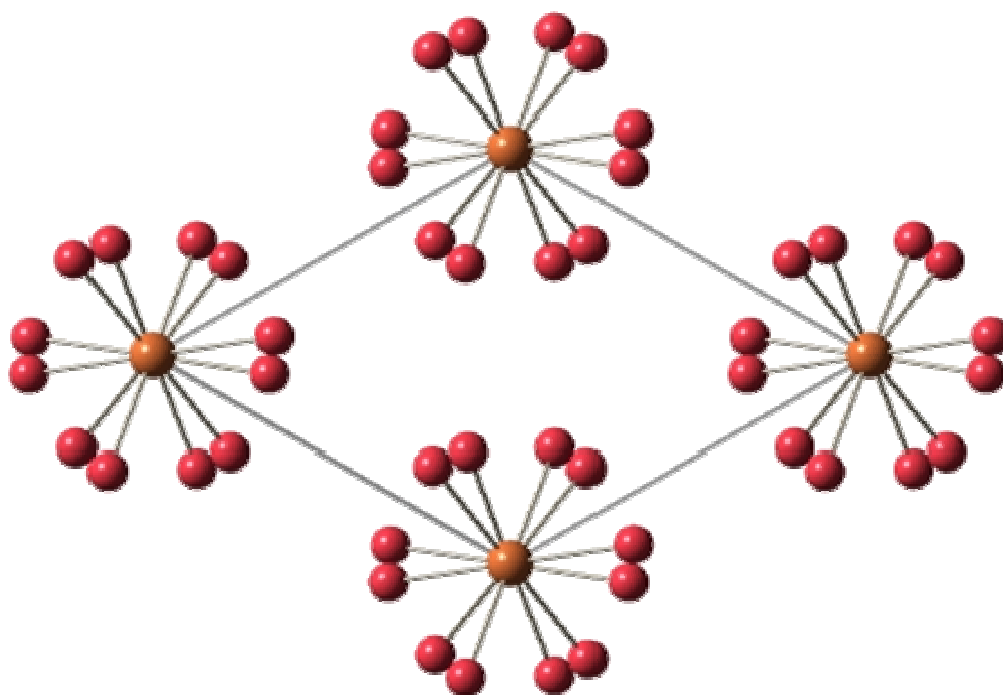
Figure 4.31: View of $BaSr_2LaNb_2TaO_{12}$ structure along the z-axis showing tilting of the octahedra, tilt angle 9° [$a^- a^- a^-$] (octahedra omitted for clarity). (Red spheres O^{2-}, orange sphere Nb^{5+}/Ta^{5+}).
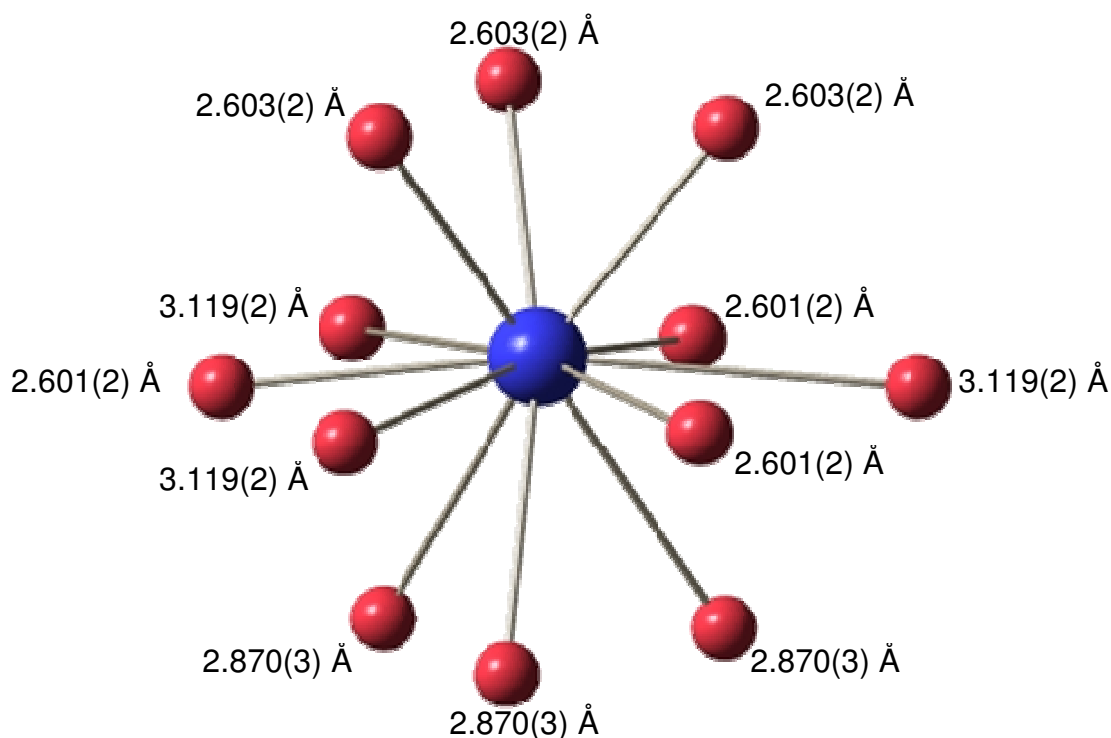
Figure 4.32: Cubo-octahedral environment of A(1) cations located within the triple layer of BO_6 octahedra with Ba^{2+} / Sr^{2+} / La^{3+} distribution of 0.06 / 0.44 / 0.50 (red spheres O^{2-}, blue sphere Ba^{2+} /Sr^{2+} / La^{3+}). Bond lengths are labelled.
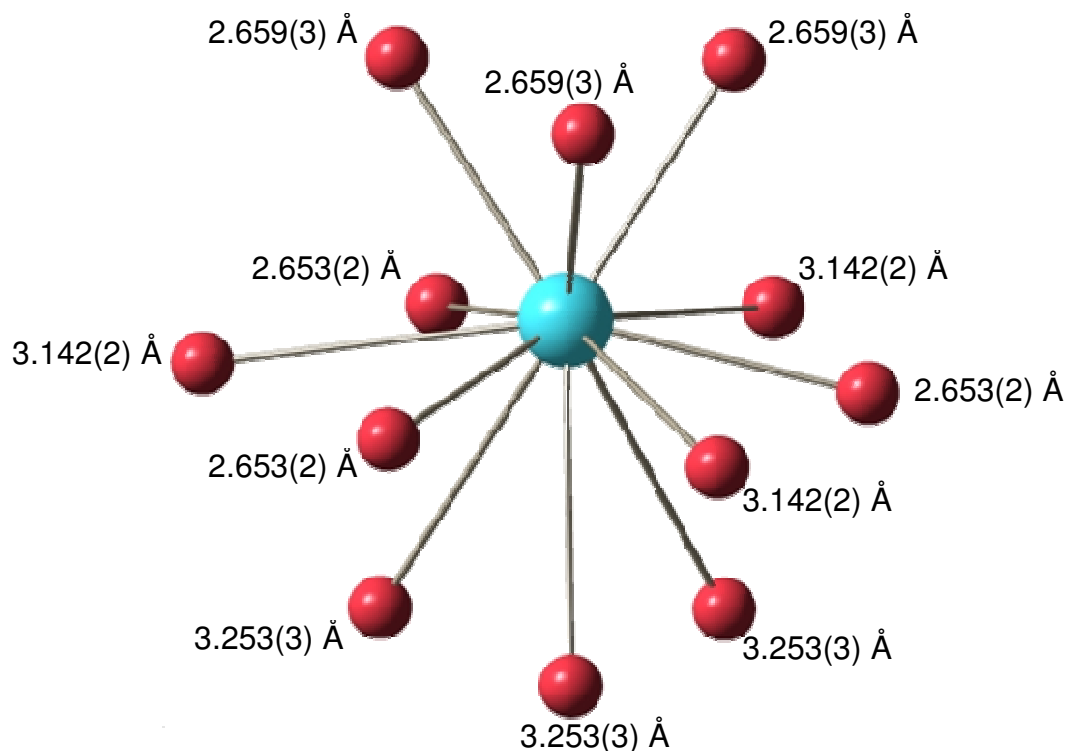
Figure 4.33: Cubo-octahedral environment of A(2) cations located in "shifted" region with a Ba^{2+} / Sr^{2+} / La^{3+} distribution of 0.44 / 0.56 / 0.00 (red spheres O^{2-}, blue sphere Ba^{2+} / Sr^{2+} / La^{3+}).Bond lengths are labelled.
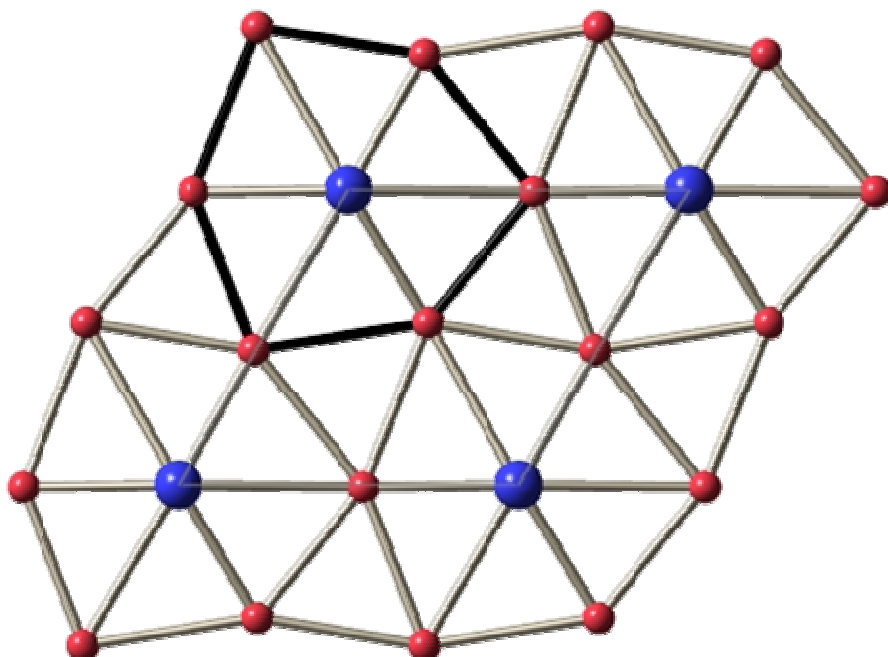
Figure 4.34: View of the distorted A(1)-O lattice along the *z*-axis, O^{2-} ions not parallel to the *xy*-plane are omitted for clarity. Black outline shows a "slice" through the AO_{12} polyhedra, 3 x A(1)-O bonds of 3.119(2) Å and 3 x A(1)-O bonds of 2.601(2) Å parallel to the *xy*-plane. A-cations are located on the corners of the unit cell, outlined in grey. (Red spheres O^{2-}, blue spheres $Ba^{2+}/Sr^{2+}/La^{3+}$).
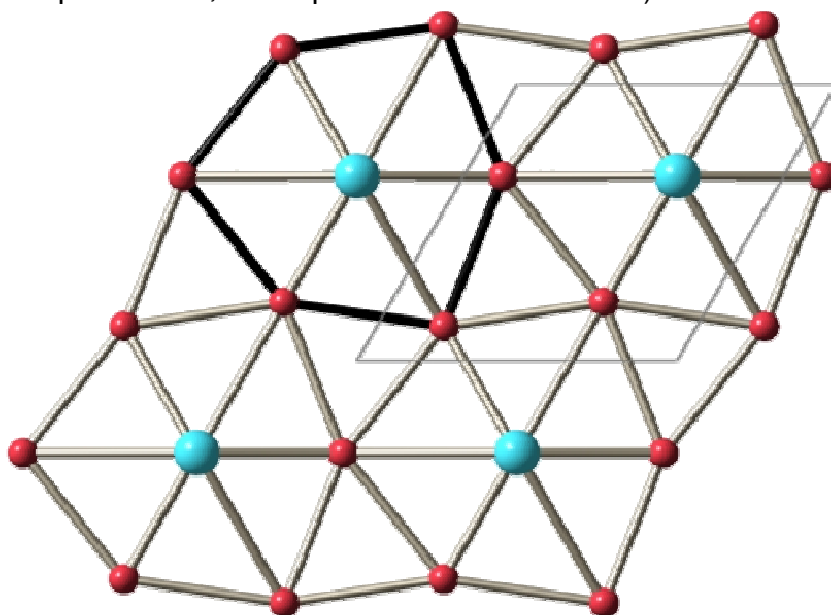
Figure 4.35: View of the distorted A(2)-O lattice along the *z*-axis, O^{2-} ions not parallel to the *xy*-plane are omitted for clarity. Black outline shows a "slice" through the AO_{12} polyhedra, 3 x A(1)-O bonds of 3.142(2) Å and 3 x A(1)-O bonds of 2.653(2) Å parallel to the *xy*-plane. unit cell is outlined in grey. (Red spheres O^{2-}, blue spheres $Ba^{2+}/Sr^{2+}/La^{3+}$).

167
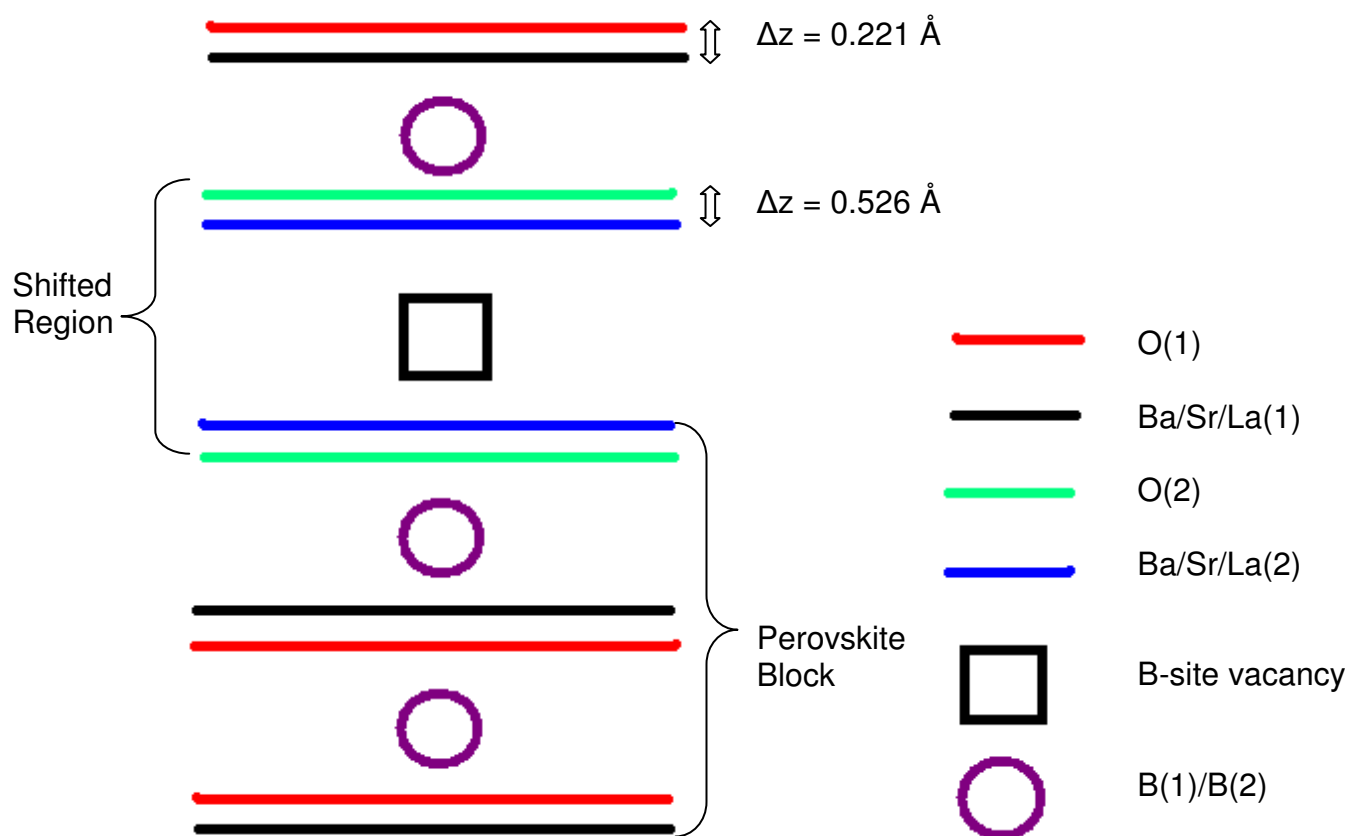
Figure 4.36: A schematic diagram showing A-O displacement along the *z*-axis (Δz) for BaSr$_2$LaNb$_2$TaO$_{12}$ (not to scale).

$BaSr_2LaNb_2TaO_{12}$ has a variance of 12.67 x 10^{-4}, as illustrated in **figure 4.27**. (For clarity, Δ values are quoted in figures omitting the factor 10^{-4}).

Δ = 12.67

(a)

(b)
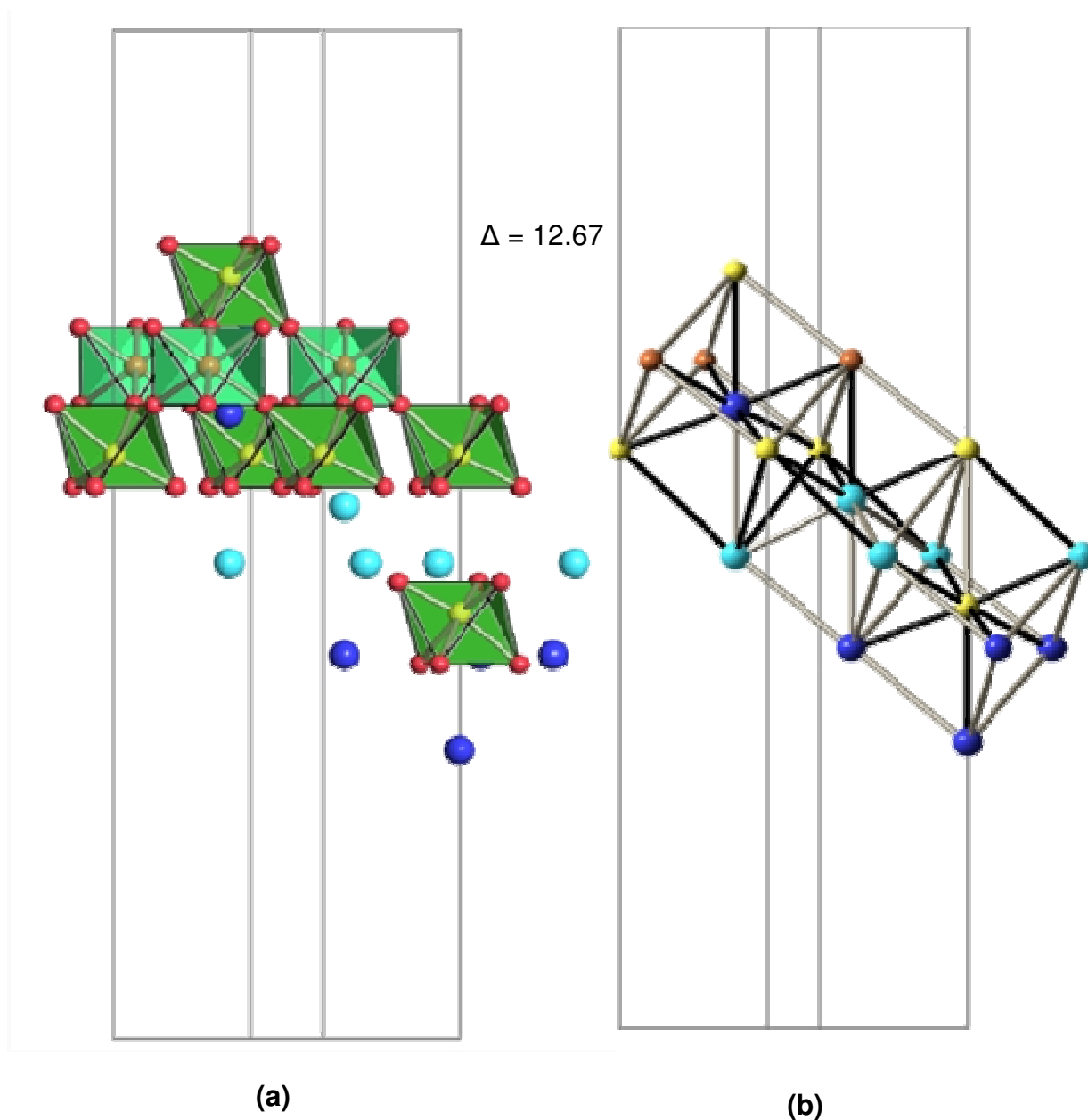
Figure 4.37: **(a)** A- and B-cations involved in the three *bcc* unit cells (O^{2-} ions shown not involved in the *bcc* cation sublattice) **(b)** Structural view of the *bcc* lattice along the *xy*-direction, for $BaSr_2LaNb_2TaO_{12}$. Black bonds highlight the A-B distances (bond lengths) selected for calculation of the variance, Δ. (Red spheres O^{2-}, blue spheres $Ba^{2+}/Sr^{2+}/La^{3+}$, yellow / orange spheres Nb^{5+}/Ta^{5+}).

4.3.1.4 Sr$_3$LaNb$_2$TaO$_{12}$

4.3.1.4.1 Joint XRPD and NPD refinement

The refinement results are summarised below in *figures 4.38* and *4.39* and *tables 4.13* and *4.14*. Refinement statistics and lattice parameters are given in *figure 4.38*.

Space group R-3

$\chi^2 = 3.550$; R$_{wp}$ = 7.93%; R$_p$ = 6.15%

$a = 5.6653(1)$ Å; $c = 27.2376(3)$ Å

$\alpha = \beta = 90°$; $\gamma = 120°$

Volume = 757.093(1) Å^3
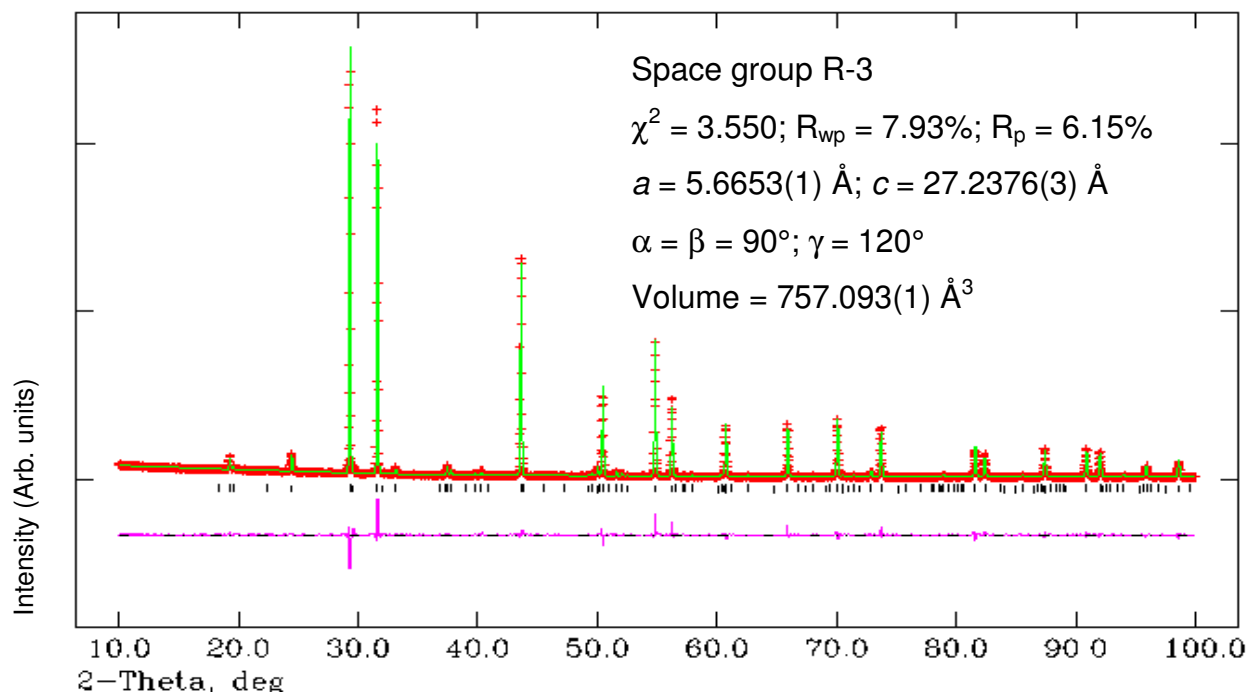
Figure 4.38: Calculated (green), experimental (red) and difference (pink) profile plot for Sr$_3$LaNb$_2$TaO$_{12}$ XRPD data. Tick marks represent Bragg peak positions.
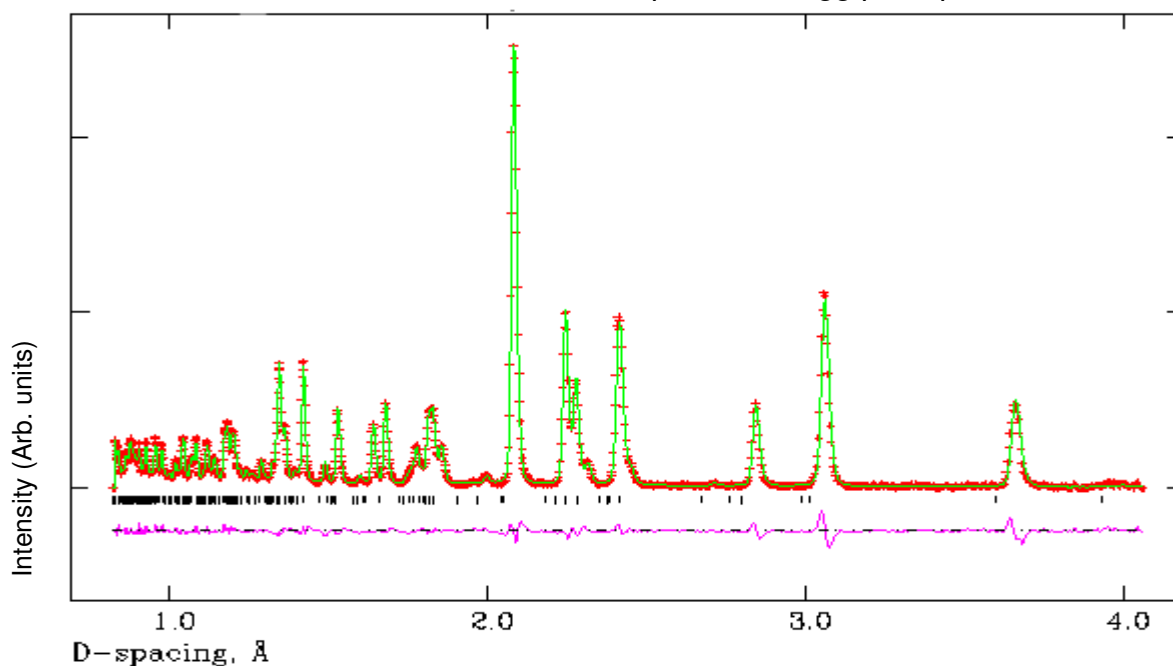
Figure 4.39: Calculated (green), experimental (red) and difference (pink) profile plot for Sr$_3$LaNb$_2$TaO$_{12}$ NPD data collected on GEM, Bank 4. Tick marks represent Bragg peak positions.

Atom	Wyckoff	x	y	z	$U_{iso}*100$ $(\mathring{A}^2)$	Frac.
Sr/La1	6c	0	0	0.2861(1)	1.26(7)	0.64(1)/0.36(1)
Sr/La2	6c	0	0	0.1387(1)	0.81(7)	0.86(1)/0.14(1)
Nb/Ta1	6c	0	0	0.4237(1)	0.24(6)	0.75(1)/0.25(1)
Nb/Ta2	3a	0	0	0	0.52(8)	0.50(1)/0.50(1)
O1	18f	0.1133(6)	0.7871(6)	0.6273(1)	0.98(6)	1
O2	18f	0.1082(5)	0.7723(4)	0.4541(1)	0.98(6)	1

Table 4.13: Refinement results for $Sr_3LaNb_2TaO_{12}$ (XRPD and NPD RT data)

Bond lengths (Å)			Bond Angles (°)		
Sr/La(1)-O(1) =	2.863(3)	(x3)	O(1)-Nb/Ta(1)-O(1) =	82.3(1)	(x3)
Sr/La(1)-O(1) =	3.123(2)	(x3)	O(1)-Nb/Ta(1)-O(2) =	165.6(1)	(x3)
Sr/La(1)-O(1) =	2.559(2)	(x3)	O(1)-Nb/Ta(1)-O(2) =	87.8(1)	(x3)
Sr/La(1)-O(2) =	2.603(3)	(x3)	O(1)-Nb/Ta(1)-O(2) =	86.0(1)	(x3)
			O(2)-Nb/Ta(1)-O(2) =	101.0(1)	(x3)
Sr/La(2)-O(1) =	3.190(3)	(x3)			
Sr/La(2)-O(2) =	3.208(2)	(x3)	O(1)-Nb/Ta(2)-O(1) =	94.0(1)	(x6)
Sr/La(2)-O(2) =	2.541(2)	(x3)	O(1)-Nb/Ta(2)-O(1) =	86.0(1)	(x6)
Sr/La(2)-O(2) =	2.608(3)	(x3)	O(1)-Nb/Ta(2)-O(1) =	180.0	(x3)
Nb/Ta(1)-O(1) =	2.138(4)	(x3)			
Nb/Ta(1)-O(2) =	1.876(3)	(x3)			
Nb/Ta(2)-O(1) =	2.006(4)	(x6)			

Table 4.14: Bond lengths and angles from refinement results for $Sr_3LaNb_2TaO_{12}$

The joint XRPD and NPD Rietveld refinement proceeded smoothly in space group R-3. No separate XRPD refinement was required as only two A-cations are present in the composition. Details of the refinement can be found in **figures 4.38** and **4.39** and **tables 4.13** and **4.14**. The refinement converged with lattice parameters a = 5.6653(1) Å and c = 27.2376(3) Å with associated statistics, χ^2 = 3.550, R_{wp} = 7.93% and R_p = 6.15%. The resultant crystal structure can be seen in **figure 4.40**.
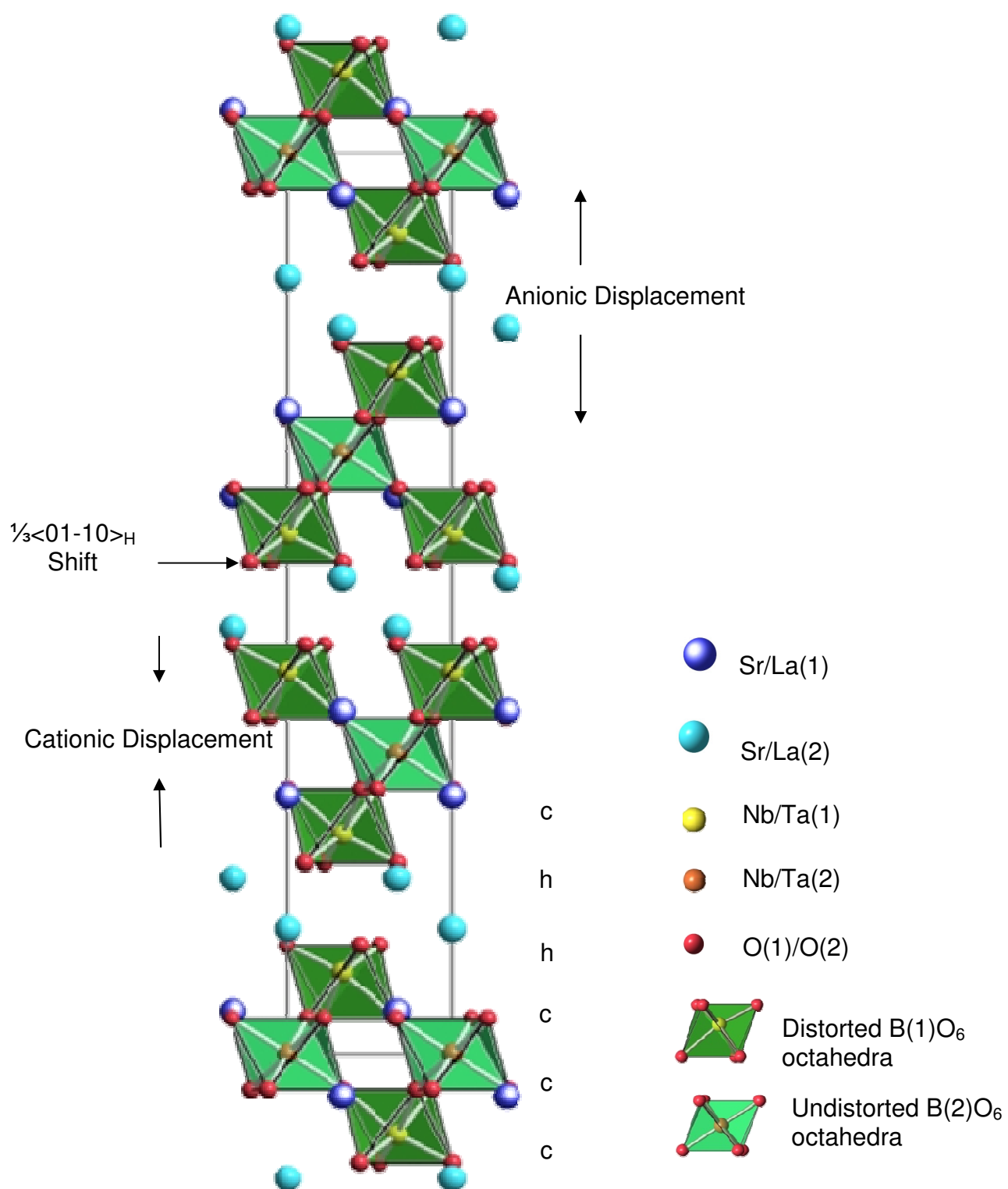
Figure 4.40: Structure of $Sr_3LaNb_2TaO_{12}$ viewed along the *x*-axis.

The Nb^{5+} cations display a preference for B(1) in the distorted octahedra with an occupancy of 75%. There is then an equal distribution of Nb^{5+} / Ta^{5+} across B(2) (50% and 50% respectively) within the undistorted octahedra. This preference of Nb^{5+} to inhabit B(2) is the same preference as that displayed by $Ba_3LaNb_2TaO_{12}$, $Ba_2SrLaNb_2TaO_{12}$ and $BaSr_2LaNb_2TaO_{12}$. Therefore it is postulated that when two pentavalent B-cations are present, Nb^{5+} and Ta^{5+}, the Nb^{5+} cations display a strong preference to inhabit the distorted environment of B(1). The two different B-cation octahedra can be seen in **figures 4.41** and **4.42**.

The Δd value for B(1) is 42.60 and the Δd value for B(2) is 0. The BO_6 octahedra are antiphase tilted about the z-axis by an angle of 9.5°, **figure 4.43**.

The dominant cation within the structure, Sr^{2+} displays a preference for A(2) in the "shifted" region with an occupancy of 86 %, whereas A(1) has a 2:1 distribution across the site for Sr^{2+} and La^{3+} respectively.

The AO_{12} polyhedra are depicted in **figures 4.44** and **4.45.** There are 3 x A(1)-O bonds of 2.603(3) Å and 3 x A(1)-O bonds of 2.863(3) Å pointing towards neighbouring octahedra within the perovskite block, and 3 x A(1)-O bonds of 2.559(2) Å and 3 x A(1)-O bonds of 3.123(2) Å parallel to the xy-plane within the $A(1)O_{12}$ polyhedra.

The $A(2)O_{12}$ polyhedra have 3 x A(2)-O bonds of 2.608(3) Å pointing into vacant "shifted" region and 3 x A(2)-O bonds of 3.190(3) Å pointing towards triple layers of B-site cations, and 3 x A(2)-O bonds of 3.208(2) Å and 3 x A(2)-O bonds of 2.541(2) Å bonds parallel to xy-plane pointing towards NbO_6 units in the same octahedral layer. The A(2) cations are displaced into shifted region and the degree of shift for both A-cations can be seen in **figure 4.48.**

As expected the AO_{12} polyhedra reveal a more distorted environment in the "shifted" region, than in the perovskite block, with distortion values of $\Delta d = 117.70$ and $\Delta d = 65.74$ correspondingly. This can be seen more clearly in **figures 4.46** and **4.47**, the distorted A-O lattices are projected along the z-axis.

Bond valence sums (BVS) were performed for A(1), A(2), B(1) and B(2) (refer to **section 1.1.1, equation 1.2** and **1.3**), values are listed in **table 4.15**. Overall the

BVS calculations performed suggest the refined crystal structure is valid, however significantly large values are witnessed for the B-sites due to complexity related with the site.

Cation	Theoretical BVS	Calculated BVS	Status
A(1)	2.33	2.44	Over-bonded
A(2)	2.17	2.14	Under-bonded
B(1)	5.05	5.54	Over-bonded
B(2)	5.00	5.55	Over-bonded

Table 4.15: BVS calculation results for $Sr_3LaNb_2TaO_{12}$
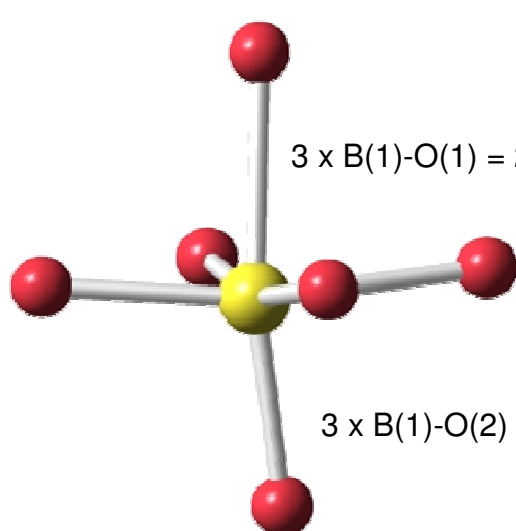
Figure 4.41: Distorted B(1)O6 octahedron adjacent to the "shifted" region (red spheres O^{2-}, yellow sphere B(1) cation). Associated bond lengths labelled.

3 x B(1)-O(1) = 2.138(4) Å

3 x B(1)-O(2) = 1.876(3) Å
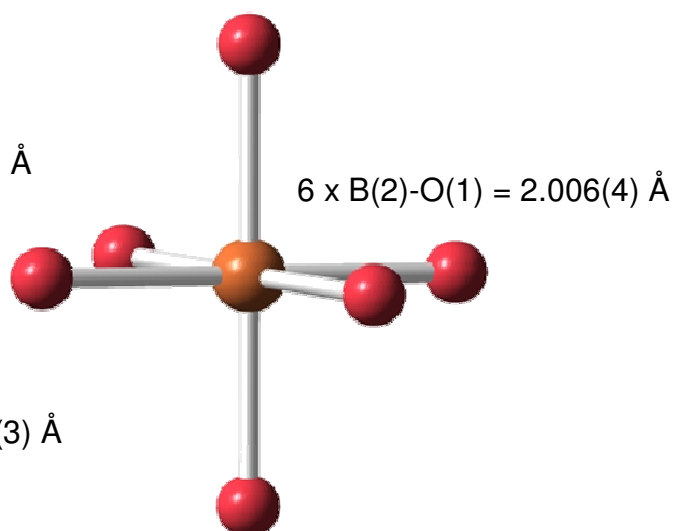
Figure 4.42: Undistorted B(2)O6 octahedron in the centre of the perovskite block (red spheres O^{2-}, orange sphere B(2) cation). Associated bond lengths labelled.

6 x B(2)-O(1) = 2.006(4) Å
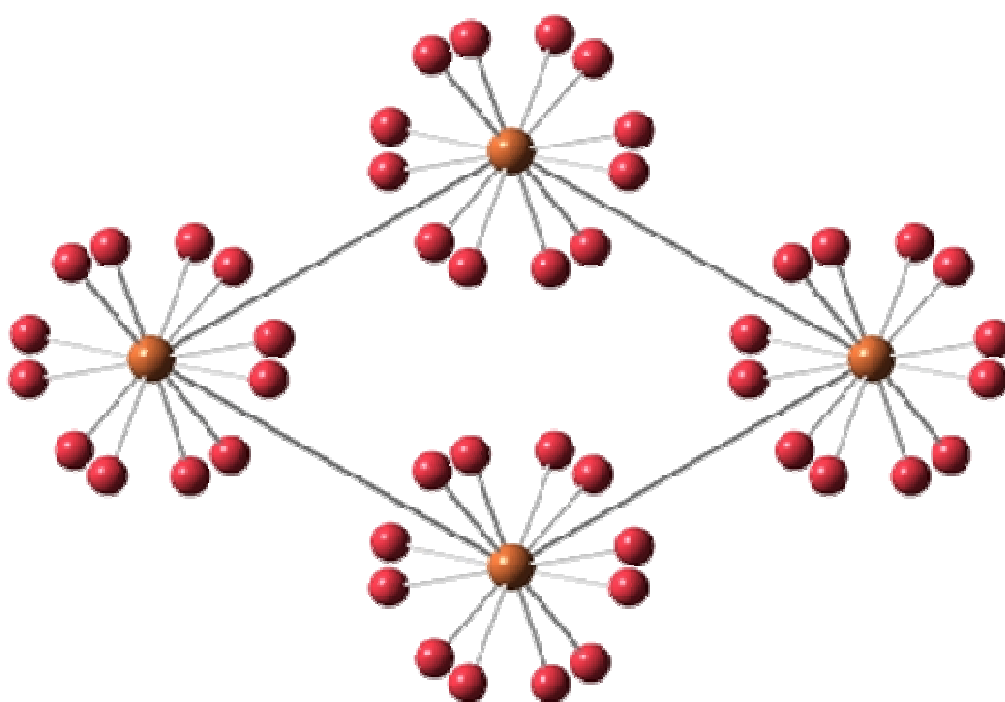
Figure 4.43 View of $Sr_3LaNb_2TaO_{12}$ structure along the *z*-axis showing tilting of the octahedra, tilt angle 9.5° [a^- a^- a^-] (octahedra omitted for clarity). (Red spheres O^{2-}, Orange spheres Nb^{5+}/Ta^{5+}).
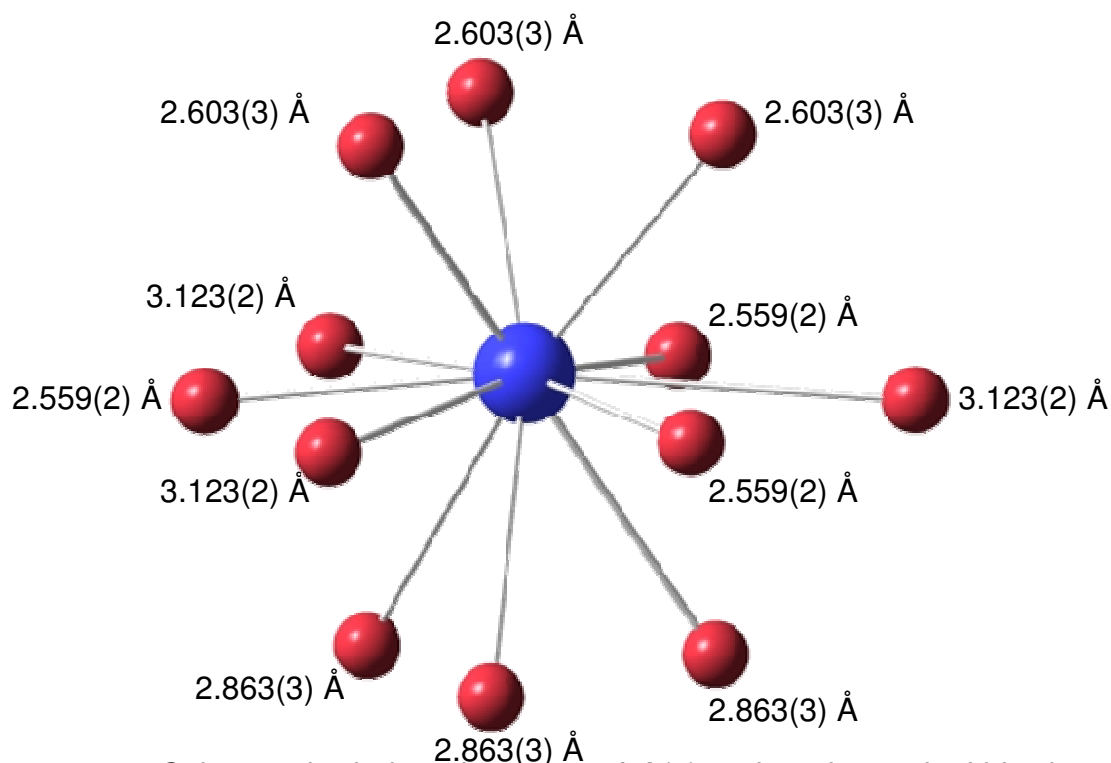
Figure 4.44: Cubo-octahedral environment of A(1) cations located within the triple layer of BO_6 octahedra with Sr^{2+} / La^{3+} distribution of 0.64 / 0.36 (red spheres O^{2-}, blue sphere Sr^{2+} / La^{3+}). Bond lengths are labelled.
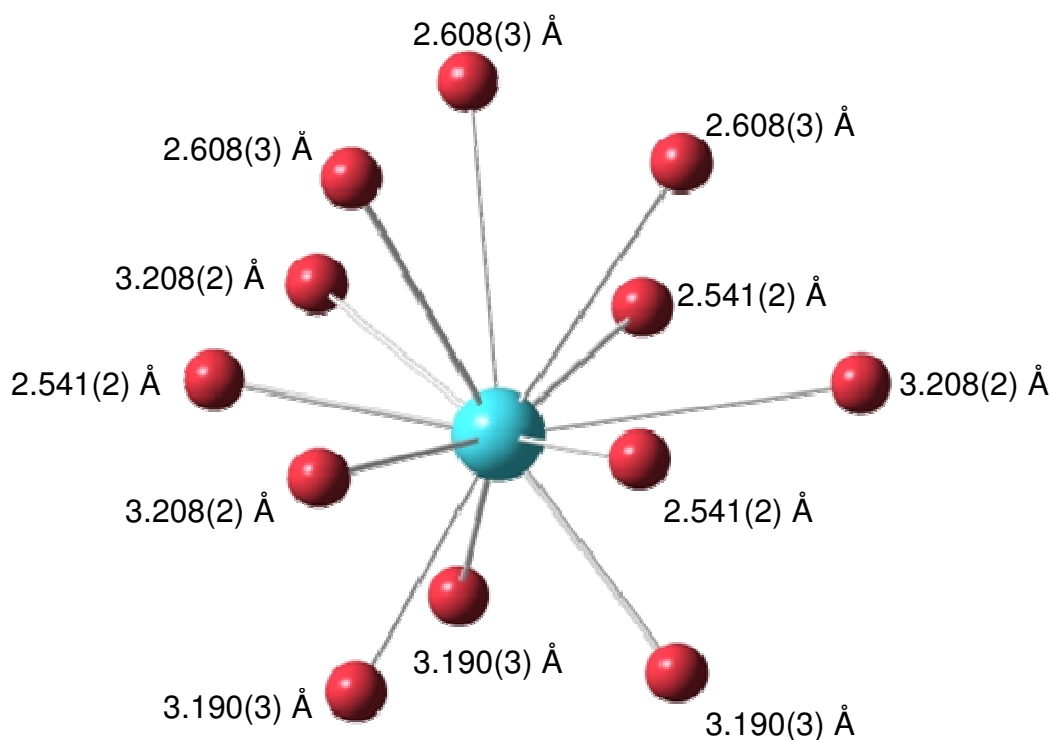
Figure 4.45: Cubo-octahedral environment of A(2) cations located in "shifted" region with a Sr^{2+} / La^{3+} distribution of 0.86 / 0.14 (red spheres O^{2-}, blue sphere Sr^{2+} / La^{3+}). Bond lengths are labelled.
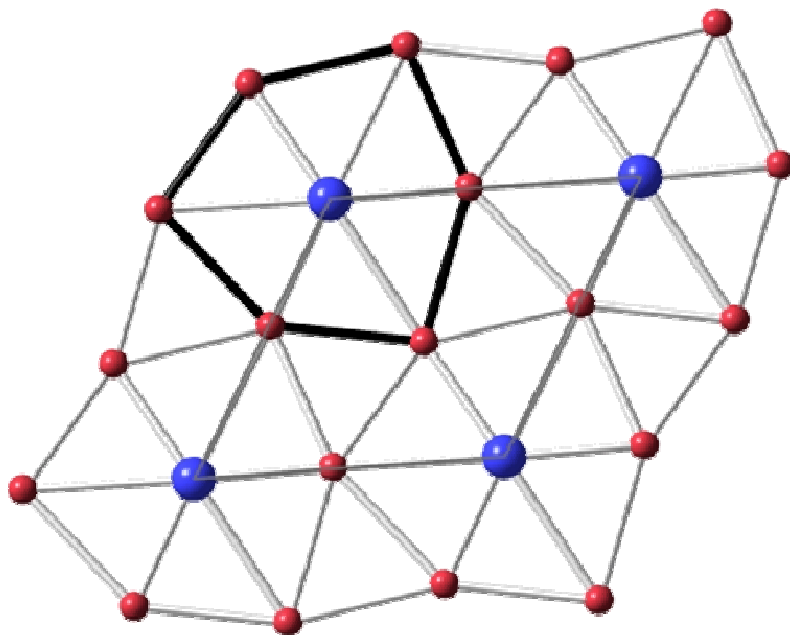
Figure 4.46: View of the distorted A(1)-O lattice along the *z*-axis, O^{2-} ions not parallel to the *xy*-plane are omitted for clarity. Black outline shows a "slice" through the AO_{12} polyhedra, 3 x A(1)-O bonds of 3.123(2) Å and 3 x A(1)-O bonds of 2.559(2) Å parallel to the *xy*-plane. A-cations are located on the corners of the unit cell, outlined in grey. (Red spheres O^{2-}, blue spheres Sr^{2+} / La^{3+}).
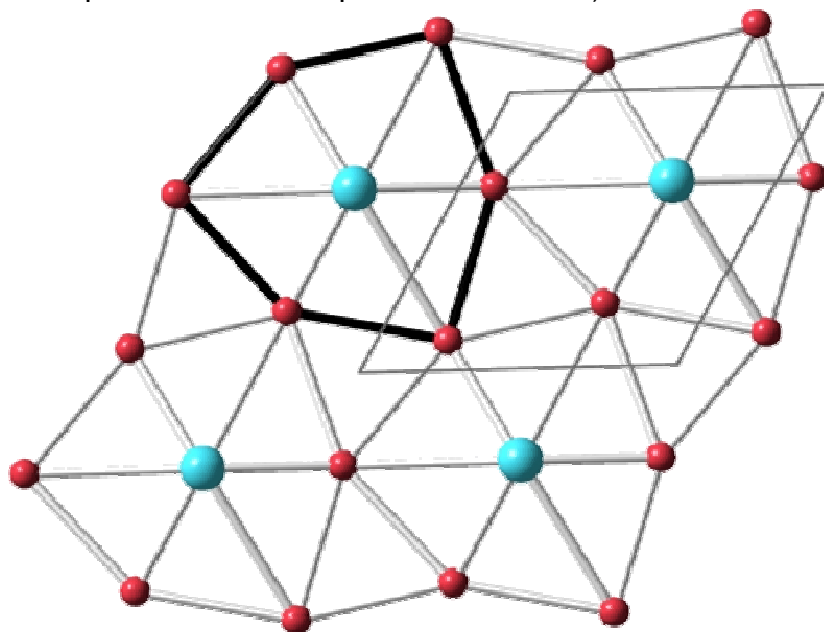
Figure 4.47: View of the distorted A(2)-O lattice along the *z*-axis, O^{2-} ions not parallel to the *xy*-plane are omitted for clarity. Black outline shows a "slice" through the AO_{12} polyhedra, 3 x A(1)-O bonds of 3.208(2) Å and 3 x A(1)-O bonds of 2.541(2) Å parallel to the *xy*-plane. Unit cell is outlined in grey. (Red spheres O^{2-}, blue spheres Sr^{2+} / La^{3+}).
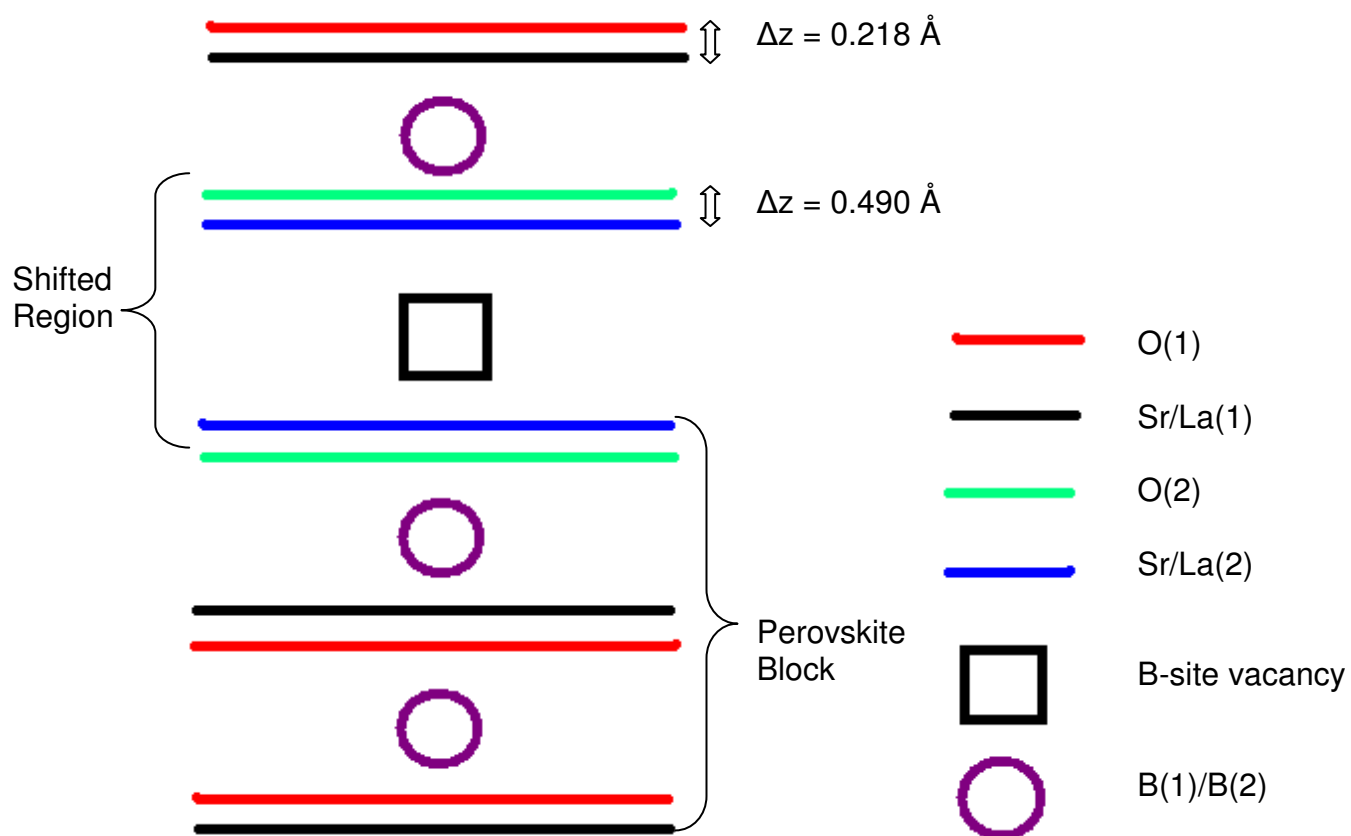
Figure 4.48: A schematic diagram showing A-O displacement along the *z*-axis (Δz) for $Sr_3LaNb_2TaO_{12}$ (not to scale).

$Sr_3LaNb_2TaO_{12}$ has a variance value of 11.40×10^{-4}, as depicted in **figure 4.49**. (For clarity, Δ values are quoted in figures omitting the factor 10^{-4}).

$\Delta = 11.40$

(a)   (b)
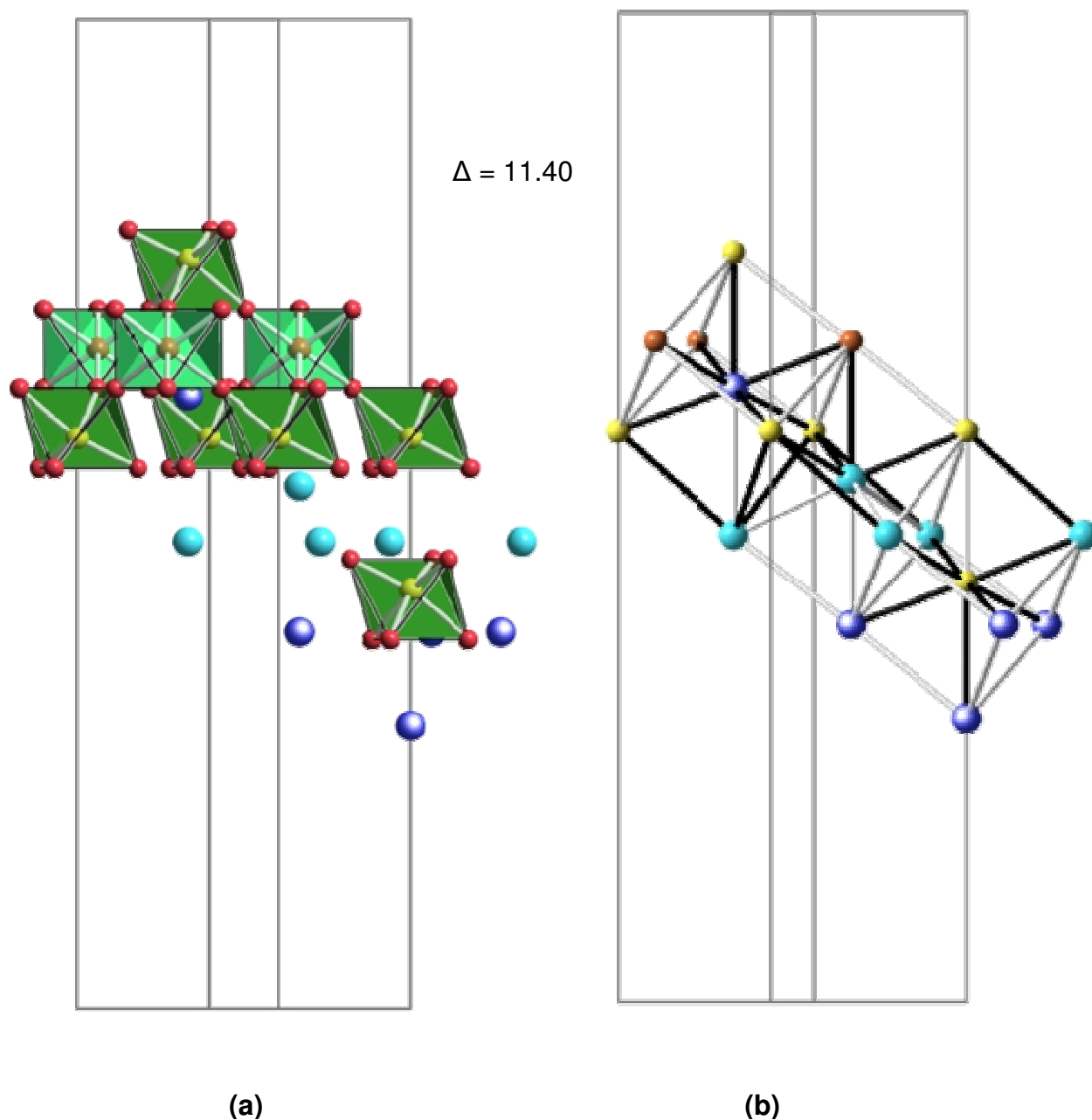
Figure 4.49: **(a)** A- and B-cations involved in the three *bcc* unit cells (O^{2-} ions shown not involved in the *bcc* cation sublattice) **(b)** Structural view of the *bcc* lattice along the *xy*-direction, for $Sr_3LaNb_2TaO_{12}$. Black bonds highlight the A-B distances (bond lengths) selected for calculation of the variance, Δ. (Red spheres O^{2-}, blue spheres Sr^{2+} / La^{3+}, yellow / orange spheres Nb^{5+}/Ta^{5+}).

4.3.2 Discussion

All solid solution members, $Ba_3LaNb_2TaO_{12}$, $Ba_2SrLaNb_2TaO_{12}$, $BaSr_2LaNb_2TaO_{12}$ and $Sr_3LaNb_2TaO_{12}$ crystallise in the 12R structure with antiphase tilting of the BO_6 octahedra along the z-axis.

As previously found for the $Ba_{3-x}Sr_xLaNb_3O_{12}$ series, due to the vacancies within the crystal structures the anion sublattice is under tension and the cation sublattice is compressed. To prevail over these structural impediments the anions and cations are displaced in opposite directions. This displacement relieves the strain within the structure and allows relaxation of the cationic sublattice, which facilitates the reconstruction of the *bcc* cationic sublattice. The reconstruction of the *bcc* cationic sublattice therefore contributes to the stability of the crystal structures.

The variance, Δ for the solid solution members is depicted in ***figure 4.50***. It was found that as Sr^{2+} content within the structure is increased the variance, Δ across the "shifted" region decreases.
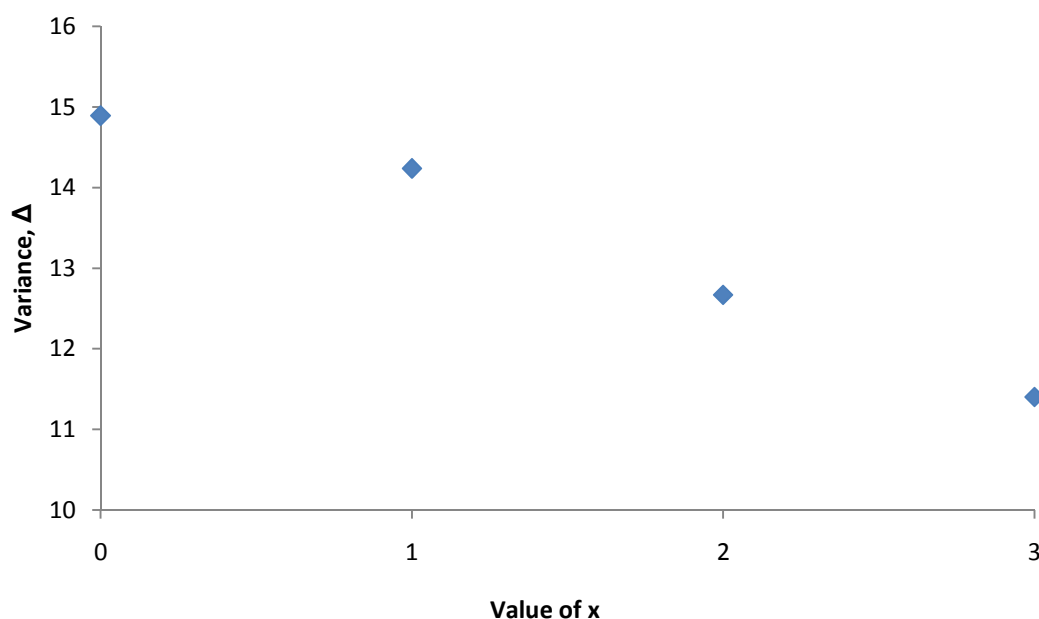
Figure 4.50: Variance, Δ for the $Ba_{3-x}Sr_xLaNb_2TaO_{12}$ series.

The anions and cations in the structures are cooperatively displaced in opposite directions along the z-axis. This displacement between O^{2-} anions and A-cations is

quantified by the Δz shift values seen in **figures 4.10, 4.23, 4.38** and **4.48**, for $Ba_3LaNb_2TaO_{12}$, $Ba_2SrLaNb_2TaO_{12}$, $BaSr_2LaNb_2TaO_{12}$ and $Sr_3LaNb_2TaO_{12}$ respectively. The Δz shift values summarised in **table 4.16**, clearly demonstrate that the A-cations and O^{2-} anions in the "shifted" region are more displaced than in the perovskite block. Across the series a reduction in Δz shift values for both A-sites is witnessed as Sr^{2+} content increases. However when there are three A-cations present and the dominant A-cation is Ba^{2+}, the A(1)-O(1) Δz shift value is larger than that for the rest of the series. This can be attributed to the majority A-cation being larger than the other two A-cations and hence some of it must occupy A(1), its un-preferred site where more distortion occurs. Alternatively when Sr^{2+} is the dominant A-cation when three A-cations are present, the A(2)-O(2) Δz shift value is larger than that for the rest of the series. As Sr^{2+} is one of the smaller A-cations it is forced to occupy A(2) within the "shifted" region which is the preferred site of Ba^{2+} hence there is more distortion in this region.

Composition	$Ba_3LaNb_2TaO_{12}$	$Ba_2SrLaNb_2TaO_{12}$	$BaSr_2LaNb_2TaO_{12}$	$Sr_3LaNb_2TaO_{12}$
A(1)-O(1) Perovskite block Δz (Å)	0.225	0.280	0.221	0.212
A(2)-O(2) "Shifted region" Δz (Å)	0.506	0.503	0.526	0.490

Table 4.16: Summary of Δz shift values for $Ba_{3-x}Sr_xLaNb_2TaO_{12}$ series

As a consequence of the cooperative displacement of anions and cations in opposite directions the AO_{12} polyhedra become distorted, consisting of unequal bond lengths. The distortion within the AO_{12} polyhedra has been quantified by the parameter Δd (previously discussed in **section 1.1.2, equation 1.4**) the distortion values for the series are summarised in **table 4.17**. As the Sr^{2+} content is increased the Δd value increases, this in turn is reflected not only by the increasing BO_6 octahedral tilt angle values but also by a clear distortion in the oxygen sublattice.

Composition	$Ba_3LaNb_2TaO_{12}$	$Ba_2SrLaNb_2TaO_{12}$	$BaSr_2LaNb_2TaO_{12}$	$Sr_3LaNb_2TaO_{12}$
$A(1)O_{12} \Delta d$ (x 10^{-4})	24.95	45.63	59.09	65.74
$A(2)O_{12} \Delta d$ (x 10^{-4})	43.89	61.04	87.35	117.70

Table 4.17: Summary of the Δd values for the AO_{12} polyhedra.

The AO_{12} polyhedral distortion is larger for the A(2) cations located within the "shifted" region and the difference between the extent of distortion between A(1) and A(2) cations is increased as Sr^{2+} content increases.

It is clear from the A-site occupancies listed in **table 4.18** that compared to the $Ba_{3-x}Sr_xLaNb_3O_{12}$ series when Ta^{5+} is introduced on the A-site it induces some form of ordering on the A-site. When there are two A-cations, and Ba^{2+} is the majority A-cation, the A-site is fully ordered with the Ba^{2+} preferring to reside in the "shifted" region and an equal distribution of Ba^{2+} and La^{3+} across A(1). For $BaSr_2LaNb_2TaO_{12}$ there are distinct preferences for sites displayed as is the case for $Ba_2SrLaNb_2TaO_{12}$. Therefore it appears due to the presence of three A-cations the process of ordering is not as easily achieved as more structural complications are introduced with an extra A-cation. For the $Sr_3LaNb_2TaO_{12}$ composition a definite preference for A(2) is exhibited, however, there is no distinct ordering as witnessed in the Ba-rich counterpart.

Structure	Element	A(1) occupancy	A(2) occupancy
$Ba_3LaNbTa_2O_{12}$	Ba / La	0.50/0.50	1.00/0.00
$Ba_2SrLaNbTa_2O_{12}$	Ba / Sr / La	0.25(2)/0.36/0.40(2)	0.76(2)/0.14/0.11(2)
$BaSr_2LaNbTa_2O_{12}$	Ba / Sr / La	0.06(1)/0.44(1)/0.50	0.44(1)/0.56(1)/0.00
$Sr_3LaNbTa_2O_{12}$	Sr / La	0.64(1)/0.36(1)	0.86(1)/0.14(1)

Table 4.18: A-site occupancies for the $Ba_{3-x}Sr_xLaNb_2TaO_{12}$ series.

The cationic and anionic displacements result in the B-cations in the octahedra adjacent to the "shifted" region being displaced toward one triangular octahedron face pointing to the "shifted" region. Therefore the octahedral environment of B(1) is distorted and B(2) is undistorted. Once again the degree of distortion within the BO_6

octahedra has been quantified by the parameter Δd and the results are summarised in **table 4.19**. As opposed to the increased distortion witnessed for the AO_{12} polyhedra as Sr^{2+} content is increased the degree of distortion within the BO_6 octahedra reduces upon increased Sr^{2+} content.

Composition	$Ba_3LaNb_2TaO_{12}$	$Ba_2SrLaNb_2TaO_{12}$	$BaSr_2LaNb_2TaO_{12}$	$Sr_3LaNb_2TaO_{12}$
B(1)O$_6$ Δd (x 10^{-4})	56.17	50.34	44.36	42.60

Table 4.19: Summary of the Δd values for the B(1)O$_6$ octahedra.

The BO_6 octahedra in all of the structures are rotated about the *z*-axis resulting in anti-phase tilting. The degree of tilting within the structures is quantified by the tilt angle, listed in **table 4.20**.

Composition	$Ba_3LaNb_2TaO_{12}$	$Ba_2SrLaNb_2TaO_{12}$	$BaSr_2LaNb_2TaO_{12}$	$Sr_3LaNb_2TaO_{12}$
Tilt Angle (°)	4.5	7	9	9.5

Table 4.20: Table summarising the room temperature tilt angles for the $Ba_{3-x}Sr_xLaNb_2TaO_{12}$ series.

As all of the structures are tilted it is postulated that a similar phenomenon may occur for this series as with the $Ba_{3-x}Sr_xLaNb_3O_{12}$ series, wherein a tilt transition may occur from R-3 to R-3m at elevated temperatures. A peak in permittivity may occur for members of this series, however, based on the evidence from the $Ba_{3-x}Sr_xLaNb_3O_{12}$ series, the temperature at which the peak occurs may not correlate to the temperature at which the tilt transition occurs. As Nb^{5+} and Ta^{5+} are the same size the tolerance factors for this series are the same as for the $Ba_{3-x}Sr_xLaNb_3O_{12}$ series, *i.e.* 1.022, 1.007, 0.992 and 0.977 for $Ba_3LaNb_2TaO_{12}$, $Ba_2SrLaNb_2TaO_{12}$, $BaSr_2LaNb_2TaO_{12}$ and $Sr_3LaNb_2TaO_{12}$ respectively.

Interestingly when two pentavalent B-cations are present in the structure, Nb^{5+} and Ta^{5+} which are the same size and charge, the Nb^{5+} cations display a preference to occupy the distorted environment of B(1). There is no simple electrostatic or site related reason why this would occur therefore it seems when both Nb^{5+} and Ta^{5+} are present together something more complex is occurring. Furthermore it seems when Ba^{2+} is the dominant A-cation a higher percentage of Nb^{5+} occupies the distorted

octahedra than when Sr^{2+} is the dominant A-cation. The relevant occupancies are listed in **table 4.21**.

Structure	Ba$_3$LaNb$_2$TaO$_{12}$	Ba$_2$SrLaNb$_2$TaO$_{12}$	BaSr$_2$LaNb$_2$TaO$_{12}$	Sr$_3$LaNb$_2$TaO$_{12}$
B(1) Nb/Ta occupancy	0.79(1)/0.21(1)	0.80(2)/0.20(2)	0.72(1)/0.28(1)	0.75(1)/0.25(1)
B(2) Nb/Ta occupancy	0.42(2)/0.58(2)	0.40(3)/0.60(3)	0.57(2)/0.43(2)	0.50(1)/0.50(1)

Table 4.21: B-site occupancies for the Ba$_{3-x}$Sr$_x$LaNb$_2$TaO$_{12}$ series.

4.4 Electrical Characterisation

4.4.1 Microwave Dielectric Properties

The microwave dielectric properties for the Ba$_{3-x}$Sr$_x$LaNb$_2$TaO$_{12}$ series are summarised in **table 4.22**.

Composition	ε_r	Q (GHz)	TCF (ppm / °C)	Relative Density
Ba$_3$LaNb$_2$TaO$_{12}$	33	6242	20	87%
Ba$_2$SrLaNb$_2$TaO$_{12}$	30	9803	9	90%
BaSr$_2$LaNb$_2$TaO$_{12}$	28	16932	14	89%
Sr$_3$LaNb$_2$TaO$_{12}$	25	3777	7	85%

Table 4.22: Microwave dielectric properties of Ba$_{3-x}$Sr$_x$LaNb$_2$TaO$_{12}$ series

The microwave dielectric properties of the series must be interpreted with caution due to the extrinsic effects associated with the low density of some pellets, which is known to influence Q values and to provide unreliable TCF values. The LCR data provided, however, should provide a reasonable idea of behaviour with temperature.

A comparison of the theoretical values of ε_r (calculated using the CM equation) and the experimental values of ε_r are listed in **table 4.23**. The theoretical values are slightly different to the experimental values. Experimentally Ta-based compounds

are often known to give a lower slightly lower ε_r values compared to Nb-based compounds. The reason for this difference is unknown however a recent paper[8] suggests that the difference is due to a larger covalency associated with the Ta-O bond compared to the Nb-O bond which affects the oscillation of the O^{2-} anions, which in turn influence the ε_r values. This issue of covalency may also be the reason for the interesting structural results obtained concerning B-site ordering.

Composition	Experimental ε_r	Theoretical ε_r^*
$Ba_3LaNb_2TaO_{12}$ (x=0)	33	32
$Ba_2SrLaNb_2TaO_{12}$ (x=1)	30	26
$BaSr_2LaNb_2TaO_{12}$ (x=2)	28	41
$Sr_3LaNb_2TaO_{12}$ (x=3)	25	35

*Modified αNb^{5+} and αTa^{5+} values were used when, tolerance factor > 1 αNb^{5+} = 3.8 $Å^3$, αTa^{5+} = 2.7 $Å^3$ [9] and tolerance factor < 1 αNb^{5+} = 4.65 $Å^3$, αTa^{5+} = 4.55 $Å^3$ [10].

Table 4.23: Comparison of experimental ε_r and theoretical ε_r calculated using the Clausius-Mossotti equation (**section 1.2.1.1, equation 1.6**).

A reduction in $\mathbf{\varepsilon_r}$ is witnessed as the Sr^{2+} content is increased (**figure 4.51**), this is expected as Sr^{2+} has a smaller ionic polarisability than Ba^{2+}. The $\mathbf{\varepsilon_r}$ values for this series are significantly lower than those displayed by the $Ba_{3-x}Sr_xLaNb_3O_{12}$ series, however this is expected of ceramics containing Ta^{5+}. Conversely the Q value increases as Sr^{2+} content increases, (**figure 4.52**) this can be explained by the reduction in size difference over the A-site as more Sr^{2+} is introduced in place of Ba^{2+}. However the Q value for $Sr_3LaNb_2TaO_{12}$ does not follow this trend and has a significantly lower value than $BaSr_2LaNb_2TaO_{12}$.

It was hypothesised that the introduction of Ta^{5+} on the B-site would improve the Q values compared to the $Ba_{3-x}Sr_xLaNb_3O_{12}$ series. However it was established from previous work[1, 2] that the Sr-rich phase sees a reduction in Q value upon the introduction of Ta^{5+}, but the Ba-rich phase exhibits a marked improvement. The microwave results for the $Ba_{3-x}Sr_xLaNb_2TaO_{12}$ series did not entirely reflect this concept. The introduction of one Ta^{5+} cation on the B-site leads to an improvement

in the Q value for the intermediate compositions, and a reduction in this value for the end members compared to the $Ba_{3-x}Sr_xLaNb_3O_{12}$ series.
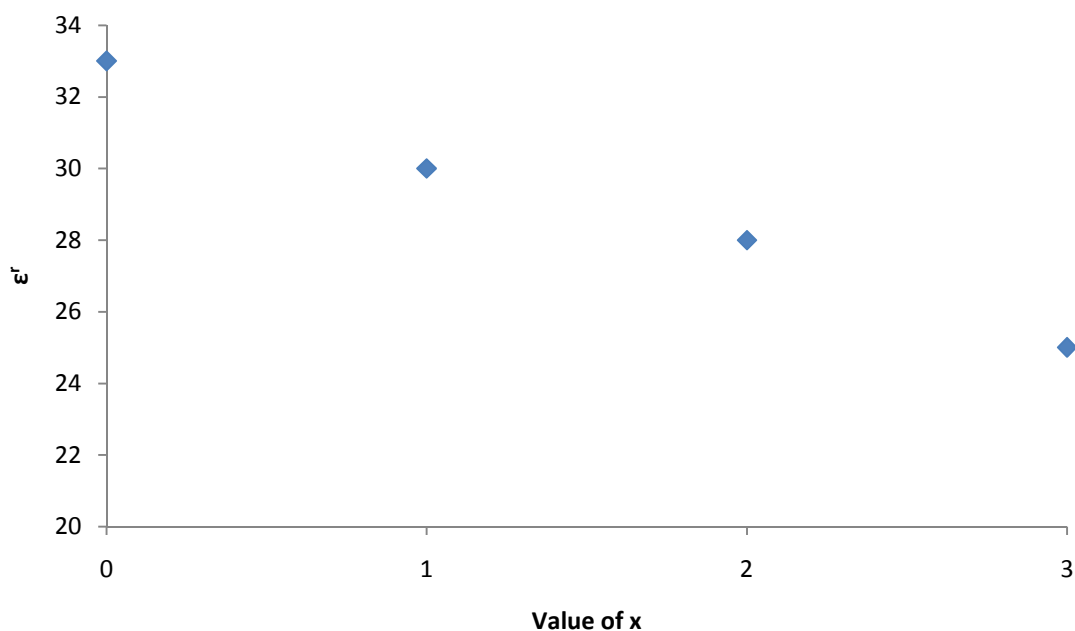

Figure 4.51: Graph to show the evolution of ε_r as Sr^{2+} content increases
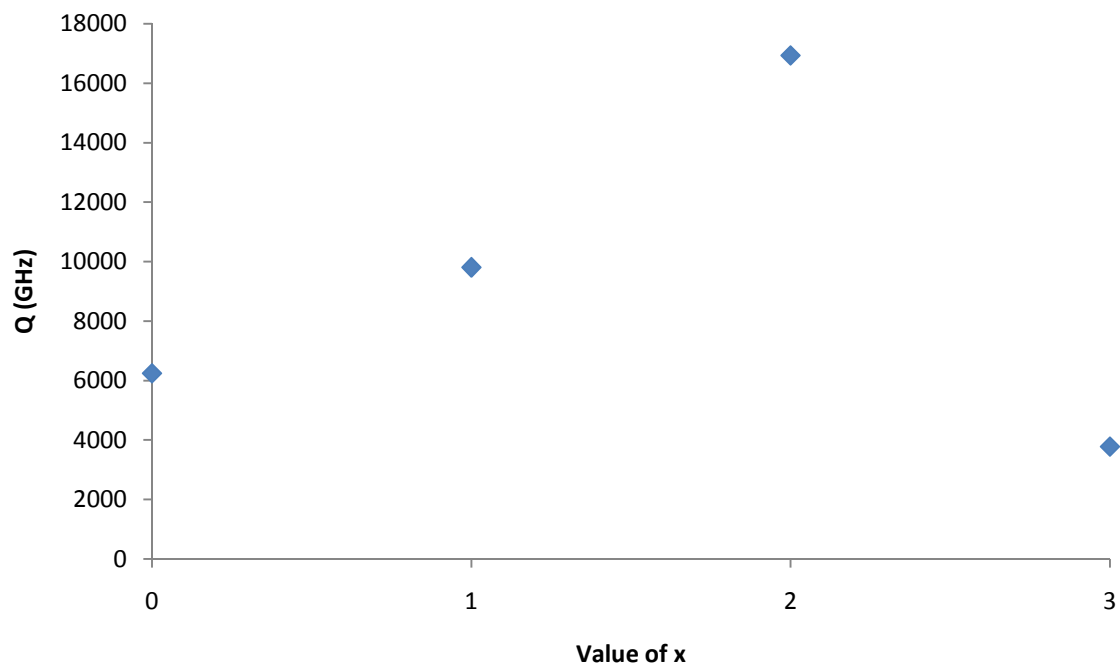
Figure 4.52: Graph to show the evolution of Q as Sr^{2+} content increases.

The TCF values for the series are all positive and relatively small. Compared to the $Ba_{3-x}Sr_xLaNb_3O_{12}$ series, the introduction of one Ta^{5+} has significantly improved the TCF values for the Ba- and Sr-rich phases, and has only slightly affected the values for the intermediate compositions. In comparison to the $Ba_{3-x}Sr_xLaNb_3O_{12}$ series, these are significantly different, and in some cases improved TCF values may be attributed to the increased covalency of the Ta-O bonds compared to the Nb-O bonds.

Although the tolerance factors for members of this series are the same as members of the $Ba_{3-x}Sr_xLaNb_3O_{12}$ series, it appears that the introduction of Ta^{5+} has a different effect on the relationship between TCF and tolerance factor, as depicted in **figure 4.53**. The range of TCF values for the series is smaller and no direct link as yet can be made between tolerance factor and TCF value. Therefore it seems the introduction of Ta^{5+} on the B-site increases the complexity of the structure more than when just three A-cations are present. This in turn has had an effect on the relationship between TCF and tolerance factor, which cannot be fully understood without variable temperature powder diffraction data to establish cation preferences with increasing temperature, and further electrical data.
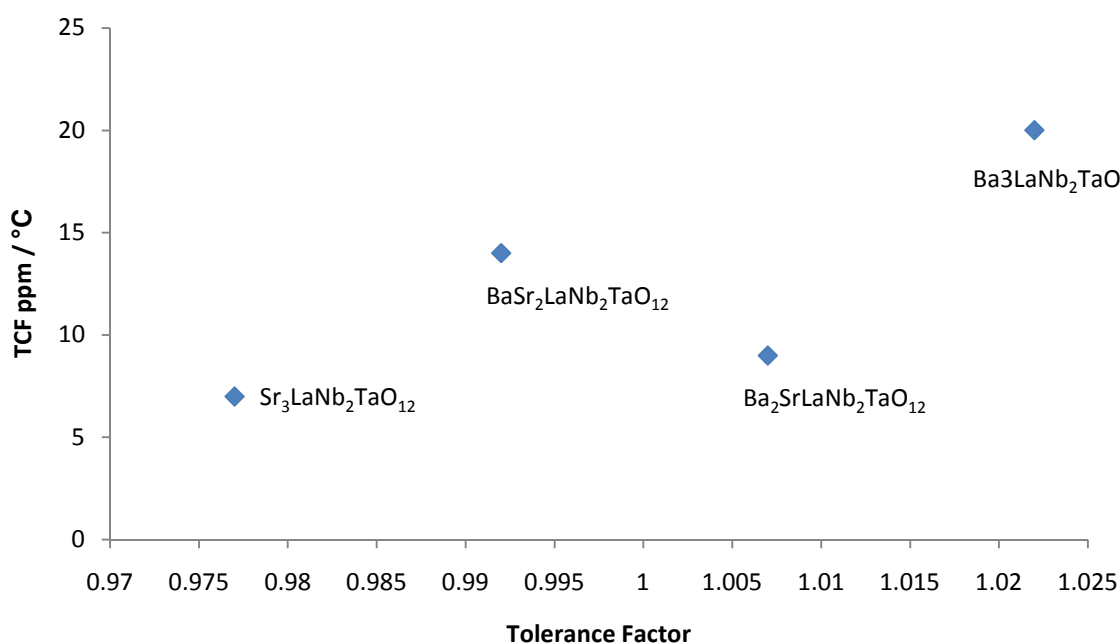

**Figure 4.53**: TCF vs. Tolerance factor for the $Ba_{3-x}Sr_xLaNb_2TaO_{12}$ series.

There is a distinct possibility that the room temperature TCF values obtained may not be representative of a wider temperature range and that these TCF values sit on an unrepresentative region of permittivity, and that if lower temperature electrical data were to be collected it would aid in the explanation of these values. Although due to the low density of pellets this may along with the possible presence of secondary phases be contributing to the unusual TCF values displayed, which would generally be expected to be negative, due to a positive temperature coefficient of permittivity.

4.4.2 LCR Data

LCR data were only collected for $Ba_3LaNb_2TaO_{12}$ and $Sr_3LaNb_2TaO_{12}$, due to time and equipment limitations, the resulting data can be seen in **figures 4.54** and **4.55** respectively.
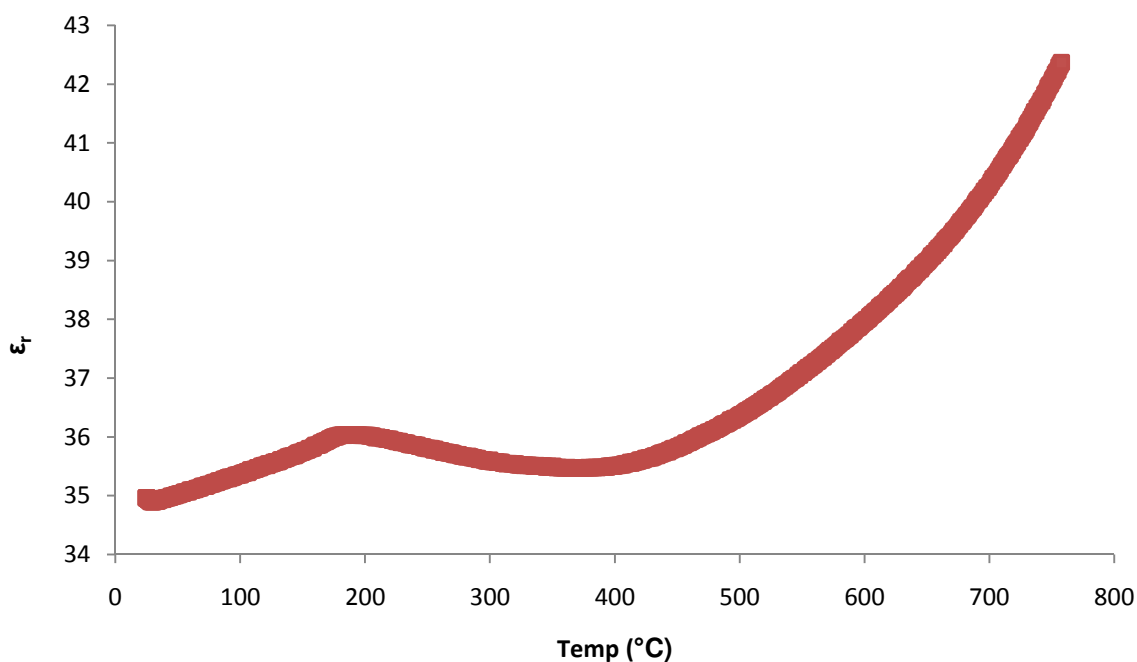
Figure 4.54: Plot of ε_r vs. Temperature for $Ba_3LaNb_2TaO_{12}$ at 1 MHz.
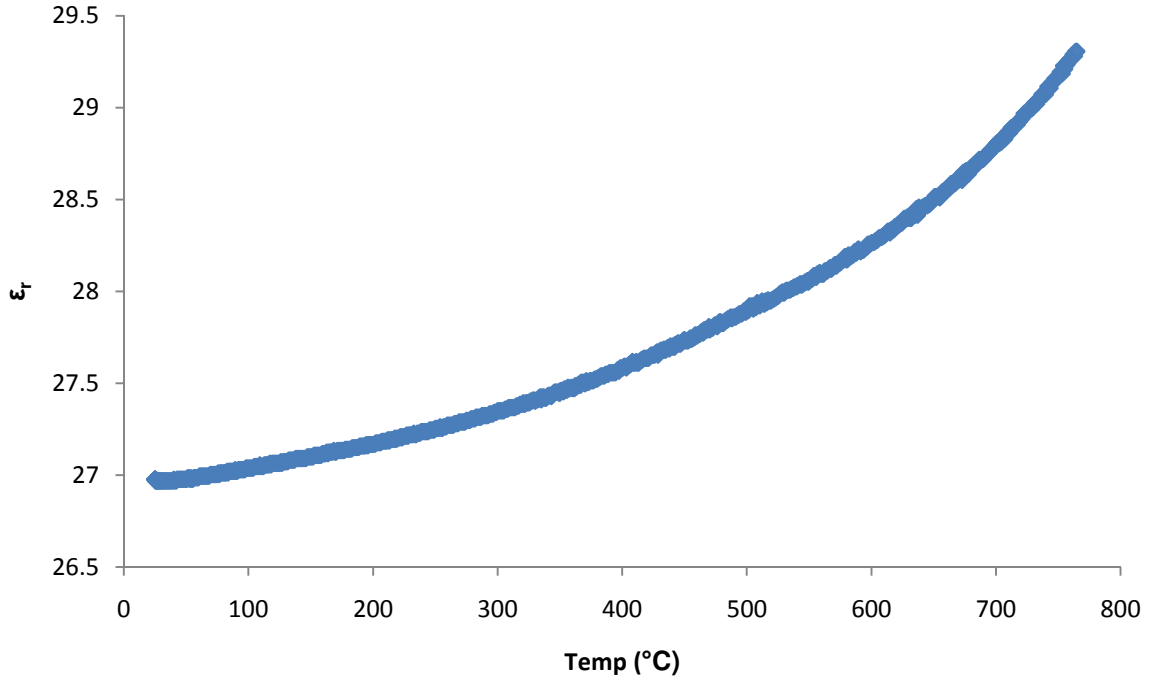
Figure 4.55: Plot of ε_r *vs.* Temperature for $Sr_3LaNb_2TaO_{12}$ at 1 MHz.

It can clearly be seen for $Ba_3LaNb_2TaO_{12}$ that a distinct peak in permittivity occurs at approximately 200 °C at 1 MHz. It is possible that this temperature correlates to the temperature at which a tilt transition occurs, similar to that observed in $Ba_3LaNb_3O_{12}$.[11] Therefore if variable temperature powder diffraction data were to be collected, it is hypothesised that at this temperature and at temperatures below this, structural evidence of this transition would be found.

$Sr_3LaNb_2TaO_{12}$, on the other hand, does not at any temperature display any clear peak or even inflection in permittivity at 1 MHz. This is not surprising since $Sr_3LaNb_3O_{12}$ only exhibits a slight inflection in permittivity at ~447 °C at 1 MHz.[11] Variable temperature NPD data collected for $Sr_3LaNb_3O_{12}$ showed that up to 900 °C the structure remained tilted, and no correlation between the peak in permittivity at 1 MHz and any structural phenomenon could be found. Therefore it is highly possible that the introduction of Ta^{5+} increases the temperature at which the tilt transition occurs at, or that no peak is observed because there is high degree of structural complexity related to the electrical response.

It would be useful to obtain LCR data for the intermediate compositions $Ba_2SrLaNb_2TaO_{12}$ and $BaSr_2LaNb_2TaO_{12}$ to see if any peaks in permittivity occur,

189

and if so, if they are at similar temperatures to the intermediate compositions of the $Ba_{3-x}Sr_xLaNb_3O_{12}$ series. Ultimately variable temperature powder diffraction data are required to investigate the evolution of the crystal structures with increasing temperature, which will also aid in the interpretation of the electrical data obtained.

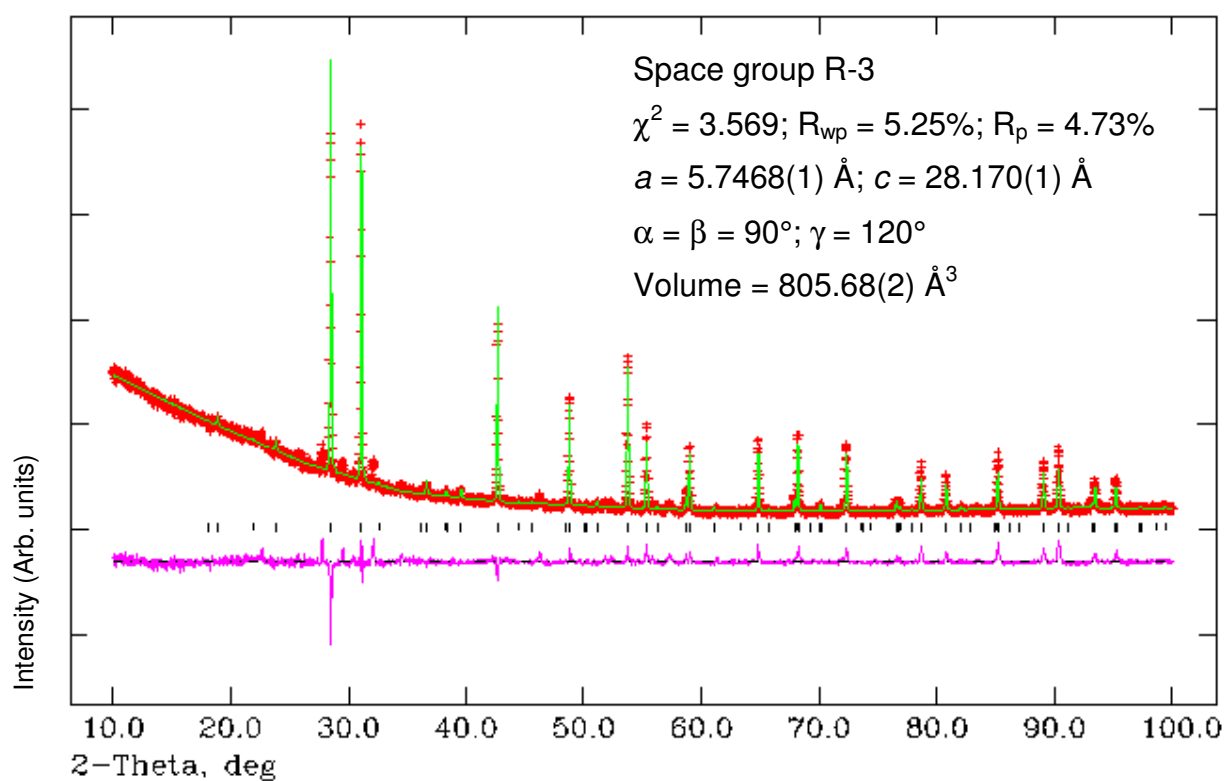## 4.5 Structural Characterisation of $Ba_{3-x}Sr_xLaNbTa_2O_{12}$ Series

4.5.1 X-ray Powder Diffraction (XRPD) and Neutron Powder Diffraction (NPD)

Refer to **section 4.3.1** for XRPD and NPD refinement specifics and data collection sources for the $Ba_{3-x}Sr_xLaNbTa_2O_{12}$ Series. Joint XRPD and NPD refinements of the models is performed for the compositions containing only two A-cations and method (iv) is followed for the refinements of models of compositions containing three A-cations.

4.5.1.1 $Ba_3LaNbTa_2O_{12}$

4.5.1.1.1 Joint XRPD and NPD refinement

The refinement results are summarised below in **figures 4.56** and **4.57,** and **tables 4.24** and **4.25** Refinement statistics and lattice parameters are given in **figure 4.56**.

Space group R-3

χ^2 = 3.569; R_{wp} = 5.25%; R_p = 4.73%

a = 5.7468(1) Å; c = 28.170(1) Å

$\alpha = \beta = 90°$; $\gamma = 120°$

Volume = 805.68(2) $Å^3$

Figure 4.56: Calculated (green), experimental (red) and difference (pink) profile plot for $Ba_3LaNbTa_2O_{12}$ XRPD data. Tick marks represent Bragg peak positions.
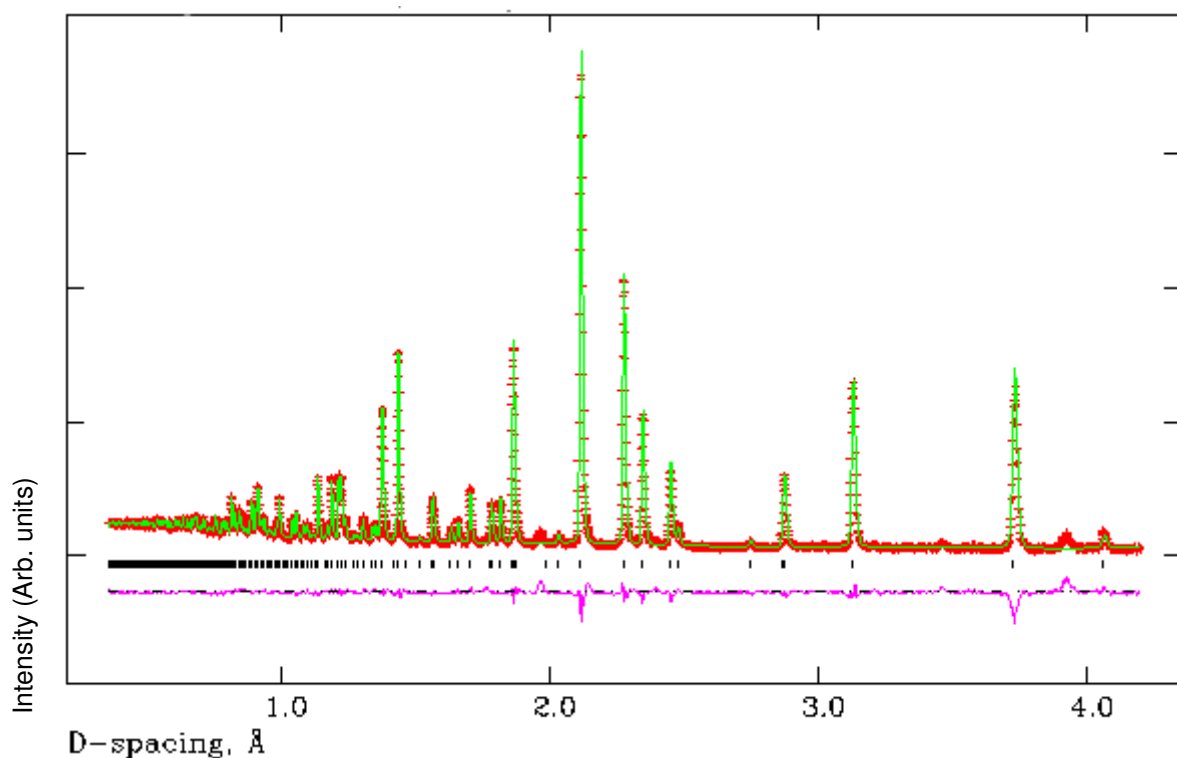
Figure 4.57: Calculated (green), experimental (red) and difference (pink) profile plot for $Ba_3LaNbTa_2O_{12}$ NPD RT data on POLARIS (bank 1). Tick marks represent Bragg peak positions.

Atom	Wyckoff	x	y	z	$U_{iso}*100$ $(\mathring{A}^2)$	Frac.
Ba/La1	6c	0	0	0.2864(1)	0.11(2)	0.50/0.50
Ba/La2	6c	0	0	0.1376(1)	1.00	1.0/0.0
Nb/Ta1	6c	0	0	0.4205(1)	0.09(2)	0.32(2)/0.68(2)*
Nb/Ta2	3a	0	0	0	1.00	0.37(5)/0.64(5)*
O1	18f	0.1786(5)	0.8505(5)	0.6284(1)	1.50(3)	1
O2	18f	0.1879(4)	0.8558(4)	0.4516(1)	0.91(3)	1

*Due to rounding up the B-site occupancies are slightly over/under the stated composition.

Table 4.24: Refinement results for $Ba_3LaNbTa_2O_{12}$ (XRD & POLARIS RT data)

Bond lengths (Å)			Bond Angles (°)		
Ba/Sr/La(1)-O(1) =	2.903(2)	(x3)	O(1)-Nb/Ta(1)-O(1) =	83.0(1)	(x3)
Ba/Sr/La(1)-O(1) =	2.800(3)	(x3)	O(1)-Nb/Ta(1)-O(2) =	167.7(1)	(x3)
Ba/Sr/La(1)-O(1) =	2.967(3)	(x3)	O(1)-Nb/Ta(1)-O(2) =	87.1(1)	(x3)
Ba/Sr/La(1)-O(2) =	2.613(2)	(x3)	O(1)-Nb/Ta(1)-O(2) =	88.7(1)	(x3)
			O(2)-Nb/Ta(1)-O(2) =	99.9(1)	(x3)
Ba/Sr/La(2)-O(1) =	3.267(2)	(x3)			
Ba/Sr/La(2)-O(2) =	2.801(2)	(x3)	O(1)-Nb/Ta(2)-O(1) =	93.7(1)	(x6)
Ba/Sr/La(2)-O(2) =	3.048(2)	(x3)	O(1)-Nb/Ta(2)-O(1) =	86.3(1)	(x6)
Ba/Sr/La(2)-O(2) =	2.748(3)	(x3)	O(1)-Nb/Ta(2)-O(1) =	180.0	(x3)
Nb/Ta(1)-O(1) =	2.138(2)	(x3)			
Nb/Ta(1)-O(2) =	1.875(2)	(x3)			
Nb/Ta(2)-O(1) =	2.002(2)	(x6)			

Table 4.25: Bond lengths and angles from refinement data for $Ba_3LaNbTa_2O_{12}$

Rietveld refinement of $Ba_3LaNbTa_2O_{12}$ following method (iv) proceeded smoothly in space group R-3, although traces of an impurity phase were evidenced, due to additional weak reflections between 28° and 32° 2θ. Details of the refinement can be found in **figures 4.56** and **4.57** and **tables 4.24** and **4.25**. The refinement converged with χ^2 = 3.569, R_{wp} = 5.25%, R_p = 4.73%, with lattice parameters a = 5.7468(1) Å and c = 28.170(1) Å. The resulting structure of $Ba_3LaNbTa_2O_{12}$ can be seen in **figure 4.58**.

.
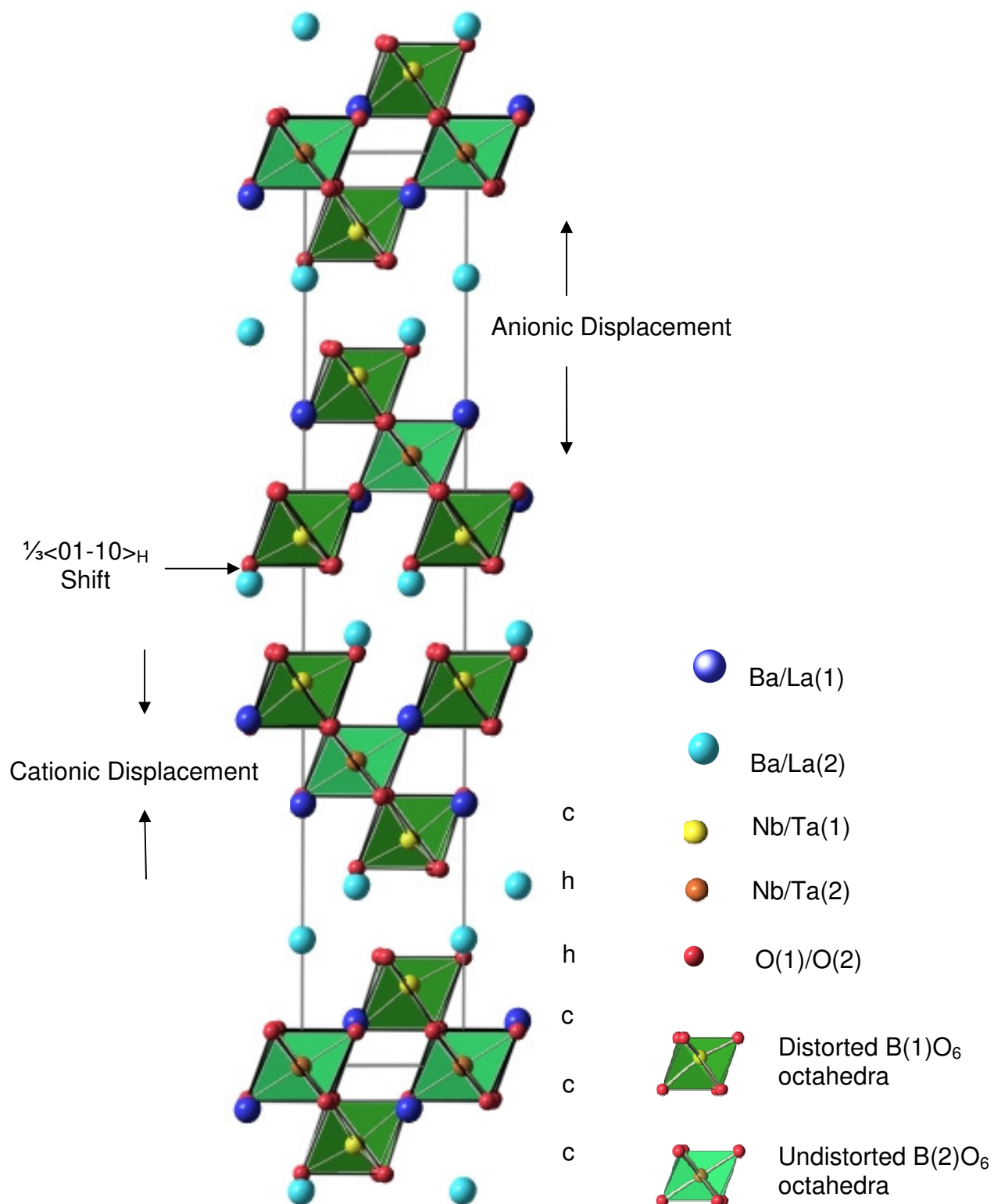
Figure 4.58: Structure of $Ba_3LaNbTa_2O_{12}$ viewed along the *x*-axis.

There is an approximately 1:2 distribution of Nb^{5+} / Ta^{5+} across B(1) and B(2). This distribution is more statistical in terms of site preference than that witnessed for the $Ba_{3-x}Sr_xLaNb_2TaO_{12}$ series where Nb^{5+} is the dominant pentavalent cation. Here it displays a definite preference for B(1), and there is an almost equal distribution of Nb^{5+} / Ta^{5+} across B(2). These random B-site distributions imply that when Ta^{5+} is the dominant B-site cation it does not display a preference for the distorted environment of B(1) like Nb^{5+}. Therefore there is a subtle difference between these cations, of the same charge and size, but that has a definite effect on site preference when both are present on the B-site together. The two different B-cation octahedra can be seen in *figures 4.59* and *4.60*.

Distortion values were calculated for the two types of BO_6 octahedra. The Δd value for the $B(1)O_6$ octahedra is 42.94, and the the Δd value for $B(2)O_6$ is 0. BO_6 octahedra are antiphase tilted about the *z*-axis by an angle of 3°, *figure 4.61*.

The A-sites within the structure are completely ordered with A(2) being composed of 100% Ba^{2+} and a 1:1 split of Ba^{2+} and La^{3+} across A(1). Ba^{2+} preferentially occupies A(2) within the "shifted" region, this is similar to preferences observed in $Ba_3LaNb_2TaO_{12}$.

The cubo-octahedral environment of the A-cations is shown in *figures 4.62* and *4.63*. There are 3 x A(1)-O bonds of 2.613(2) Å and 3 x A(1)-O bonds of 2.903(2) Å pointing towards neighbouring octahedral layers of B-cations (along the direction of the *z*-axis) and 3 x A(1)-O bonds of 2.800(3) Å and 3 x A(1)-O bonds of 2.967(3) Å parallel to the *xy*-plane pointing towards BO_6 units in the same octahedral layer.

For the A(2) cations there are 3 x A(2)-O) bonds of 2.748(3) Å pointing into vacant shifted region and 3 x A(2-)O bonds of 3.267(2) Å pointing towards triple layers of B-site cations in the perovskite block, and 3 x A(2)-O bonds of 3.048(2) Å and 3 x A(2)-O bonds of 2.801(3) Å bonds parallel to *xy*-plane pointing towards NbO_6 units in the same octahedral layer. The A(2) cations are displaced into shifted region and the degree of shift for both A-cations can be seen in *figure 4.66.*

Similar to the trend observed for the Nb-analogues and the $Ba_{3-x}Sr_xLaNb_2TaO_{12}$ series, the AO_{12} polyhedra disclose a more distorted environment in the "shifted" region, A(2) than in the perovskite block, A(1) with corresponding distortion values

Δd = 48.90 and Δd = 22.54. This can be seen more clearly in ***figures 4.64*** and ***4.65*** where the distorted A-O lattices are projected along the *z*-axis.

Bond valence sums (BVS) were performed for the structure (***section 1.1.1, equation 1.2*** and ***1.3***), the values are listed in ***table 4.26***. Overall the BVS calculations performed suggest the refinement is reasonable, however significantly larger than expected values are obtained for the B-sites, this is most likely due to the level of structural complexity associated with the site.

Cation	Theoretical BVS	Calculated BVS	Status
A(1)	2.50	2.63	Over-bonded
A(2)	2.00	2.19	Over-bonded
B(1)	5.00	6.43	Over-bonded
B(2)	5.05	5.99	Over-bonded

Table 4.26: BVS calculation results for $Ba_3LaNbTa_2O_{12}$

3 x B(1)-O(1) = 2.138(2) Å

6 x B(2)-O(1) = 2.002(2) Å

3 x B(1)-O(2) = 1.875(2) Å
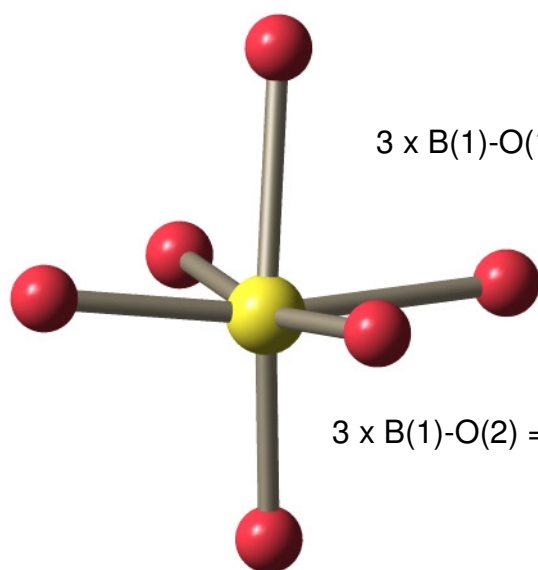
Figure 4.59: Distorted B(1)O_6 octahedron adjacent to the "shifted" region (red spheres O^{2-}, yellow sphere B(1) cation). Associated bond lengths labelled.
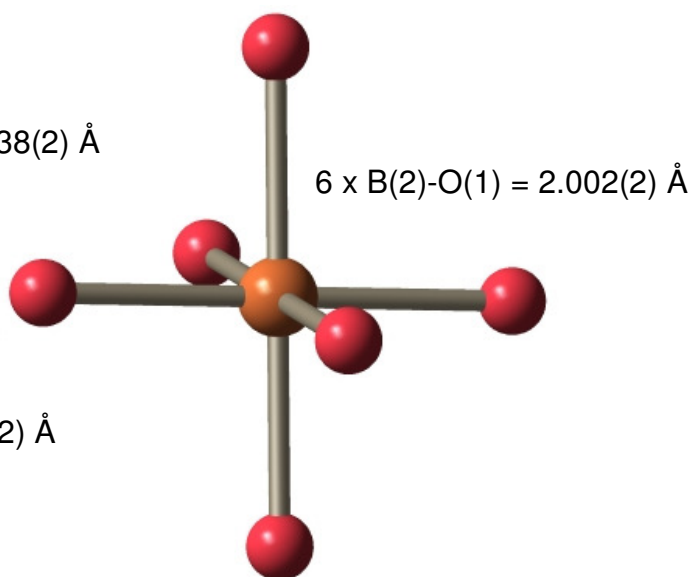
Figure 4.60: Undistorted B(2)O_6 octahedron in the centre of the perovskite block (red spheres O^{2-}, orange sphere B(2) cation). Associated bond lengths labelled.
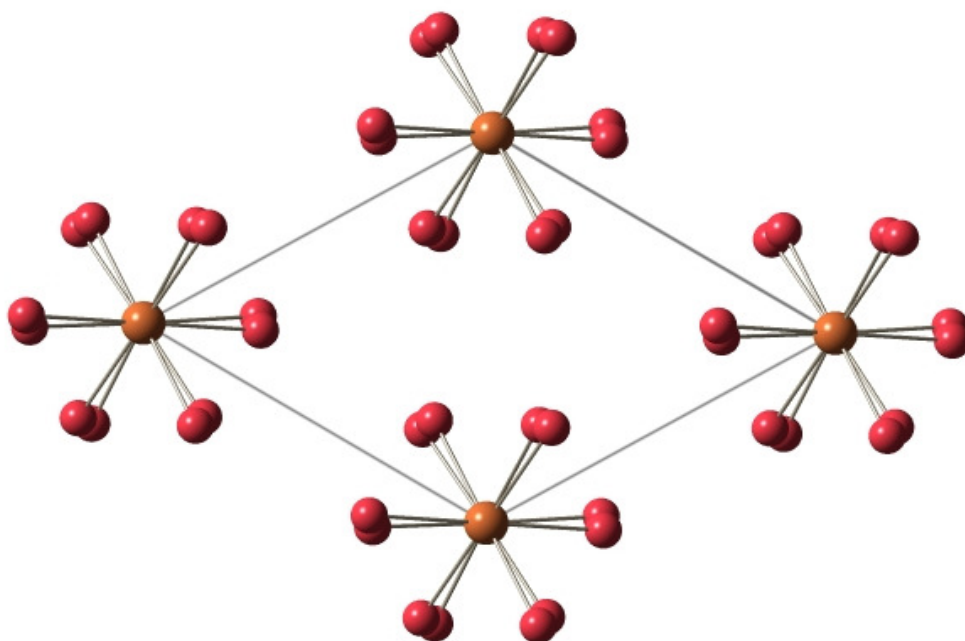

Figure 4.61: View of $Ba_3LaNbTa_2O_{12}$ structure along the z-axis showing tilting of the octahedra, tilt angle 3° [a⁻ a⁻ a⁻] (octahedra omitted for clarity). (Red spheres O^{2-}, orange spheres Nb^{5+}/Ta^{5+}).
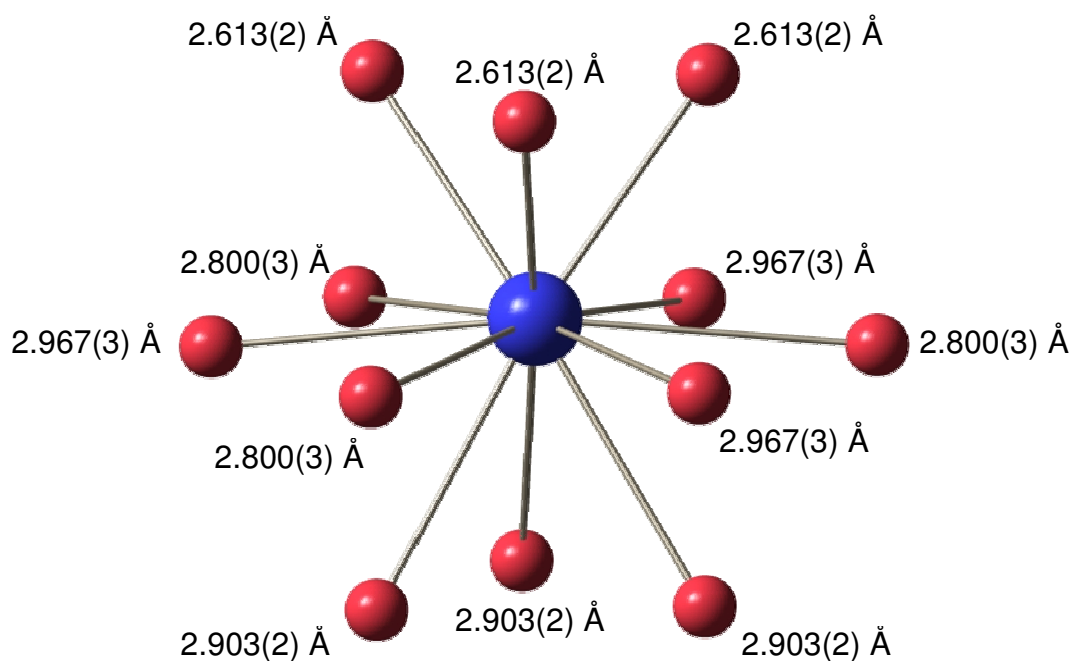
Figure 4.62: Cubo-octahedral environment of A(1) cations located within the triple layer of BO_6 octahedra with Ba^{2+} / La^{3+} distribution of 0.50 / 0.50 (red spheres O^{2-}, blue sphere Ba^{2+} / La^{3+}). Bond lengths are labelled.
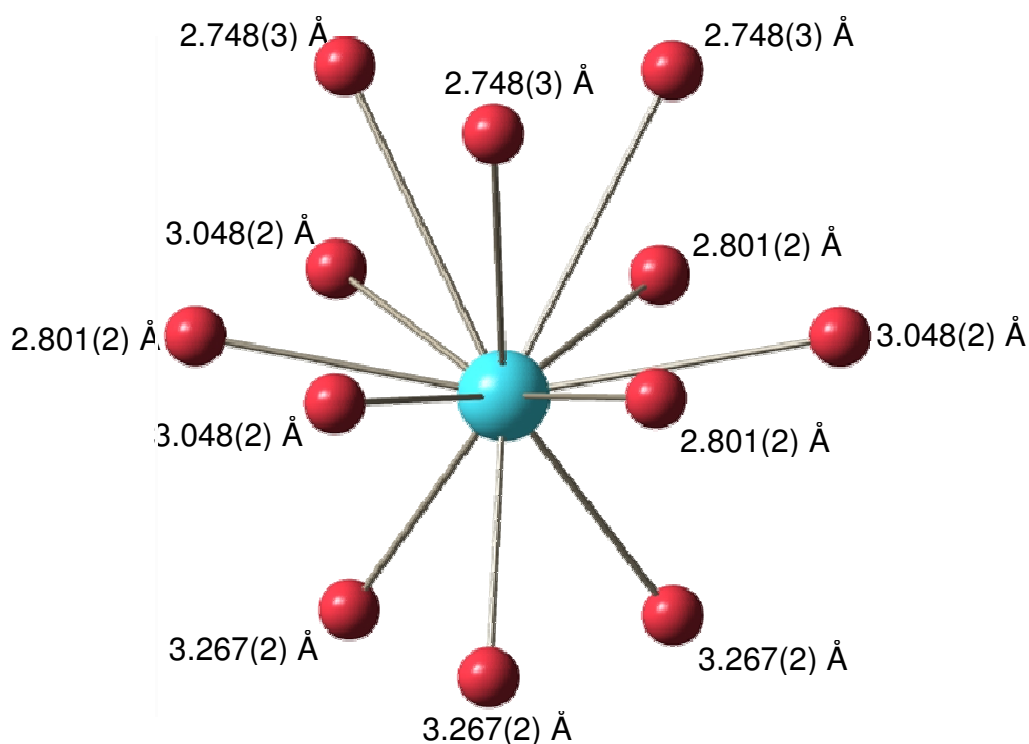

Figure 4.63: Cubo-octahedral environment of A(2) cations located in "shifted" region with a Ba^{2+} / La^{3+} distribution of 1.00 / 0.00 (red spheres O^{2-}, blue sphere Ba^{2+} / La^{3+}).Bond lengths are labelled.
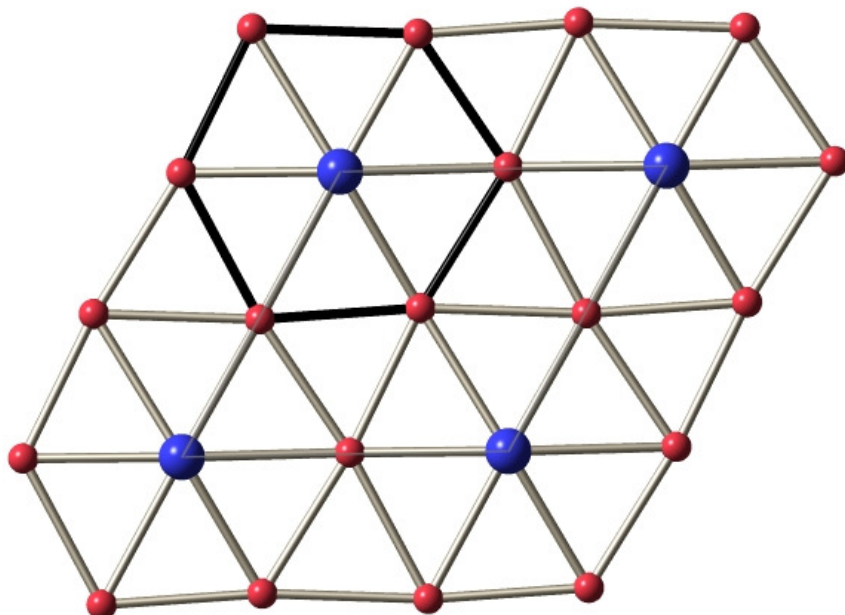
Figure 4.64: View of the distorted A(1)-O lattice along the *z*-axis, O^{2-} ions not parallel to the *xy*-plane are omitted for clarity. Black outline shows a "slice" through the AO_{12} polyhedra, 3 x A(1)-O bonds of 2.800(3) Å and 3 x A(1)-O bonds of 2.967(3) Å parallel to the *xy*-plane. A-cations are on the corners of the unit cell, outlined in grey. (Red spheres O^{2-}, blue spheres Ba^{2+} / La^{3+}).
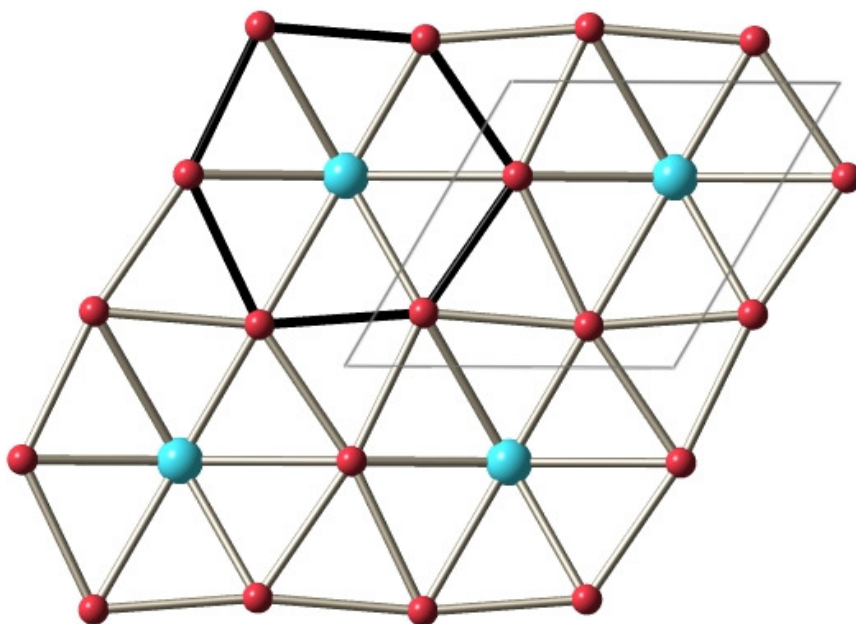

Figure 4.65: View of the distorted A(2)-O lattice along the *z*-axis, O^{2-} ions not parallel to the *xy*-plane are omitted for clarity. Black outline shows a "slice" through the AO_{12} polyhedra, 3 x A(1)-O bonds of 3.048(2) Å and 3 x A(1)-O bonds of 2.801(2) Å parallel to the *xy*-plane. Unit cell is outlined in grey. (Red spheres O^{2-}, blue spheres Ba^{2+} / La^{3+}).
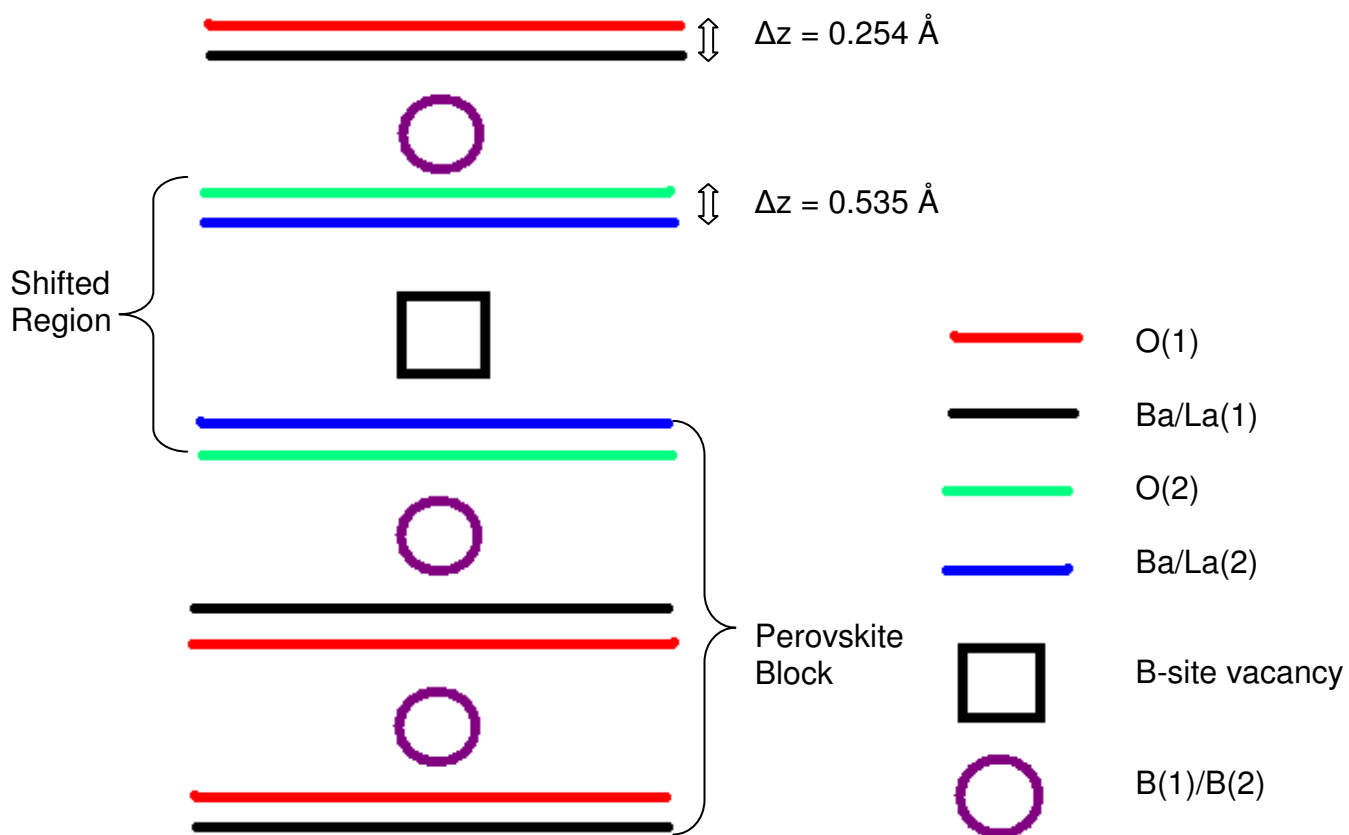
Figure 4.66: A schematic diagram showing A-O displacement along the *z*-axis (Δz) for $Ba_3LaNbTa_2O_{12}$ (not to scale).

$Ba_3LaNbTa_2O_{12}$ has a variance value of 14.66×10^{-4}, as depicted in ***figure 4.67***. (For clarity, Δ values are quoted in figures omitting the factor 10^{-4}).
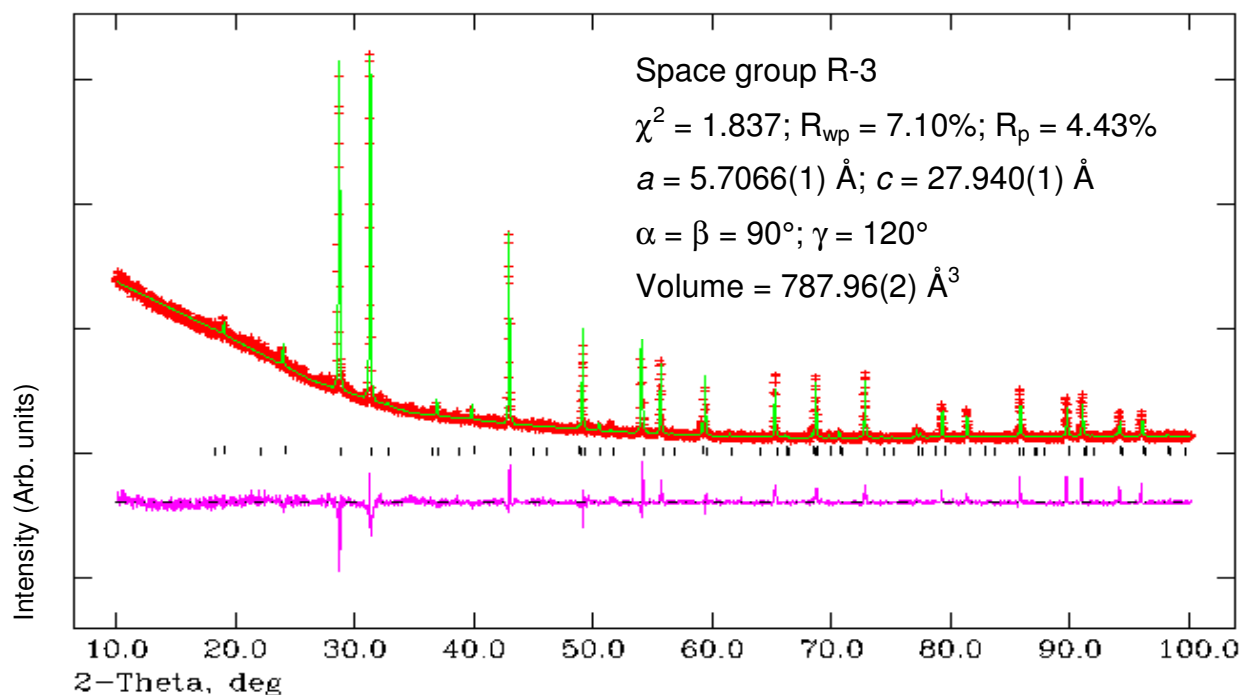

Δ=14.66

(a)   *(b)*
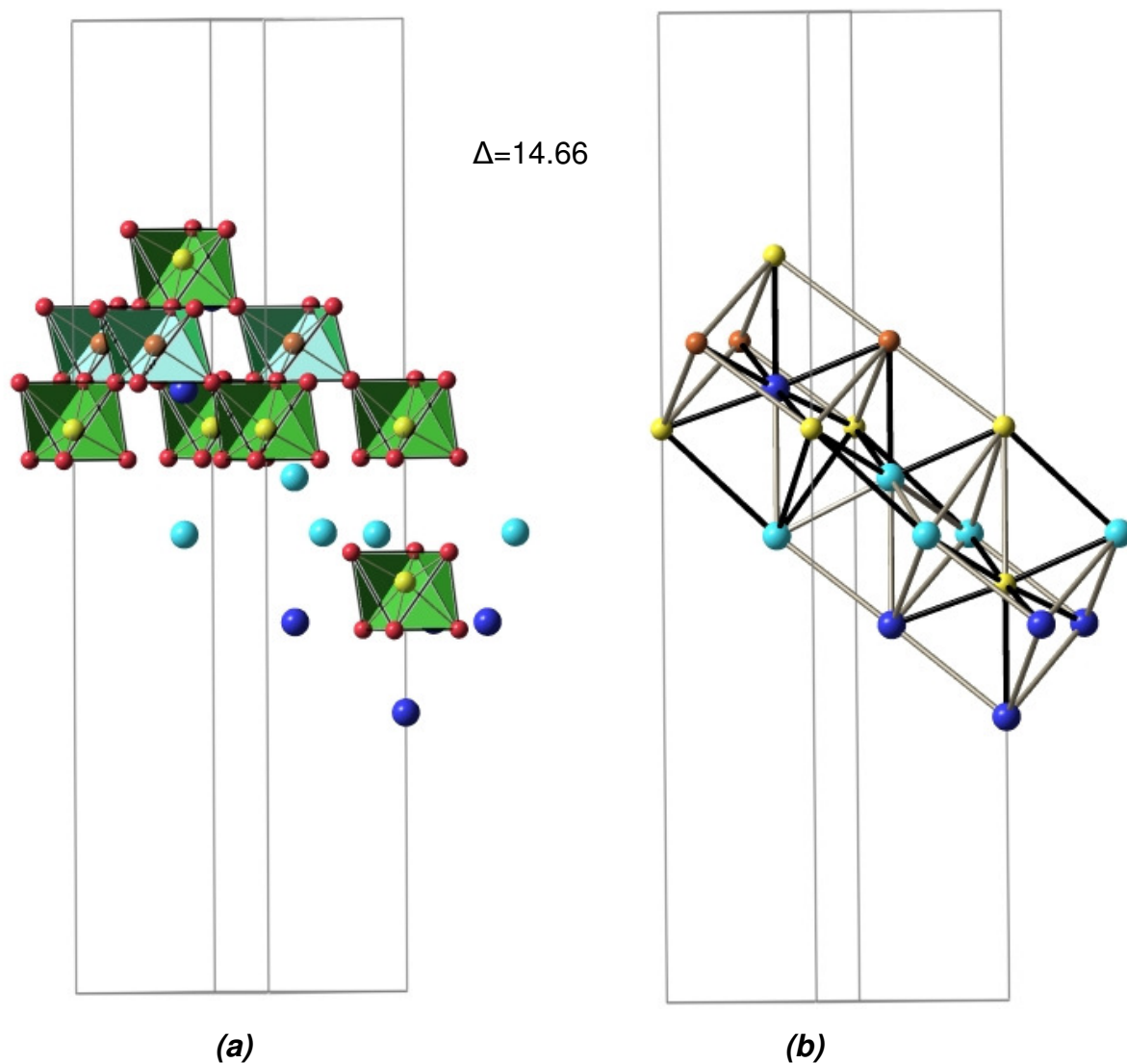
Figure 4.67: *(a)* A- and B-cations involved in the three *bcc* unit cells (O^{2-} ions shown not involved in the *bcc* cation sublattice) *(b)* Structural view of the *bcc* lattice along the *xy*-direction, for $Ba_3LaNbTa_2O_{12}$. Black bonds highlight the A-B distances (bond lengths) selected for calculation of the variance, Δ. (Red spheres O^{2-}, blue spheres Ba^{2+} / La^{3+}, orange / yellow spheres Nb^{5+}/Ta^{5+}).

4.5.1.2 Ba$_2$SrLaNbTa$_2$O$_{12}$

4.5.1.2.1 XRPD refinement

The refinement results are summarised below in **figure 4.68** and **table 4.27.** Refinement statistics and lattice parameters are given in **figure 4.68**.

Space group R-3

$\chi^2 = 1.837$; $R_{wp} = 7.10\%$; $R_p = 4.43\%$

$a = 5.7066(1)$ Å; $c = 27.940(1)$ Å

$\alpha = \beta = 90°$; $\gamma = 120°$

Volume = 787.96(2) Å^3

Figure 4.68: Calculated (green), experimental (red) and difference (pink) profile plot for Ba$_2$SrLaNbTa$_2$O$_{12}$ XRPD data. Tick marks represent Bragg peak positions.

Atom	Wyckoff	x	y	z	U$_{iso}$*100 (Å^2)	Frac.
Ba/Sr1	6c	0	0	0.2859(4)	1.00	0.81(3)*/0.19(3)
Ba/Sr2	6c	0	0	0.1414(4)	1.00	0.69(3)*/0.31(3)
Nb/Ta1	6c	0	0	0.4188(2)	1.00	0.24(2)/0.76(2)**
Nb/Ta2	3a	0	0	0	1.00	0.53(5)/0.47(5)**
O1	18f	0.193(2)	0.832(2)	0.6099(1)	1.00	1
O2	18f	0.141(6)	0.653(1)	0.4486(2)	1.00	1

*Ba^{2+} and La^{3+} entered as one element, Ba^{2+}. **The B-site compositions are slightly over/under that stated due to rounding up.

Table 4.27: Refinement results for Ba$_2$SrLaNbTa$_2$O$_{12}$ (XRD RT data)

4.5.1.2.2 Method (iv)

The refinement results are summarised below in **figures 4.69** and **4.70** and **tables 4.28** and **4.29.** Refinement statistics and lattice parameters are given in **figure 4.69**.
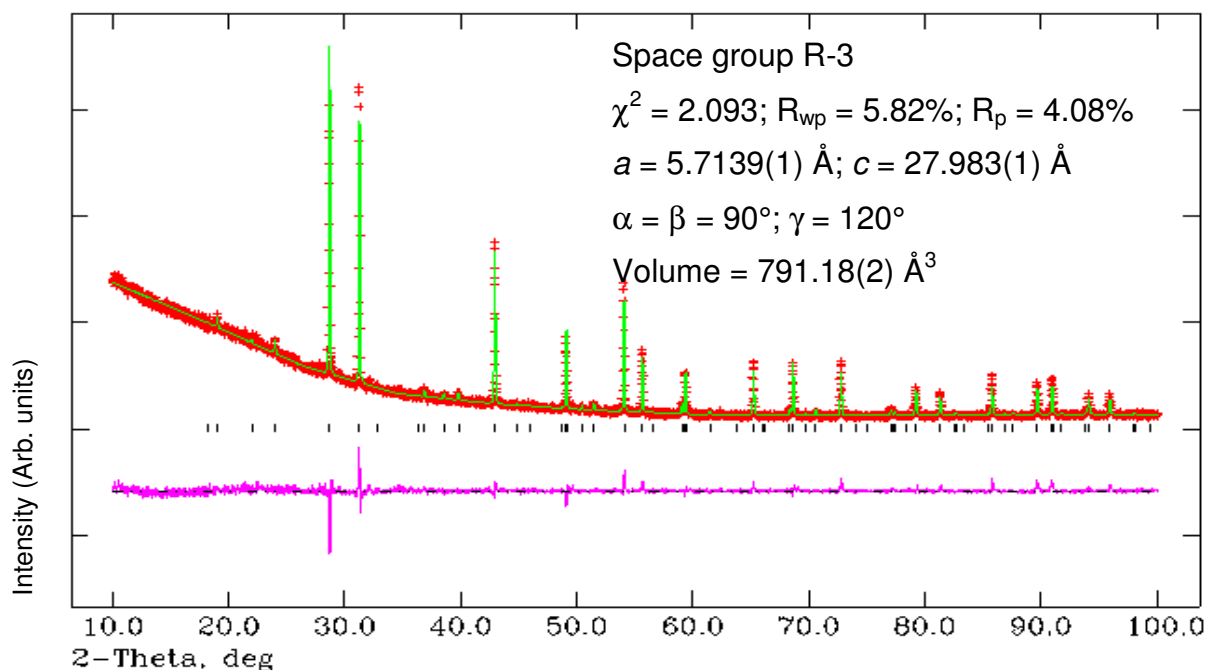
Figure 4.69: Calculated (green), experimental (red) and difference (pink) profile plot for $Ba_2SrLaNbTa_2O_{12}$ XRPD data. Tick marks represent Bragg peak positions.
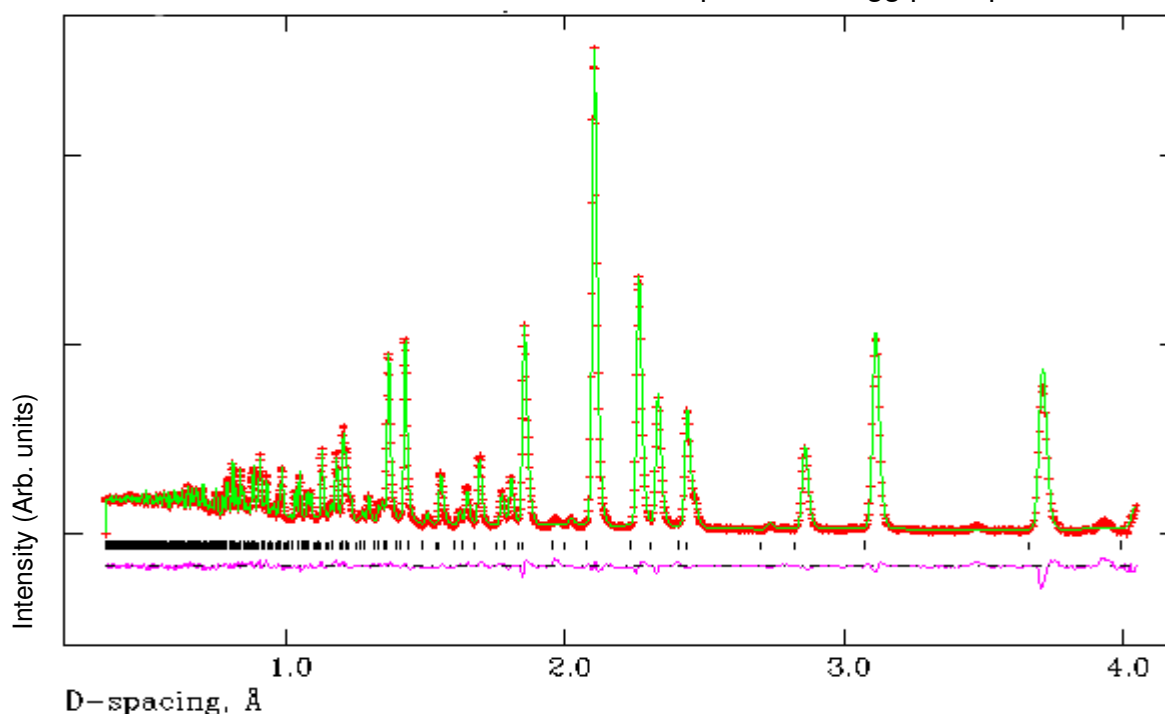
Figure 4.70: Calculated (green), experimental (red) and difference (pink) profile plot for $Ba_2SrLaNbTa_2O_{12}$ NPD data collected on GEM (bank 4). Tick marks represent Bragg peak positions.

Atom	Wyckoff	x	y	z	U_{iso}*100 ($\mathring{A}^2$)	Frac.
Ba/Sr/La1	6c	0	0	0.2865(1)	0.82(5)	0.01(1)/0.49(1)/0.50*
Ba/Sr/La2	6c	0	0	0.1380(1)	0.08(5)	0.99(1)/0.01(1)/0.00*
Nb/Ta1	6c	0	0	0.4208(1)	0.08(3)	0.38(2)/0.62(2)
Nb/Ta2	3a	0	0	0	0.25(6)	0.24(4)/0.76(4)
O1	18f	0.2015(5)	0.8737(5)	0.6291(1)	1.25(4)	1
O2	18f	0.1943(5)	0.8598(5)	0.4516(1)	1.08(4)	1

*Sr^{2+} occupancy values were fixed from the XRPD refinement, however La^{3+} displayed a preference for A(1). Therefore La^{3+} occupancy values were fixed and Sr^{2+} and Ba^{2+} were subsequently allowed to refine with constraints.

Table 4.28: Refinement results for $Ba_2SrLaNbTa_2O_{12}$ (XRD & GEM RT data)

Bond lengths (Å)			Bond Angles (°)		
Ba/Sr/La(1)-O(1) =	2.874(3)	(x3)	O(1)-Nb/Ta(1)-O(1) =	82.4(1)	(x3)
Ba/Sr/La(1)-O(1) =	2.655(2)	(x3)	O(1)-Nb/Ta(1)-O(2) =	166.8(1)	(x3)
Ba/Sr/La(1)-O(1) =	3.083(2)	(x3)	O(1)-Nb/Ta(1)-O(2) =	89.1(1)	(x3)
Ba/Sr/La(1)-O(2) =	2.592(2)	(x3)	O(1)-Nb/Ta(1)-O(2) =	86.5(1)	(x3)
			O(2)-Nb/Ta(1)-O(2) =	101.5(1)	(x3)
Ba/Sr/La(2)-O(1) =	3.279(3)	(x3)			
Ba/Sr/La(2)-O(2) =	2.758(2)	(x3)	O(1)-Nb/Ta(2)-O(1) =	94.7(1)	(x6)
Ba/Sr/La(2)-O(2) =	3.062(3)	(x3)	O(1)-Nb/Ta(2)-O(1) =	85.3(1)	(x6)
Ba/Sr/La(2)-O(2) =	2.716(3)	(x3)	O(1)-Nb/Ta(2)-O(1) =	180.0	(x3)
Nb/Ta(1)-O(1) =	2.152(3)	(x3)			
Nb/Ta(1)-O(2) =	1.873(2)	(x3)			
Nb/Ta(2)-O(1) =	1.990(3)	(x6)			

Table 4.29: Bond lengths and angles from refinement results for $Ba_2SrLaNbTa_2O_{12}$

The refinement, using method (iv), progressed well in space group R-3. A small amount of impurity phase is present in the sample, evidenced by the additional weak reflections in the angular range of 28° to 32° 2θ. This was not modelled in the refinement. Once the Sr^{2+} occupancies were fixed, the La^{3+} cations became completely ordered with all the La^{3+} occupying A(1) (50%). Therefore the La^{3+} occupancies were subsequently fixed and the Ba^{2+} / Sr^{2+} occupancies were then allowed to refine, with constraints. Details of the refinement can be found in **figures 4.69** and **4.70** and **tables 4.28** and **4.29**. The refinement converged with lattice parameters a = 5.7139(1) Å and c = 27.983(1) Å with associated statistics, χ^2 = 2.093, R_{wp} = 5.82%, and R_p = 4.08%. The resultant crystal structure can be seen in **figure 4.71**.

Anionic Displacement

⅓<01-10>$_H$
Shift

Cationic Displacement

Ba/Sr/La(1)

Ba/Sr/La(2)

Nb/Ta(1)

Nb/Ta(2)

O(1)/O(2)

Distorted B(1)O$_6$
octahedra

Undistorted B(2)O$_6$
octahedra

c

h

h

c

c

c
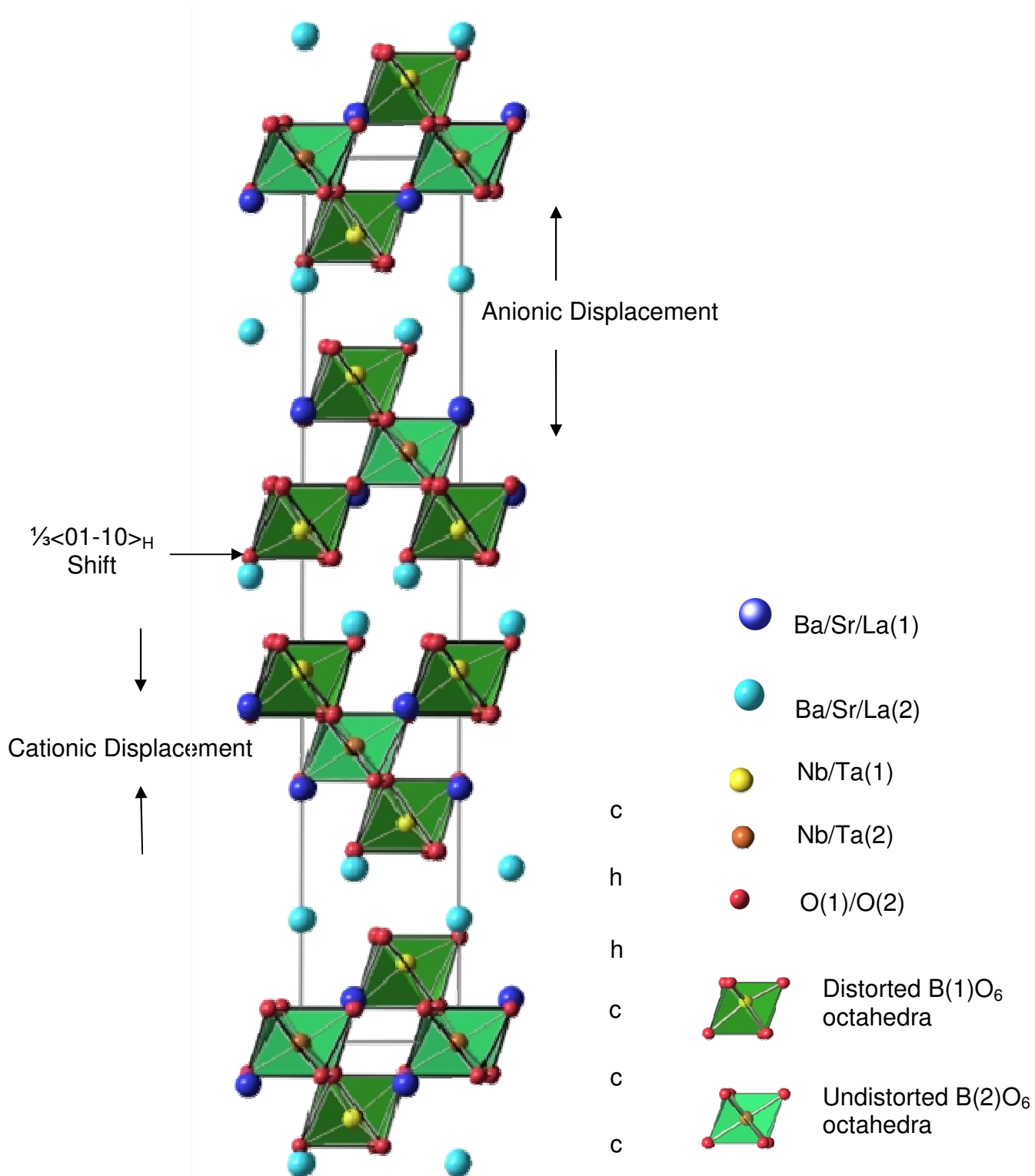
Figure 4.71: Structure of Ba$_2$SrLaNbTa$_2$O$_{12}$ viewed along the *x*-axis.

From method (iv) Ta^{5+} displays a preference for B(2) with an occupancy of 76% and Nb^{5+} displays a preference for B(1) with an occupancy of 38%. When Ta^{5+} is the dominant pentavalent B-cation, no preference to inhabit the distorted B(1) site is displayed. However for the $Ba_{3-x}Sr_xLaNb_2TaO_{12}$ series where Nb^{5+} is the dominant B-cation a preference for this cation to occupy the distorted B(1) site prevails. The two different B-cation environments can be seen in **figures 4.72** and **4.73**.

The Δd values are 48.05 and 0 for B(1) and B(2) respectively. The BO_6 octahedra are antiphase tilted about the z-axis by an angle of 7.5°, **figure 4.74**.

The dominant divalent A-cation in the structure, Ba^{2+} displays a preference for A(2) with a 99% occupancy, whereas Sr^{2+} and La^{3+} exhibit a preference for A(1) with occupancies in this site of 49% and 50% respectively. The A-sites are very close to being completely ordered similar to the refined crystal structure of $Ba_3LaNbTa_2O_{12}$.

The cubo-octahedral environment of the A-cations can be seen in **figures 4.75** and **4.76**. There are 3 x A(1)-O bonds of 2.592(2) Å and 3 x A(1)-O bonds of 2.874(3) Å pointing towards neighbouring octahedral layers, along the direction of the z-axis and the remaining six bonds labelled are parallel to the xy-plane pointing towards octahedral units in the same octahedral layer.

For the A(2) cations there are 3 x A(2)-O bonds of 2.716(3) Å pointing into vacant shifted region and 3 x A(2)-O bonds of 3.279(3) Å pointing towards triple layers of B-site cations, and the remaining six bonds labelled are parallel to xy-plane. The A(2) cations are displaced into shifted region and the degree of shift for both A-cations can be seen in **figure 4.79.**

The AO_{12} polyhedra again are in a more distorted environment in the "shifted" region, A(2), than in the perovskite block, A(1), with distortion values of Δd = 60.85 and Δd = 47.75 correspondingly. This can be seen more clearly in **figures 4.77** and **4.78** where the distorted A-O lattices are projected along the z-axis.

Bond valence sums (BVS) were performed for the structure (refer to **section 1.1.1, equation 1.2** and **1.3**), values are listed in **table 4.30**. Overall the BVS calculations reveal some considerably inflated values for B(2), which suggest there are problems with the refinement. Considering the presence of an impurity phase and the

differences observed in the B-site occupancies for the XRPD refinement compared to the joint refinement, then these results must be interpreted with caution. It is likely that there are other factors to consider for the $Ba_2SrLaNbTa_2O_{12}$ phase, but no other suitable refinement approach has yet been found.

Cation	Theoretical BVS	Calculated BVS	Status
A(1)	2.50	2.34	Under-bonded
A(2)	2.00	2.32	Over-bonded
B(1)	5.00	5.05	Over-bonded
B(2)	5.00	8.53	Over-bonded

Table 4.30: BVS calculation results for $Ba_2SrLaNbTa_2O_{12}$
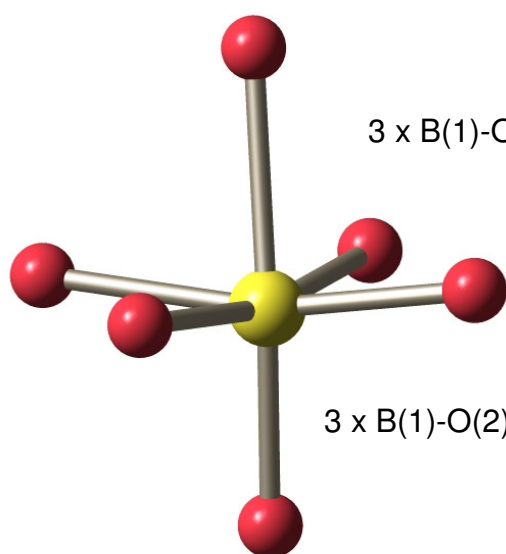
Figure 4.72: Distorted B(1)O$_6$ octahedron adjacent to the "shifted" region (red spheres O^{2-}, yellow sphere B(1) cation). Associated bond lengths labelled.

3 x B(1)-O(1) = 2.152(3) Å

3 x B(1)-O(2) = 1.873(2) Å
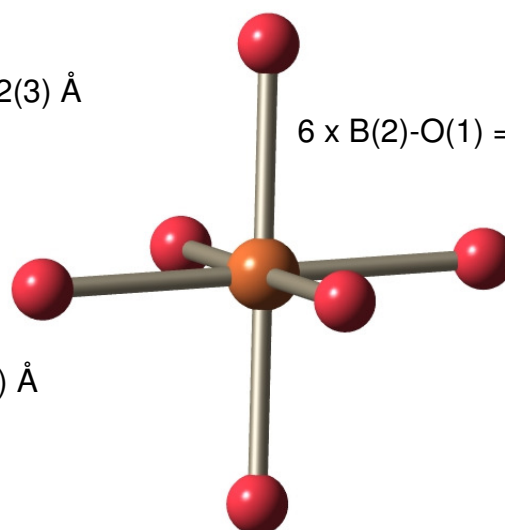
Figure 4.73: Undistorted B(2)O$_6$ octahedron in the centre of the perovskite block (red spheres O^{2-}, orange sphere B(2) cation). Associated bond lengths labelled.

6 x B(2)-O(1) = 1.990(3) Å
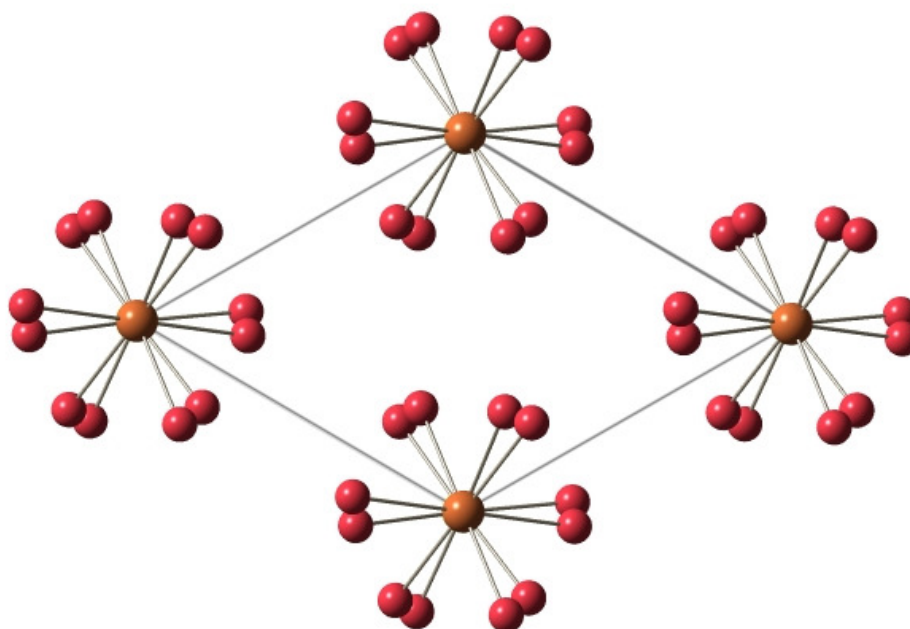
Figure 4.74: View of Ba$_2$SrLaNbTa$_2$O$_{12}$ structure along the *z*-axis showing tilting of the octahedra, tilt angle 7.5° [a$^-$ a$^-$ a$^-$] (octahedra omitted for clarity). (Red spheres O^{2-}, Orange spheres Nb^{5+}/Ta^{5+}).
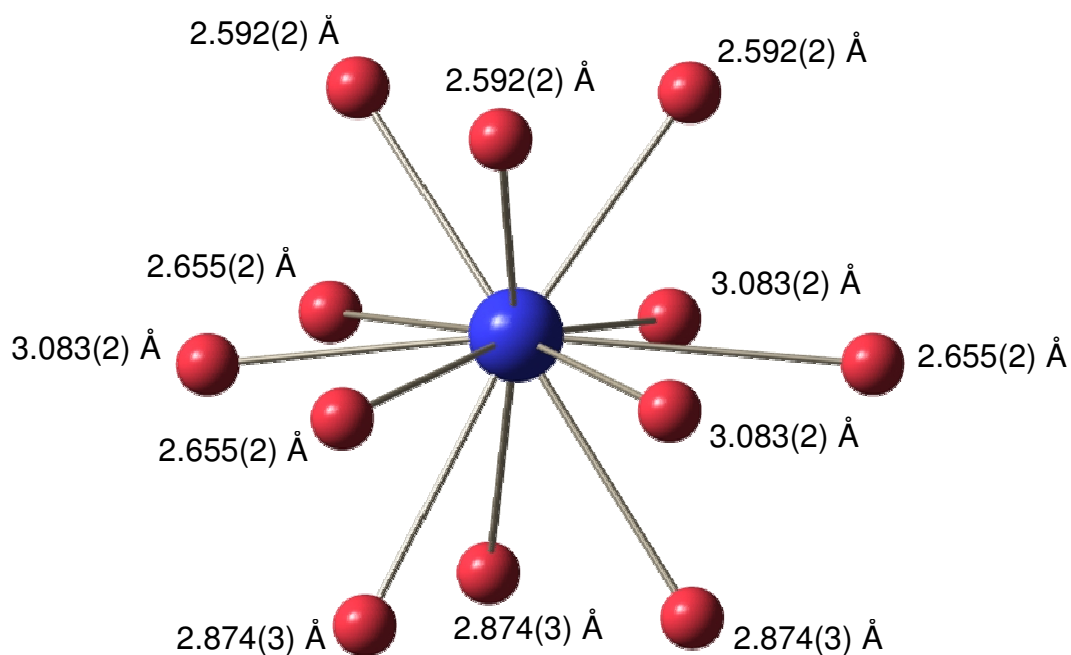
Figure 4.75: Cubo-octahedral environment of A(1) cations located within the triple layer of BO_6 octahedra with Ba^{2+} / La^{3+} / Sr^{2+} distribution of 0.01 / 0.49 / 0.50 (red spheres O^{2-}, blue sphere Ba^{2+} / La^{3+}/ Sr^{2+}). Bond lengths are labelled.
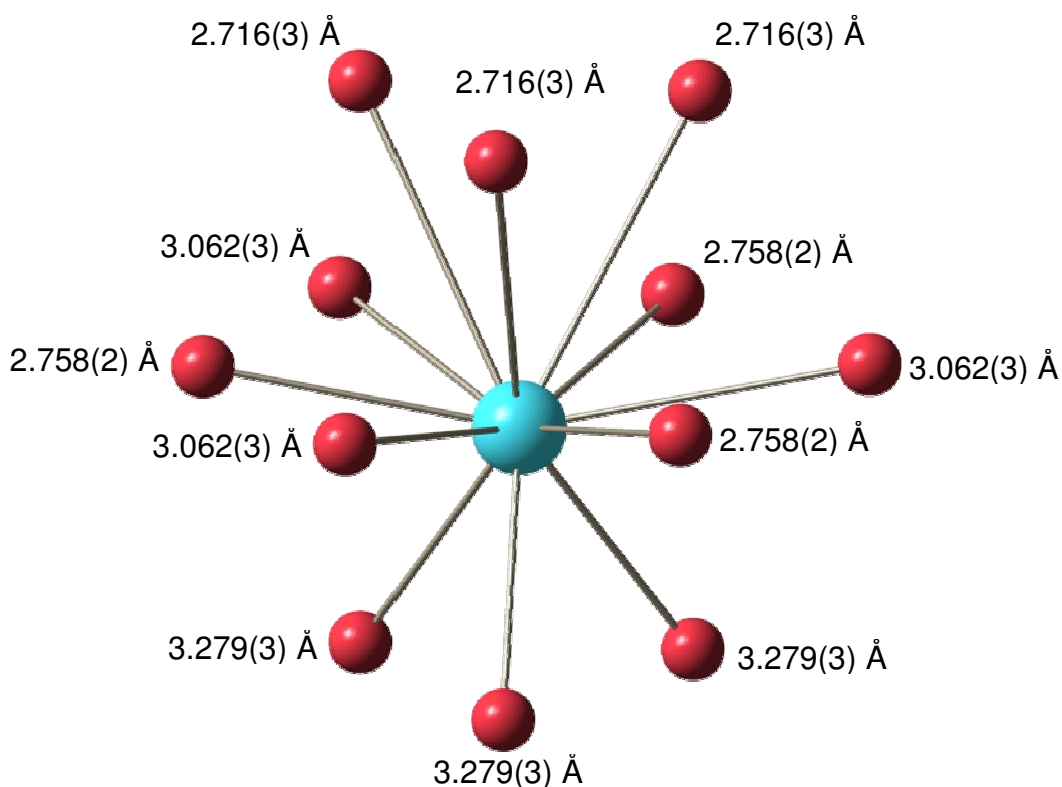

Figure 4.76: Cubo-octahedral environment of A(2) cations located in "shifted" region with a Ba^{2+} / La^{3+} / Sr^{2+} distribution of 0.99 / 0.01 / 0.00 (red spheres O^{2-}, blue sphere Ba^{2+} / La^{3+} / Sr^{2+}).Bond lengths are labelled.
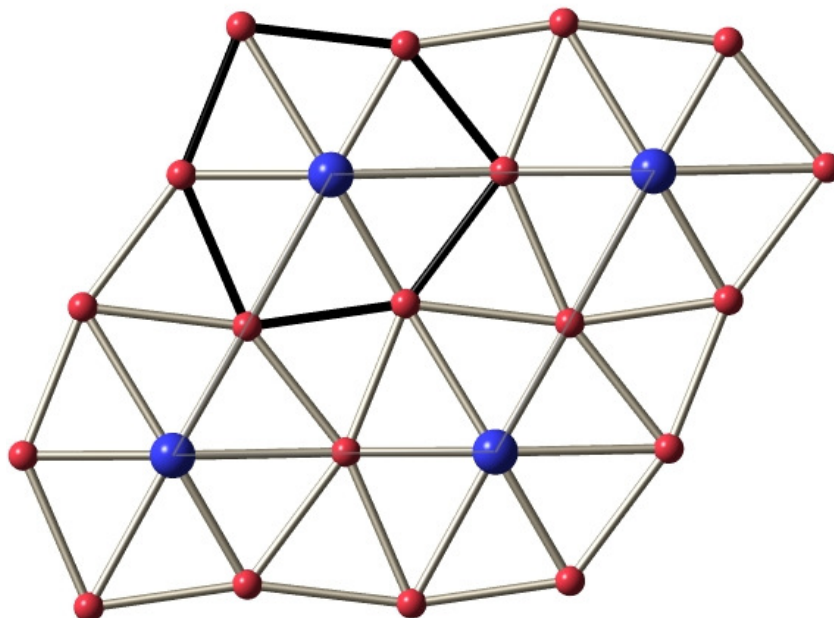
Figure 4.78: View of the distorted A(1)-O lattice along the *z*-axis, O^{2-} ions not parallel to the *xy*-plane are omitted for clarity. Black outline shows a "slice" through the AO_{12} polyhedra, 3 x A(1)-O bonds of 2.655(2) Å and 3 x A(1)-O bonds of 3.083(2) Å parallel to the *xy*-plane. A-cations are on the corners of the unit cell, outlined in grey. (Red spheres O^{2-}, blue spheres Ba^{2+} / La^{3+} / Sr^{2+}).
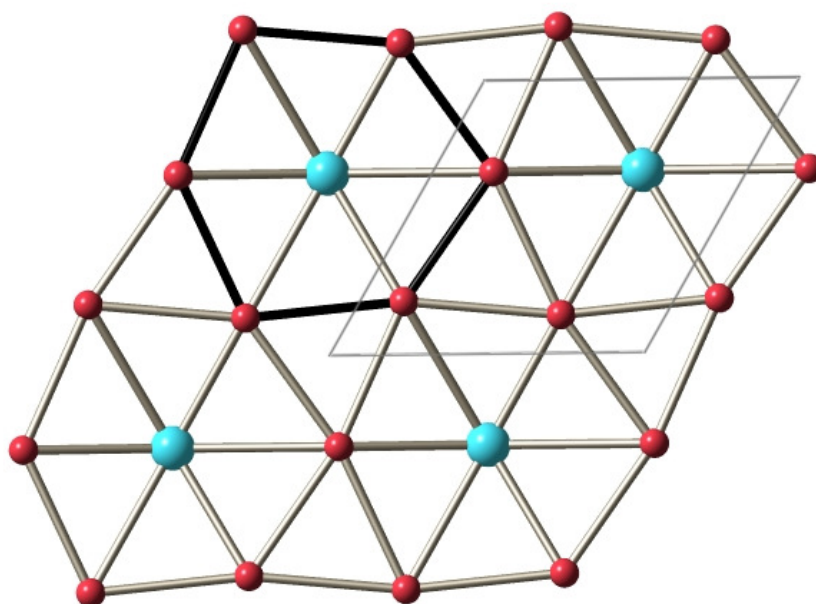

Figure 4.79: View of the distorted A(2)-O lattice along the *z*-axis, O^{2-} ions not parallel to the *xy*-plane are omitted for clarity. Black outline shows a "slice" through the AO_{12} polyhedra, 3 x A(1)-O bonds of 3.062(3) Å and 3 x A(1)-O bonds of 2.758(2) Å parallel to the *xy*-plane. Unit cell is outlined in grey. (Red spheres O^{2-}, blue spheres Ba^{2+} / La^{3+} / Sr^{2+}).
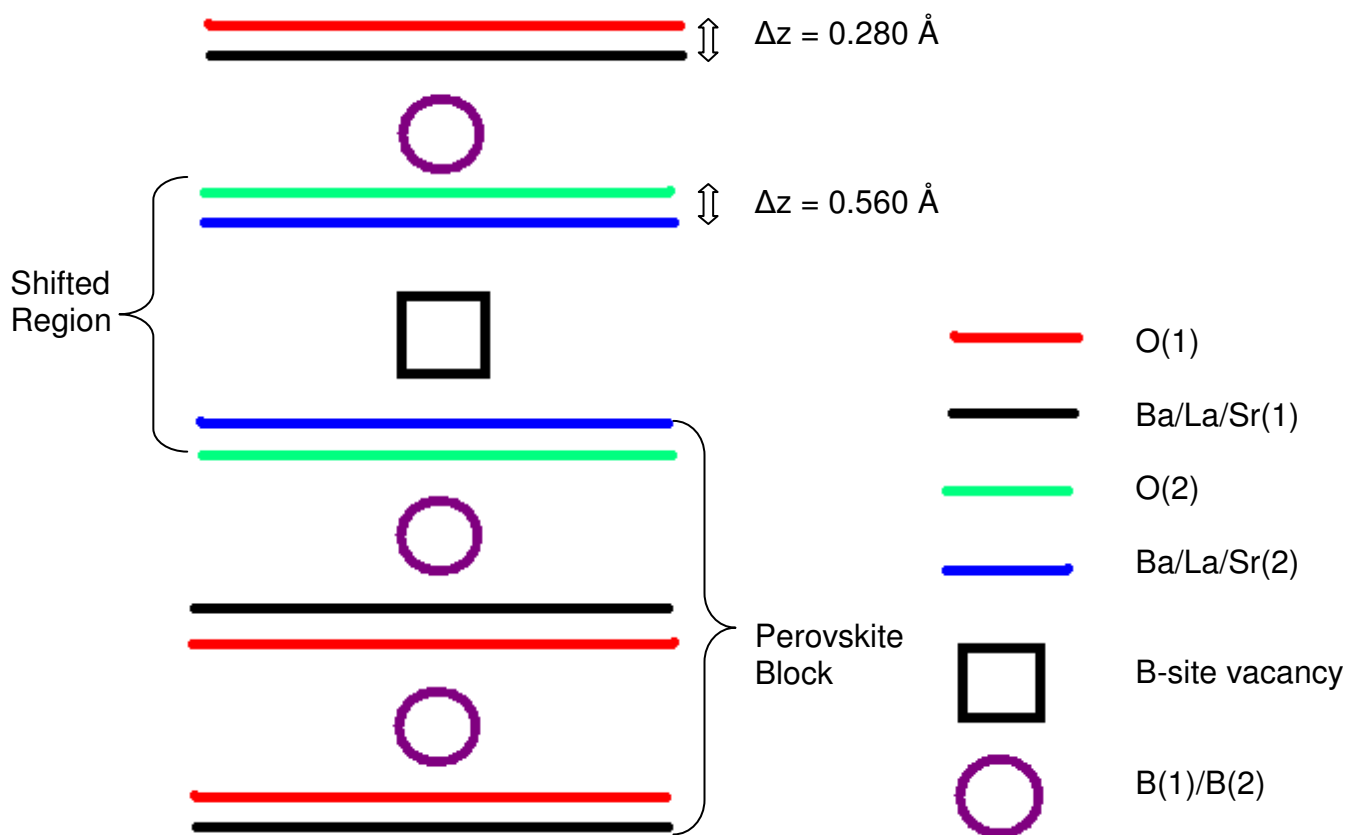
Figure 4.80: A schematic diagram showing A-O displacement along the *z*-axis (Δz) for $Ba_2SrLaNbTa_2O_{12}$ (not to scale).

$Ba_2SrLaNbTa_2O_{12}$ has a variance value of 14.00×10^{-4}, as depicted in *figure 4.81*. (For clarity, Δ values are quoted in figures omitting the factor 10^{-4}).
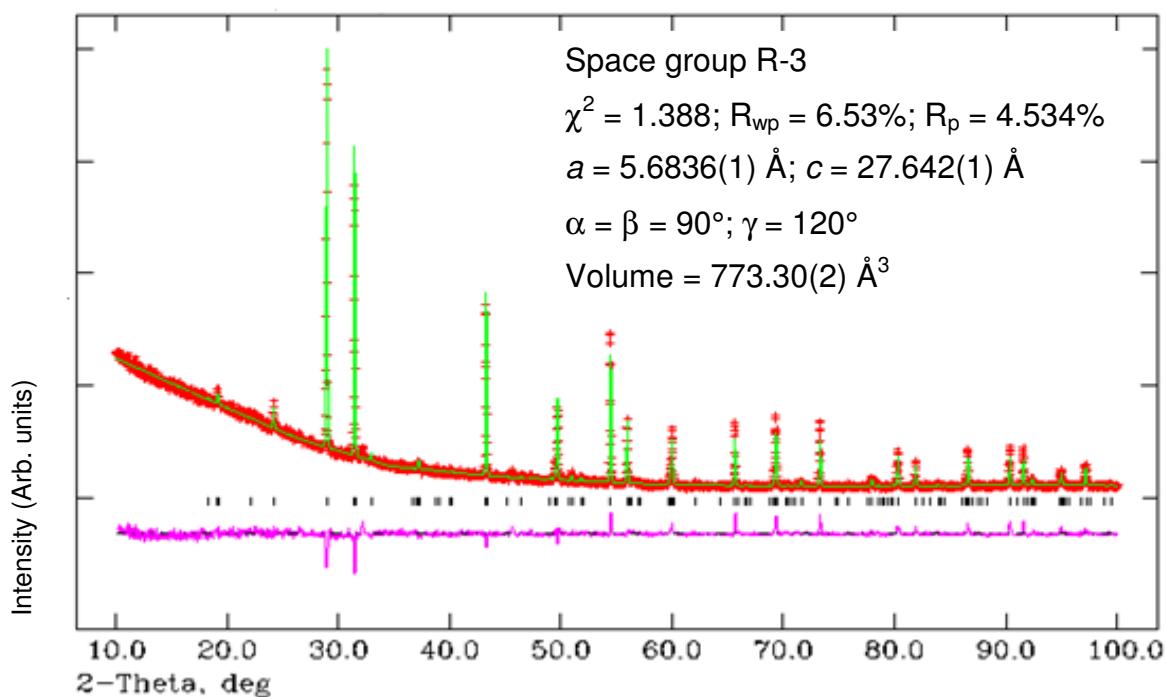

$\Delta=14.00$

(a)   *(b)*
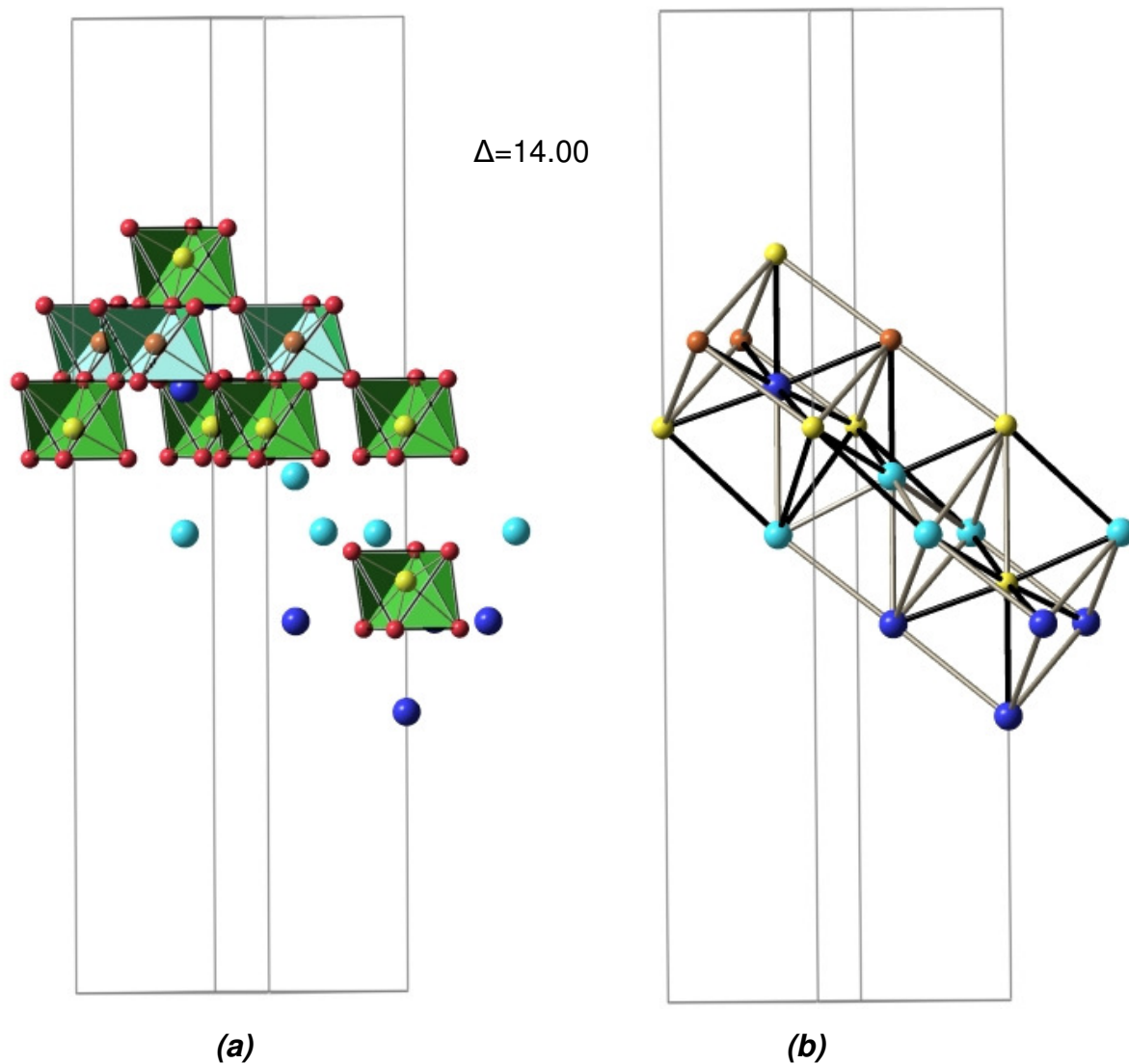
Figure 4.81: (a) A- and B-cations involved in the three *bcc* unit cells (O^{2-} ions shown not involved in the *bcc* cation sublattice) *(b)* Structural view of the *bcc* lattice along the *xy*-direction, for $Ba_2SrLaNbTa_2O_{12}$. Black bonds highlight the A-B distances (bond lengths) selected for calculation of the variance, Δ. (Red spheres O^{2-}, blue spheres Ba^{2+} / La^{3+} / Sr^{2+}, yellow / orange spheres Nb^{5+}/Ta^{5+}).

4.5.1.3 BaSr$_2$LaNbTa$_2$O$_{12}$

4.5.1.3.1 XRPD refinement

The refinement results are summarised below in **figure 4.82** and **table 4.31.** Refinement statistics and lattice parameters are given in **figure 4.82**.

Space group R-3

$\chi^2 = 1.388$; $R_{wp} = 6.53\%$; $R_p = 4.534\%$

$a = 5.6836(1)$ Å; $c = 27.642(1)$ Å

$\alpha = \beta = 90°$; $\gamma = 120°$

Volume = 773.30(2) Å^3

Figure 4.82: Calculated (green), experimental (red) and difference (pink) profile plot for BaSr$_2$LaNbTa$_2$O$_{12}$ XRPD data. Tick marks represent Bragg peak positions.
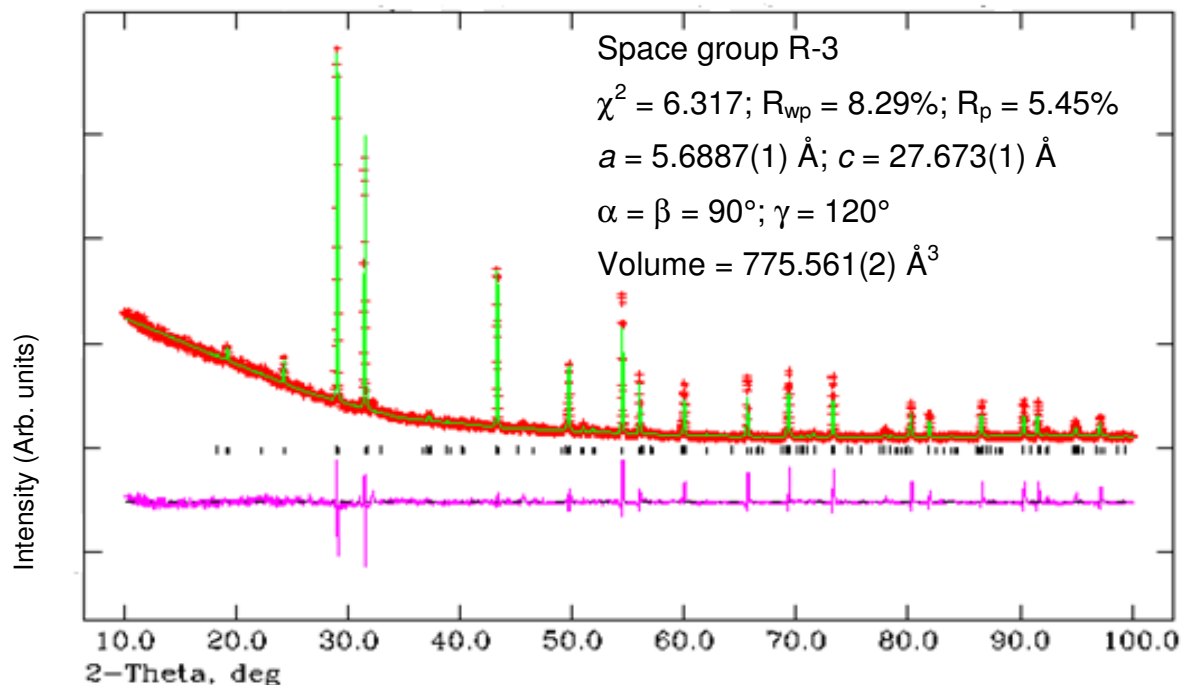
Atom	Wyckoff	x	y	z	U$_{iso}$*100 (Å^2)	Frac.
Ba/Sr1	6c	0	0	0.2880(3)	1.00	0.55(2)*/0.45(2)
Ba/Sr2	6c	0	0	0.1404(3)	1.00	0.45(2)*/0.55(2)
Nb/Ta1	6c	0	0	0.4219(2)	1.00	0.67/0.33
Nb/Ta2	3a	0	0	0	1.00	0.00/1.00
O1	18f	0.128(7)	0.772(6)	0.6280(1)	1.00	1
O2	18f	0.120(6)	0.770(6)	0.4519(1)	1.00	1

*Ba^{2+} and La^{3+} entered as one element, Ba^{2+}.

Table 4.31: Refinement results for BaSr$_2$LaNbTa$_2$O$_{12}$ (XRD RT data)

4.5.1.3.2 Method (iv)

The refinement results are summarised below in **figures 4.83** and **4.84** and **tables 4.32** and **4.33.** Refinement statistics and lattice parameters are given in **figure 4.83**.

Space group R-3

$\chi^2 = 6.317$; $R_{wp} = 8.29\%$; $R_p = 5.45\%$

$a = 5.6887(1)$ Å; $c = 27.673(1)$ Å

$\alpha = \beta = 90°$; $\gamma = 120°$

Volume = 775.561(2) Å^3

Figure 4.83: Calculated (green), experimental (red) and difference (pink) profile plot for BaSr$_2$LaNbTa$_2$O$_{12}$ XRPD data. Tick marks represent Bragg peak positions.
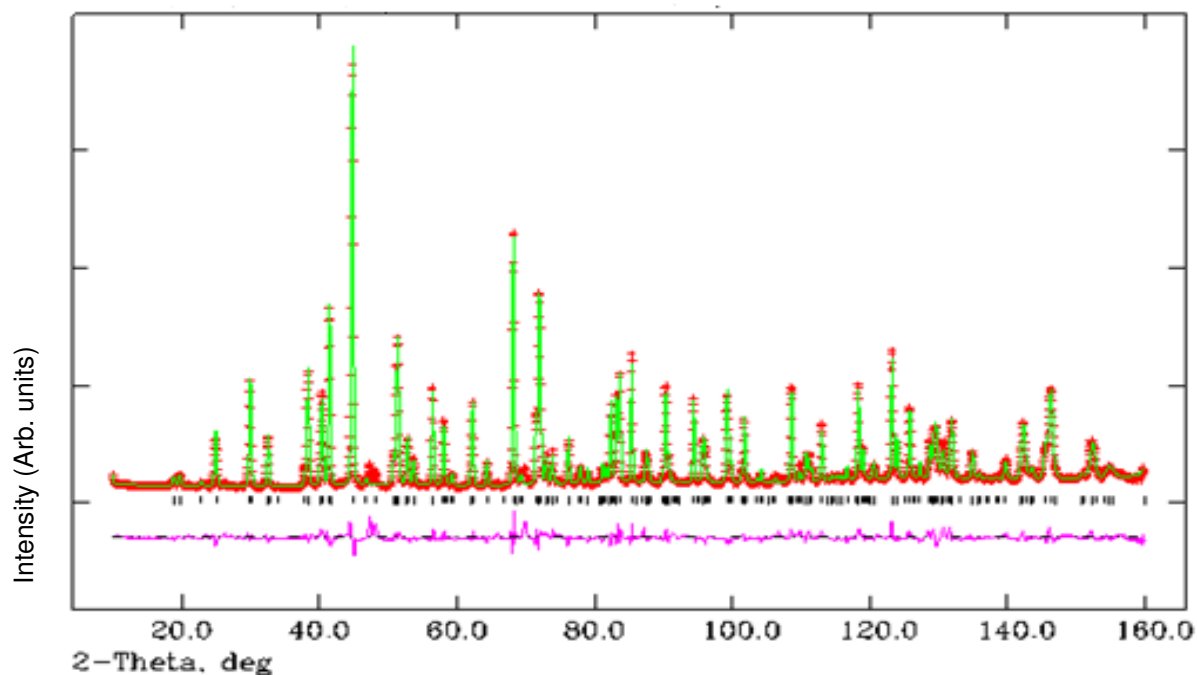
Figure 4.84: Calculated (green), experimental (red) and difference (pink) profile plot for BaSr$_2$LaNbTa$_2$O$_{12}$ NPD data collected on D2B. Tick marks represent Bragg peak positions.

214

Atom	Wyckoff	x	y	z	$U_{iso}*100$ $(\mathring{A}^2)$	Frac.
Ba/Sr/La1	6c	0	0	0.2870(8)	0.24(6)	0.17(1)/0.38*/0.45(1)
Ba/Sr/La2	6c	0	0	0.1391(1)	0.52(7)	0.33(1)/0.62*/0.05(1)
Nb/Ta1	6c	0	0	0.4224(1)	1.00	0.31(3)/0.69(3)**
Nb/Ta2	3a	0	0	0	1.00	0.37(6)/0.63(6)**
O1	18f	0.1210(4)	0.7814(4)	0.6282(1)	1.60(4)	1
O2	18f	0.1224(3)	0.7883(3)	0.4526(1)	1.13(4)	1

*Sr^{2+} occupancy values were fixed from the XRPD refinement. **B-site composition slightly over/under stated composition due to rounding up.

Table 4.32: Refinement results for $BaSr_2LaNbTa_2O_{12}$ (XRD & D2B RT data)

Bond lengths (Å)			Bond Angles (°)		
Ba/Sr/La(1)-O(1) =	2.890(4)	(x3)	O(1)-Nb/Ta(1)-O(1) =	82.5(1)	(x3)
Ba/Sr/La(1)-O(1) =	3.104(5)	(x3)	O(1)-Nb/Ta(1)-O(2) =	166.2(1)	(x3)
Ba/Sr/La(1)-O(1) =	2.608(5)	(x3)	O(1)-Nb/Ta(1)-O(2) =	87.2(1)	(x3)
Ba/Sr/La(1)-O(2) =	2.590(4)	(x3)	O(1)-Nb/Ta(1)-O(2) =	87.2(1)	(x3)
			O(2)-Nb/Ta(1)-O(2) =	101.4(1)	(x3)
Ba/Sr/La(2)-O(1) =	3.250(3)	(x3)			
Ba/Sr/La(2)-O(2) =	3.146(2)	(x3)	O(1)-Nb/Ta(2)-O(1) =	94.0(1)	(x6)
Ba/Sr/La(2)-O(2) =	2.647(2)	(x3)	O(1)-Nb/Ta(2)-O(1) =	86.0(1)	(x6)
Ba/Sr/La(2)-O(2) =	2.657(3)	(x3)	O(1)-Nb/Ta(2)-O(1) =	180.0	(x3)
Nb/Ta(1)-O(1) =	2.161(3)	(x3)			
Nb/Ta(1)-O(2) =	1.864(2)	(x3)			
Nb/Ta(2)-O(1) =	1.986(3)	(x6)			

Table 4.33: Bond lengths and angles from refinement results for $BaSr_2LaNbTa_2O_{12}$

The refinement, using method (iv), progressed well in space group R-3. A small amount of impurity phase is present in the sample, indicated by the additional weak reflections in the region of 28° to 32° 2θ. Details of the refinement can be found in **figures 4.83** and **4.84** and **tables 4.32** and **4.33**. The refinement converged with lattice parameters a = 5.6887(1) Å and c = 27.673(1) Å with associated statistics, χ^2 = 6.317, R_{wp} = 8.29%, and R_p = 5.44%. The resultant crystal structure can be seen in **figure 4.85**.
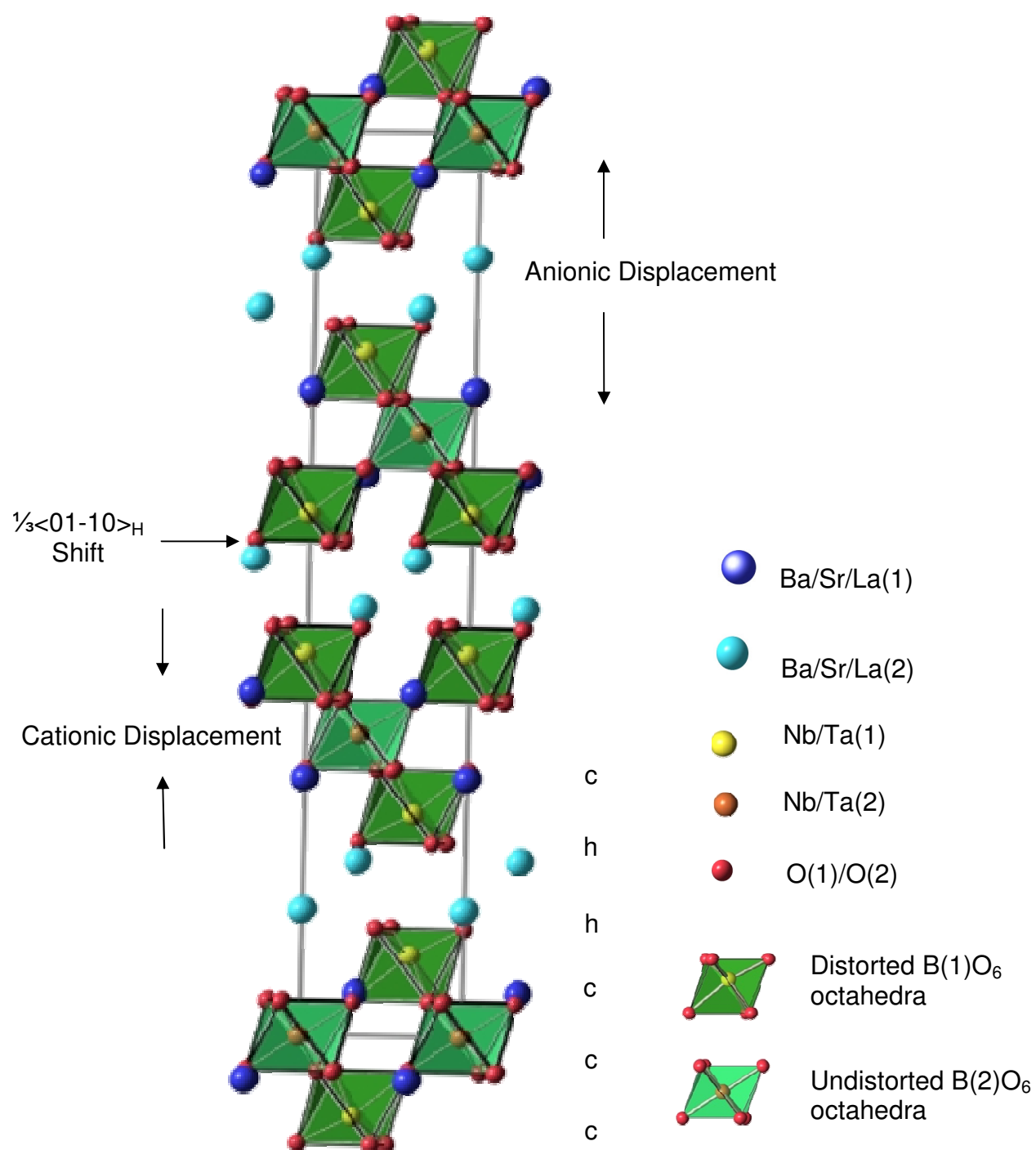
Figure 4.85: Structure of BaSr$_2$LaNbTa$_2$O$_{12}$ viewed along the *x*-axis.

Using method (iv) only slight site preferences are displayed by the B-cations with 69% of Ta^{5+} preferring to occupy B(1) and 37% of Nb^{5+}. These results are unexpected, as previous results would suggest the opposite. Therefore as the preference is only slight, it is still valid to suggest that when Ta^{5+} is the dominant pentavalent B-cation, no significant preference to inhabit the distorted B(1) site is displayed. The two different B-cation environments can be seen in *figures 4.86* and *4.87*.

The Δd values are 54.45 and 0 for B(1) and B(2) respectively. The BO_6 octahedra are antiphase tilted about the z-axis by an angle of 9.5°, *figure 4.88*.

The dominant divalent A-cation in the structure, Sr^{2+} displays a preference for A(2) with a 62% occupancy, as does Ba^{2+} with an occupancy of 33%. Whereas La^{3+} exhibits a preference for A(1) with an occupancy in this site of 45%.

The cubo-octahedral environment of the A-cations can be seen in *figures 4.89* and *4.90*. There are 3 x A(1)-O bonds of 2.590(4) Å and 3 x A(1)-O bonds of 2.890(4) Å pointing towards neighbouring octahedral layers, along the direction of the z-axis, and 3 x A(1)-O bonds of 2.608(5) Å and 3 x A(1)-O bonds of 3.104(5) Å parallel to the xy-plane pointing towards BO_6 units in the same octahedral layer.

For the A(2) cations there are 3 x A(2)-O bonds of 2.657(3) Å pointing into vacant shifted region and 3 x A(2)-O bonds of 3.250(3) Å pointing towards triple layers of B-site cations, and 3 x A(2)-O bonds of 2.647(2) Å and 3 x A(2)-O bonds of 3.146(2) Å parallel to the xy-plane pointing towards BO_6 units in the same octahedral layer. The A(2) cations are displaced into shifted region and the degree of shift for both A-cations can be seen in *figure 4.93.*

The AO_{12} polyhedra again are in a more distorted environment in the "shifted" region, A(2), than in the perovskite block, A(1), with distortion values of $\Delta d = 88.71$ and $\Delta d = 57.95$ correspondingly. This can be seen more clearly in *figures 4.91* and *4.92* where the distorted A-O lattices are projected along the z-axis.

Bond valence sums (BVS) were performed for the structure (refer to *section 1.1.1, equation 1.2* and *1.3*), values are listed in *table 4.34* Overall the BVS calculations reveal some considerably inflated values for B(2) and B(1), which suggest there are

issues with the refinement. Taking into consideration the presence of an impurity phase and the differences observed in the B-site occupancies for the XRPD refinement compared to the joint refinement, then these results must be interpreted with care. It is probable that there are other factors to consider for the $BaSr_2LaNbTa_2O_{12}$ composition, but another suitable refinement approach has yet been found.

Cation	Theoretical BVS	Calculated BVS	Status
A(1)	2.44	2.37	Under-bonded
A(2)	2.06	2.38	Over-bonded
B(1)	5.00	6.39	Over-bonded
B(2)	5.00	6.23	Over-bonded

Table 4.34: BVS calculation results for $BaSr_2LaNbTa_2O_{12}$

3 x B(1)-O(1) = 2.161(3) Å

6 x B(2)-O(1) = 1.986(3) Å

3 x B(1)-O(2) = 1.864(2) Å
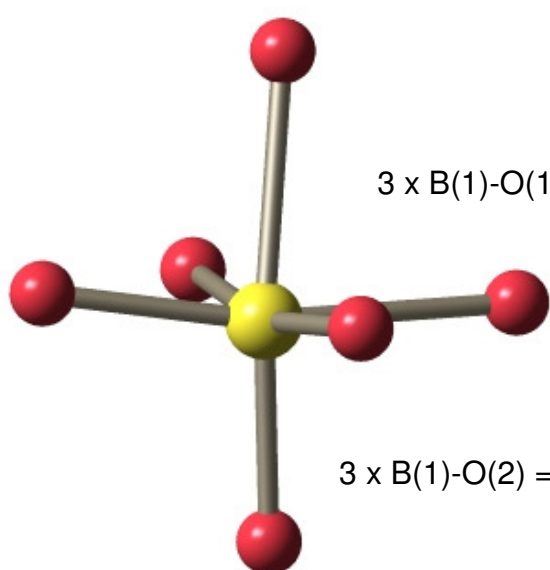
Figure 4.86 Distorted B(1)O$_6$ octahedron adjacent to the "shifted" region (red spheres O^{2-}, yellow sphere B(1) cation). Associated bond lengths labelled.
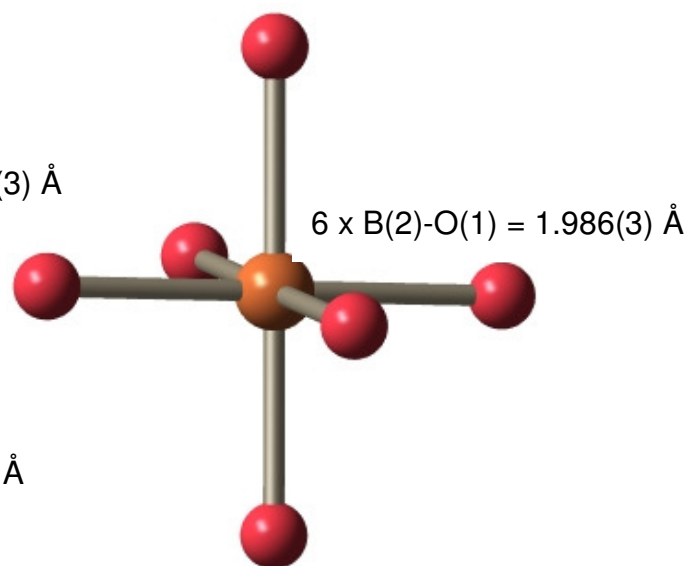
Figure 4.87: Undistorted B(2)O$_6$ octahedron in the centre of the perovskite block (red spheres O^{2-}, orange sphere B(2) cation). Associated bond lengths labelled.
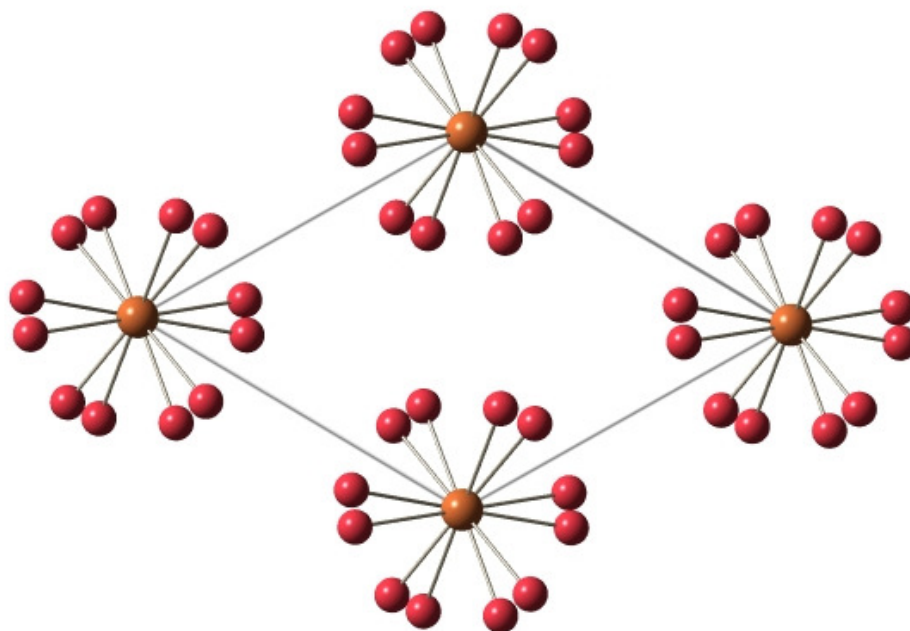

Figure 4.88: View of BaSr$_2$LaNbTa$_2$O$_{12}$ structure along the z-axis showing tilting of the octahedra, tilt angle 9.5° [a$^-$ a$^-$ a$^-$] (octahedra omitted for clarity). (Red spheres O^{2-}, orange spheres Nb^{5+}/Ta^{5+}).
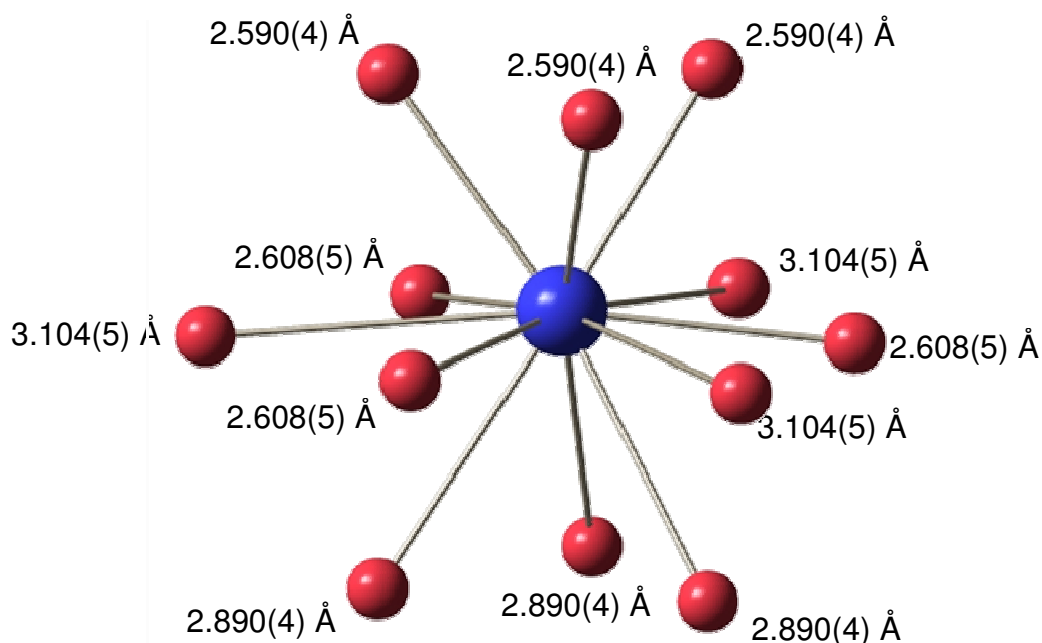
Figure 4.89: Cubo-octahedral environment of A(1) cations located within the triple layer of BO_6 octahedra with Ba^{2+} / La^{3+} / Sr^{2+} distribution of 0.17 / 0.38 / 0.45 (red spheres O^{2-}, blue sphere Ba^{2+}/ La^{3+}/ Sr^{2+}). Bond lengths are labelled.
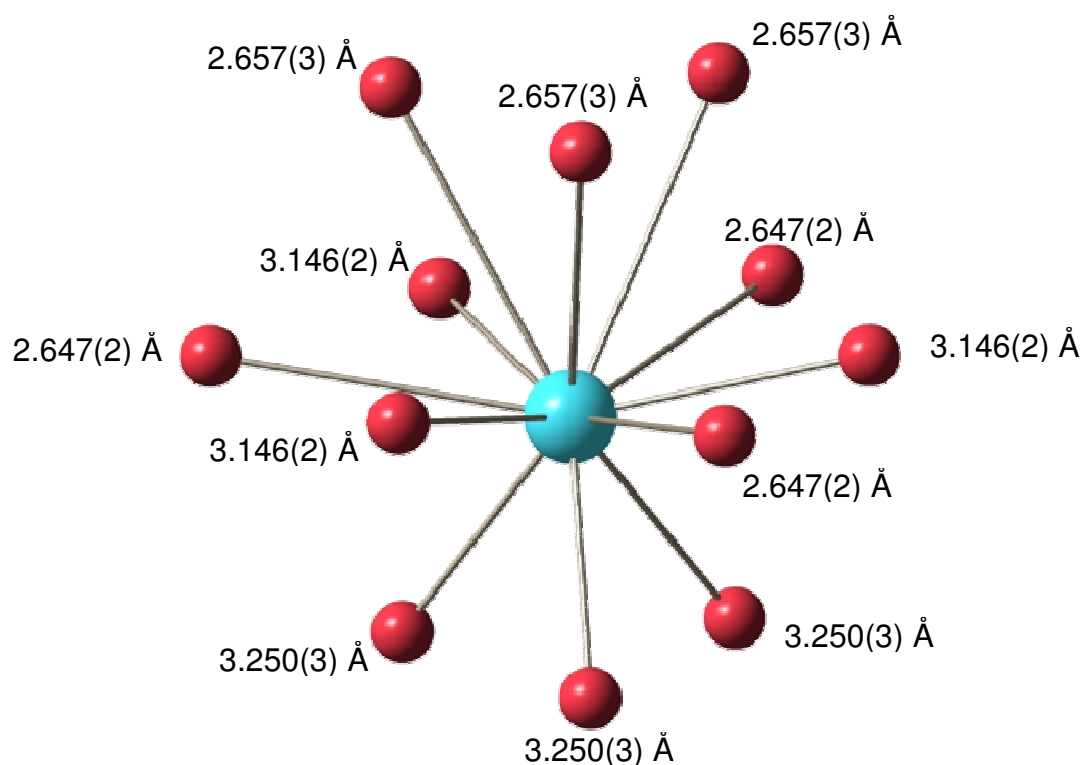

Figure 4.90: Cubo-octahedral environment of A(2) cations located in "shifted" region with a Ba^{2+} / La^{3+} / Sr^{2+} distribution of 0.33 / 0.62 / 0.05 (red spheres O^{2-}, blue sphere Ba^{2+}/ La^{3+}/ Sr^{2+}).Bond lengths are labelled.
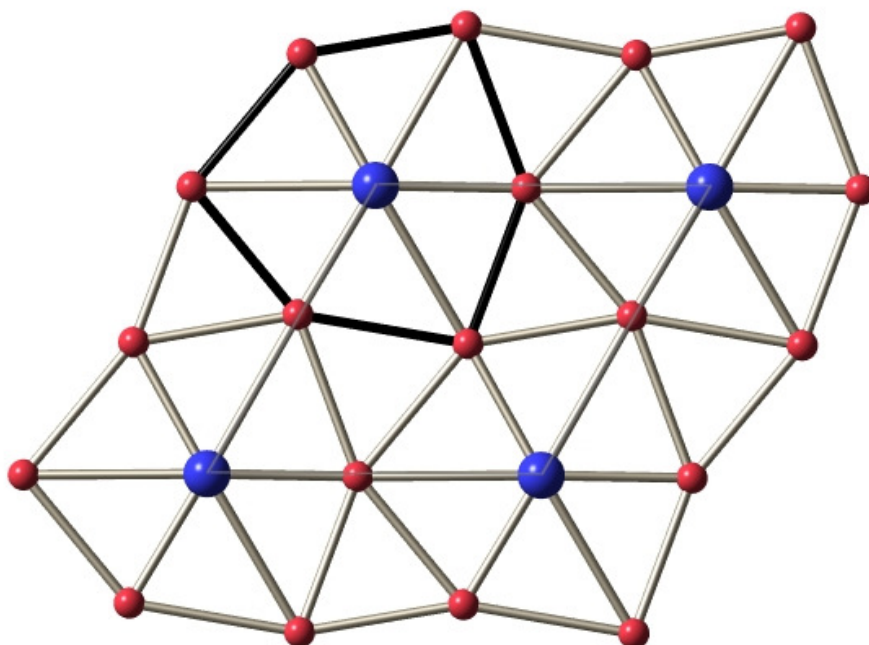
Figure 4.91: View of the distorted A(1)-O lattice along the *z*-axis, O^{2-} ions not parallel to the *xy*-plane are omitted for clarity. Black outline shows a "slice" through the AO_{12} polyhedra, 3 x A(1)-O bonds of 2.608(5) Å and 3 x A(1)-O bonds of 3.104(5) Å parallel to the *xy*-plane. A-cations are on the corners of the unit cell, outlined in grey. (Red spheres O^{2-}, blue spheres Ba^{2+} / La^{3+}/ Sr^{2+}).
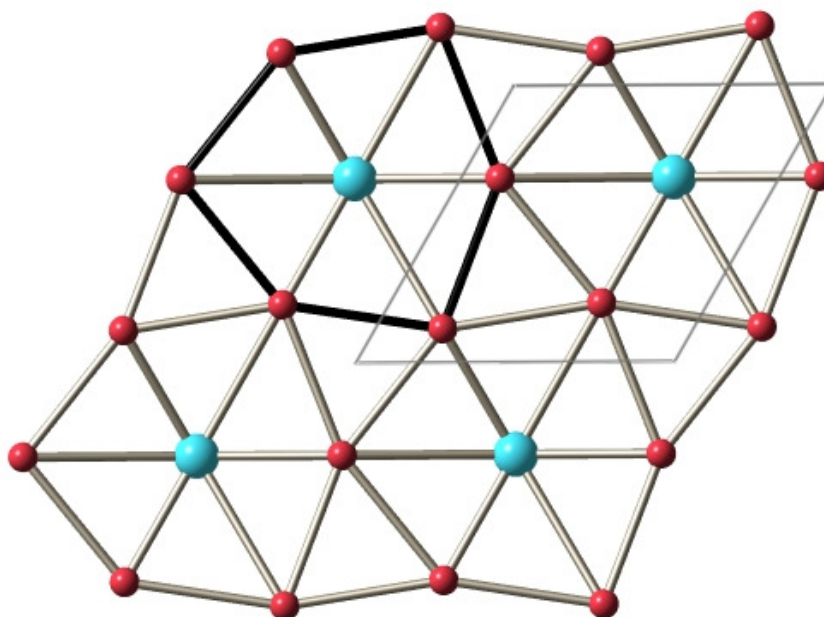
Figure 4.92: View of the distorted A(2)-O lattice along the *z*-axis, O^{2-} ions not parallel to the *xy*-plane are omitted for clarity. Black outline shows a "slice" through the AO_{12} polyhedra, 3 x A(1)-O bonds of 3.146(2) Å and 3 x A(1)-O bonds of 2.647(2) Å parallel to the *xy*-plane. Unit cell is outlined in grey. (Red spheres O^{2-}, blue spheres Ba^{2+} / La^{3+}/ Sr^{2+}).
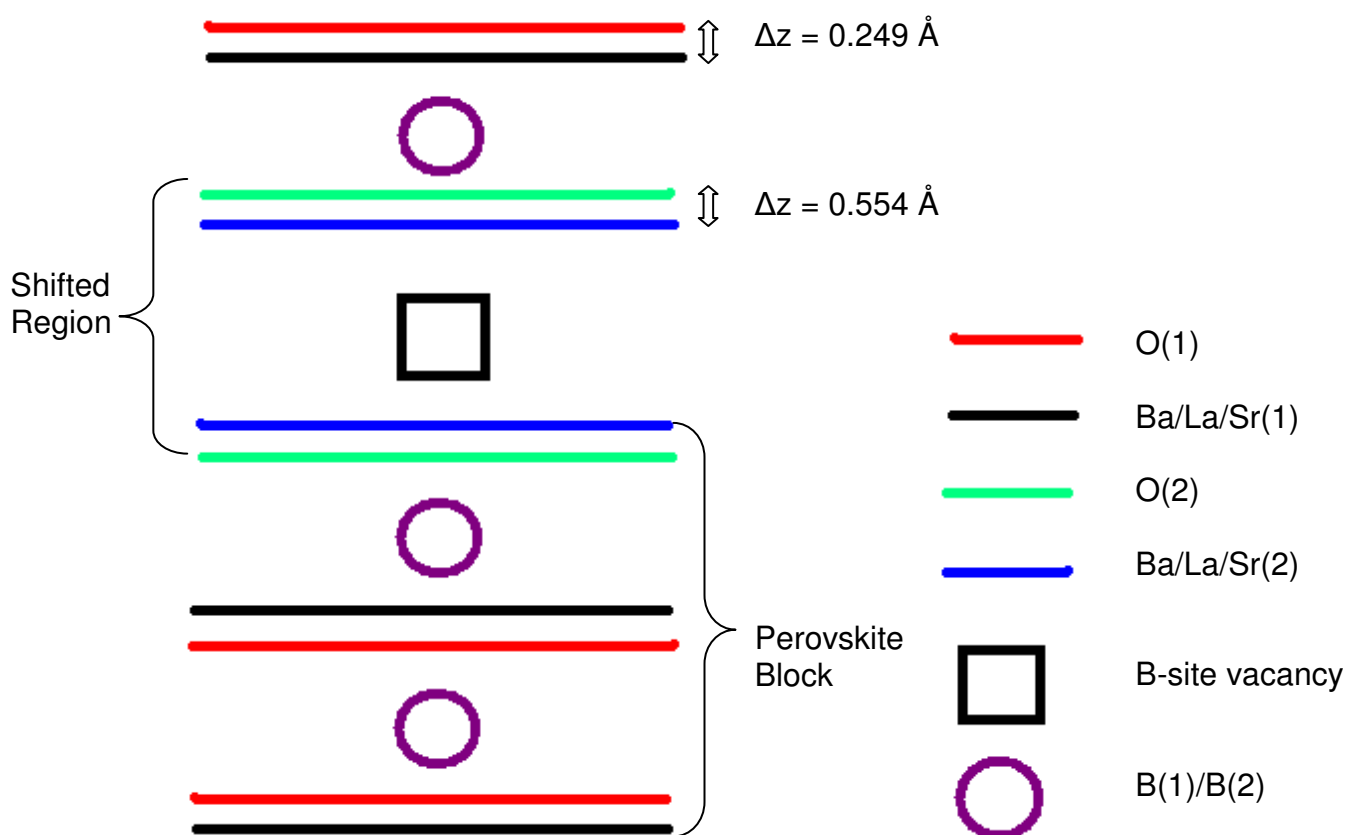
Figure 4.93: A schematic diagram showing A-O displacement along the *z*-axis (Δz) for BaSr₂LaNbTa₂O₁₂ (not to scale).
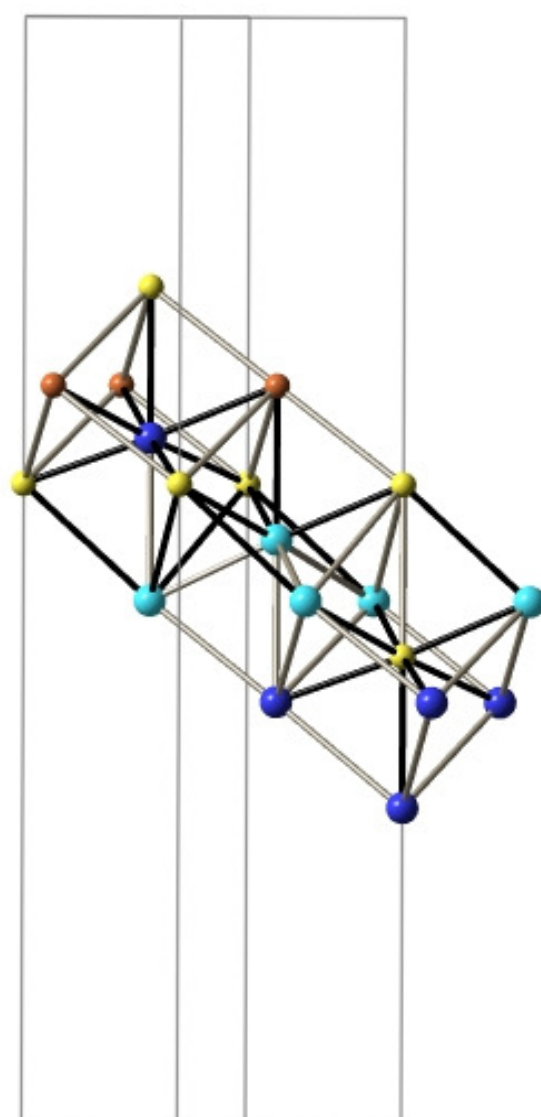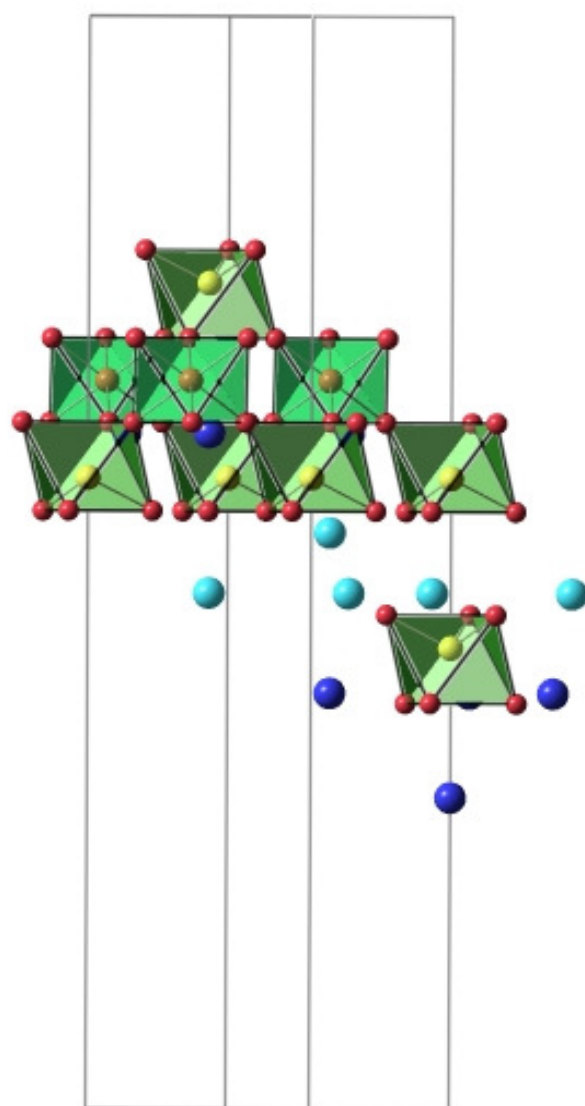
ERROR: undefined
OFFENDING COMMAND: '~

STACK: